Formation and Decay of a Bose-Einstein Condensate in Atomic Hydrogen

by

Stephen C. Moss

Submitted to the Department of Physics
in partial fulfillment of the requirements for the degree of

Doctor of Philosophy

at the

MASSACHUSETTS INSTITUTE OF TECHNOLOGY

June 2002

Author ....
Department of Physics
March 1, 2002

Certified by. ....
Daniel Kleppner
Lester Wolfe Professor of Physics
Thesis Supervisor

Certified by.... ....
Thomas J. Greytak
Professor of Physics
Thesis Supervisor

Accepted by.. ....
Thomas J. Greytak
Chairman, Department of Physics Graduate Committee

Formation and Decay of a Bose-Einstein Condensate in Atomic Hydrogen

by

Stephen C. Moss

Submitted to the Department of Physics
on March 1, 2002, in partial fulfillment of the
requirements for the degree of
Doctor of Philosophy

Abstract

The formation and decay of a Bose-Einstein condensate (BEC) in atomic hydrogen is studied. Magnetically trapped hydrogen atoms were evaporatively cooled close to the onset of Bose-Einstein condensation and then suddenly quenched below the transition temperature. The subsequent condensate formation and decay were observed using time-resolved laser spectroscopy of the two-photon $1S-2S$ transition.

Theory is developed to quantitatively describe the formation and decay of the condensate using a modified version of the time-dependent theory developed previously by Bijlsma, Zaremba and Stoof [Phys. Rev. A **62**, 063609 (2000)]. The modifications consist of properly including dipolar spin-relaxation processes that occur in a doubly spin-polarized atomic gas and the experimental evaporative cooling procedure used to quench the gas below the critical temperature. The modifications are essential for understanding the hydrogen condensate formation experiments, and our simulations are in good quantitative agreement with experiment.

In our comparison between theory and experiment, we find that a condensate of atomic hydrogen has the same collisional frequency shift of the two-photon $1S-2S$ resonance as a noncondensed gas at the same density. This finding contradicts theoretical predictions of the collisional shift for trapped samples with a homogeneous density. We suggest that elastic collisions occuring during the laser excitation process destroy correlations between the excited $2S$ atom and the $1S$ background, leading to a collisional frequency shift for the noncondensed gas half as large as predicted.

Thesis Supervisor: Daniel Kleppner
Title: Lester Wolfe Professor of Physics

Thesis Supervisor: Thomas J. Greytak
Title: Professor of Physics

Acknowledgments

I am very fortunate in my life to be surrounded by caring, supportive people. The most influential people in my life are my parents, Calvin and Fay Moss. As a child they encouraged me to ask questions, try new things, and perform at a high level. This thesis is dedicated to them because they taught me the fundamental skills necessary to complete a Ph.D. thesis.

Near the end of my undergraduate studies at Rice University, I met Jennifer Goldman. We began a wonderful relationship just before I graduated, and our relationship blossomed into something very special. In fact, we were married just eleven days after I defended this thesis! Throughout my graduate career she supported me without question. She encouraged me when I was frustrated and celebrated my successes. She even tolerated my physics jokes. I am very fortunate to be married to her.

My house mate for the past three years, Ryan Lawrence, also livened my graduate school years. Ryan was also a physics graduate student and was familiar with the ups and downs of experimental science. In addition to offering sound advice about equipment and calculations, he made sure I never forgot to take a break and have some fun. I value his friendship greatly, and I expect it will continue for a long time to come.

When I arrived at MIT, I had the choice of working in several different labs. The people I met in the lab of Professor Daniel Kleppner and Professor Thomas Greytak made the decision easy. Daniel Kleppner and Thomas Greytak served as coadvisors for this thesis. Their hands-off approach allows students to take ownership of both successes and failures. This creates an excellent environment in which to become a skilled experimental physicist. Successes were met by praise and good questions. Failures were met by encouragement and more good questions! I particularly enjoyed weekends of water sports at Professor Greytak's summer home and leaf-peeping trips to Professor Kleppner's Vermont home.

This thesis would not have been possible without the close collaboration of Pro-

fessor Henk Stoof of the University of Utrecht in The Netherlands. Professor Stoof's theoretical contributions to the problem of Bose condensation underly most of the theoretical content of this thesis. I am very fortunate that Professor Stoof spent two months at MIT during early 2001 and that we were able to work together on the problems presented in this thesis. Professor Stoof renewed my enthusiasm for physics and taught me much about theoretical physics. His full-time students are fortunate to have such an excellent mentor.

I am greatly indebted to both David Landhuis and Lorenz Willmann. David and I joined the group within about one month of each other and quickly became friends. Our talents and interests were complementary to one another. He grew into the role of expert laser operator while I favored the cryogenic portion of the experiment. This thesis would not have been possible without his tireless attention to maintaining and improving the laser system. Lorenz joined the group as a postdoc a few months after me. He brought with him a wealth of experience, and he immediately applied it to the experiment. More than his physics knowledge, I appreciated his wit, our physics/coffee chats on the stairs of the student center, and his friendship. Without his professional and personal contributions, this thesis would have taken a lot longer and been a lot less fun!

The educational model in our group is one of mentorship. Three early mentors taught me about low-temperature physics and how to survive graduate school: Dale Fried, Tom Killian, and Adam Polcyn. Dale and I shared an office for about three years. His enthusiasm for the experiment, his passion for tinkering in the lab, and his desire to completely understand the physics at hand were all contagious and carried me through the early years of graduate school. Tom was the laser expert when I arrived at MIT. He not only taught me about the laser but about how to work hard and to think through tough problems. Tom is one of the most balanced people I know, and I wish him success at my alma mater: Rice University. While I was at MIT, Adam spend most of his time working on a different low temperature experiment. We shared many competitive games of tennis together, and he served as a sounding board for me. Having spent time on the hydrogen experiment, he was both knowledgeable and detached – a very valuable combination for an advisor. His encouragement was instrumental in seeing me through the general exams.

David, Lorenz, and I are now moving on to other things, but we are leaving the experiment in the capable hands of Julia Steinberger, Kendra Vant, Lia Matos and Cort Johnson. Julia is another soul who prefers to work late into the evening. We spent many late nights working away to strange music (e.g. *Tunak, tunak, tun*) and drinking coffee. Julia brings a healthy skepticism to bear on the experiment. Her ability to critically examine the system will serve her well as she conducts her thesis research. I will most remember Julia for being a reliable coffee buddy – always ready to go for a cup. A special thanks goes to Julia for housing me after my lease expired and for helping me jump through administrative hoops on the way to submitting this thesis. Kendra also deserves special thanks since she spent most of the late nights with me in the lab collecting the data in this thesis. Without her careful attention to detail, I am certain the experiments would have taken much longer. She brings a tenacious quest for understanding to the experiment, and I am sure that her time at MIT will be marked by success. Lia also possesses a deep desire for knowledge. Lia and I have shared an office for the past two and a half years. Her disposition is among the sunniest in physics, and her energy and enthusiasm are contagious. Her willingness to take risks in learning about new subjects will serve her well as she moves through her career. Cort is one of the newest members of the lab. His patience and gentle disposition will serve him well on this experiment.

MIT undergraduates have also contributed to our lab. Among these are Sourav Mandal and Mukund Vengalattore. I have enjoyed spending time with both of them, and it has been a pleasure to watch them develop as physicists. Both bring a passion toward learning and a desire to craft an elegant solution to problems. Sourav helped me to design the diode laser setup in the group, and Mukund is a master of both electronics and tennis. I wish them both well in their careers.

The lab has also been home to a number of visitors over the past few years. Among these Jan Heemskerk and Walter Joffrain stand out. Jan brought levity and dutch cryogenic know-how to the group. Walter, better known as "The Pope" within our group, was a quiet, hard-working fellow with a passion for history and music, not to mention physics. I will not forget the ice cream parties he threw for the group. His kindness and generosity will serve him well in life.

The atomic physics community at MIT is a special one. In many ways, it functions like a large family. Two of my "brothers" in this family are Tony Roberts and Simon Rainville. I met both Tony and Simon during my first month of graduate school. We shared the first year grind and weathered the general exams together. It was through experiences such as studying for the oral exam that we became close friends. I will never forget my epic tennis matches with Tony nor windsurfing the Charles River with Simon. Both Tony and Simon are destined for success because of their patience and quiet determination.

James Thompson and Joel DeVries also played a key role in my graduate experience: getting me out of the lab! Our weekly basketball games gave me an opportunity to blow off steam and to mingle with people in other labs at different points in their graduate careers. Joel's perseverance in carrying out a difficult experiment largely alone will probably make his future lab projects look easy. I have always been impressed by James' ability to ask penetrating questions and to break down problems quickly. This ability will serve him well in his career.

I should also not fail to mention our neighbors in building 13. Especially during my job search and the writing of my thesis, Paul Glicofridis (of the Ashoori group) was a valuable friend. I learned much from him in terms of standing up for myself and seeing things in a cut-and-dried way. We kept each other company during our 18 hour days of thesis writing. Without him I am not sure I could have kept up the pace. Gary Steele and Oliver Dial, also students of Professor Ashoori, gave timely and valuable assistance with our computer network. I have a special bond with Gary in that he has inherited my responsibilities with the helium liquefier. He is the perfect successor; he is reliable, organized, and has a good feel for mechanical devices. I am confident that these abilities in combination with his enthusiasm for condensed matter physics will produce an excellent physicist.

Several other people in the MIT Physics Department played an important role. In addition to my advisors, Professor Wolfgang Ketterle was always available to answer questions and discuss difficult problems. Friday lunches with him were a particular pleasure. Carol Costa is well-known within the MIT atomic physics community as the person who keeps things going. Her assistance in setting up meetings with professors, scheduling rooms, and navigating internal bureaucracy made many things easier for me at MIT. Carol Breen was always a source of encouragement to me. She sympathized with me when I had trouble and provided sage advice. She also made sure I got away from the lab, especially on sunny days when it was a crime to be inside. I will miss her wit and MIT faculty anecdotes.

Looking back on my MIT career I will most remember the people I met. They enriched my life, and I tried to learn from the lessons they taught me. I hope that I will see all of them again soon.

Contents

List of Figures

List of Tables

Chapter 1

Introduction

In the period immediately preceding the 1995 observation of Bose-Einstein condensation (BEC) in trapped atomic gases [2, 13, 21], experimentalists in laboratories scattered around the world struggled to observe the second-order phase transition predicted by Einstein in 1925 [28]. Meanwhile, an intense debate raged among theorists concerning the likely rate of formation. Predictions for the time scale of formation ranged from infinite [75] to very short [113]. The experimental observation of condensates in Rb [2], Na [21], and Li [13] proved that condensates form in a relatively short time. The excitement surrounding the discovery of BEC shifted most activity into the investigation of the equilibrium properties of these novel systems, and a substantial body of experimental and theoretical information is now available (see for example [19]).

In 1998 our laboratory achieved a BEC in atomic hydrogen [31], culminating a twenty year search. Hydrogen condensates share many characteristics with condensates of alkali metal atoms, but there are several notable differences. Among these is the anomalously small *s*-wave scattering length, a. Consequences of the small scattering length include large condensate densities and a low elastic scattering rate. The low scattering rate retards evaporative cooling and complicates the production of H condensates, but it also increases the time scale for formation of the condensate, simplifying the task of studying condensate growth in detail.

The dynamics of a system near a second-order phase transition is of interest for many areas of physics. The study of critical dynamics has a long history, but in recent years interest has been renewed due to the growing number of systems displaying signatures of a quantum phase transition [103]. In addition to BEC in trapped atomic gases [60, 75, 76, 109, 112, 113, 115], the general problem of second-order phase transitions is relevant to problems ranging from superfluidity in ^{4}He [48] to cosmology [43, 64, 77, 137]. Until recently there has been little experimental data that could be compared directly with theory.

In this thesis we report detailed experimental observations of the formation and decay of a Bose-Einstein condensate in trapped atomic hydrogen. Other experimental studies of condensate growth have been performed: in ^{7}Li [38], in ^{23}Na [83], and in ^{87}Rb [72]. Interestingly, the physics of condensate growth is different in each of the four atomic species. Atomic ^{7}Li is a Bose gas with effectively attractive interactions, whereas atomic H, ^{23}Na, and ^{87}Rb have effectively repulsive interactions. In the case of ^{7}Li, Bose-Einstein condensation competes with ordinary (classical) condensation; the condensate population is limited to a relatively small number [5, 12, 54, 101, 102] and undergoes growth and collapse cycles [104, 105]. Consequently, the ^{7}Li experiment provides experimental data that is particularly suited for studying the initial stage of condensate growth when the mean field interaction is still small compared to the energy-level spacing of the harmonic trapping potential. This is known as the weak-coupling or single-mode regime and is dominated by incoherent, i.e. kinetic, processes.

For a gas with repulsive interactions, there is no limit to the condensate number, and subsequent stages of condensate growth can be studied experimentally. In these stages the mean-field interaction energy becomes much larger than the energy-level spacing in the harmonic trap. This is the strong-coupling or multi-mode regime in which both coherent and incoherent processes lead to a further growth of the condensate [20, 60, 113, 114, 116]. In the case of atomic hydrogen, decay of the trapped gas due to inelastic two-body collisions has a significant influence on the formation of the condensate and must be included for quantitative comparison of theory with experiment. Previous theoretical work was devoted primarily to understanding the ^{23}Na experiment and did not require a description of the decay of the gas [7, 22, 37]. In collaboration with Professor Henk Stoof,[1] we have extended the work of Bijlsma *et al.* [7] to include decay processes and the effects of rf evaporation on the thermal cloud. The theory presented in this thesis is of a mean-field nature. As a result it cannot immediately be applied to the recent ^{87}Rb experiment [72] that appears to investigate the intermediate coherent stage of condensate growth. For that stage we need a theory that also includes the effect of density and phase fluctuations of the condensate, for example by solving an appropriate stochastic nonlinear Schrödinger equation [118].

This thesis presents detailed experimental and theoretical studies of the formation and decay of a Bose-Einstein condensate of atomic hydrogen. The thesis is organized as follows. Chapter 2 discusses the fundamental aspects of condensation of a gas of bosons and introduces concepts and quantities that will be used throughout the thesis. Chapter 3 describes the techniques and apparatus used to trap and cool atomic hydrogen to degeneracy. The cryogenic aspects of the hydrogen experiment lead to unique challenges in the design of the trapping apparatus. Chapter 4 covers the design and construction of the trapping cell used in these experiments. Near the degenerate regime, hydrogen is probed using high-resolution two-photon spectroscopy of the $1S$-$2S$ transition. Spectroscopy of the trapped sample is described in Chapter 5, and techniques for observing and understanding the condensate contribution to the $1S$-$2S$ spectrum are described in Chapter 6. The experimental observations of the formation and decay of the hydrogen condensate are presented in Chapter 7. Finally, the theory describing the growth and decay of the hydrogen condensate is developed in Chapter 8, and a quantitative comparison is made between experiment and theory in Chapter 9.

---

[1] Institute for Theoretical Physics, University of Utrecht, The Netherlands

Chapter 2

Elementary Theory of Bose-Einstein Condensation

This chapter gives a brief overview of the physics of Bose-Einstein condensation. Its purpose is to review concepts that are necessary for understanding the work in this thesis and to define quantities that will be used later in describing the growth and decay of a hydrogen condensate. Two much more extensive reviews of BEC theory are [14, 19].

2.1 Bosons and Bose Statistics

Classical statistical mechanics no longer applies when a collection of identical particles is brought to a regime where quantum effects become important. In the quantum regime, particles are described by wavepackets or wavefunctions. A quantum-mechanical description of a system of N identical particles consists of wavefunctions that are either symmetric or anti-symmetric under the exchange of two particles. Particles described by symmetric wavefunctions obey Bose-Einstein statistics and are called *bosons.* Anti-symmetric wavefunctions, on the other hand, describe *fermions* which obey Fermi-Dirac statistics.

Using relativistic quantum field theory, one can show an intimate connection between the statistics governing the behavior of particles and their intrinsic spin [89]. Bosons are particles with integer (in units of $\hbar$) quantum-mechanical spin, while fermions have half-integer spin. Some examples of bosons include photons, phonons, ^{4}He atoms, and hydrogen atoms. Fermions include electrons, protons, neutrons, and ^{3}He atoms.

Consider a gas of N identical noninteracting bosons in a box of volume V in the thermodynamic limit ($N, V \rightarrow \infty$ with N/V = constant). The occupation function for single particle energy eigenstates is given by

$$f_{BE}(\epsilon) = \frac{1}{e^{(\epsilon-\mu)/k_BT} - 1}. \tag{2.1}$$

The Lagrange multipliers μ and T constrain the system to have the correct total population and total energy through [55]

$$N = \int d\epsilon \, \rho(\epsilon) f_{BE}(\epsilon) \tag{2.2}$$

and

$$E = \int d\epsilon \, \epsilon\rho(\epsilon) f_{BE}(\epsilon) \ , \tag{2.3}$$

where $\rho(\epsilon)$ is the density of single particle states as a function of energy. The physical interpretation of the Lagrange multipliers is that μ represents the chemical potential and T the temperature of the system.

2.2 What is Bose-Einstein Condensation?

In 1925 Einstein considered N noninteracting, nonrelativistic bosonic particles in a cubic box of volume L^3 with periodic boundary conditions [28]. In the thermodynamic limit, a phase transition occurs at a temperature T_c defined by:

$$n\lambda_{dB}^3(T_c) = \zeta(3/2) = 2.612\ldots \tag{2.4}$$

where n is the number density of the particles. The de Broglie wavelength is a function of temperature

$$\lambda_{dB}(T) = \left(\frac{2\pi\hbar^2}{mk_BT}\right)^{1/2}, \tag{2.5}$$

and $\zeta(\alpha) = \sum_{k=1}^{\infty} 1/k^{\alpha}$ is the Riemann Zeta function. In other words, Bose-Einstein condensation is a phase transition that occurs when a collection of identical bosons is cooled to the point that their quantum mechanical de Broglie waves overlap. This phase transition takes place in the absence of interactions between the bosons; it is completely statistical in nature.

The single particle ground state of this system is a plane wave with momentum $\mathbf{p} = 0$. If we denote the number of particles in the ground state by N_0, the order parameter of this phase transition is the fraction N_0/N of particles in the ground state. For temperatures above the critical temperature, $T > T_c$, the fraction of particles in the ground state is in effect zero. In contrast for $T < T_c$,

$$\frac{N_0}{N} = 1 - \left(\frac{T}{T_c}\right)^{3/2}. \tag{2.6}$$

and a macroscopic fraction of the particles occupy the ground state. In other words, a Bose-Einstein condensate in $\mathbf{p} = 0$ has formed. The macroscopic occupation of a single quantum state is the key feature of a Bose-Einstein condensate.

2.3 Ideal Bose Gas in a Harmonic Trap

In this section we consider Bose-Einstein condensation of a noninteracting gas in a harmonic trap. Although interactions play an important role in our experiments, a quick study of the noninteracting gas points to important length and energy scales in the problem.

2.3.1 Noninteracting Condensate

The magnetic trapping potential in most BEC experiments can be safely approximated by an anisotropic harmonic oscillator potential

$$U_{\text{ext}}(\mathbf{r}) = \frac{m}{2}(\omega_x^2 x^2 + \omega_y^2 y^2 + \omega_z^2 z^2). \tag{2.7}$$

The single particle eigenvalues for the eigenstates of this potential are given by

$$\epsilon_{n_x n_y n_z} = \left(n_x + \frac{1}{2}\right)\hbar\omega_x + \left(n_y + \frac{1}{2}\right)\hbar\omega_y + \left(n_z + \frac{1}{2}\right)\hbar\omega_z, \tag{2.8}$$

where $\{n_x, n_y, n_z\}$ are nonnegative integers. If N noninteracting bosons are confined by the potential in Eq. (2.7), the ground state can be obtained by putting all of the particles in the lowest single particle state ($n_x = n_y = n_z = 0$). That is, $\phi(\mathbf{r}_1, \ldots, \mathbf{r}_N) = \prod_i \varphi(\mathbf{r}_i)$, where

$$\varphi_0(\mathbf{r}) = \left(\frac{m\bar{\omega}}{\pi\hbar}\right)^{3/4} \exp\left[-\frac{m}{2\hbar}\left(\omega_x x^2 + \omega_y y^2 + \omega_z z^2\right)\right]. \tag{2.9}$$

The geometric average of the harmonic oscillator frequencies has been introduced as $\bar{\omega} = (\omega_x \omega_y \omega_z)^{1/3}$. This single parameter characterizes the magnetic trap both in this simple theory and in the more complicated interacting, nonequilibrium theory that is discussed in Chapter 8.

In the absence of interactions, the ground state density distribution for particles in the trap at $T = 0$ grows with N, $n(\mathbf{r}) = N|\varphi_0(\mathbf{r})|^2$, but the size of the cloud is fixed by the *harmonic oscillator length*

$$\ell = \left(\frac{\hbar}{m\bar{\omega}}\right)^{1/2}, \tag{2.10}$$

independent of N. This introduces the first length scale in the problem and can be understood as the mean half width of the Gaussian ground state (Eq. 2.9). For typical hydrogen condensates in this thesis, $\bar{\omega} \sim 2\pi \times 245$ Hz giving $\ell = 6.4$ μm.

As we saw above, at finite temperatures only a fraction of the atoms occupy the ground state of the potential, while the remaining atoms are thermally distributed throughout the excited states. We will restrict our discussion to the interesting regime $k_B T \gg \hbar\bar{\omega}$. Here Bose-Einstein statistics allow the accumulation of many particles in the lowest quantum state while having the system in contact with a thermal bath at a temperature much greater than the average level spacing in the trap $\hbar\bar{\omega}$ – a result completely at odds with classical Boltzmann statistics. In the opposite regime, $k_B T \ll \hbar\bar{\omega}$, even Boltzmann statistics would allow large occupation of the ground state.

A crude estimate of the radius of the thermal cloud can be made by assuming that the density of the thermal cloud is given by a classical Boltzmann distribution, $n_{\text{th}}(r) \propto \exp\left[-U_{\text{ext}}(r)/k_B T\right]$. Using $U_{\text{ext}} = (1/2)m\bar{\omega}^2 r^2$ gives the half width of the Gaussian thermal cloud, $R_{\text{th}} = \ell(k_B T/\hbar\bar{\omega})^{1/2}$. For a typical hydrogen condensate at $T \sim 40$ μK in a trap where $\hbar\bar{\omega} = 12$ nK, $R_{\text{th}} = 374$ μm which is much larger than ℓ.

Momentum space distribution

We can also find the momentum space distribution of the condensate by the taking the Fourier transform of the ground state wavefunction. Since the position space wavefunction is a Gaussian, the momentum space distribution is also a Gaussian centered at zero momentum with a width proportional to $1/\ell$. Again assuming a classical distribution function for the thermal cloud, one finds a momentum distribution proportional to $(k_B T)^{1/2}$. We will see this again in Sec. 5.5.2. For an ideal gas in a harmonic trap, the momentum distributions of the condensed and noncondensed particles are exactly the same as the density distributions n_0 and n_{th}.

The discussion above illustrates that condensation in a trap manifests itself as a narrow peak in *both* position and momentum space. This is in contrast to the uniform gas where condensation takes place only in momentum space. In our experiment both manifestations are detected.

2.4 Trapped Bosons at $T > 0$

At finite temperatures the grand canonical ensemble is used to describe the trapped Bose gas. In particular, the total number of particles at a temperature T is given by

$$N = \sum_{n_x, n_y, n_z} \frac{1}{e^{\beta(\epsilon_{n_x n_y n_z} - \mu)} - 1}, \tag{2.11}$$

where $\beta = 1/k_B T$ and μ is the chemical potential. The energy of the lowest state is given by $3/2\,\hbar\,\omega_{\mathrm{avg}}$, where $\omega_{\mathrm{avg}} = (\omega_x + \omega_y + \omega_z)/3$. As T is lowered, μ, which starts out negative, increases in order to maintain the value of the sum at N. At some temperature T_{c} this process brings μ up to the energy of the single particle ground state, $3/2\,\hbar\,\omega_{\mathrm{avg}}$. At that point the mean occupation number of the ground state becomes undefined (i.e. infinite). For $T = T_{\mathrm{c}}$ and all lower temperatures, Eq. (2.11) must be supplemented by a separate expression for the occupation of the single particle ground state. The occupation will be macroscopic, that is a finite fraction of all the atoms in the gas. For $T \leq T_{\mathrm{c}}$, μ remains pinned at the single particle ground state energy. The macroscopic occupation of the single particle ground state corresponds to the onset of Bose-Einstein condensation.

Transition temperature

We can calculate the temperature at which condensation occurs for trapped bosons in the absence of interactions. The usual approach is to separate the contribution due to the ground state from the sum in Eq. (2.11) and replace the sum over harmonic oscillator states by an integral over energy, making use of Eq. (2.8). This semiclassical approximation is excellent in our case since $k_B T \gg \hbar\bar{\omega}$, i.e. the characteristic excitation energy of particles in the trap is much larger than the harmonic oscillator level spacing. It yields

$$N - N_0 = \int_0^\infty \frac{\rho(\epsilon) d\epsilon}{exp(\beta\epsilon) - 1}, \tag{2.12}$$

where we have introduced the energy density of states $\rho(\epsilon)$ and taken the ground state single particle energy to be zero. For the anisotropic harmonic oscillator $\rho(\epsilon) = (1/2)(\hbar\bar{\omega})^{-3}\epsilon^2$, and using this result one finds

$$N - N_0 = \zeta(3)\left(\frac{k_B T}{\hbar\bar{\omega}}\right)^3 , \tag{2.13}$$

where $\zeta(n)$ is the Riemann Zeta function. Finally, we can find the critical temperature by requiring that $N_0 \to 0$ at the transition:

$$k_B T_c = \hbar\bar{\omega}\left(\frac{N}{\zeta(3)}\right)^{1/3} = 0.94\,\hbar\bar{\omega}N^{1/3} \tag{2.14}$$

Equation (2.14) points out two energy scales in the trapped boson system: the transition temperature $k_B T_c$ and the average oscillator spacing $\hbar\bar{\omega}$. In current experiments N ranges from $\sim 10^3 - 10^{11}$, indicating that $k_B T_c$ is typically 20 to 4600 times larger than $\hbar\bar{\omega}$. The trapping potential sets the scale for the oscillator spacing, and for many of the condensate experiments in this thesis $\hbar\bar{\omega}/k_B = 12$ nK. Condensation occurs at $T_c \sim 35$ μK, indicating $N = 3.25 \times 10^{10}$, consistent with our observations.

Condensate fraction

The thermodynamic limit is obtained by taking $N \to \infty$ and $\bar{\omega} \to 0$ while keeping $N\bar{\omega}^3$ constant. Applying this limit to (2.14) and inserting the result into (2.13) yields the temperature dependence of the condensate fraction in a harmonic trap:

$$\frac{N_0}{N} = 1 - \left(\frac{T}{T_c}\right)^3 , \tag{2.15}$$

which can be compared to Eq. (2.6). Note that the condensate fraction grows more rapidly with decreasing temperature in the harmonic potential than in a uniform potential. For small excursions below T_c in the harmonic trap $N_0/N \approx 3(\Delta T/T_c)$. Although the number of atoms in present day traps is certainly finite, both (2.14) and (2.15) closely reproduce experimental results. At the very least these expressions can be used to guide the experimenter's intuition.

Density of thermal particles

The total density in the trap is the sum of the condensate and thermal particle densities, $n(\mathbf{r}) = n_{\mathrm{c}}(\mathbf{r}) + n_{\mathrm{th}}(\mathbf{r})$. The condensate density is again given by $n_{\mathrm{c}}(\mathbf{r}) = N_{\mathrm{c}}|\varphi_0(\mathbf{r})|^2$, and the thermal density is found by integrating the distribution function over momentum space. The result is:

$$n_{\mathrm{th}}(\mathbf{r}) = \lambda_{\mathrm{dB}}^{-3} g_{3/2}(1) \left[e^{-\beta U_{\mathrm{ext}}(\mathbf{r})}\right] , \tag{2.16}$$

where λ_{dB} is the de Broglie or thermal wavelength defined in Eq. (2.5), and $g_{3/2}(1) = 2.612\ldots$ [55]. For completeness we note that the distribution of thermal particles in momentum space can be obtained in a similar way:

$$n_{\mathrm{th}}(\mathbf{p}) = (\lambda_{\mathrm{dB}} m\bar{\omega})^{-3} g_{3/2} \left[e^{-\beta p^2/2m}\right] . \tag{2.17}$$

2.5 Ground State with Interactions

In our experiments atoms interact with one another, and the behavior of the condensate cannot be understood without taking into account these interactions. This is accomplished through quantum many-body theory. An enormous amount of work has gone into the development of the theory, but we discuss only the results critical to understanding our system.

2.5.1 Gross-Pitaevskii Equation

In second quantization the Hamiltonian describing the many-body system of N interacting bosons confined in an external potential U_{ext} is

$$H = \int d\mathbf{r}\hat{\Psi}^{\dagger}(\mathbf{r}) \left[-\frac{\hbar^2}{2m}\nabla^2 + U_{\text{ext}} \right] \hat{\Psi}(\mathbf{r}) + \frac{1}{2}\int d\mathbf{r}d\mathbf{r}'\hat{\Psi}^{\dagger}(\mathbf{r})\hat{\Psi}^{\dagger}(\mathbf{r}')V(\mathbf{r}-\mathbf{r}')\hat{\Psi}(\mathbf{r}')\hat{\Psi}(\mathbf{r}) \tag{2.18}$$

where $\hat{\Psi}^{\dagger}(\mathbf{r})$ and $\hat{\Psi}(\mathbf{r})$ are boson field operators that respectively create and destroy a particle at position $\mathbf{r}$. The two-body interaction potential is given by $V(\mathbf{r}-\mathbf{r}')$. In principle one could solve this equation and get exact results, but this is generally impractical for systems such as ours which have a large number of particles ($N > 10^8$). Instead, mean field approaches have been developed that avoid these calculational difficulties and allow the system of interacting bosons to be understood in terms of a few parameters with a clear physical meaning. In fact, mean field theory has been remarkably successful in quantitatively describing static, dynamic, and thermodynamic properties of trapped bosons [19].

In 1947, Bogoliubov formulated the mean field description of a dilute Bose gas [11] found in standard many-body theory textbooks. The salient feature is the separation of the condensate contribution from the bosonic field operator. The generalization of Bogoliubov's method to describe a nonuniform, time-dependent system is given by replacing the field operator by

$$\hat{\Psi}(\mathbf{r},t) = \Phi(\mathbf{r},t) + \hat{\Psi}'(\mathbf{r},t). \tag{2.19}$$

The function $\Phi(\mathbf{r},t)$ is usually called *the wave function of the condensate* but is more correctly a classical field with the meaning of an order parameter. The condensate density is given by the modulus, $n_c(\mathbf{r},t) = |\Phi(\mathbf{r},t)|^2$.

The wave function for the condensate is found using the Heisenberg equation of motion, and the Hamiltonian given in Eq. (2.18):

$$i\hbar\frac{\partial}{\partial t}\hat{\Psi}(\mathbf{r},t) = [\hat{\Psi}, H] = \left[-\frac{\hbar^2\nabla^2}{2m} + U_{\text{ext}}(\mathbf{r}) + \int d\mathbf{r}'\hat{\Psi}^\dagger(\mathbf{r}',t)V(\mathbf{r}'-\mathbf{r})\hat{\Psi}(\mathbf{r}',t)\right]\hat{\Psi}(\mathbf{r},t). \tag{2.20}$$

In what follows we make the assumption that $\hat{\Psi}' \equiv 0$ in Eq. (2.19). This is strictly true only in the limit of zero temperature when all particles are in the condensate, but the results we derive under this assumption remain valid as long as $\hat{\Psi}'$ is small, i.e. the condensate is not significantly depleted by thermal excitations. Under this assumption the operator $\hat{\Psi}$ is replaced with the classical field Φ.

In the cold, dilute gases that concern us only low energy, two-body collisions are important. These collisions involve only a single partial wave and are completely characterized by a single parameter, the s-wave scattering length, a. In this case, one can replace the actual interaction $V(\mathbf{r}'-\mathbf{r})$ in Eq. (2.20) with an effective interaction $V(\mathbf{r}'-\mathbf{r}) = U_0\delta(\mathbf{r}'-\mathbf{r})$ where the *pseudopotential* U_0 is proportional to the scattering length a through

$$U_0 = \frac{4\pi\hbar^2 a}{m}\ . \tag{2.21}$$

In the method of pseudopotentials, the actual Hamiltonian which contains a real potential is replaced by an effective Hamiltonian which contains a "pseudopotential" such that the ground state and low-lying energy levels of the system are given equally well by the new Hamiltonian. This replacement leads to mathematical simplification because the pseudopotential is not concerned with the details of the real potential; it tries only to reproduce the key parameters of the problem, e.g. the scattering length. An excellent discussion of the method of pseudopotentials can be found in [88].

The use of the pseudopotential yields the following equation for the condensate wavefunction:

$$i\hbar\frac{\partial}{\partial t}\Phi(\mathbf{r},t) = \left(-\frac{\hbar^2\nabla^2}{2m} + U_{\text{ext}}(\mathbf{r}) + U_0|\Phi(\mathbf{r},t)|^2\right)\Phi(\mathbf{r},t). \tag{2.22}$$

This is the famous Gross-Pitaevskii (GP) equation which was derived independently by Gross [41, 42] and Pitaevskii [93]. As long as the distance between particles is much greater than the s-wave scattering length and the number of condensate atoms is large, the GP equation may be used to study the macroscopic behavior of the system at low temperature. In other words, the product of the average gas density $\bar{n}$ and the scattering volume $|a|^3$ should be small. For hydrogen $\bar{n} \sim 10^{15}$ cm^3 and $a_{1S-1S} = 0.0648$ nm, so that $\bar{n}a_{1S-1S}^3 = 2.7 \times 10^{-10}$.

As Dalfovo [19] points out, however, the smallness of $\bar{n}|a|^3$ guarantees that the system is "weakly interacting", but it does not mean that the interactions are unimportant, especially for the large hydrogen condensates. We can see the importance of interactions by comparing the kinetic energy of atoms in the trap, E_{kin}, with the interaction energy, E_{int}. As an approximation we will consider a single particle ground state of the harmonic oscillator. The interaction energy is $N_{\text{c}}U_0\bar{n}$ where the average density is proportional to N_{c}/ℓ^3 so that $E_{\text{int}} \propto N_{\text{c}}^2|a|/\ell^3$, while the kinetic energy is approximately $N_{\text{c}}\hbar\bar{\omega}$ so that $E_{\text{kin}} \propto N_{\text{c}}\ell^{-2}$. The ratio is then

$$\frac{E_{\text{int}}}{E_{\text{kin}}} \propto \frac{N_{\text{c}}|a|}{\ell}\,, \tag{2.23}$$

which indicates the relative importance of interactions to the kinetic energy and shows that the single particle ground state would be a very poor approximation to $\Phi(\mathbf{r}, t)$. For hydrogen, with $N_{\text{c}} = 10^9$ and $\bar{\omega} = 2\pi \times 245$ Hz, $N_{\text{c}}|a|/\ell = 10^4$. This result suggests that the inclusion of the interaction term is vital to Eq. (2.22), and the kinetic or "quantum pressure" term in Eq. (2.22) may be neglected. This is what is known as the Thomas-Fermi approximation.

2.5.2 Ground State in the Thomas-Fermi Approximation

In this section we obtain an explicit expression for the condensate wavefunction in the presence of interactions. We begin by writing the condensate wavefunction as $\Phi(\mathbf{r}, t) = \phi(\mathbf{r})\exp(-i\mu t/\hbar)$, where μ is the chemical potential and $\phi(\mathbf{r})$ is a real function that is normalized to the total number of particles, $\int d\mathbf{r}\phi^2 = N_c = N$. The

GP equation then becomes

$$\left(-\frac{\hbar^2\nabla^2}{2m} + U_{\text{ext}} + U_0\phi^2(\mathbf{r})\right)\phi(\mathbf{r}) = \mu\phi(\mathbf{r}) \ , \tag{2.24}$$

from which it is apparent that the mean-field interaction term is proportional to the condensate density $n(\mathbf{r}) = \phi^2(\mathbf{r})$. One should notice that in the absence of interactions, this equation reduces to the ordinary Schrödinger equation for harmonic confinement where the energy eigenvalue has been replaced by the chemical potential.

In the previous section we discussed the effect of increasing the ratio $N_c a/\ell$. Specifically, as this ratio increases, the kinetic term becomes unimportant compared to the interaction energy except at the condensate boundary. As a result, we can completely neglect the kinetic term in Eq. (2.24) and find the density profile of the condensate where $\mu > U_{\text{ext}}$:

$$n_c(\mathbf{r}) = \phi^2(\mathbf{r}) = \begin{cases} \frac{m}{4\pi\hbar^2 a}\left(\mu - U_{\text{ext}}\right) & \mu > U_{\text{ext}} \\ 0 & \text{elsewhere} \end{cases} \tag{2.25}$$

The approximation of neglecting the kinetic energy term relative to the interaction term is known as the *Thomas-Fermi* (TF) *approximation.* The density profile described by Eq. (2.25) is referred to as the *Thomas-Fermi profile*, and we will make frequent reference to it later in this thesis. The same expression can be obtained by using a hydrodynamic approach to the weakly interacting Bose gas and applying the principal of hydrostatic equilibrium to the gas. We can define the peak condensate density $n_p \equiv \mu/U_0$ as the largest density which occurs at the center of the trap.

The normalization of $n(\mathbf{r})$ ($\int d\mathbf{r}n(\mathbf{r}) = N_c$) determines a relation between the chemical potential and the number of particles in terms of the dimensionless parameter $N_c a/l$:

$$\mu = \frac{\hbar\bar{\omega}}{2}\left(\frac{15N_c a}{\ell}\right)^{2/5} . \tag{2.26}$$

Using this expression we can find a convenient relation between the peak condensate density and the condensate population:

$$N_{\rm c} = \frac{1}{15}\left(\frac{\ell}{a}\right)\left[\frac{2n_{\rm p}U_0}{\hbar\bar{\omega}}\right]^{5/2} . \tag{2.27}$$

This relation between $N_{\rm c}$ and $n_{\rm p}$ will play an important role in the interpretation of experiments in this thesis because our ability to determine $n_{\rm p}$ through spectroscopy will in turn affect our knowledge of $N_{\rm c}$.

2.6 Dipolar Spin-Relaxation in the Condensate

Until now we have said nothing about loss processes in the condensate. In hydrogen, the major loss process in the condensate is due to two-body dipolar spin-relaxation (see also Sec. 3.2.2). For the moment, we will consider only dipolar spin-relaxation involving two condensate atoms. We will return to the subject in Chapter 8 when we also consider dipolar relaxation involving noncondensed atoms.

Dipolar spin-relaxation involves weak dipole-dipole collisions between two atoms that result in transitions to other spin states. This two-body process takes place locally and obeys the equation

$$\left.\frac{dn}{dt}\right|_{\rm dip} = -gn^2 . \tag{2.28}$$

To calculate the rate at which atoms are lost from the condensate due to dipolar decay, we integrate over the square of the density distribution given in Eq. (2.25):

$$\frac{dN_{\rm c}}{dt} = -\frac{g}{2!}\int_0^{R_{\rm TF}} d\mathbf{r}\,[n_{\rm c}(\mathbf{r})]^2 , \tag{2.29}$$

where $g = 1.1 \times 10^{-15}$ cm^3/s [120] (see the discussion in Sec. 3.2.2), and we have introduced in the integration limits the *Thomas-Fermi radius* $R_{\rm TF} \equiv \sqrt{2\mu/m\bar{\omega}^2}$, where $n_{\rm c}(\mathbf{r}) \to 0$ (see Eq. (2.25)). Note that $R_{\rm TF}$ depends on $N_{\rm c}$ through μ. The factor of 2! in Eq. (2.29) accounts for the two-body coherence of the condensate [59, 119].

Carrying out the integration we obtain

$$\frac{dN_{\rm c}}{dt} = -\frac{16\pi}{105} g \left(\frac{\mu}{U_0}\right)^2 R_{\rm TF}^3. \tag{2.30}$$

The introduction of $R_{\rm TF}$ provides another convenient way to express the condensate population

$$N_{\rm c} = \frac{8\pi}{15}\frac{\mu}{U_0} R_{\rm TF}^3. \tag{2.31}$$

In anticipation of our need to express $dN_{\rm c}/dt$ in terms of $N_{\rm c}$ we introduce the ratio of lengths $R_{\rm TF}/\ell = \sqrt{2\mu/\hbar\bar{\omega}}$ and write

$$\frac{dN_{\rm c}}{dt} = -\frac{g}{420\pi}\frac{1}{a^2\ell}\left[\frac{15N_{\rm c}\,a}{\ell}\right]^{7/5}. \tag{2.32}$$

Taking the ratio of Eq. (2.32) to Eq. (2.31) allows us to identify the characteristic decay rate for atoms in a harmonic potential

$$\frac{\dot{N}_{\rm c}}{N_{\rm c}} = -\frac{2}{7} g n_p. \tag{2.33}$$

For a peak density of $n_p = 2 \times 10^{15}$ cm^{-3} the characteristic decay rate is 0.63 s^{-1}.

2.7 Ioffe-Pritchard Potential

The results presented to this point in the chapter assume that the BEC is confined in an anisotropic harmonic potential. For samples with $T < 200$ μK, the anharmonicity of the trap shape can be described by the "Ioffe-Pritchard" (IP) potential [79, 95]. The Ioffe-Pritchard potential is cylindrically symmetric and has the form

$$V_{\rm IP}(\rho, z) = \sqrt{(\alpha\rho)^2 + (\beta z^2 + \theta)^2} - \theta \tag{2.34}$$

where ρ is the radial coordinate and z is the axial coordinate. The potential is completely specified by three parameters: the radial potential energy gradient α (with units energy/length), the axial potential energy curvature 2β (units energy/length^2), and the bias potential energy θ. As we will see below, our previous results for the condensate are still valid since the minimum of the IP potential is well approximated by a harmonic potential.

2.7.1 Harmonic Approximation

For energies much smaller than the bias potential energy ($\alpha\rho \ll \theta$), the Ioffe-Pritchard potential given by Eq. (2.34) may be expanded in powers of $(\alpha\rho)^2/(\beta z^2+\theta)^2$ yielding

$$V_{\mathrm{IP}}(\rho, z) = \beta z^2 + \frac{1}{2}\frac{\alpha^2}{\beta z^2+\theta}\rho^2 - \frac{1}{8}\frac{\alpha^4}{(\beta z^2+\theta)^3}\rho^4 + \ldots. \tag{2.35}$$

By comparison with Eq. (2.7) it is easy to see that the IP potential is harmonic in the ρ and z directions provided that the third term is much smaller than the second term. By setting the third term equal to the second term, we can define a radius at which the potential ceases to be harmonic:

$$\rho_{\mathrm{anharm}} \equiv 2\,\frac{\beta z^2+\theta}{\alpha}. \tag{2.36}$$

Physically, the IP potential varies linearly with radial distance far from the center but is curved in a parabolic fashion near the minimum. The "anharmonic radius" identifies the distance at which the functional behavior of the potential changes.

Near the origin the trap appears harmonic in all directions. For short samples, and especially for the condensate, the radial oscillation frequency is essentially constant along the length of the sample. From Eq. (2.7) and Eq. (2.35) we can identify the axial oscillation frequency

$$\omega_z = \sqrt{\frac{2\beta}{m}} \tag{2.37}$$

	Trap A	Trap B
α (mK/cm)	15.9	9.5
β (μK/cm^2)	25	25
θ (μK)	65-190	123-132
$\omega_\rho\vert_{z=0}$	$2\pi \times 1860$ Hz ($\theta = 154$ μK)	$2\pi \times 1200$ Hz ($\theta = 132$ μK)
ω_z	$2\pi \times 10.3$ Hz	$2\pi \times 10.3$ Hz
$\rho_{\mathrm{anharm}}\vert_{z=0}$ (μm)	193 ($\theta = 154$ μK)	278 ($\theta = 132$ μK)

Table 2.1: Parameters describing the two magnetic traps used to confine condensates in this thesis. The parameters α, β, θ characterize the Ioffe-Pritchard potential according to Eq. (2.34). Parameters α and β are calculated from the known magnet geometry, and θ is measured. Typical values for ω_z and ω_ρ are given.

and the radial oscillation frequency

$$\omega_\rho = \sqrt{\frac{1}{m}\frac{\alpha^2}{\beta z^2 + \theta}}. \tag{2.38}$$

By equating the thermal energy with the radial potential energy, we can identify a temperature below which atoms experience a harmonic potential: $T \ll 2\theta/k_B$.

Table 2.1 summarizes the parameters describing the magnetic traps used to confine condensates in this thesis. The two traps are referred to as "Trap A" and "Trap B." The larger value of α for Trap A indicates that this trap is more tightly confining and is used to produce condensates which are more dense and warmer than condensates produced in Trap B. In both traps θ was varied between experimental runs. Its value was always measured prior to a run. The range of θ used is reported in the table.

Higher-order terms

Although the low energy approximation of the Ioffe-Pritchard potential by a harmonic potential simplifies calculations involving the condensate, a truly harmonic potential is separable and prevents exchange of motional energy in the ρ and z directions. In the IP trap, the dependence of ω_ρ on z (see Eq. (2.38)) permits coupling of the ρ and z motion. Mixing of motional degrees of freedom is important for cooling the trapped gas using "magnetic saddlepoint evaporation" (see Sec. 3.3.1).

The strength of mixing can be characterized by the rate at which the radial oscillation frequency changes as the atom moves along the z axis. Strong mixing occurs when the "adiabaticity parameter" is close to unity:

$$\frac{\dot{\omega}_\rho}{\omega_\rho} \sim 1. \tag{2.39}$$

For a typical hydrogen sample confined in Trap A at $T = 100\ \mu\mathrm{K}$, $\dot{\omega}_\rho/\omega_\rho \sim 10^{-3}$ [32]. As a result, mixing is very slow and magnetic saddlepoint evaporation becomes inefficient below $T \sim 200\ \mu\mathrm{K}$. This required us to implement radio frequency evaporation for hydrogen – a technique that does not require mixing of motional degrees of freedom (see Sec. 3.3.2).

For $T > 200\ \mu\mathrm{K}$, Eq. (2.34) is only an approximation to the true magnetic potential. In reality there are small, higher-order contributions involving products of the ρ and z coordinates that break the cylindrical symmetry and lead to strong coupling of the motional degrees of freedom. In this regime saddlepoint evaporation regains its efficiency. Additional information can be found in [79, 123].

2.8 Summary

The main purpose of this chapter was to introduce concepts and quantities useful for understanding the remainder of this thesis. In particular, length and energy scales that appear frequently in the problem of BEC in a harmonic potential were defined. For convenience they are summarized in Table 2.2.

Length Scales	
$\ell = \sqrt{\hbar/m\bar{\omega}}$	Harmonic oscillator length
a	s-wave scattering length
$R_{\mathrm{TF}} = \sqrt{2\mu/\hbar\bar{\omega}}$	Thomas-Fermi radius
$R_{\mathrm{th}} = \ell\,(k_BT/\hbar\bar{\omega})^{1/2}$	Thermal radius

Energy Scales	
$\hbar\bar{\omega}$	Average oscillator energy
k_BT	Thermal energy
$n_pU_0 \equiv \mu$	Mean-field energy (chemical potential)

Table 2.2: Summary of important length and energy scales in the problem of BEC in a harmonic potential. These quantities appear frequently in descriptions of trapped Bose gases.

Chapter 3

Apparatus and Methods

The techniques used to produce and study a Bose-Einstein condensate (BEC) of atomic hydrogen differ significantly from techniques used in alkali atom experiments. This chapter provides an overview of the current hydrogen trapping, cooling, and spectroscopy techniques that have been developed and refined since the group began studying spin-polarized hydrogen in 1976.

The suggestion that observation of BEC in hydrogen might be possible is due to Hecht [47]. Using a quantum theory of corresponding states, Hecht argued that spin-polarized hydrogen should remain a gas down to absolute zero. This argument was strengthened in 1976 by Stwalley and Nosanow with the publication of a many-body calculation confirming that the ground state of spin-polarized hydrogen was indeed a gas [121]. Following a 1978 session of the American Physical Society dedicated to spin-polarized hydrogen, experimental work began in Amsterdam, British Columbia, Cornell, MIT, Moscow and Turku.

The attraction of BEC in dilute atomic gases was clear: weak interactions. Although London had connected the macroscopic occupation of a single ground state with superfluidity in 1938 [78], superfluid helium with its strong interactions behaves quite differently from the ideal gas discussed by Einstein the mid 1920s. Hydrogen was the leading candidate because of its light mass and corresponding high transition temperature for a given atomic density. In fact, it was the only candidate before laser cooling was invented.

3.1 Cryogenic Confinement of Spin-Polarized Hydrogen

The initial approach for stabilizing spin-polarized hydrogen was to confine atoms in a region of high magnetic field against a cryogenically cooled surface of superfluid helium. The low binding energy of hydrogen to liquid helium, ~ 1 K, permitted the creation of high densities and long sample lifetimes. The closest approach to the degenerate regime was by the MIT group at a temperature of 0.55 K and a density of 4.5×10^{18} cm^{-3}. At these densities, three-body recombination limits the lifetime of the sample to a fraction of a second; BEC was not realized. An alternate method was needed. [1].

3.1.1 Hydrogen in a Magnetic Field

When a neutral atom with a magnetic moment μ enters a magnetic field $\mathbf{B}$, it experiences a force $\mathbf{F} = \nabla(\mu \cdot \mathbf{B})$, since $-\mu \cdot \mathbf{B}$ is the interaction energy of a magnetic dipole with an external magnetic field. The spins of the proton and electron in hydrogen interact through the hyperfine interaction resulting in four hyperfine states: a - d. States a and b are the high-field seeking states and are attracted to regions of high magnetic field, while the low-field seeking states c and d are expelled from high-field regions. This behavior is shown in Fig. 3-1.

In 1986, Hess suggested that hydrogen atoms in the low-field seeking states could be confined away from walls in the local minimum of a magnetic field and cooled using forced evaporation [50]. High-field seekers can not be confined in this way since a local maximum of magnetic field in a source free region is forbidden [134]. The first demonstrations of trapping in an Ioffe-Pritchard potential and of evaporative cooling

---

[1] For reviews of this early work see [40, 111, 129]

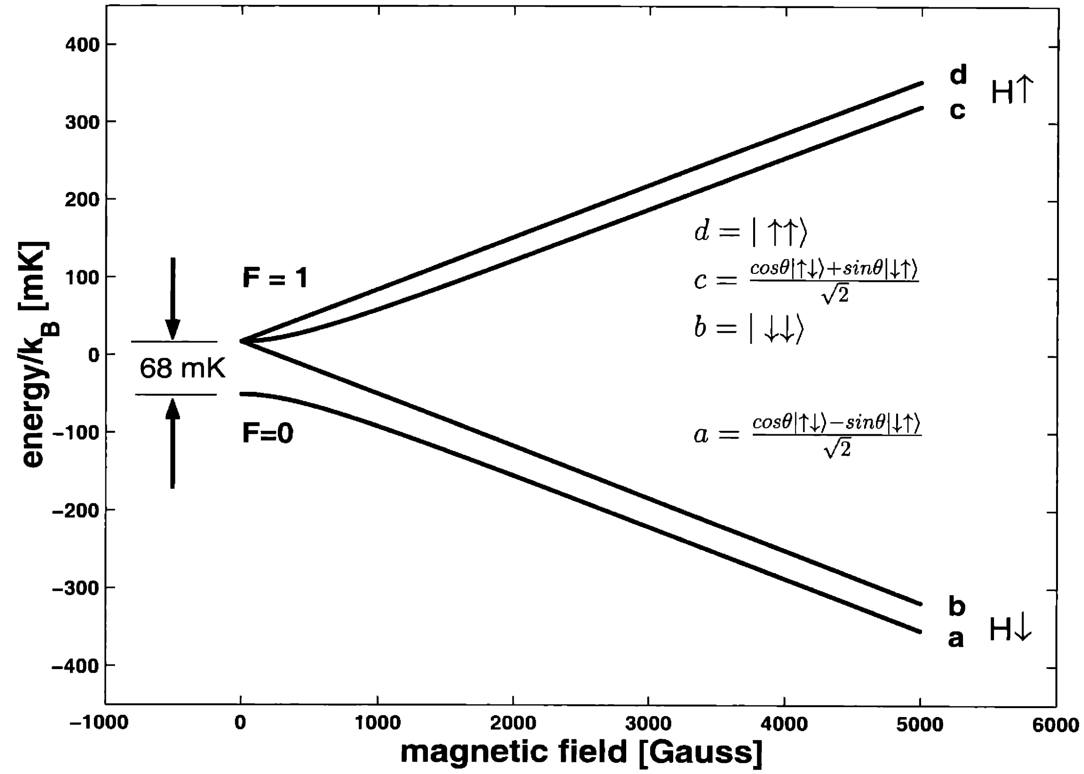

Figure 3-1: The four hyperfine states of hydrogen show different behaviors in the presence of a magnetic field. States c and d are low-field seeking states that are captured in the magnetic trap. Only d atoms survive because spin-relaxation processes quickly remove c atoms from the trapped sample.

followed quickly [49, 82].

3.1.2 Trapping Cell

The characteristic energy for hydrogen in a magnetic field, $\mu_B B$, where μ_B is the Bohr magneton, corresponds to a temperature $T' = \mu_B B / k_B$. For a 1 Tesla magnetic field, $T' = 0.6$ K. Since trapping requires $T \ll T'$, for practical hydrogen traps, the atoms must be precooled to a fraction of a Kelvin by cryogenic cooling. In contrast, alkali atoms are typically loaded from magneto-optic traps where they have been laser cooled to microkelvin temperatures. Such laser cooling techniques are not practical for hydrogen since the cooling transition, $1^2S_{1/2} - 2^2P_{3/2}$, at 121.57 nm is difficult to access. Instead atoms are cooled through cryogenic techniques.

The trapping cell in which the atoms are magnetically confined is shown in Fig. 3-2. The cell is cylindrically symmetric and consists of two G-10 tubes [33] approximately 65 cm in length in a double-walled design. The volume between walls is filled with superfluid ^{4}He for efficient thermal transport along the length of the cell. The inner cell wall is coated with a thin layer of Cu (see Sec. 4.1.3) and covered with a slightly sub-saturated film of ^{4}He to reduce the binding energy of hydrogen atoms to the wall during the initial loading, before the atoms are magnetically confined. The bottom of the cell consists of a MgF_2 window and a mirror used for spectroscopy of the trapped atoms (see Sec. 4.2.3). At the top of the cell is a cryogenic dissociator for producing atomic hydrogen. The dissociator is anchored to the mixing chamber of a ^{3}He - ^{4}He dilution refrigerator.

3.1.3 Magnetic Trap

The magnetic trap is cylindrically symmetric and is produced using superconducting magnets. The magnets and the resulting field profile on axis are shown in Fig. 3-3. The largest field (4 T) is due to the source magnet, a large superconducting solenoid operated in persistent current mode. The large field created in the region of the

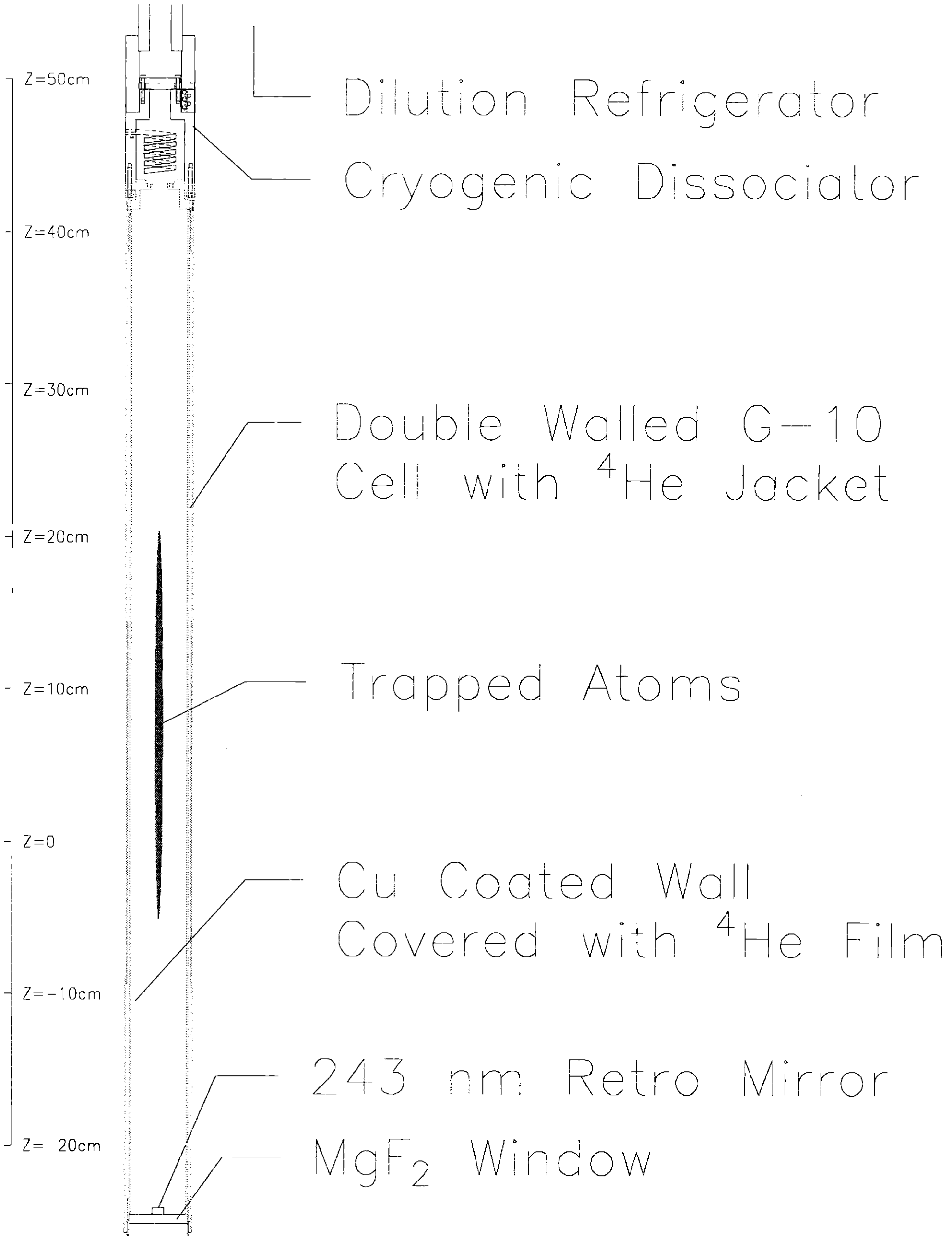

Figure 3-2: Cutaway view of the cylindrically symmetric trapping cell and dissociator. The approximate location of trapped atoms is shown. Not shown is the cylindrical vacuum can that surrounds the trapping cell and separates it from the 4 K He bath.

dissociator expels the low-field seeking c and d state atoms while drawing in the high-field seeking a and b states. Radial confinement in the trapping region is provided by a quadrupole magnet whose field increases linearly with increasing radial coordinate, ρ. Two large "pinch" solenoids provide confinement in the axial direction. A smaller "bias" solenoid in between the pinch magnets assures that $|\mathbf{B}|$ never vanishes and prevents nonadiabatic spin flips due to the atom's motion. The low-field seekers are confined in the approximately uniform field region about 20 cm in length.

3.2 Trap Loading

Molecular hydrogen is frozen onto the walls of the dissociator during the initial cooldown of the cell. Enough ^{4}He is introduced into the cell to create a slightly sub-saturated superfluid ^{4}He film covering the cell walls and the dissociator. The film is self-healing and covers all surfaces accessible to the atoms.

Loading the trap begins by driving the dissociator (a cryogenic radio frequency (rf) discharge) in a pulsed mode with rf at about 298 MHz. The resonant $\lambda/4$ helical coil inside the copper dissociator body evaporates the helium film and vaporizes and dissociates some of the hydrogen molecules. The resulting gas cloud expands into the trapping region below. The helium serves as a buffer gas to help transport the hydrogen and assist in thermalization with the 250 - 300 mK cell walls. The presence of the ^{4}He film reduces the wall-H binding energy to about 1 K. The temperature of the cell walls is maintained high enough so that hydrogen atoms that happen to stick to the cell walls equilibrate and desorb before having a chance to recombine into molecules.

3.2.1 Collisions and Spin Polarization

Hydrogen atoms are produced in the dissociator in all four hyperfine states. The pressure of the gas puff is sufficient to drive the high-field seekers (states a and b) out of the high-field region of the dissociator. Subsequent collisions with the cell

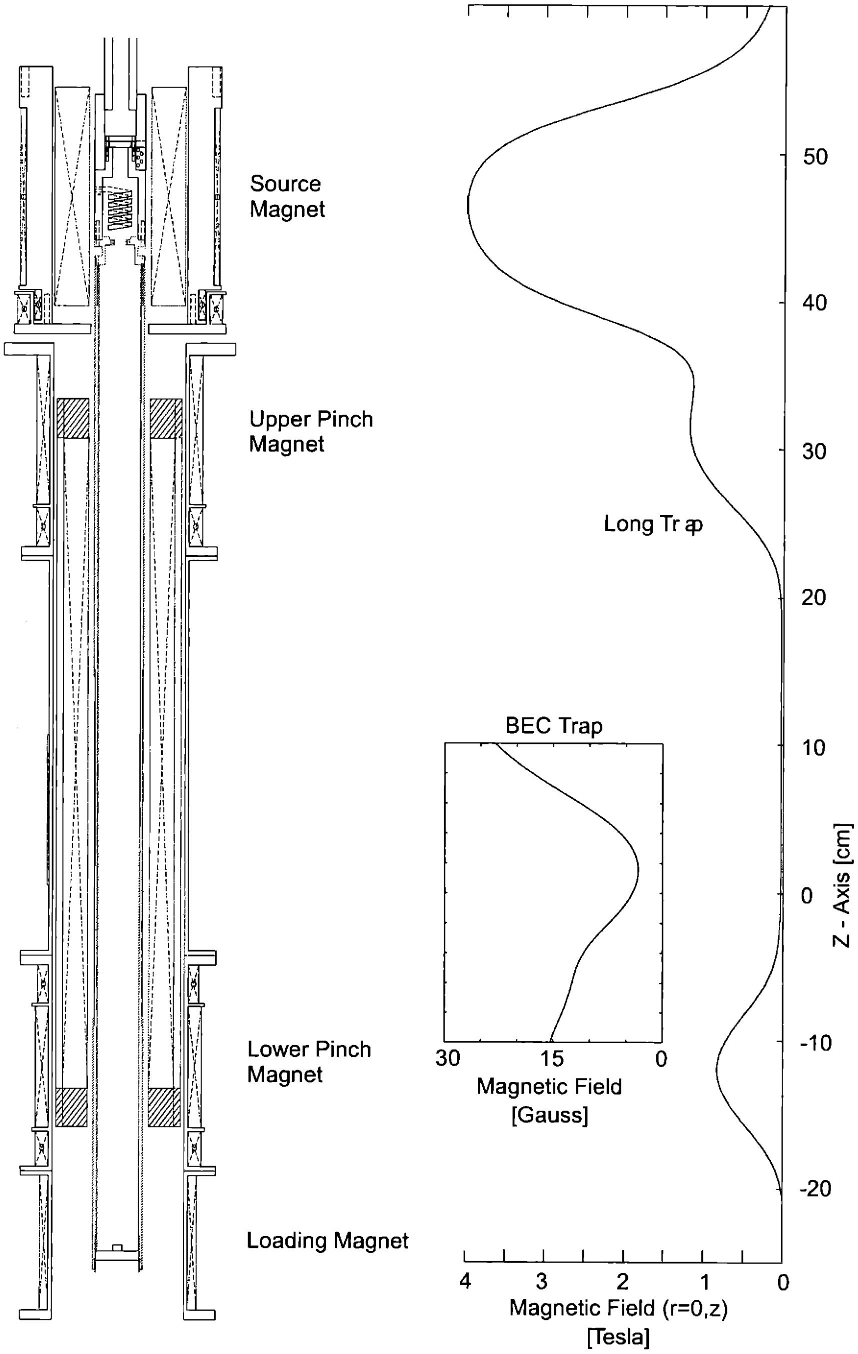

Figure 3-3: The trapping cell is shown surrounded by the large superconducting magnets that form the magnetic trap. Two field profiles are shown. The Long Trap profile indicates the field configuration along the z-axis immediately after the loading magnet is ramped down. The BEC Trap profile indicates the final magnetic trap in which a BEC is confined. Note the difference in scales of the ordinates.

walls allow the high-field seeking atoms to dissipate energy before being pulled to the cell walls and back into the dissociator by the magnetic field gradient. The low-field seekers (states c and d) remain in the trapping volume and settle into the magnetic field minimum through atom-atom collisions. The helium recondenses on the cell walls.

Collisions between atoms in the trapping region are essential for loading the trap. Without collisions, atoms emerging from the source region would accelerate down the magnetic hill, traverse the trapping region and be lost over the trap threshold near the bottom of the cell to stick to a wall. There they would equilibrate, desorb, and again traverse the trapping region to stick to another wall. Radially, atoms would simply bounce back and forth between the cell walls. Due to collisions, however, a fraction of the atoms end up with sufficiently low energy to become trapped. The high energy collision partner reaches the cell wall where it can dissipate its excess energy.

Nuclear spin polarization occurs due to spin-exchange collisions such as $c + c \rightarrow b + d$. The c atoms are eliminated from the sample and the b atoms return to the source region. After about three seconds the remaining atoms are all in the d state – doubly spin-polarized.

3.2.2 Loss Processes

The maximum density of d state atoms that one can attain in the trap during loading is fundamentally determined by the balance of input flux from the dissociator and loss due to dipolar spin-relaxation. In dipolar spin-relaxation weak dipole-dipole collisions between two atoms in the gas result in a finite probability of making a transition to another spin state. Since this process involves two bodies and takes place locally, it obeys the equation

$$\dot{n}_{dip} = -gn^2 \tag{3.1}$$

where n is the local density. The loss rate constant, $g = 2(G_{dd\rightarrow ac} + G_{dd\rightarrow aa} + G_{dd\rightarrow ad})$, is the sum of the dominant decay channels governing doubly spin-polarized samples. The rates for all decay channels have been calculated [120] as a function of magnetic field and temperature. Below 500 μK and 10^{-2} T, the rate constants change by only a few percent from their $B = 0$, $T = 0$ values. During a dipolar decay event in this experiment both atoms are lost since the trap depth is less than half the hyperfine energy (68 mK, see Fig. 3-1) liberated; hence the factor of two in the expression for g. Although an experimental value for g has been measured [128], the theoretical value is believed to be very reliable so we take its $B = 0$, $T = 0$ value, $g = 1.1 \times 10^{-15}$ cm^3/s. The measured value agrees with 17% uncertainty. Since dipolar relaxation is a two-body process, it takes place preferentially where the density of atoms is the highest. As a result, atoms with the least energy are lost, leading to heating of the trapped sample.

Although the fundamental limit of achievable loading density is set by the balance between input flux and dipolar relaxation, atoms can also be lost through relaxation processes on the wall surface. During loading atoms in the bulk gas are in equilibrium with the surface. While on the surface an atom may spin relax due to small magnetic impurities on the wall. Typically the relaxation would proceed $d \rightarrow c \rightarrow b$. The relaxed atoms either recombine quickly or are drawn toward the source region. In addition a small surface density of a and b state atoms is present on the wall in the trapping region. While on the wall a d state atom can recombine to form a hydrogen molecule with either of the a or b states since the interaction is through the singlet potential and the wall allows for conservation of energy and momentum.

3.2.3 Thermal Disconnect from the Cell Wall

To maintain equilibrium during loading, the wall temperature is kept sufficiently high ($>$ 250 mK) that an atom bound to the surface will likely desorb and return to the trapped sample before suffering either a magnetic impurity induced spin flip or a surface recombination. After loading is complete, the cell wall temperature is lowered as quickly as possible to < 100 mK. At this lower temperature the cell wall becomes "sticky"; the residence time of an atom on the wall becomes long compared to the characteristic $H + H \rightarrow H_2$ recombination time. Thus, atoms that escape the trap and reach the wall recombine and do not return to heat the trapped sample. Soon all atoms with energy greater than the trap depth are lost to the walls, and the trapped atoms come to a quasi-equilibrium. Through further collisions the trapped atoms redistribute their energy; the atoms in the high energy tail of the distribution escape and the remaining atoms equilibrate to a lower temperature and settle deeper into the trap. This "spontaneous" evaporation is very similar to the evaporation from a cup of coffee; the "hottest" water molecules leave the cup, allowing the remaining liquid to cool. After thermal disconnect from the walls, typically a few times 10^{14} atoms remain in the trap at a temperature of about 40 mK.

3.3 Cooling

Evaporative cooling is the principal technique used to reach BEC in atomic gases. The technique is based on preferential removal of atoms having an energy greater than the average energy of the confined sample, followed by rethermalization of the remaining sample by elastic collisions. Even though the technique results in the removal of some atoms from the trap, those that remain have a lower temperature and occupy a smaller volume at the bottom of the trap, thereby increasing their density [25, 50, 63].

Initially, evaporative cooling occurs spontaneously when the sample disconnects from the cell wall and settles into the trap. If the trap depth is denoted by ϵ_{trap}, then we can define a quantity $\eta = \epsilon_{trap}/k_B T$, the ratio between trap depth and sample temperature. In the 40 mK deep trap $\eta \approx 13$ [32]. The peak density at the magnetic field minimum is $n_0 \approx 10^{13}$ cm^{-3}. The spatial density is then given by $n(\mathbf{r}) = n_0 \exp(-U_{\text{ext}}(\mathbf{r})/k_B T)$, where $U_{\text{ext}}(\mathbf{r})$ is the magnetic trapping potential. Table 3.1 summarizes the trapped sample parameters just prior to forced evaporation.

To sustain the cooling process, E_{trap} can be continuously lowered, resulting in a

hyperfine state	d
number of atoms	2×10^{14}
density on axis	2×10^{13} cm^{-3}
temperature	40 mK
lifetime	200 sec

Table 3.1: Trapped sample after filling and thermal disconnect from the cell wall.

continuous decrease in sample temperature. This technique is known as forced evaporation. Several models have been developed to describe this process, the simplest of which is due to Davis *et al.* [21] and is useful for developing one's intuition. In this model the trap depth is lowered in a single step and the effect on thermodynamic quantities such as temperature, density, and volume is calculated. By repeating the procedure for many successive steps, the true evaporation process can be approximated. The simple model makes several basic assumptions:

1. The distribution of atoms in phase space depends only on the total energy of the atoms. This is the assumption of *sufficient ergodicity.*
2. The gas obeys classical statistics and is far from the BEC transition.
3. Only s-wave scattering takes place, with a cross section given by $\sigma = 8\pi a^2$, where a is the scattering length. (Elastic collisions are assumed to dominate over inelastic.)
4. The distribution of atoms is never far from thermal. That is, the thermalization rate is faster than the cooling rate.
5. Atoms that escape from the trap do not collide or exchange energy with the remaining atoms.

In the first part of the cooling process these assumptions are all valid for our system. As discussed below, however, assumptions 1 and 5 can be violated in the hydrogen experiment. Actually, it was the violation of these assumptions that prevented the attainment of BEC in atomic hydrogen until 1998.

Although the simple model describes many aspects of the evaporation process, it does not provide information about the time scale. Experimental results have shown that ~ 2.7 elastic collisions are necessary to effectively thermalize the gas [84]. Luiten *et al.* [79] have described the process using the Boltzmann equation to calculate evolution of the phase space density $\rho(\mathbf{r}, \mathbf{p})$. Their calculations show that assumption 4 remains valid since the energy distribution remains close to Maxwell-Boltzmann. They find, however, that the high-energy tail takes many more than 2.7 collisions to relax to equilibrium, arguing therefore that there is a difference between evaporation and thermalization.

Finally, an important question to ask is: how fast should the evaporation process be carried out? The canonical extreme example is to assume a very large η such that one simply has to wait for a single particle to possess the entire energy of the sample and evaporate, cooling the sample to zero temperature [63]. Not only would such a strategy require an impractical length of time but inelastic processes leading to losses would likely make it impossible. Realistically, one must lower E_{trap} sufficiently quickly so that inelastic collisions do not dominate. At the same time, lowering E_{trap} too quickly will prevent thermalization from taking place, leading to inefficiencies in the cooling process and the spilling of atoms from the trap.

The principle of detailed balance can be used to find the speed of evaporation [63]. Atoms with energy larger than $\eta k_B T$ are produced at a rate given by the number of atoms with energy larger than this divided by their collision time. The fraction of atoms in the Maxwell-Boltzmann distribution with energy $\epsilon > \eta$ for large η is given by

$$f(\epsilon > \eta) = e^{-\eta}\sqrt{3\eta/2} \tag{3.2}$$

The elastic collision rate is $\Gamma_{el} = n\sigma v$, where $v = \sqrt{2\eta k_B T/M} = \bar{v}\sqrt{3\eta/2}$ and $\bar{v}$ is the average velocity for a given temperature. Thus the rate of evaporated atoms is

$$\frac{dN}{dt} = -Nf(\epsilon > \eta)\Gamma_{el} = -n\sigma\bar{v}\eta e^{-\eta}N \equiv \Gamma_{ev}N \tag{3.3}$$

Since the average collision rate per atom is given by $\sqrt{2}n\sigma\bar{v} \propto \sqrt{T}$ (the $\sqrt{2}$ is due to the atom's relative velocity), the ratio of evaporation time to elastic collision time becomes

$$\frac{\tau_{ev}}{\tau_{el}} = \frac{\sqrt{2}e^{\eta}}{\eta} \tag{3.4}$$

which increases exponentially with η.

On the other hand, the inelastic collision rate of dipolar relaxation, gn, becomes a constant at low temperatures. One can define a characteristic temperature at which the probability for an elastic (*good*) collision equals the probability for an inelastic (*bad*) collision [79]. For hydrogen "bad collisions" are due to dipolar relaxation, and we find the characteristic limiting temperature to be:

$$k_B T_{evap} = \frac{\pi M g^2}{16\sigma^2} \ . \tag{3.5}$$

For hydrogen, using $g = 1.1 \times 10^{-15}$ cm^3/s and $a = 0.0648$ nm, $T_{evap} \sim 3$ nK. In practice, the cooling limit is about 10^3 times higher [63]. Luiten *et al.* [79] have studied the problem carefully for atomic hydrogen and found the minimum temperature at which the density n_0 reaches its maximum value, $T \sim 20$ μK with $\eta \sim 4$. This is in good agreement with experiments performed in this thesis.

3.3.1 Magnetic Saddlepoint Evaporation

After the trapped gas has thermally disconnected from the cell walls, the first stage of forced evaporative cooling is realized by lowering the magnetic field saddlepoint that defines the depth of the trap, ϵ_t. This technique was first demonstrated in the current experiment by Masuhara et al. [82]. The saddlepoint is lowered continuously for 260 - 300 seconds during which the magnetic field is reduced from 0.8 T to 15-20$\times 10^{-4}$T. The peak density of the sample increases to nearly 10^{14}cm^{-3}, the temperature is reduced from 40 mK to about 200 μK, and the atom number is reduced from a few times 10^{14} to a few times 10^{11}. This process is illustrated in Fig. 3-4. The quadrupole field providing confinement in the radial direction is also lowered during saddlepoint

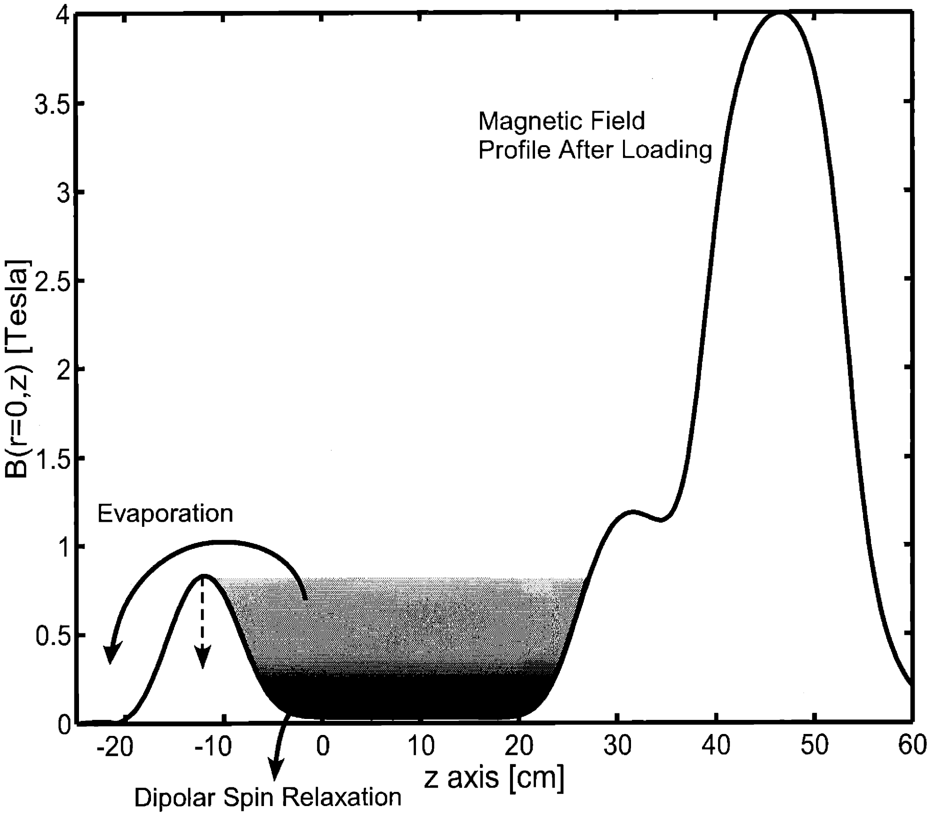

Figure 3-4: Diagram illustrating magnetic saddlepoint evaporation. The magnetic field profile shown describes the field on axis prior to the beginning of forced evaporation. The rate at which the barrier is lowered is determined by the competing effects of efficient thermalization of the sample and dipolar spin-relaxation losses.

evaporation. Otherwise, tight confinement in the radial direction would lead to large densities and increased dipolar relaxation losses.

Below ~200 μK magnetic saddlepoint evaporation becomes inefficient. Our group observed the inefficiency and had a crude explanation for its origin, but a detailed explanation of the problem was given by the hydrogen group in Amsterdam in the context of a similar experiment [92]. Subsequently, our group confirmed their explanation [32]. An important concept to understand is the "effective dimension of evaporation" [124]. Ergodic evaporation (evaporation in which all atoms acquiring a total energy in excess of the trap depth are quickly lost) is "three dimensional" (3D) since the criterion for escape from a trap is based on the total energy of the atom. Ergodic evaporation says nothing about the direction of motion of the atoms, but whether collisionless motion of the atoms is regular or stochastic can affect the effective dimension of evaporation. When the motional degrees of freedom of the atom are uncoupled and the motional energy of the atom in only one dimension determines the escape, the evaporation is said to be "one dimensional" (1D).

In magnetic saddlepoint evaporation the effective dimension of evaporation becomes 1D as the trapped sample cools. Atoms escape from only one end of the trap. However, the evaporation is still efficient when the sample has low density and is relatively warm. The mean free path between collisions is long, allowing energetic atoms to reach the end of the trap where the atoms access anharmonic regions of the Ioffe-Pritchard potential, causing motional degrees of freedom to mix. As the sample cools and becomes more dense, atoms settle into the harmonic region of the trap, where the radial and axial degrees of freedom are effectively uncoupled. An atom with radial energy greater than ϵ_t will likely suffer a collision before it can escape (due to its reduced mean free path) and redistribute its energy so that neither it nor its colliding partner have sufficient energy to escape. Because only atoms with axial energy greater than ϵ_t have a reasonable probability of escaping, the evaporation is said to be 1D and inefficient. In fact, all else being equal, the rate of 1D evaporation is slower than that of 3D evaporation by a factor approximately four times η [124]. Near the BEC transition in hydrogen $\eta \sim 7$ implying that 1D evaporation is ~ 30 times less efficient than 3D evaporation. Ultimately, it was loss of evaporation efficiency that prevented both our group and the Amsterdam hydrogen group from attaining BEC using magnetic saddlepoint evaporation.

3.3.2 RF Evaporation

Radio frequency (rf) evaporation was introduced into our cryogenic apparatus to restore efficiency to the evaporative cooling process. An rf magnetic field is used to transfer atoms from a trapped to an untrapped state in an energy-selective way.

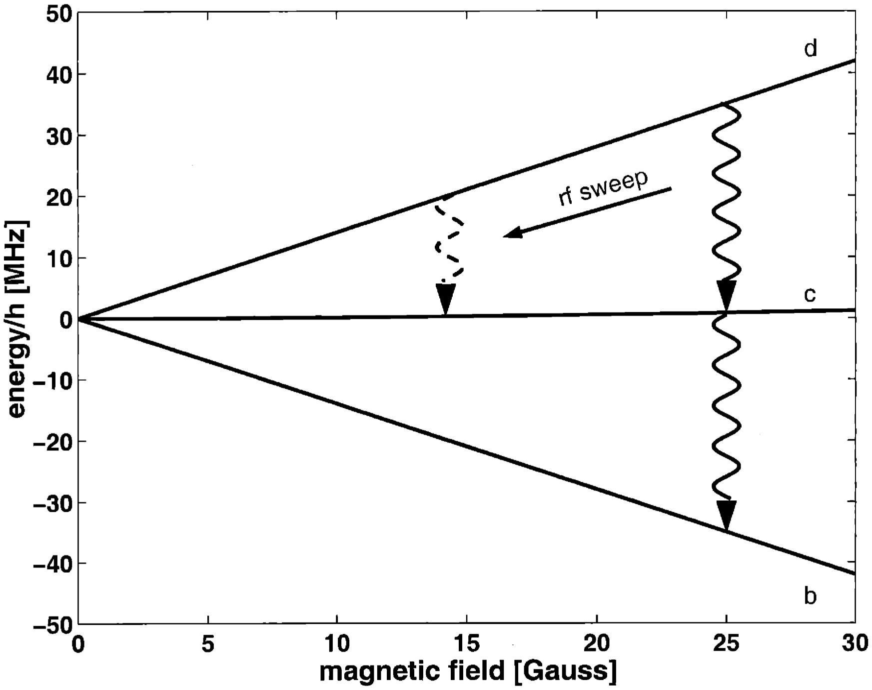

Figure 3-5: An applied rf magnetic field is used to transfer atoms from the trapped d-state to the untrapped c and b states. RF evaporation is carried out by reducing the rf frequency.

Energy selectivity is possible since there is a one-to-one correspondence between the atom's Zeeman shift and potential energy in a magnetic trap. The rf frequency, ω_{rf}, defines a resonance surface where the magnetic field has constant magnitude, $B \approx \hbar\omega_{\mathrm{rf}}/\mu_B$. Atoms with sufficient energy in any motional direction can climb the magnetic potential, enter the resonance region, and be ejected from the trap. By gradually reducing the rf frequency (subject to the previous constraints regarding speed of evaporation), evaporation is forced. This process is illustrated in Fig. 3-5.

The original suggestion of rf evaporation is due Pritchard *et al.* [96], and the use of rf-induced evaporation was first reported at the 1993 OSA meeting [62]. It is the standard technique for the final cooling of laser-cooled atoms and has been used to cool Rb [2], Na [21], Li [13, 12], metastable ^{4}He* [108, 100], as well as H [31] to Bose-Einstein condensation. It is also an important technique in the sympathetic

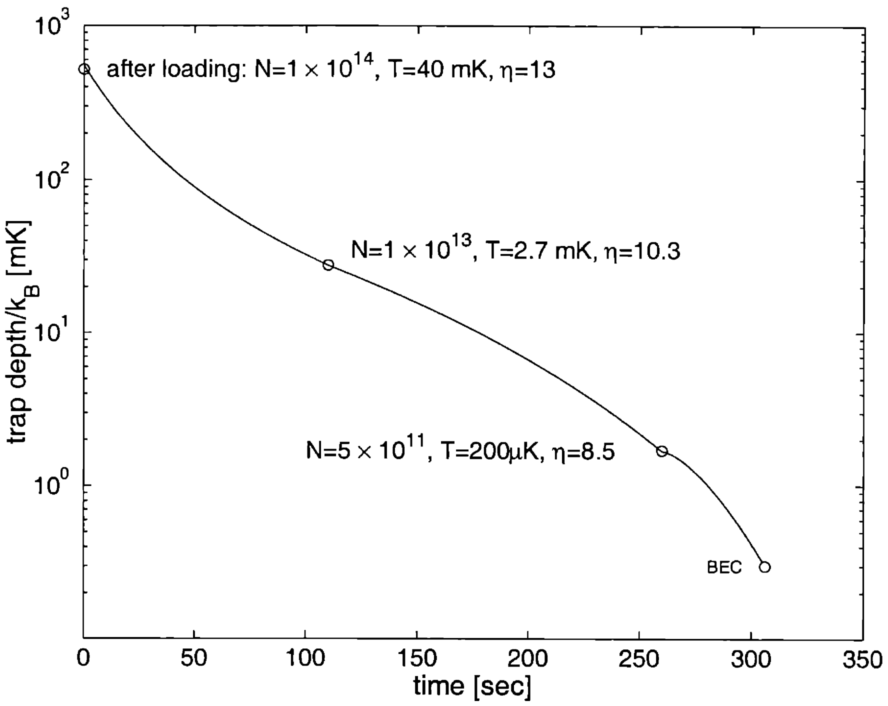

Figure 3-6: Evaporative cooling path for preparing samples of Bose-condensed hydrogen. The majority of the cooling is performed by magnetic saddlepoint evaporation, but rf evaporation is necessary to reach degeneracy.

cooling of fermions ^{6}Li [126] and ^{40}K [23] below the Fermi temperature. Recently, an experiment utilizing a crossed optical dipole trap has succeeded in reaching BEC without rf techniques [3].

In our experiment a typical rf evaporation begins at a frequency of 35 MHz, corresponding to a trap depth of 1.7 mK and a sample temperature of about 200 μK. In 50 seconds we lower the frequency to 5 MHz, producing a trap depth of 240 μK and a sample temperature of about 40 μK. The full cooling path from loading to BEC is shown in Fig. 3-6. By sweeping the rf frequency much faster, we can violate the conditions for efficient evaporation and produce a sample out of thermal equilibrium. This technique has been used extensively in the work reported in this thesis and will be discussed in detail in Chapters 7 and 8.

The introduction of rf magnetic fields into our cryogenic apparatus required substantial changes to the trapping cell in order to eliminate metal components susceptible to rf eddy current heating [32]. As little as 100 μW deposited near the trapping region could raise the temperature of the cell, leading to an increased ^{4}He vapor pressure within the trapping region, and a substantially reduced sample lifetime. Details of the construction of the non-metallic cell can be found in Chapter 4 and in [32].

Dimension of rf-induced Evaporation

Spin-flips due to rf magnetic fields occur on a resonant shell surrounding the trapped atoms. RF-induced evaporation can be considered 3D evaporation as long as the shells with constant $|\mathbf{B}|$ are equipotential surfaces. This is true in dc magnetic traps provided that gravity is neglected. Gravity, however, pulls the trapped cloud downward and causes the bottom of the cloud to experience a higher magnetic field. Evaporating atoms typically have about $(\eta + 1)k_BT$ of energy. Thus, evaporation occurs mainly at the bottom of the trapped cloud when the energy due to gravity varies by more than $\pm k_BT$ over the equipotential surface $U = \eta k_BT$ [63].

In our experiment at low temperatures, the atoms experience a harmonic potential along the z-axis (shown in the inset of Fig. 3-3) $U = U''z^2/2$ where U'' is the curvature of the potential. The equipotential surface is at $z \approx \sqrt{2\eta k_BT/U''}$. Setting $mg_{\text{grav}}z = k_BT$, we can find a characteristic temperature below which evaporative cooling becomes one-dimensional

$$k_BT_{1D} < \frac{2\eta(mg_{\text{grav}})^2}{U''} \tag{3.6}$$

where m is the mass of the atom and g_{grav} is the gravitational constant. Defining the magnetic field gradient that counterbalances gravity $B'_{grav} = mg/\mu_B$ (0.18 G/cm for the d state of hydrogen) and the magnetic field curvature B''_z along the z-axis, allows us to express Eq. 3.6 as

$$k_BT_{1D} < \frac{2\eta\mu_B B'^2_{grav}}{B''_z} \tag{3.7}$$

For hydrogen in our magnetic trap with $B''_z = 0.37$ G/cm^2 and $\eta = 6$, the characteristic temperature is $T_{1D} = 67\ \mu\text{K}$. Since we routinely reach temperatures in the $20 - 40\ \mu\text{K}$ range, it is likely that our rf evaporation is losing its 3D character. This is mostly due to weak confinement along the z-axis. One solution to this problem is to orient the long axis of the Ioffe-Pritchard trap perpendicular to the gravitational axis. Unfortunately, this would require a major redesign of the current cryogenic system. A more practical, immediate solution is to simply increase B_z''. A scheme for accomplishing this is discussed in Sec. 4.1.2.

3.4 Bolometry of the Trapped Gas

When hydrogen atoms leave the trap they undergo molecular recombination on the cell walls, liberating energy that can be detected by a sensitive bolometer [25, 135]. By lowering the magnetic barrier and allowing atoms to escape from the trap, the bolometer can be used reliably to measure the temperature [24] and density [82] of the hydrogen sample. It can also be used to monitor the evaporative cooling process and is an essential component of rf-ejection spectroscopy.

3.4.1 Bolometric Temperature and Density Measurements

As the magnetic barrier defining the trap depth is lowered, atoms escape, stick to a wall, recombine, and deposit energy on the bolometer. The detection process is described in detail in [25], but the essential point is that the energy deposited on the bolometer is proportional to the number of atoms that escaped from the trap. If the time to release the atoms is shorter than the thermalization time of the sample, the energy distribution will not change much, and the bolometer signal can be combined with knowledge of the magnetic field configuration to deduce the sample temperature. Bolometric determination of the temperature is reliable for samples with temperatures between $100\ \mu\text{K}$ and $5\ \text{mK}$ and densities below $10^{14}\ \text{cm}^{-3}$.

The sample density can be measured using the bolometer by releasing the atoms from the trap after holding them for different times t following the forced evaporation.

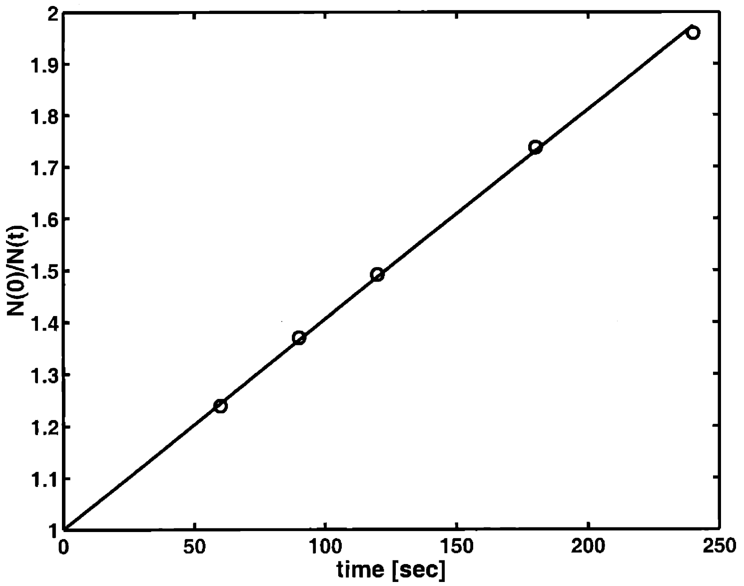

Figure 3-7: Dipolar spin-relaxation of a trapped hydrogen sample. The sample is held for various times following evaporative cooling before the sample is released from the trap. The number of escaping atoms is inferred from the bolometer signal. The data is fit to a straight line according to Eq. (3.8), allowing us to extract $n_0(0)$.

The total recombination energy deposited on the bolometer is proportional to $N(t)$, the number of atoms remaining in the trap at time t. $N(t)$ decreases with time due to dipolar spin-relaxation, which removes atoms from the sample at a density-dependent rate (Fig. 3-7). This process obeys Eq. 3.1. When averaged over the density distribution in the trap, this implies that $N(t)$ obeys [82]

$$\frac{N(0)}{N(t)} = 1 + \kappa g n_0(0)t \tag{3.8}$$

Here, $n_0(t)$ is the maximum density in the sample at time t, and κ is a numerical factor which depends on the trap geometry. Computations show that κ is typically in the range $0.2 - 0.3$. For a given geometry, the uncertainty in κ is about 10%, arising from imperfect knowledge of the trapping fields. The ratio of $N(0)/N(t)$ changes linearly with time according to Eq. (3.8). Figure 3-7 shows measurements made at five different times fit to a straight line. The fit allows us to extract $n_0(0)$.

For temperatures below about 100 μK, the trapping fields are quite small in magnitude, and contributions from magnetic materials and trapped fluxes in the superconducting magnets distort the trap and make bolometric measurements of n_0 unreliable.

Chapter 4

Cell Design and Improvements

A significant portion of this thesis involved design and construction of a cryogenic cell to trap and study Bose-Einstein condensates of atomic hydrogen. This chapter discusses important considerations in the design of the cell as well as construction techniques. The original superfluid ^{4}He jacket design is due to Fried [32]. A number of improvements to the original design have been made and include: better cell temperature control due to relocation of the rf antennas for evaporation and improved spectroscopy due to screening of stray electric fields with a thin Cu film. These and other improvements are discussed in detail, and measurements characterizing the improved cell are presented.

4.1 Source Region

Figure 4-1 shows a detailed view of the cryogenic dissociator and cell top region. Two principal concerns dictate the mechanical design of this region: thermal conductivity from cell to mixing chamber of the dilution refrigerator and superfluid leak-tight joints. The cell top, dissociator body, and anchor to the mixing chamber are all made from OFHC copper to ensure good thermal conductivity. Connections between these components are made with large overlap areas and are held in place securely with titanium screws. Titanium screws were chosen for their strength and non-magnetic

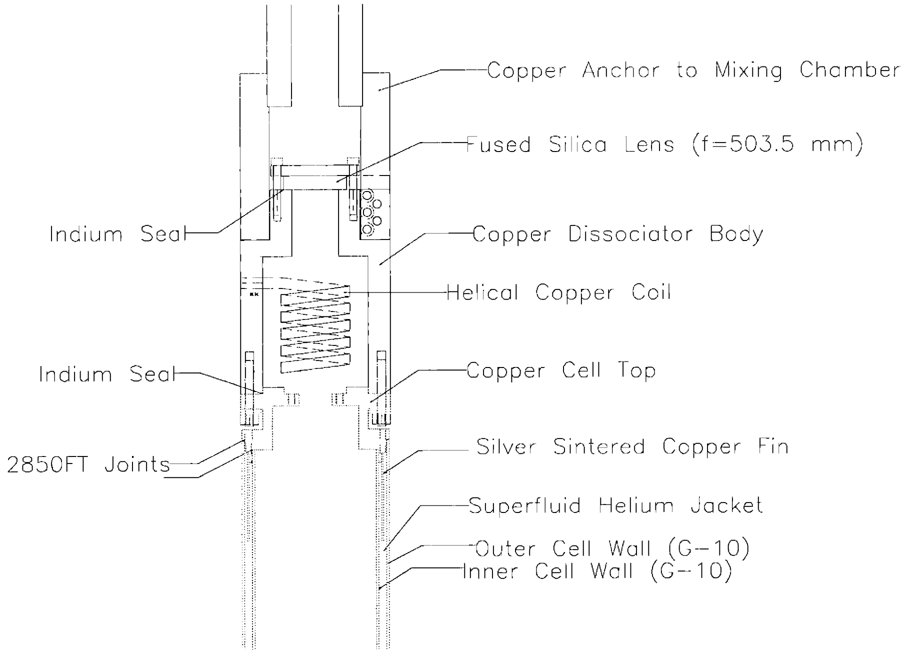

Figure 4-1: The dissociator and cell top are shown in detail. The inlet tube used for loading gas into the dissociator is not shown.

properties since the dissociator is located in a 4 T magnetic field. The large magnetic field quenches the superconductivity of the indium seals and allows them to become good thermal conductors. Thermal conductivity from the bottom to the top of the cell is provided by superfluid helium in a jacket surrounding the cell. Silver sintered copper fins extending from the cell top into the superfluid ^{4}He jacket provide a large effective surface area for heat transport across the metal - superfluid boundary.

Outside the dissociator and cell walls is a vacuum space that thermally isolates the cell and refrigerator from a 4 K liquid helium bath. To maintain the vacuum it is imperative that the cell and the dissociator are superfluid leak-tight. Indium wire seals are well known to be leak-tight to superfluid. One such seal joins the copper cell top and dissociator body. The second seals the lens used during spectroscopy at the top of the dissociator. These seals are extremely reliable when made properly. Epoxy joints between the G-10 tubes and metal and glass surfaces, as well as some wire feed-throughs are made using Stycast 2850FT cured with 24LV catalyst [122].

We have performed extensive studies to characterize the dissociator. Typically the dissociator and cell are held at 250 - 300 mK while pulses of 800 μs length at a repetition rate of 50 Hz are applied for 8 seconds. The flux from the dissociator is greater than 10^{14} s^{-1}. In general great care is taken to make sure that none of the surfaces in the discharge become too warm, producing spots bare of helium film where accelerated molecular recombination can take place. This is accomplished by good thermal anchoring of all surfaces and operating the dissociator in a pulsed, i.e. low average power, mode. A full discussion of the characterization of the dissociator is given in the thesis of Landhuis [73].

4.1.1 RF Antennas

The introduction of rf into the cryogenic environment proved to be a significant challenge but one whose successful solution led to the observation of BEC. The original rf antennas were composed of several loops of superconducting wire wrapped on the outside of the inner cell tube and cooled by the superfluid ^{4}He in the cell jacket [32]. The antennas were carefully arranged to maximize the rf magnetic field strength in the vicinity of the trapped atoms while minimizing eddy current heating in metal components connected to the dilution refrigerator. In addition to the geometry of the antennas, serious thought was given to the design of coaxial conductors used to transport the rf power from 300 K to the $\sim$ 100 mK cell. Good electrical conductivity was required without introducing a significant heat leak. Short coaxial segments with low thermal conductivity but significant electrical losses were spliced into the high thermal conductivity, low loss coaxial cable leading out of the cryostat.

Although the initial design was a success, it possessed several limitations. First, rf evaporation could not be started above $\sim$ 23 MHz due to heating of the cell and refrigerator. Some of this heating was probably due to eddy currents, but it is likely that most of the heating took place at the splicing joints in the coaxial cable leading to the cell. The impedance mismatch between the two types of cable led to heating. Second, because of the proximity of the rf antennas in the jacket to the electrical leads from the thermometers and bolometer at the cell bottom, it was difficult to monitor the cell temperature and the flux of atoms to the bolometer during rf evaporation. This presented a signal to noise limitation for using the bolometer to observe rf ejection [32] and eliminated the possibility of detecting a condensate using the bolometer (instead of by $1S$-$2S$ optical excitation: all non-optical BEC). Finally, the location of the antennas inside the superfluid jacket made repairs or adjustments difficult and risky to the entire cell assembly.

To circumvent all of these limitations, we relocated the rf antennas to the vacuum can that isolates the cell from the 4 K ^{4}He bath. This placement has the advantage that the antennas and the accompanying leads are completely separate from the refrigerator. Heat is deposited in the large heat capacity helium bath. The vacuum can is a 1/32 inch thick brass tube with an outer diameter of 5.08 cm and an overall length of 86.6 cm. It fits snugly inside the bore of the quadrupole magnet assembly. To avoid screening of the rf fields by this metallic tube, a section 19 cm in length was removed and replaced by an epoxy coated G-10 tube 1 15/16 inch id, 1/32 inch wall thickness, and 22 cm in length. The rf antennas were glued on the *inside* of this G-10 segment to maximize the distance between the antenna conductors and the brass bore of the quadrupole assembly.

The antenna was wound in a four turn helix pattern on a wax paper covered tube with a diameter slightly less than 4.73 cm using superconducting wire (Cu clad NbTi wire). The configuration of the 19 cm long, 4.73 cm diameter antenna is shown in Fig. 4-2. Small dots of Stycast 1266 epoxy were placed at the points where the wire crossed itself. After curing the epoxy, the tube was slid out from the wax paper, allowing the antenna and paper to be gently folded. The folded antenna was carefully placed inside the G-10 segment coated sparingly with additional 1266 epoxy. The epoxy was allowed to cure, and the wax paper was peeled away leaving the antenna securely attached to the inside of the G-10 segment.

The G-10 segment was then glued inside the upper and lower portions of the brass vacuum tube using Stycast 2850FT epoxy overlap joints. Great care was taken to

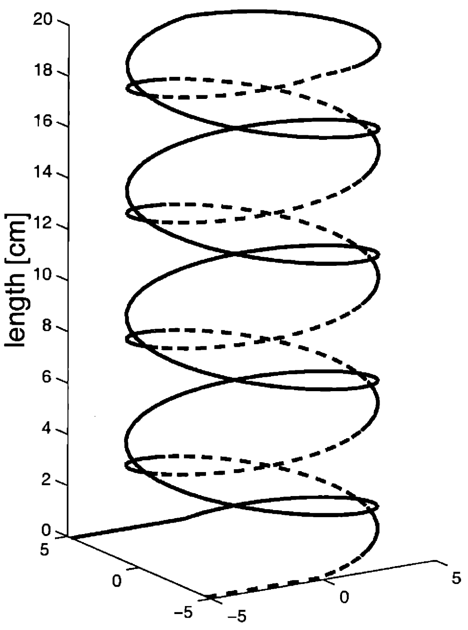

Figure 4-2: The helix-shaped rf antenna is located on the *inside* of a G-10 section of the inner vacuum can. The antenna extends 19 cm along the z-axis of the trap and has a diameter of 4.73 cm.

insure that the assembly was not kinked. Thermal contraction is always a concern in such cryogenic assemblies, but we found the brass/G-10 overlap joints to be reliable and superfluid leak-tight.

Constricted superfluid jacket

Before the insertion of the G-10 segment, the separation between the brass vacuum can and the outer cell was a comfortable 2.4 mm. This allowed for some misalignment of the 66 cm cell and the 86 cm brass can. The smaller diameter of the G-10 segment reduced this spacing to a mere 1.4 mm. To reduce the danger of thermal contact between the 100 mK cell and the 4 K vacuum can, we also reduced the diameter of a segment of the outer cell tube. A 23.7 cm long segment of G-10 tube of 42.8 mm outer diameter was inserted into the outer cell using 5 mm long 2850FT epoxy overlap joints. These overlap joints are separated vertically from the brass/G-10 overlap joints by 4 cm to allow for differential thermal contraction between the G-10 cell and the brass/G-10 vacuum can. The lower pair of 1 cm overlap joints can be seen near the top of Fig. 4-9.

The constriction in the superfluid jacket was a concern because of its reduced thermal conductivity. In superfluid ^{4}He, heat transport is due to phonons, and the heat carried by a material of cross section A and length L with a thermal conductivity coefficient κ is given (for small ΔT) by

$$S = \frac{\dot{Q}}{\Delta T} = \frac{\kappa A}{L} \tag{4.1}$$

The thermal conductivity of a tube of superfluid ^{4}He below 0.4 K is $\kappa = (20\,\mathrm{W/K^4\ cm^2}) d T^3$ where d is the diameter of the tube and T the temperature of the liquid [94].

For sensitive bolometric detection Fried estimated that the conductivity must be at least $S = 10\ \mu\mathrm{W}/10$ K for temperatures below 100 mK so that $S/T^3 = 2\ \mathrm{W/K^4}$ [32]. For a similar cell without the constricted jacket S/T^3 was measured to be 4 W/K^4 [32]. Using Eq. 4.1 we estimate that the constriction in the superfluid jacket will reduce the thermal conductivity by a factor of 0.8.

The value of κ given above assumes diffuse reflection of the phonons from the walls of the tube. Specular reflection of the phonons from the walls of the jacket can dramatically improve the thermal transport. Since the characteristic phonon wavelength at 100 mK is 300 nm [30], a surface that appears "shiny" at optical wavelengths will specularly reflect phonons. For this reason, great care was taken to give the G-10 tubes comprising the cell a smooth, shiny surface using epoxy coating techniques. The technique developed is described in Appendix A.

4.1.2 Z-axis Compression Coils

In addition to the rf antennas, the G-10 section of the vacuum can carries three new solenoid magnets. The purpose of these coils is to produce a "dimple" in the magnetic potential to increase the z-axis oscillation frequency ω_z. The 2 mm long main coil is wound from 16 turns of 3 mil superconducting wire centered at $z = +1.4$ cm and has a diameter of 4.93 cm.[1] The other coils are compensation coils and consist of 6 turns of wire wound in the opposite direction. They are located ±2.1 cm away from the main coil. The three coils are wound from the same strand of wire whose ends run along a shallow groove machined along the length of the brass vacuum tube. The fragile leads are fixed in the groove with Stycast 1266 epoxy for protection.

The magnetic potential along the z-axis is shown in Fig. 4-3 for various z-axis compression currents I_{dimple}. The solid line shows the magnetic field of our "standard" trap with $I_{\text{dimple}} = 0.0$ A, giving a curvature of $\beta = 25\ \mu\text{K/cm}^2$. The open circles ($\circ$) are a calculation of the same potential with $I_{\text{dimple}} = 0.5$ A. A harmonic potential with a curvature of $\beta = 55\ \mu\text{K/cm}^2$ is fit to the calculation, but it is clear that the potential away from the minimum is anharmonic. Finally, a trap with high bias field and $I_{\text{dimple}} = 4.0$ A (near the maximum current for the coil) is shown with open boxes ($\Box$). The curvature near the minimum is $\beta = 350\ \mu\text{K/cm}^2$. Since $\omega_z = \sqrt{2\beta/m}$, the

---

[1] The $z = 0$ point is defined in terms of the magnet forms shown in Fig. 3-3.

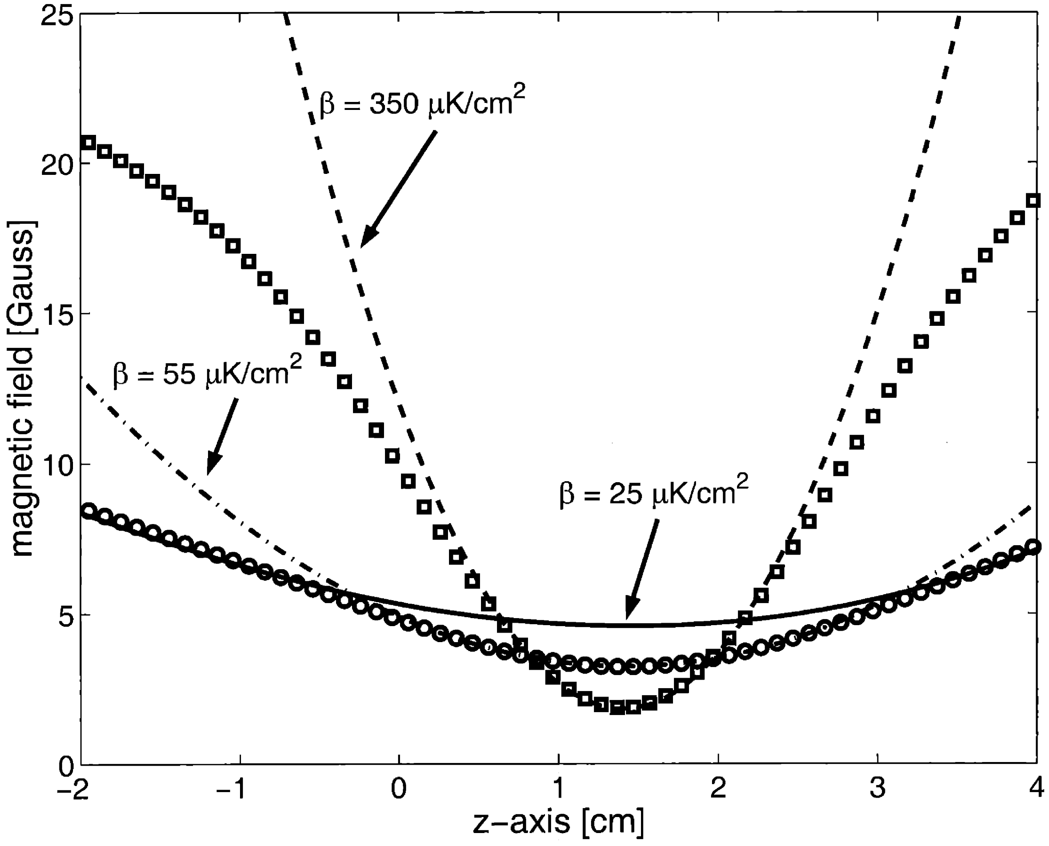

Figure 4-3: The magnetic field due to the z-axis compression coils is shown. The solid line shows the magnetic field without the z-axis compression coils. The open circles (○) indicate the field with 0.5 A in the coils, and the open boxes (□) indicate the field with 4.0 A in the coils.

z-axis oscillator frequency can be varied by a factor of ~ 4. When combined with a decrease in the stiffness of the trapping potential in the radial direction, the aspect ratio of the trapped cloud ω_ρ/ω_z can be changed by a factor of 20.

4.1.3 Thin Metallic Coating

A significant improvement over the previous G-10 trapping cell was achieved by reducing the stray electric fields in the vicinity of the trapped atoms. By itself G-10 is an excellent electric insulator, and patches of charge can build up leading to stray electric fields. The low temperatures of the cryogenic environment immobilize the charge on the timescale of hours. The exact source of these patch charges is unknown, but the hydrogen dissociator is a likely source.

Stray electric fields have no observed effect on the trapping of atoms, but they strongly affect the $1S-2S$ spectroscopy used to probe the hydrogen sample (see Chapter 5). One of the attractions of spectroscopy involving the $2S$ state is its metastability. Unperturbed, the $2S-1S$ radiative decay channel [127] is via two photons at a rate of $\gamma_{2S} = 8.23\ \mathrm{s}^{-1}$ [70], giving a lifetime of $\tau^0_{2S} = 121.5$ ms. In the presence of a dc electric field ε, however, the short-lived $2P$ state is mixed with the $2S$ state shortening its lifetime according to [6]

$$\frac{1}{\tau_{2S}(\varepsilon)} = \frac{1}{\tau^0_{2S}} + \frac{1}{\tau_{2P}}\left(\frac{\varepsilon}{475}\frac{\mathrm{cm}}{\mathrm{V}}\right)^2 \tag{4.2}$$

where $\tau_{2P} = 1.6$ ns is the $2P$ lifetime. Accelerated decay in the presence of dc electric fields is known as "Stark quenching." In previous spectroscopy experiments [15] conducted in a metallic trapping cell, the observed $2S$ lifetime was comparable to the theoretical value of 121.5 ms. In the previous G-10 cell, however, the $2S$ lifetime was typically a few milliseconds, indicating the presence of stray fields of about 0.5 V/cm. There were occasions when the stray fields were large enough to prevent the observation of a clean spectroscopic signal.

To overcome the problem of stray electric fields, we coated the inside of the trapping cell with a thin Cu film. This conductive layer prevents the accumulation of charges but allows the penetration of rf fields used for evaporation. Details of the coating process are found in Appendix B. Three issues are important for our experiment: dc conductivity of the film to reduce stray fields; heating of the cell by the rf fields; and attenuation of the rf field by the film. We can characterize the Cu film through its resistivity and attenuation of rf magnetic fields.

Properties of the Cu film

The resistance of a cylindrical conducting shell is related to its thickness by

$$t = \frac{\rho L}{2\pi r R} \tag{4.3}$$

where t is the thickness of the film, L the length of the cylinder, r the radius of the cylinder, and R the resistance along the length of the cylinder of resistivity ρ. We measured $R = 3.5\ \Omega$ for the tube of $L = 81$ cm and $r = 1.8$ cm. Using the bulk resistivity for Cu, $\rho_B = 1.6 \times 10^{-6}\ \Omega \cdot \mathrm{cm}$, $t = 3.4 \times 10^{-6}$ cm. This is a crude estimate of the film thickness.

As the thickness of a metal film becomes comparable in magnitude with the mean free path (mfp) of conduction electrons in the metal, the film boundaries impose a geometrical limitation on the movement of the conduction electrons and thus the effective value of the mfp. Physical effects arising from the geometrical limitation of the mfp are known as "mean-free-path" or "size" effects. There are more complicated theories that describe how the measured resistance can be used to determine the film thickness (e.g. [17]), but these theories apply to continuous films. The Cu film of the cell is discontinuous in some places and is mesh-like in others. This is due to the difficulty of the fabrication process. All large Cu regions were joined together and small bare spots covered up by applying a conductive graphite colloid (Aerodag [1]).

Another way to characterize the Cu film is to measure the attenuation of rf fields through the film. The results of measuring the attenuation at 60 MHz and 100 MHz

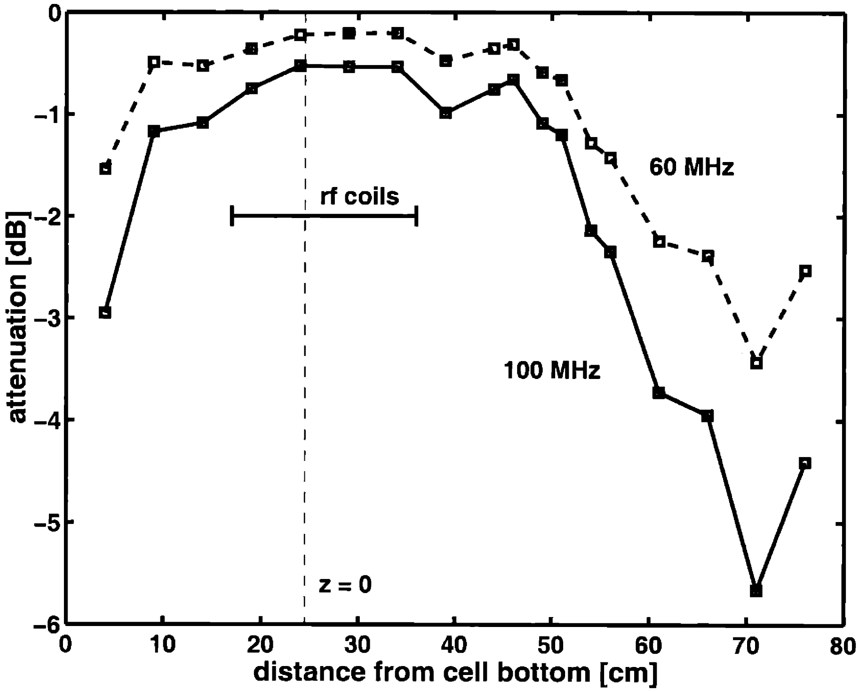

Figure 4-4: The attenuation of an rf magnetic field by the Cu coated cell tube at room temperature. The location of the rf coils is also shown. The Cu film was not slit along its length for these measurements.

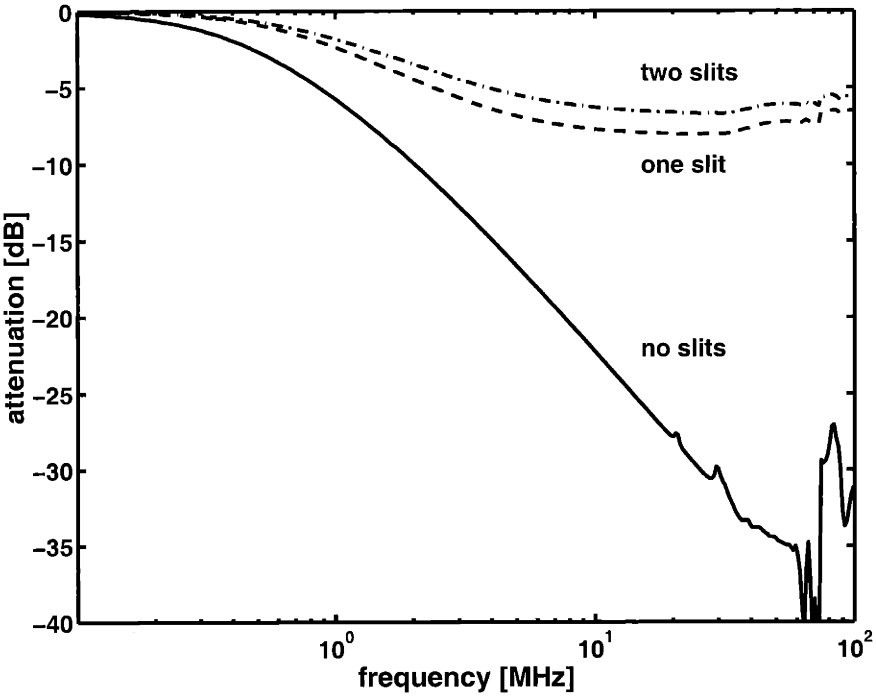

Figure 4-5: The reduction of rf attenuation is shown for three cases: an unslit tube with a thick Cu coating, the same tube with one slit, and the same tube with two slits.

at various locations along the cell tube at room temperature are shown in Fig. 4-4. The location of the rf antennas for evaporation is indicated in the figure along with the coordinate system of magnetic trapping (see Fig. 3-3). The location of the antennas coincides with the minimum attenuation, ensuring that the rf field seen by the atoms will be a maximum while the heating due to absorption of rf power will be a minimum.

Attenuation of rf fields in the cell is further reduced by slitting the Cu film along the length of the cylinder. Fig. 4-5 shows the effect of one and two slits on the attenuation of a thickly coated Cu tube. Without slits an applied rf field induces a current in the film around the circumference of the cylinder that tends to cancel the driving field inside the tube. Slits along the length of the cylinder interrupt the current and dramatically reduce the attenuation.

RF heating

We have measured the heating of the cell due to applied rf power. An rf power of +27 dBm outside the cryostat was applied to the rf antennas for 60 s, and the temperatures of the cell bottom and cell top were monitored using two resistance thermometers. The steady-state temperature of the cell for various applied frequencies is shown in Fig. 4-6. A resonance is apparent around 30 MHz where the cell bottom temperature rises above 200 mK. Above 35 MHz, the typical rf evaporation starting frequency, cell heating increases. This is consistent with the rf attenuation measurements shown in Fig. 4-4; increased rf attenuation and increased cell heating go hand in hand. For this reason, we believe that most of the heating is due to rf eddy currents in the Cu film. When the applied rf power is switched off, the cell cools rapidly, indicating that the heat capacity of the heated object is small. Again, this is consistent with absorption of rf power in the Cu film.

The cell bottom temperature is consistently higher than the cell top since rf heating occurs predominantly near the middle of the cell, and heat can only be removed through the cell top. In practice, the applied rf power used for evaporation and diagnostics of the trapped sample is much lower, meaning that bolometric detection of atoms remains possible even during rf evaporation. For example, +8 dBm applied outside the cryostat at 10 MHz (typical for coupling atoms out of the trap for diagnostic purposes) results in a cell bottom temperature of 70 mK; a temperature at which the bolometer has high sensitivity.

4.1.4 Integrated Electrodes

Placing narrow slits in the Cu film also allows one to fabricate electrodes which can be used to apply dc electric fields across the trapped sample. Applying dc fields has two purposes. First, one can null out any residual electric fields by applying a small (typically a few tens of mV/cm), constant offset. This will maximize the $2S$ state lifetime according to Eq. (4.2). Second, by applying a larger field of ≥ 10 V/cm,

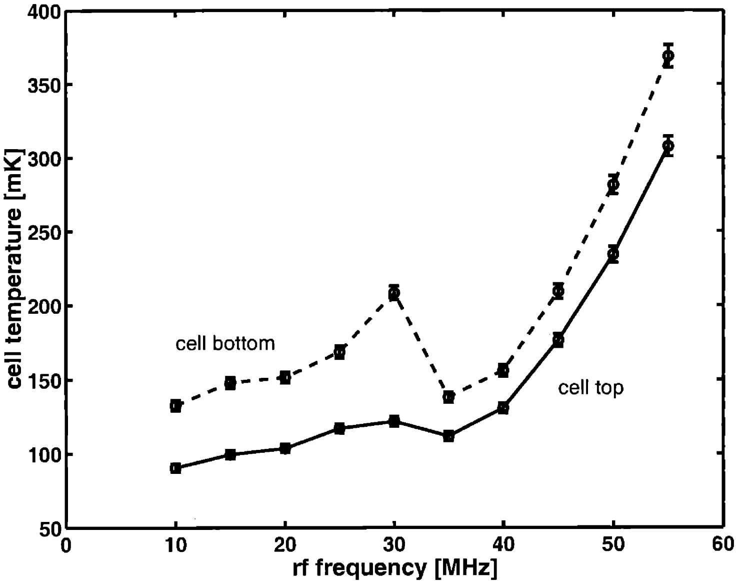

Figure 4-6: The cell temperature was measured as a function of frequency for +27 dBm applied outside the cryostat to the 4 K rf antennas. The solid line indicates the temperature of the cell top, and the dashed line indicates the cell bottom temperature. These measurements were made with the Cu film slit along the length of the tube.

one can induce the entire $2S$ state population to decay rapidly; a technique used in spectroscopy of the trapped sample (see Chapter 5). For these reasons, we integrated electrodes with the Cu film lining the cell.

Figure 4-7 shows the configuration of the electrodes integrated into the Cu film. The top half of the figure indicates the position of the electrodes as if the cell tube were slit along its length and unrolled. The electrodes are approximately 40 cm in length and cover the region where atoms are trapped (see Fig. 3-4). The electrodes were formed by scratching through the Cu film using a narrow file while holding the cell tube in a lathe. Contacts were made to the electrodes and ground plane using 5 mil manganin wire [81] and silver epoxy. The leads were then passed through small holes into the superfluid jacket space and later filled with Stycast 2850FT epoxy.

The lower half of Fig. 4-7 indicates the electrical connections of the Cu film electrodes. Applying a voltage to $V1$ and $V2$ changes the electric field experienced by the trapped atoms at the center of the cell. The ground plane shares the ground of the dilution refrigerator. Figure 4-8 is an example of a measurement of the $2S$ decay rate for different applied dc fields for a single trapped sample. The applied field plate voltage is $\Delta V = V1 - V2$. A parabola is fit to the data points indicating the quadratic dependence of the $2S$ decay rate in accordance with Eq. (4.2). The fit indicates the offset voltage at which the minimum decay rate occurs; this is the offset voltage used during spectroscopy. We do not expect the minimum decay rate to correspond to the natural decay rate ($\gamma_{2S} = 8.23\ \mathrm{s}^{-1}$) since stray fields are not compensated along the z-axis of the trap nor along the radial direction perpendicular to the $V1$-$V2$ axis. Even so, the 80 ms $2S$ lifetime indicated by the fit is a vast improvement over the lifetimes observed in the G-10 cell without a Cu film.

4.2 Detection Region

The detection region of the trapping apparatus was modified substantially in an effort to improve the efficiency of detecting Lyman-α fluorescence produced during

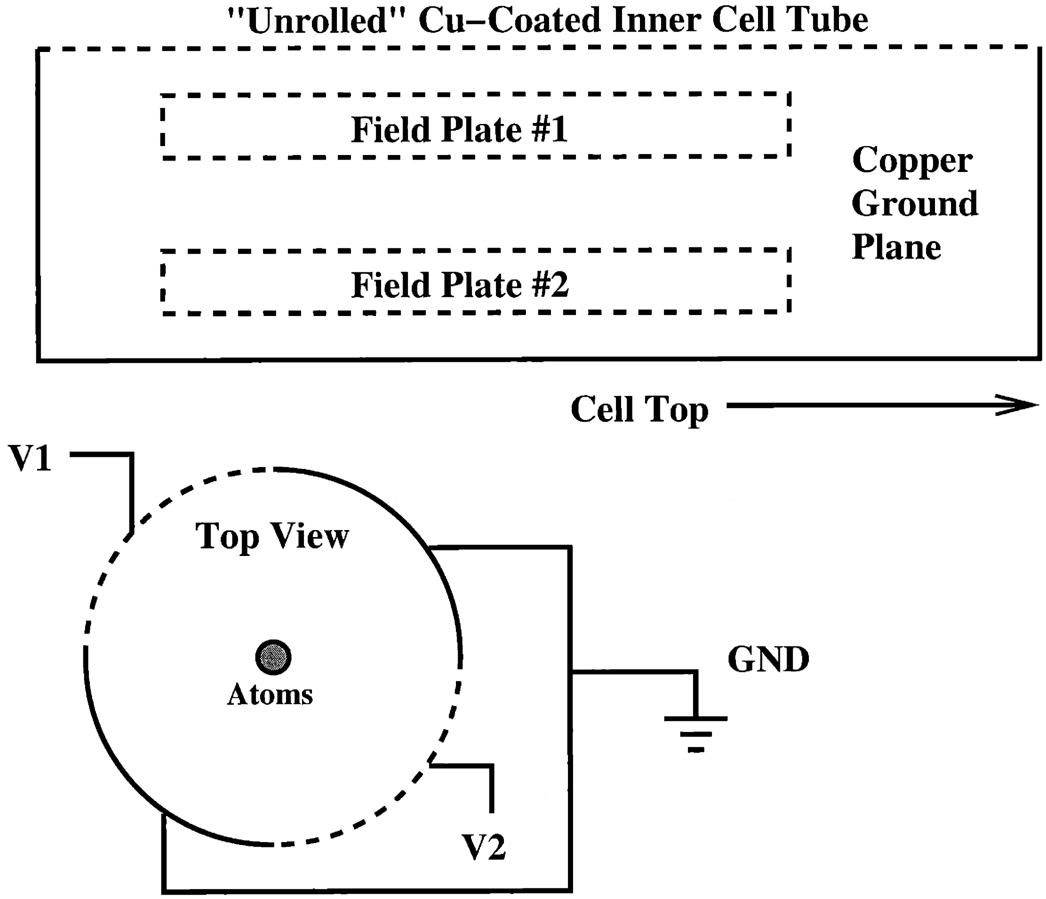

Figure 4-7: Electrodes for applying dc electric fields across the trapped sample were integrated into the Cu film lining the cell. Their configuration is shown in the upper half of the figure as if the cell tube were slit along its length and unrolled. The lower half of the figure shows the electrical configuration in the cell. Changing the voltage applied at $V1$ and $V2$ allows the electric field across the cell to be adjusted.

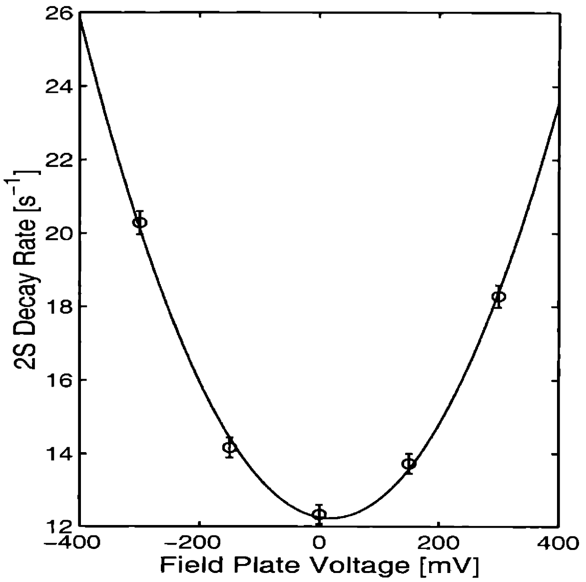

Figure 4-8: An example measurement of the $2S$ decay rate found by applying different dc voltages to a single trapped sample. The quadratic fit indicates the dependence of the $2S$ decay rate on the applied field strength (see Eq. (4.2)), and the minimum of the fit indicates the offset voltage to be used during spectroscopy.

spectroscopy of the trapped sample. The details of $1S$-$2S$ spectroscopy are discussed in Chapter 5, but the geometrical restrictions on detection can be understood from Fig.4-9.

4.2.1 Increased Solid Angle

Trapped atoms promoted to the $2S$ state through laser excitation are stimulated to fluoresce through application of a dc field as discussed in Sec. 4.1.4. The resulting fluorescence is detected by a microchannel plate (MCP) detector shown in Fig. 4-9. Additional details are presented in Sec. 5.3.1. Only photons that pass through both MgF_2 windows can be counted by the detector. The 243 nm retromirror glued to the cell MgF_2 window casts a shadow on the MCP since the mirror substrate (BK7) blocks uv radiation. To reduce the size of this shadow, the cell was lengthened to increase the distance from the mirror to the trapped sample, and the detection chamber body

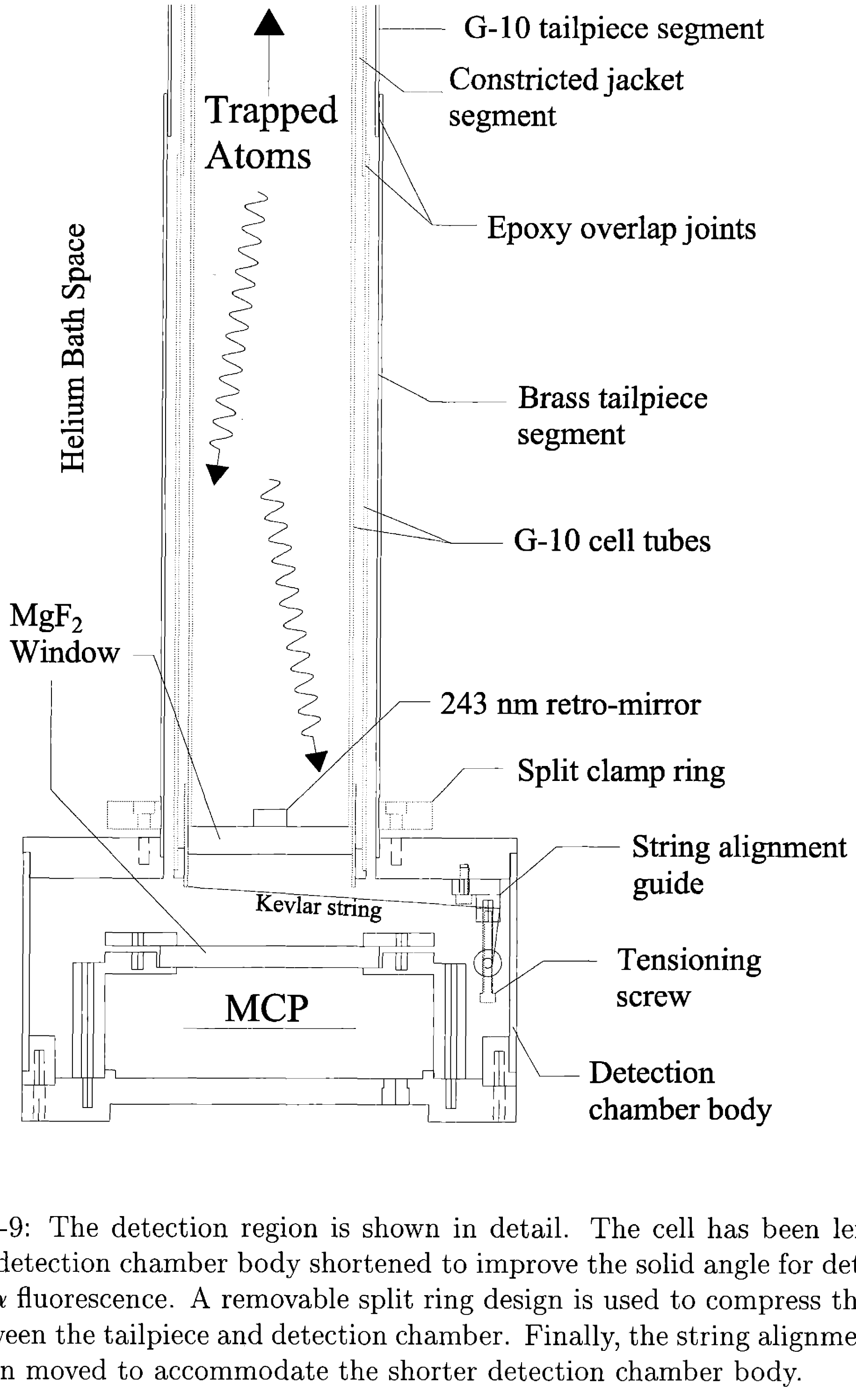

Figure 4-9: The detection region is shown in detail. The cell has been lengthened and the detection chamber body shortened to improve the solid angle for detection of Lyman-α fluorescence. A removable split ring design is used to compress the indium seal between the tailpiece and detection chamber. Finally, the string alignment guides have been moved to accommodate the shorter detection chamber body.

was shortened to move the detector closer to the atoms.

4.2.2 Detection Efficiency

An upper bound on the detection efficiency can be estimated from geometry and the properties of the optical components. The collection solid angle is 1.2×10^{-2} sr, and each MgF_2 window absorbs approximately 60% of the Lyman-α fluorescence. The quantum efficiency of the MCP was found to be about 25% based on comparisons with a calibrated photomultiplier tube (see [66]). Thus, the detection efficiency ε_{det} is at most 4×10^{-5}. It is likely that the actual detection efficiency is lower due to surface absorption losses, a lower quantum efficiency, and radiative reabsorption by the trapped sample. For a cold, dense sample, Landhuis [73] has measured $1.2 \times 10^{-6} < \varepsilon_{\text{det}} < 1.8 \times 10^{-6}$. There is much room for improvement in detection efficiency, but the biggest gains will come in an apparatus designed for spectroscopy.

4.2.3 Mechanical Design

Optical components

The lower end of the cell vacuum space is sealed by a MgF_2 window using a G-10 collar and 2850FT epoxy. The 7.64 mm diameter mirror, high-reflection (HR) coated for 243 nm and 656 nm radiation, was glued to the window center using an alignment jig and a small dot of Stycast 1266 epoxy. To block fluorescence from the HR coating, the sides of the mirror were coated with a thick layer of the graphite colloid Aerodag [1]. In addition after the window/mirror assembly had been glued to the cell, a small disc of brass shim stock was glued to the bottom of the MgF_2 window.

Great care was taken to ensure that the window was fixed perpendicular to the axis of the cell, providing good alignment for the laser beam to reflect from the 243 nm retromirror. The cell was attached to the dilution refrigerator and an adjustable alignment jig was constructed to hold the window/mirror assembly during gluing. The laser was present in the cell during the gluing process to continually monitor the

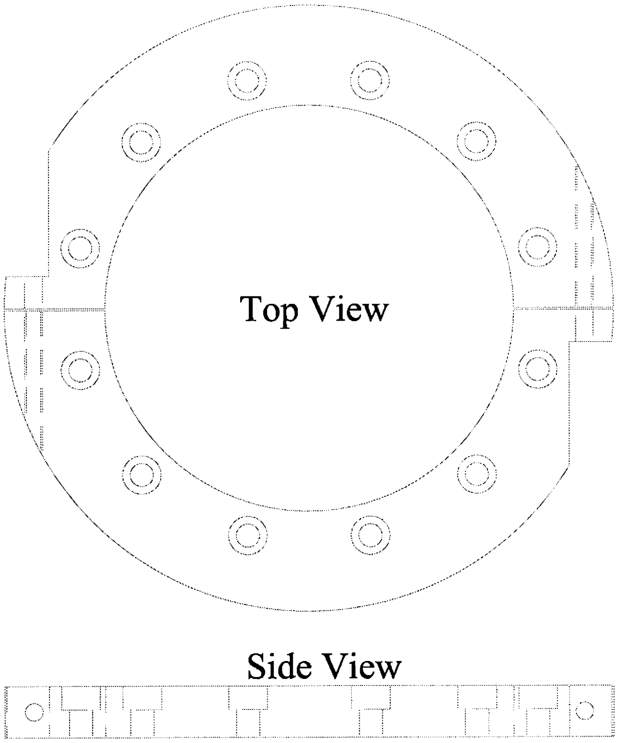

Figure 4-10: Split clamp ring used to form the indium seal between the tailpiece and detection chamber. This design serves as a removable flange.

mirror alignment. The care taken has paid off since alignment, quality, and power in the reflected 243 nm beam are excellent.

Split clamp ring

Lengthening the cell required a redesign of the indium seal made between the brass tailpiece segment and the detection chamber body. There is no longer space for a bolt circle inside the brass tailpiece, and the diameter of the tailpiece cannot exceed 2.000" due to restrictions of the quadrupole magnet assembly. To overcome these limitations, we designed a removable split clamp ring that attaches to a 0.050" deep groove cut into the tailpiece. The ring forms a bolt circle which is then used to squeeze an indium seal between the end of the tailpiece and the detection chamber body. The ring is shown in Fig. 4-10.

Alignment strings

During cooling from 300 K to base temperature, the trapping apparatus is subject to thermal contraction. Since it is vital to thermally isolate the trapping cell from the 4 K vacuum cans, three Kevlar strings are employed to keep the cell centered with respect to the vacuum cans. The strings are tied through holes in the cell bottom and pass through an alignment guide to a tensioning device. The tensioning device is a small spool around which the string is wrapped. The string is placed under tension using screws that pass through threaded holes in the spool. Care should be taken not to over-tension the strings at room temperature since the strings are also subject to thermal contraction.

Chapter 5

$1S$-$2S$ Spectroscopy of Hydrogen

Our principle diagnostic technique for studying cold, dense trapped samples is laser spectroscopy of the $1S$-$2S$ transition. It is our only technique for observing Bose-Einstein condensation and has been used to collect most of the data in this thesis. Although the laser system was designed and built by others [16, 107], a brief overview is given here. In addition, T. Killian and D. Landhuis have made significant contributions, improving the performance and reliability of the original system. Further details are available in their theses [66, 73].

This chapter also gives a brief theoretical description and experimental observations of the lineshapes resulting from $1S$-$2S$ spectroscopy in a trap. An understanding of the origins of the lineshapes will be useful for interpreting data presented in Chapter 7. More details are available in [16, 66, 73, 107].

5.1 The Two-Photon $1S$-$2S$ Transition

The two-photon $1S$-$2S$ transition in hydrogen was first observed by Hänsch and collaborators in a gas cell in 1975 [45]. In our laboratory Cesar *et al.* [15] reported the first observation of the $1S$-$2S$ transition of hydrogen confined in a magnetic trap. This was not the first optical spectroscopy of hydrogen in a magnetic trap. The Amsterdam hydrogen group had used the $1S$-$2P$ (Lyman-α) transition, with its large

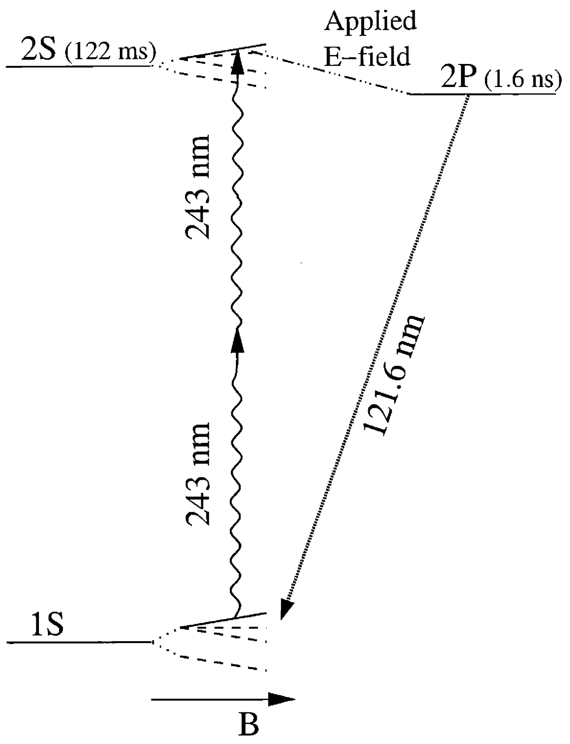

Figure 5-1: A simple level diagram indicating the energy levels involved in $1S$-$2S$ spectroscopy of hydrogen in a magnetic trap. An atom in the $F = 1, m_F = 1$ ground state absorbs two 243 nm photons and is promoted to the long lived $2S$ state. An applied electric field Stark mixes the $2S$ state with the $2P$ state causing prompt radiative decay by Lyman-α fluorescence to all magnetic sublevels of the ground state.

single-photon transition rate, to study trapped samples in the millikelvin regime [80]. Later they also performed Doppler cooling and light-induced evaporation [110], but the $1S$-$2P$ transition has a large linewidth (100 MHz) and limits measurements of sample temperature to a few millikelvin. In principle, one can use transitions to higher S and D states to circumvent this problem [91], but this procedure is complicated because one has to work in the vacuum ultraviolet (VUV).

The attractions of the $1S$-$2S$ transition are its inherently small natural linewidth, 1.3 Hz, and the efficiency of Doppler-free two-photon excitation. Possibilities for metrology and fundamental physics have been impressively demonstrated using this transition [71] – precise measurements of the Lamb shift of the $1S$ and other states [74, 132], the hydrogen $1S$-$2S$ isotope shift [74], and determination of the Rydberg constant [10]. In fact, the determination of the absolute $1S$-$2S$ transition frequency has revolutionized optical frequency metrology through the development of the optical frequency comb generator utilizing femtosecond mode-locked lasers [53]. The frequency $f_{1S-2S} = 2,466,061,413,187.29(37)$ kHz is one of the most accurately known frequencies in the optical or UV region [99].

The $1S$-$2S$ transition cannot be excited by a single photon because both states have angular momentum zero. Two-photon excitation can take place through intermediate virtual P states. The relevant levels in our case are shown in Fig. 5-1. Two 243 nm photons are absorbed by the atom in a time less than $\hbar/\Delta$, where $\Delta = (E_P - h\nu)$ is the laser detuning from the P level. The single-photon transition rate scales as I, the laser intensity, but the two-photon transition rate scales as I^2. The two-photon transition rate is much weaker than the single-photon rate for the same laser intensity. For similar reasons, the $2S$ state can only radiatively decay to the ground state through spontaneous emission of two photons [127], leading to its long natural lifetime, $\tau_{1S} = 122$ ms.

5.2 UV Laser System

The laser system used for spectroscopy of trapped atomic hydrogen is based on a design from the group of T. Hänsch in Munich [61]. Fig. 5-2 shows a simplified schematic of the the system. A few details are given here.

An Innova 200 Krypton ion laser pumps a Coherent model 699 ring dye laser using Coumarin 480 dye to produce 600 mW of linearly polarized 486 nm light in the TEM_{00} mode. The dye laser frequency is actively stabilized to an external Fabry-Perot reference cavity using a piezo-mounted mirror, a galvo-mounted brewster plate, and an intracavity electro-optic modulator (EOM). The laser frequency is locked to a transmission fringe of the cavity using the Pound-Drever-Hall locking scheme [26], resulting in a laser linewidth of less than 1 kHz. The laser frequency is tuned rela-

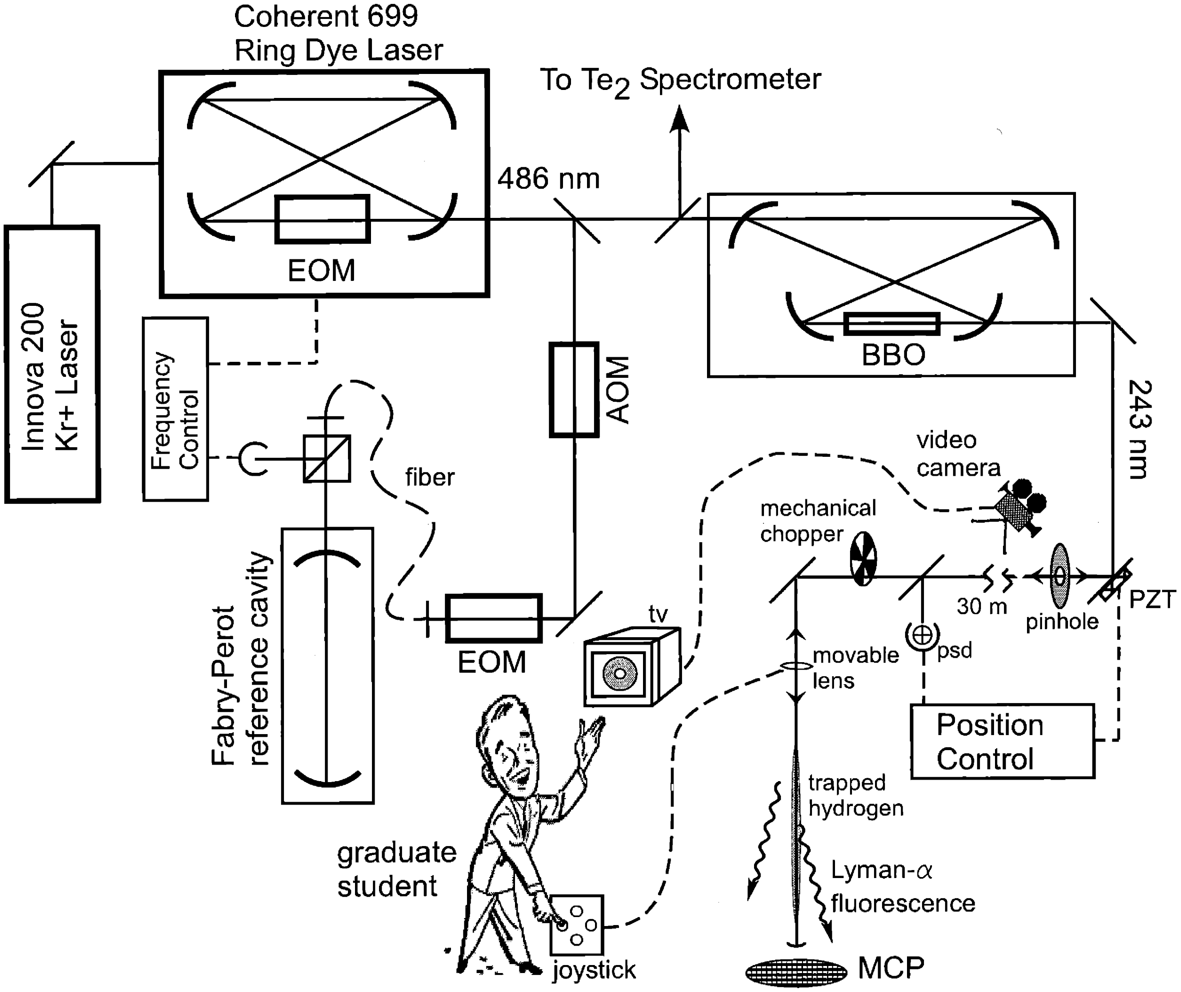

Figure 5-2: A simplified diagram of the UV laser system used for spectroscopy of the 1S-2S transition. Descriptions of some of the components can be found in the text. Note the human component in the servo system used to maintain laser alignment with the trapped sample.

tive to the cavity by changing the rf drive frequency of an acousto-optic modulator (AOM) in the optical path to the cavity. The laser frequency can be determined absolutely to within a few hundred kHz by performing Doppler-free saturated absorption spectroscopy of molecular $^{130}\mathrm{Te}_2$.

Most of the 486 nm light is delivered to a second harmonic generation (SHG) cavity to produce the 243 nm radiation needed for $1S$-$2S$ spectroscopy. The SHG cavity is arranged in a bow tie configuration to enhance the blue power in the beta barium borate (BBO) doubling crystal. The Hänsch-Couillaud locking scheme [44] is used to maintain the cavity in resonance with the 486 nm light. The cavity produces almost 40 mW of 243 nm light from 450 mW of 486 nm light.

The laser system and the cryostat containing the trapped hydrogen are separated by 30 m. To perform Doppler-free spectroscopy of the trapped atoms, good spatial overlap of the incoming and return beam must be maintained. This is accomplished through a two point beam steering system. The 243 nm beam from the optical table is launched via a piezo-mounted mirror (PZT-mirror) into an air-filled conduit which transports the beam to the room containing the cryostat. A small fraction of the beam is directed onto a position-sensing photodiode (PSD) on top of the cryostat. Position control electronics servo the PZT-mirror to maintain the beam position on the PSD. The main beam enters the cryostat, passes through the trapped sample, reflects from the retro-mirror and returns to the optical table 30 m away. A tiny video camera monitors a pinhole in a small fluorescent card above the PZT-mirror. If the beam alignment drifts, the card will fluoresce. A graduate student monitoring the card in another room corrects for the drift using game controllers to adjust the position of a stepper motor mounted lens. This system works surprisingly well due to the 30 m separating the two beam steering points.

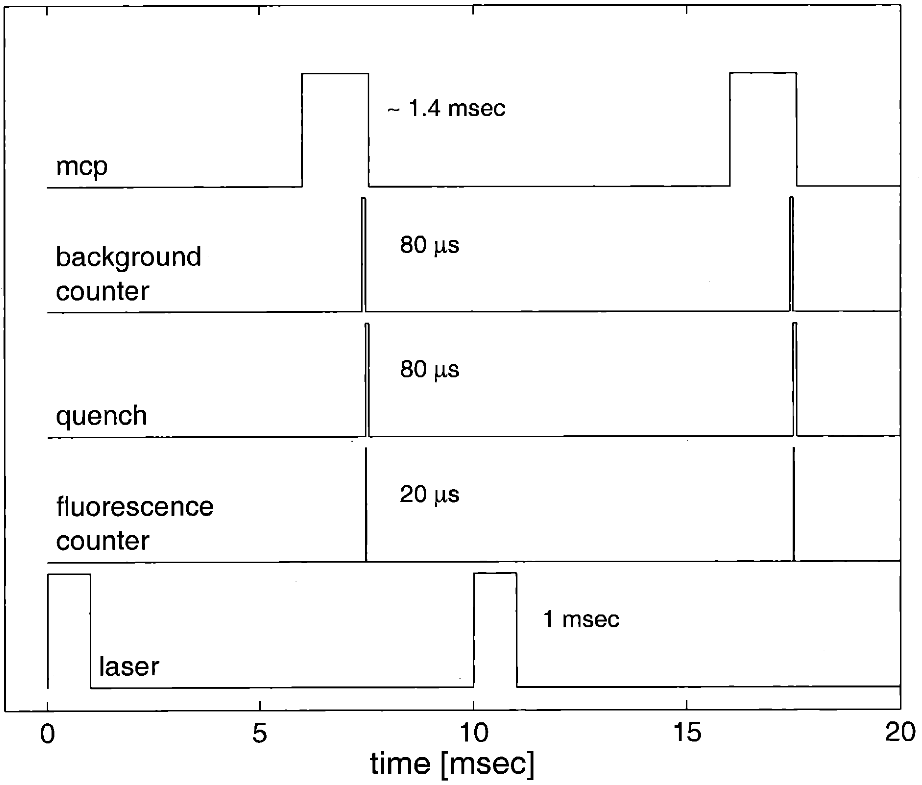

Figure 5-3: A typical timing sequence for excitation and detection. The full cycle is 10 ms long. The MCP detector is switched on $\sim 5 - 8$ ms after the end of the laser pulse to allow background fluorescence to diminish. The 80 μs electric field pulse causes prompt decay of the $2S$ state. A 20 μs signal counter records the decay photons. Two other fluorescence counters are not shown.

5.3 Excitation/Detection Scheme

The photoexcitation of the trapped sample is detected by monitoring the fluorescence from the excited atoms. The atoms are excited and detected using a pulsed scheme shown in Fig. 5-3. Following excitation an electric field pulse (~ 10 V/cm) is applied to Stark-mix some $2P$ ($\tau_{2P} = 1.6$ ns) character into the excited state wavefunction and cause prompt decay to the ground state by Lyman-α (121.6 nm) fluorescence. The fluorescence photons are detected by the microchannel plate detector.

For the experiments in this thesis, the laser beam is chopped at 100 Hz with a duty cycle of $\sim$ 10% by the mechanical chopper shown in Fig. 5-2. This sets a timescale of 10 ms per excitation-detection sequence. Following the 1 ms laser pulse, a delay of 7.4 ms allows background fluorescence of organic materials in the cell to decay. An 80 μs electric field pulse is applied to quench the excited atoms, and a 20 μs fluorescence counter records their decay. In addition, a background counter is open for 80 μs immediately before the quench pulse. The signal in this counter can be used to estimate the background contribution to the signal in the fluorescence counter. As discussed in App. C, the microchannel plate detector (MCP) is operated in a switched mode and requires about one millisecond to develop full sensitivity.

After the desired number of laser shots, the laser frequency is changed, and the excitation-detection sequence is repeated. The record of fluorescence counts versus laser detuning constitutes a measurement of the $1S$-$2S$ spectrum. Typically, the laser frequency is swept back and forth 50 to 400 times. It is important to note that each of these spectra is recorded from the *same* trapped sample. In this way, $1S$-$2S$ spectroscopy can be viewed as a nearly non-destructive probe.

5.3.1 Microchannel Plate Detector

The detection of fluorescence photons using a microchannel plate detector (MCP) is one aspect of the hydrogen BEC experiment that differs substantially from its alkali atom counterparts. Most alkali experiments use a CCD camera to *image* their trapped atom clouds. For hydrogen, however, the lack of 121 nm optics prevents direct imaging. A recent metastable ^{4}He BEC experiment uses an MCP to record atoms released from the trap. The MCP functions as a detector of metastable atoms because 20 eV of stored energy is released when the atoms collide with the detector surface. In our case, the MCP must be separated from the atom cloud by a $\mathrm{MgF_2}$ window (see Fig. 4-9) because of the need to confine the ^{4}He film, and cannot detect the metastable $2S$ atoms directly. Instead the MCP records the 10.2 eV Lyman-α photons emitted by the decay of the excited state atoms.

The MCP is a 0.6 mm thick, 50 mm diameter lead glass disk filled with 10 μm diameter channels. The open area of the disk is 60%. The top surface is coated with CsI to enhance the production of electrons resulting from incident ultraviolet (uv) photons. As shown in Fig. C-1, approximately 675 V is applied to guide the electrons produced by the uv photons into the channels. The electrons then collide with the channel walls to create an avalanche of electrons. In effect, each channel is a tiny photomultiplier with a gain of 10^4.

A second MCP plate is biased by 85 V with respect to the first to collect and amplify the electron shower. The total gain of the plates is about 10^6 and results in a 5 ns pulse of 1 mV amplitude into 50 Ω for each incident uv photon. The 1 mV pulse is amplified, discriminated, and converted into a logic pulse for counting. Killian [66] measured the quantum efficiency of the MCP assembly to be 25% using a calibrated photomultiplier tube.

The MCP operates in the low temperature environment of the cryostat. As a result, it can take seconds for the charge in a single channel to be replenished. During this time the channel is insensitive to incident photons. If a significant fraction of the channels fire at the same time, the efficiency of the MCP drops significantly. This is the case, for example, if unattenuated scatter from the laser strikes the detector. In the past a Lyman-α filter above the MCP reduced the intensity of 243 nm light by a factor of 500, preventing stripping of the MCP. Unfortunately, the filter also reduced the transmission of Lyman-α by 90%. We have eliminated the Lyman-α

filter and replaced it by a MgF_2 window. To protect the MCP against laser scatter, we have implemented a switching scheme that energizes the MCP after the laser pulse is finished. The MCP is then switched off before the next laser pulse (see Fig. 5-3). Details of MCP switching can be found in App. C.

5.4 The $1S-2S$ Two-Photon Transition

Two-photon transitions from a given $1S$ level involve only a single Zeeman sublevel in the $2S$ manifold since two-photon transitions obey the selection rules $\Delta F = 0$, $\Delta m_F = 0$. Virtual P-states are necessary for the two-photon transition to take place, but conceptually the system may be treated as having only two levels. This allows us to understand two-photon transitions in a familiar context.

If a trapped $1S$ atom with momentum $\mathbf{p}_{1S}$ absorbs two photons with momenta $\hbar\mathbf{k}_1$ and $\hbar\mathbf{k}_2$ and is promoted to the $2S$ state, conservation of momentum requires that $\mathbf{p}_{2S} = \mathbf{p}_{1S} + \hbar\mathbf{k}_1 + \hbar\mathbf{k}_2$. Simultaneously, conservation of energy requires that the laser frequency satisfy

$$\begin{aligned} 2h\nu_{\text{laser}} &= \sqrt{p_{2S}^2 c^2 + (mc^2 + E^0_{1S-2S})^2} - \sqrt{p_{1S}^2 c^2 + (mc^2)^2} \\ &\approx E^0_{1S-2S} + \frac{\mathbf{p}_{1S}\cdot(\hbar\mathbf{k}_1 + \hbar\mathbf{k}_2)}{m} + \frac{|\hbar\mathbf{k}_1 + \hbar\mathbf{k}_2|^2}{2m} - \frac{|\mathbf{p}_{1S} + \hbar\mathbf{k}_1 + \hbar\mathbf{k}_2|^2}{2m}\frac{E^0_{1S-2S}}{mc^2} \end{aligned} \tag{5.1}$$

where m is the rest mass of the atom. The terms on the right hand side of Eq. 5.1 are energy shifts. The second and fourth terms represent the first and second order Doppler shifts, respectively. The third term represents the energy shift due to photon recoil. The second order Doppler shift can be neglected since the shift is much less than 1 Hz for hydrogen in the submillikelvin regime.

In our experiment two-photon absorption takes place in a standing wave configuration, leading to two possibilities for absorption. If two copropagating photons are absorbed, $\mathbf{k}_1 = \mathbf{k}_2$, and the resulting spectroscopic feature includes both the first

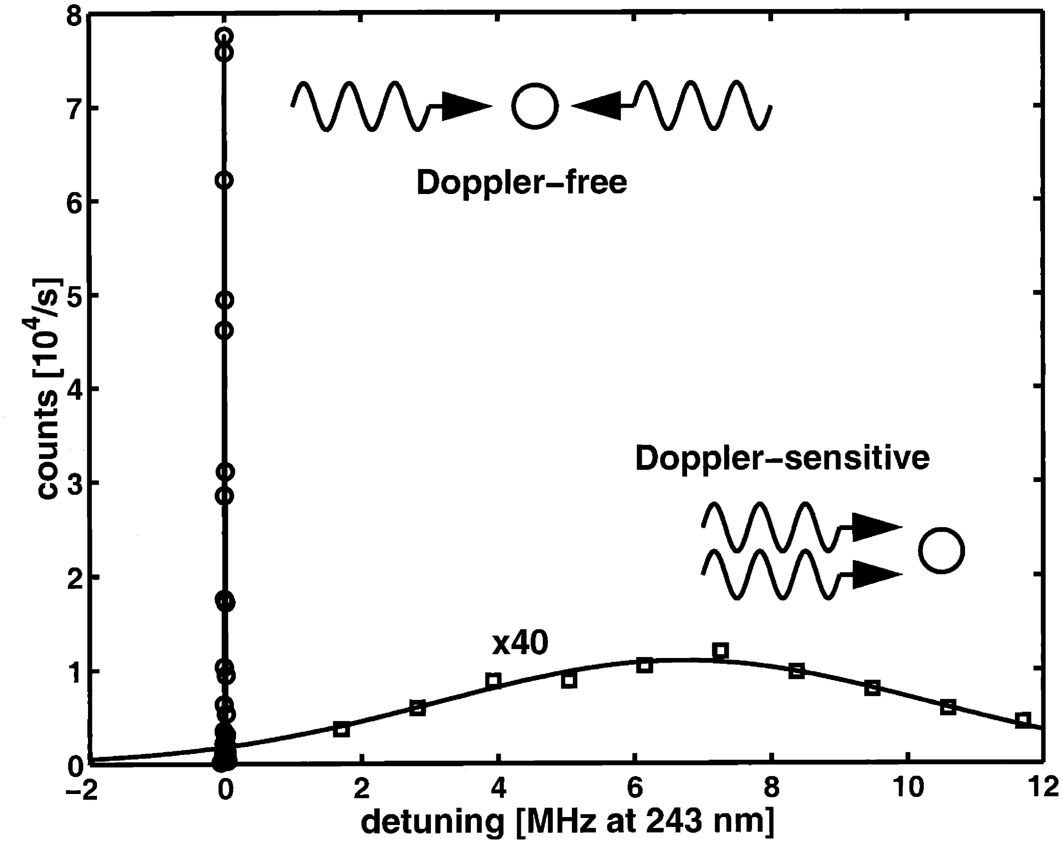

Figure 5-4: Full 1S-2S spectrum for hydrogen above degeneracy. The narrow, intense feature is due to Doppler-free absorption of two counterpropagating photons. The broad feature is due to Doppler-sensitive absorption of two copropagating photons and is shifted 6.7 MHz to the blue of the Doppler-free line by the recoil shift. The Doppler-sensitive spectrum has been magnified 40 times. Signal intensity is given in counts per laser second.

order Doppler shift, proportional to the momentum distribution of the sample, and the recoil shift ($\Delta\nu_{\mathrm{recoil}} = 6.7$ MHz (at 243 nm)). On the other hand, if two counter-propagating photons are absorbed, $\mathbf{k}_1 = -\mathbf{k}_2$, and both the first order Doppler shift and recoil shift vanish. The resulting spectroscopic feature can be very narrow and intense.

The full $1S$-$2S$ spectrum of hydrogen above degeneracy is shown in Fig. 5-4. The narrow, intense Doppler-free feature is located at the unshifted $1S$-$2S$ resonance frequency. We have observed signal rates in excess of 10^5 counts per laser second. The Doppler-sensitive feature is much broader and has been magnified 40 times. The data shown corresponds to a sample temperature of 89.2 ± 5.7 μK and is shown in detail in Fig. 5-5.

5.5 $1S - 2S$ Spectroscopy: Lineshapes

In this section a brief formal description of $1S - 2S$ spectroscopy is provided. Killian [66] provided a detailed description of the formalism describing two-photon Doppler-sensitive and Doppler-free excitation based on time-dependent perturbation theory. The results are summarized here because it is useful to understand the origins of the lineshapes that are used to determine sample temperature and density. The general excitation perturbation is discussed first. A discussion of Doppler-sensitive excitation follows. Finally, Doppler-free excitation, time-of-flight broadening, and the cold-collision shift are reviewed. Experimental data is presented illustrating each of the lineshapes.

5.5.1 Time-Dependent Perturbation Theory: Application to the $1S - 2S$ Transition

A useful and familiar way to calculate the $1S - 2S$ transition rate is to use time-dependent perturbation theory [106]. The first order transition probability vanishes since a single-photon transition cannot occur between two states with $\Delta l = 0$. Instead, we have to go to second order to find the transition rate to the $2S$ state. Fortunately, the second order transition coefficient can be reduced to the form of a first order coefficient,

$$c^{(2)}_{2S,\mathbf{p}_2}(t) = -\frac{i}{\hbar}\int_{t_0}^{t} dt''\, V_{2S,\mathbf{p}_2;1S,\mathbf{p}_1}(t'')e^{-i\omega_{1S,\mathbf{p}_1-2S,\mathbf{p}_2}(t''-t_0)}, \tag{5.2}$$

where $\hbar\omega_{1S,\mathbf{p}_1-2S,\mathbf{p}_2} = \hbar\omega_{1S-2S} + \frac{\mathbf{p}_2^2}{2m} - \frac{\mathbf{p}_1^2}{2m}$ and $V_{2S,\mathbf{p}_2;1S,\mathbf{p}_1}(t'')$ is the off-diagonal element of the effective two-level Hamiltonian.

Killian finds that

$$\begin{aligned} V_{2S,\mathbf{p}_2;1S,\mathbf{p}_1}(t) &= \hbar\left(\frac{\alpha}{2R_\infty}\right)^3 \frac{1}{3\pi^2\hbar c}\left[\frac{1}{2}\left(I_1(\mathbf{R})\delta_{\mathbf{p}_2,\mathbf{p}_1+2\hbar\mathbf{k}} + I_2(\mathbf{R})\delta_{\mathbf{p}_2,\mathbf{p}_1-2\hbar\mathbf{k}}\right) M^{11}_{2S,1S}\right. \\ &\qquad \left. + \sqrt{I_1(\mathbf{R})I_2(\mathbf{R})}\delta_{\mathbf{p}_2,\mathbf{p}_1} M^{12}_{2S,1S}\right] e^{2i\omega t}, \end{aligned} \tag{5.3}$$

where

$$I_i(\mathbf{R}) = \frac{2P}{\pi w^2(z)} \exp\left[-\frac{2(x^2+y^2)}{w^2(z)}\right] \tag{5.4}$$

is the laser intensity as a function of position assuming a TEM$_{00}$ mode. Here P is the power, and the laser beam radius is given at position z by $w(z) = w_0\sqrt{1+z^2/z_0^2}$ where $z_0 = \pi w_0^2/\lambda$ is the Rayleigh length.

The $M^{ij}_{2S,1S}$ in Eq. (5.3) are sums over dipole matrix elements with the $M^{11}_{2S,1S}$ term corresponding to the Doppler-sensitive absorption of two copropagating photons and the $M^{12}_{2S,1S}$ term giving rise to the Doppler-free absorption of two counterpropagating photons. For our particular experimental arrangement, $M^{12}_{2S,1S} = M^{11}_{2S,1S} = 11.78$ [4].

The delta functions in each term guarantee conservation of momentum. For example, $\delta_{\mathbf{p2},\mathbf{p1}+2\hbar\mathbf{k}}$ ensures that Doppler-sensitive absorption occurs with a recoil shift of $2\hbar\mathbf{k}$, while $\delta_{\mathbf{p}_2,\mathbf{p}_1}$ demands that the incoming and outgoing states have the same momentum.

The convenient way in which $V_{2S,\mathbf{p}_2;1S,\mathbf{p}_1}(t)$ is written allows us to simply read off the Rabi frequency of both types of excitation. If we define the Rabi frequency by

$$\frac{\hbar\Omega(\mathbf{R})}{2} = |V_{2S,\mathbf{p}_2;1S,\mathbf{p}_1}| , \tag{5.5}$$

then the Rabi frequency for Doppler-sensitive excitation by a single laser beam is given by

$$\Omega_i(\mathbf{R}) = M^{11}_{2S,1S}\left(\frac{\alpha}{2R_\infty}\right)^3 \frac{1}{3\pi^2\hbar c} I_i(\mathbf{R}) = 4.362\, I_i(\mathbf{R})\,\mathrm{s}^{-1}\mathrm{cm}^2\,\mathrm{W}^{-1}. \tag{5.6}$$

The Rabi frequency for Doppler-free excitation in a standing wave is given by the other term in Eq. (5.3)

$$\Omega_0(\mathbf{R}) = 2M^{12}_{2S,1S}\left(\frac{\alpha}{2R_\infty}\right)^3 \frac{1}{3\pi^2\hbar c}\sqrt{I_1(\mathbf{R})I_2(\mathbf{R})} = 9.264\,\sqrt{I_1(\mathbf{R})I_2(\mathbf{R})}\,\mathrm{s}^{-1}\mathrm{cm}^2\,\mathrm{W}^{-1}. \tag{5.7}$$

Armed with Eq. (5.3), (5.6), and (5.7), one can calculate the $1S-2S$ spectrum in the absence of other perturbations. We will review the results of these calculations before describing other shifting and broadening mechanisms.

5.5.2 Doppler-Sensitive Excitation

Driving the Doppler-sensitive transition resonantly requires that the laser frequency satisfy

$$2\hbar\omega_{\mathrm{laser}} = \hbar\omega_{1S-2S} \pm \frac{2\hbar\mathbf{k}\cdot\mathbf{p}_1}{m} + \frac{2\hbar^2k^2}{m}. \tag{5.8}$$

This result is easily derived using Fermi's Golden Rule [106] to calculate the transition rate for a single atom

$$\begin{aligned} W_{1S,\mathbf{p}_1\to 2S}(2\hbar\omega_{\mathrm{laser}}) &= \sum_{\mathbf{p}_2} W_{1S,\mathbf{p}_1\to 2S,\mathbf{p}_2} \\ &= \sum_{\mathbf{p}_2} |V_{2S,\mathbf{p}_2;1S,\mathbf{p}_1}|^2\delta(E_{2S,\mathbf{p}_2} - E_{1S,\mathbf{p}_1} - 2\hbar\omega_{\mathrm{laser}}) . \end{aligned} \tag{5.9}$$

We use Eq. (5.3) for $V_{2S,\mathbf{p}_2;1S,\mathbf{p}_1}$, and the delta functions in Eq. (5.3) and Eq. (5.9) ensure conservation of momentum and energy, respectively. The Doppler-sensitive excitation rate to the $2S$ state is

$$\begin{aligned} W_{1S,\mathbf{p}_1\to 2S}(2\hbar\omega_{\text{laser}}) &= \frac{\pi\hbar}{2}\left[\Omega_1^2(\mathbf{R})\,\delta\left(2\hbar\omega_{\text{laser}} - \hbar\omega_{1S-2S} - \frac{2\hbar^2k^2}{m} - \frac{2\hbar\mathbf{k}\cdot\mathbf{p}_1}{m}\right)\right. \\ &\quad \left. + \,\Omega_2^2(\mathbf{R})\,\delta\left(2\hbar\omega_{\text{laser}} - \hbar\omega_{1S-2S} - \frac{2\hbar^2k^2}{m} + \frac{2\hbar\mathbf{k}\cdot\mathbf{p}_1}{m}\right)\right], \end{aligned} \tag{5.10}$$

where $\Omega_i(\mathbf{R})$ is defined by Eq. 5.6. The origin of Eq. 5.8 is easily seen.

To calculate the experimentally observed excitation spectrum, we need to integrate Eq. (5.10) over the sample density and momentum distribution. The chosen coordinate system has the laser propagating along the z-axis. By assuming a Maxwell-Boltzmann distribution for the momentum in the z direction, we have

$$\begin{aligned} S_{\text{DS}}(\nu) &= \frac{1}{\sqrt{\pi}}\left(\frac{1}{2}\frac{mc^2}{k_{\text{B}}T}\frac{1}{\nu^2}\right)^{1/2}\exp\left[-\frac{1}{2}\frac{mc^2}{k_BT}\left(\frac{\nu-\nu_{0,\text{DS}}}{\nu}\right)^2\right] \\ &\quad \times \int d^3R\, n(\mathbf{R})\left[\Omega_1^2(\mathbf{R}) + \Omega_2^2(\mathbf{R})\right]. \end{aligned} \tag{5.11}$$

The spectrum is centered at

$$\nu_{0,\text{DS}} = \frac{\nu_{1S-2S}}{2} + \frac{\hbar k^2}{4\pi m}, \tag{5.12}$$

where the recoil-shift term, $\hbar k^2/4\pi m = 6.70$ MHz. $S_{\text{DS}}(\nu)$ is the number of $2S$ excitations per second, with ν in Hz. Since the Doppler-sensitive lineshape is simply a Gaussian, we can read off the rms width, $\Delta\nu = \nu_{1S,2S}\sqrt{\frac{k_{\text{B}}T}{mc^2}} = 0.374 \times 10^9\,\sqrt{T}$ Hz K$^{-1/2}$.

Because the width of the Doppler-sensitive spectrum is proportional to $\sqrt{T}$, fitting a Gaussian to the experimentally observed spectrum allows one to determine the sample temperature. This procedure is valid for samples away from degeneracy, at temperatures high enough that Bose-Einstein statistics have not yet become important. For samples close to degeneracy, there is a departure from the Maxwell-

Boltzmann distribution of velocities used to derive Eq. (5.11). Since the atoms are bosons, they are better described by a Bose-Einstein velocity distribution. This distribution is more peaked in the center, reflecting the fact that Bose statistics allow more particles at low momenta compared to classical statistics. As a result, fitting a Gaussian to data taken from a Bose-Einstein distribution results in a fitted temperature lower than the actual temperature. See also Sec. 9.1.

Experimental Observation

An example of the Doppler-sensitive spectrum is shown in Fig. 5-5 for an 89 μK sample. The sample was confined in magnetic trap A and rf evaporation was carried out down to 20 MHz. The rf frequency was held, fixing the trap depth at 825 μK. The background fluorescence contributing to the Doppler-sensitive spectrum has been subtracted, and the Gaussian fit shown by the solid line indicates that some of the Doppler-sensitive signal spills over into the Doppler-free line (at zero detuning). In practice, this poses no interpretive difficulty since the Doppler-free line is much more intense (see Fig. 5-4).

5.5.3 Doppler-Free Excitation

In two-photon Doppler-free excitation there is no recoil shift and no Doppler broadening. The transition may only take place if the initial and final states have identical momenta, and in the absence of broadening mechanisms the laser frequency must satisfy

$$2\hbar\omega_{\text{laser}} = \hbar\omega_{1S-2S}. \tag{5.13}$$

In principle the resulting spectroscopic feature could be extremely narrow, determined by the mechanism that sets the decoherence time for the system, for example the natural linewidth of the transition, $\gamma = 8.2\ \text{s}^{-1}$. In practice the motion of an atom in the trap prohibits it from interacting with the laser beam for a time long compared to the dominant decoherence time, i.e. the laser linewidth. This prevents the use of

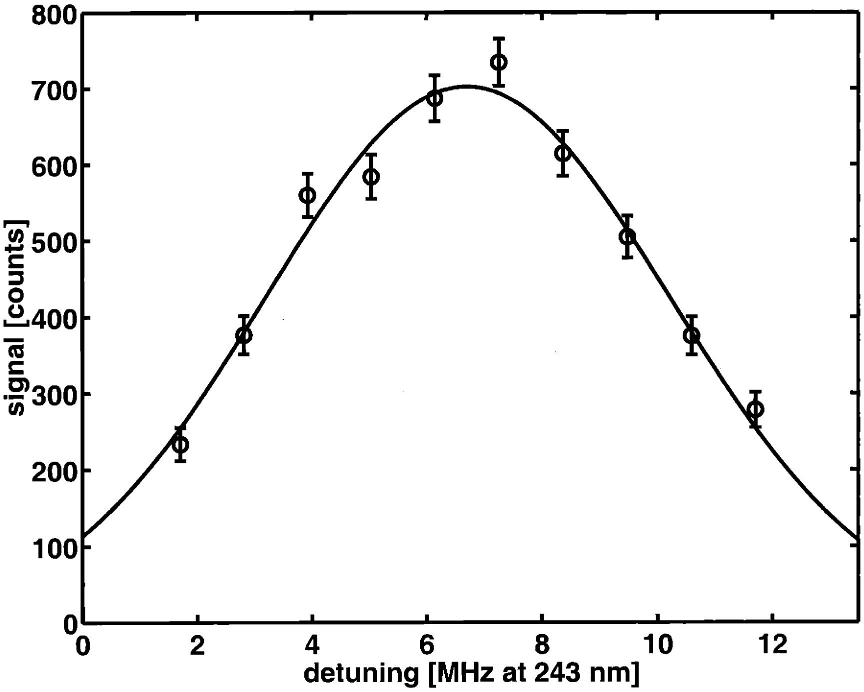

Figure 5-5: Doppler-sensitive spectrum of a sample confined in a 825 μK deep trap. The Gaussian fit indicated by the solid line yields $T = 89.2\ \mu\text{K} \pm 5.7\ \mu\text{K}$. The background fluorescence has been subtracted prior to the fit.

Fermi's Golden Rule to calculate the transition rate and results in a time-of-flight (TOF) broadened lineshape.

Effects of finite transit time

In order to calculate the modifications to the lineshape resulting from the finite time an atom in motion spends in the laser beam, we first compute the probability that an atom with a well-defined trajectory is excited while passing through the beam. We then average over the distributions of radial velocities v_r and trajectories to obtain an expression for the lineshape. The details of this calculation are presented in [9].

Since the z-axis length scales for both the trapped atoms and the laser beam are on the order of centimeters and the laser radius, w_0, is less than 50 μm, we can neglect the axial motion of the atoms. As a result, we need only the radial velocity distribution, $f(v_r) = 2v_r/u^2 \exp(-v_r^2/u^2)$, where $u = \sqrt{2k_BT/m}$ is the most probable velocity in the Maxwell-Boltzmann distribution. Finally, assuming the trapped sample is confined to a region near the laser waist, we obtain

$$S_{\mathrm{TOF}}(\omega_L) = \frac{\pi\Omega_0^2(0)}{8}\frac{1}{\delta}\pi w_0^2 \int dz\, n(z) \exp\left[-\frac{|\omega_{1S-2S} - 2\omega_L|}{\delta}\right], \tag{5.14}$$

where ω_L is the laser frequency and $\delta = u/w_0$ is a parameter that characterizes broadening due to the transit time through the laser beam. The broadening is symmetric and the two-photon transition is not shifted by this effect.

The time-of-flight lineshape is a double exponential curve whose width can be used to determine the sample temperature. Specifically, the $1/e$ half width is

$$\Delta\omega = \frac{1}{w_0}\sqrt{\frac{2k_BT}{m}}. \tag{5.15}$$

The sharp point of the lineshape is due to slow atoms that remain in the beam for a long time and contribute strongly to absorption but weakly to broadening.

A reliable determination of the sample temperature based on the $1/e$ half width requires accurate knowledge of the laser waist profile. In the current apparatus it is

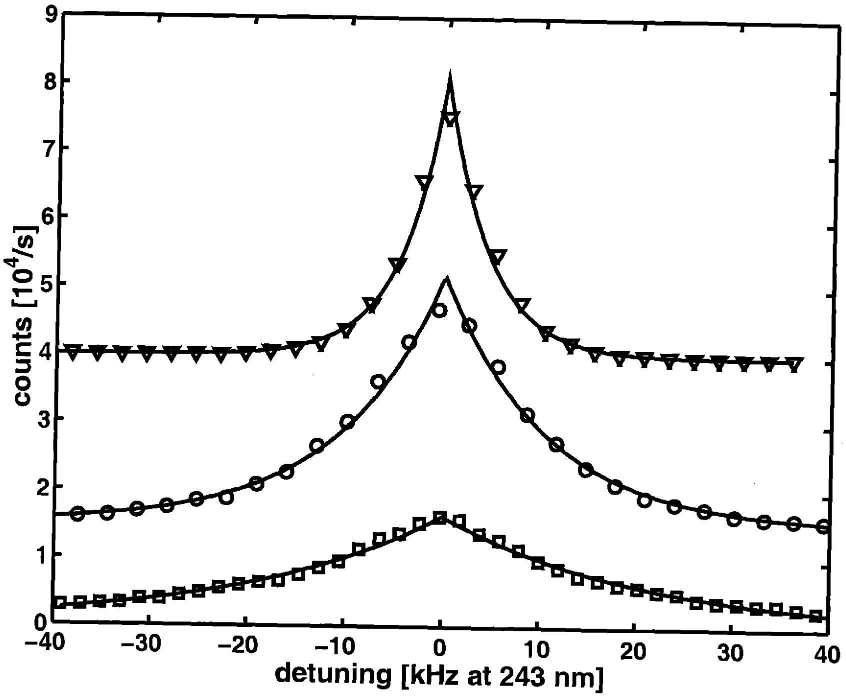

Figure 5-6: Experimental Doppler-free spectra showing the characteristic double-exponential lineshapes. Three samples are shown with different temperatures. The solid lines indicate fits to the data. The $1/e$ half widths are $\bigtriangledown$ = 4.46 kHz, $\circ$ = 9.4 kHz, and $\square$ = 20.9 kHz at 243 nm.

impossible to precisely determine the laser waist profile. During room temperature assembly of the vacuum system and cryostat, the optical alignment is changed. It is further altered during cooling to base temperature because several optical components are mounted inside the cryostat. However, if one calibrates the effective beam waist using some other technique, the time-of-flight spectrum provides a valuable relative measure of sample temperature.

Experimental observation

Figure 5-6 shows three Doppler-free spectra exhibiting the double-exponential lineshape. Each spectrum was obtained in a different magnetic trap configuration. The broadest spectrum has a $1/e$ half width of 20.9 kHz at 243 nm. The temperature in this particular trap has been measured by bolometric techniques to be 2.3 mK, but one must exercise caution in assigning temperatures to the other spectra based on this calibration. According to Eq. (5.15) this implies $w_0 = 47\,\mu$m, but the optical layout was designed to produce a 25 μm beam waist. We can understand this discrepancy because the laser waist changes significantly over the length of the 2.3 mK sample. Thus, many atoms contributing to the width experience a laser waist that is effectively larger than 25 μm. For the sample indicated by ($\circ$), the temperature was calibrated using the data in Fig. 5-5, yielding $T \sim 230\,\mu$K with an implied $w_0 = 33\,\mu$m. Finally, the narrowest spectrum was obtained using an optical layout designed to produce $w_0 = 50\,\mu$m. Using this value for the laser waist and a $1/e$ halfwidth of 4.46 kHz at 243 nm, we find $T = 120\ \mu$K. This is in good agreement with bolometric temperature measurements of this trap.

5.5.4 Cold-Collision Frequency Shift

At low sample densities the Doppler-free line can be used to measure the sample *temperature* through the time-of-flight lineshape. At higher densities the sample *density* can be measured through the cold-collision shift of the Doppler-free line. Collisional frequency shifts have also been observed in hydrogen masers [46, 131] and in atomic fountains [39], where they lead to a serious limitation in the stability of these devices. In the work reported in this thesis, the cold-collision shift has played a vital role since it allows both the condensate and non-condensate densities to be monitored *in situ.*

The cold-collision shift can be understood in a mean-field picture. Consider first an isolated atom prepared in a state α and placed in non-degenerate, homogeneous cloud of $1S$ atoms with a density of n_{1S}. In the language of quantum mechanics, this atom is *distinguishable* because it was prepared separately from the $1S$ atoms and shares no common history. In this case, the α state atom experiences a shift of its energy by an amount $4\pi\hbar^2 a_{1S-\alpha} n_{1S}/m$. The energy shift is proportional to the number of perturbers per volume, n_{1S}, and the strength of the interaction is characterized by a single parameter $a_{1S-\alpha}$, the s-wave elastic scattering length between the two species. This is the standard result from mean-field theory.

The situation changes when an atom in state α is prepared from the reservoir of $1S$ atoms. For example, if laser radiation is used to prepare an α atom, the α atom leaves behind a $1S$ "hole." In this way a correlation exists between the motion of the α atom and the $1S$ background, giving rise to an additional shift in the energy level. The total shift is a factor of two larger: $8\pi\hbar^2 a_{1S-\alpha} n_{1S}/m$. Again the energy shift is proportional to n_{1S} and $a_{1S-\alpha}$, and the result is valid for a homogeneous cloud of non-condensed $1S$ atoms.

The "factor of two" in the mean-field shift arises from the special way in which the system of $1S$ atoms and a single α state atom was prepared. As long as we do not know which $1S$ atom was prepared in the α state, the α atom can be viewed as *indistinguishable* in the sense that we have prepared a superposition state of the $1S$ background and the α atom. As a result, a proper theoretical treatment considers the full, interacting many-body system.

In our particular case both the $1S$ and $2S$ energy levels are shifted, but $|a_{1S-2S}| \gg |a_{1S-1S}|$ so that the shift of the $2S$ level is responsible for most of the change in the

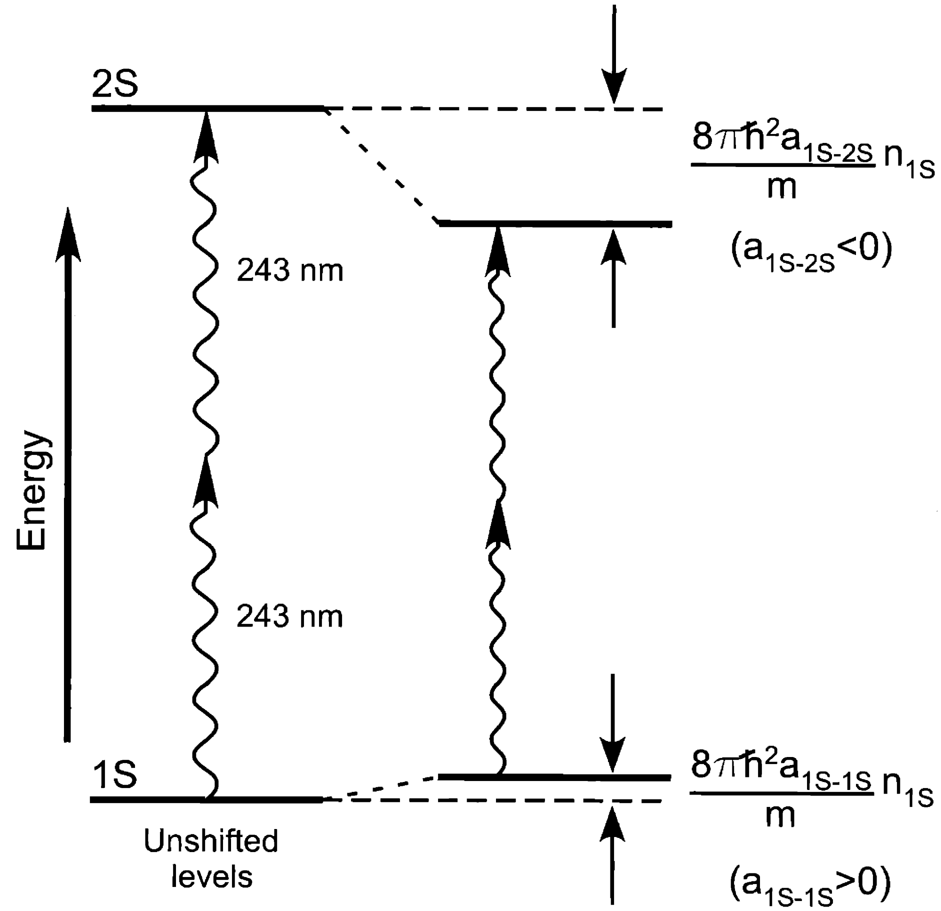

Figure 5-7: The energy levels of the $1S$ and $2S$ states are shifted due to mean field interactions with the background of $1S$ atoms. The scattering length between two $1S$ atoms is small and positive, $a_{1S-1S} = 0.0648$ nm. The scattering length between a $1S$ atom and a $2S$ atom is larger and negative, $a_{1S-2S} = -1.4$ nm [65]. The expression shown for the shift is the theoretical value for a homogeneous, non-condensed gas.

$1S-2S$ resonance. The $1S-2S$ resonance energy is shifted by an amount

$$\Delta E(\mathbf{r}) = h\chi n_{1S}(\mathbf{r})\,, \tag{5.16}$$

where $\chi = -3.8 \pm 0.8 \times 10^{-10}$ Hz cm^3 [65]. The shift of the $1S$ and $2S$ energy levels is shown schematically in Fig. 5-7. The "factor of two" is included in the diagram since we consider the $2S$ atom originating from the $1S$ background. For a non-degenerate, homogeneous sample $h\chi = \frac{8\pi\hbar^2}{m}(a_{1S-2S} - a_{1S-1S})$ is the shift per unit density. In the observed spectrum, the energy shift appears as a frequency shift at 243 nm, $\Delta_{n_{1S}} = \chi n_{1S}/2$.[1]

Killian discusses the measurements of χ in detail in [66]. The shift was measured for densities in the range 2 - 7 $\times 10^{13}$ cm^{-3} and for temperatures between 100 and 500 μK. Since the current laser system stability is about 1 kHz, this technique is limited to densities above a few times 10^{13} cm^3.

Experimental observation

Figure 5-8 shows typical Doppler-free spectra in the regime where the cold-collision frequency shift is important. Shown are four spectra out of many taken from successive sweeps across the $1S$-$2S$ resonance of a single trapped sample. The spectra clearly show a red-shift due to collisions and a broadening resulting from the inhomogeneous density in the trap. The earliest spectrum has the largest integrated area, and as the trapped sample decays, the area under the line decreases, reflecting the decreased sample population. As the sample decays the density decreases, making the cold-collision shift less important. In the spectrum corresponding to the lowest density, the time-of-flight exponential lineshape is again discernible.

The lineshapes in Fig. 5-8 reflect the density distribution of atoms in the trap. This statement contains the assumption that the *local-density approximation* is valid.

---

[1] The "factor of two" is discussed more fully in Sec. 9.5. In the hydrogen system the theoretical result may not be adequate to account for the inhomogeneous density of the $1S$ background.

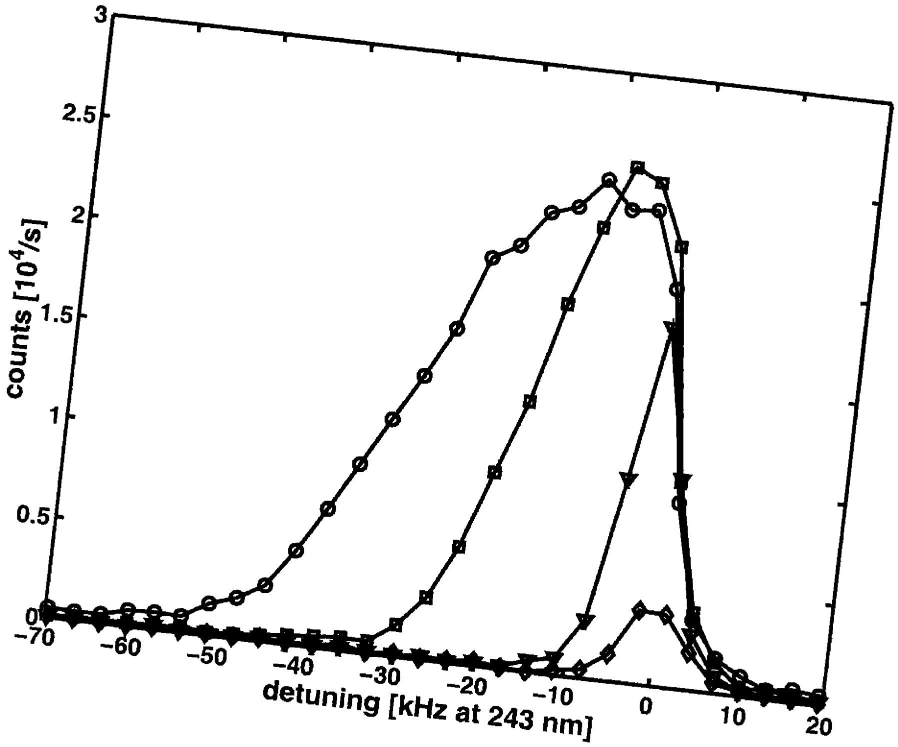

Figure 5-8: Spectra of a sample exhibiting the cold-collision frequency shift. The sample was held in trap *A* with a depth of 450 μK and a temperature of $T \sim 55\,\mu$K. The spectrum with the largest red-shift was recorded first. The initial peak density was $n_0 \sim 1.2 \times 10^{14}$ cm^{-3}. The origin of the frequency axis is the unshifted 1*S*-2*S* resonance. The lines connecting data points are guides to the eye.

The local density approximation assumes that the length scale on which cold-collisions occur is much smaller than the length scale for density variations in the system. In this way, the shift experienced by a particular atom reflects density of colliding partners in its immediate vicinity. The local density approximation is excellent for this system.

In principle, the lineshapes can be calculated by taking into account the spatial distribution of the trapped sample, the overlap of the laser beam with the sample, and the motion of atoms through the inhomogeneous density distribution and laser beam. Killian has made numerical simulations of the lineshape [66], but we are mainly interested in the frequency shift of the high-density spectra that allows us to determine the sample density.

Chapter 6

Observing a Condensate: Experimental Techniques

Observation of a hydrogen Bose-Einstein condensate in our apparatus requires peak performance from all parts of the experiment. Since the observation of the first hydrogen condensate in 1998 [31], we have developed and improved our experimental techniques. This chapter contains an overview of the methods used to optimize the spectroscopic signal from the condensate. Making use of the cold-collision frequency shift, the technique of density selective imaging is introduced. Finally, the expected $1S$-$2S$ spectrum due to the condensate is described. Data to illustrate the experimental techniques is presented.

6.1 Characterizing the Magnetic Trap

6.1.1 Loading

Loading the maximum possible number of atoms into the magnetic trap is the first step in producing a hydrogen condensate. The details of loading were discussed in Sec. 3.2 and Sec. 4.1. There are three important factors that dictate the success of the loading process: an adequate supply of molecular hydrogen, a saturated ^{4}He film, and optimized dissociator parameters.

An adequate quantity of frozen molecular hydrogen must be present in the dissociator. Molecular hydrogen is frozen on the walls of the dissociator immediately after cooling the apparatus from 300 K to 4 K. This frozen supply must be refreshed every few months.

The superfluid ^{4}He film coating the walls of the cell and dissociator should be saturated. The film thickness is measured using a bolometer burn-off technique. The energy required to evaporate the film from the bolometer is recorded. A thicker film requires more energy to bare the bolometer surface. The quantity of ^{4}He required to produce a saturated film is determined empirically for each trapping cell. The film thickness is known to diminish over a few days. This behavior is likely due to adsorption of ^{4}He onto a sponge-like accumulation of H_2 frozen in the non-discharge regions of the cell. The film thickness should be monitored regularly. *Inadequate film thickness is the most likely cause for poor loading!*

Finally, the cryogenic dissociator should be operated at the appropriate frequency and duty cycle to ensure that bare spots do not form in the superfluid film lining the path from the dissociator to the trapping region. The resonance frequency, pulse length, repetition rate, and duration of pulsing should be checked each cooldown and after each loading of molecular hydrogen. Typically, the dissociator resonance is near 298 MHz, and it is operated with pulses 800 μs long at a rate of 50 Hz for 8 seconds with +53 dBm applied outside the cryostat. Optimizing these quantities can be accomplished using the bolometer to monitor the number of atoms present in the trap after loading. A thorough discussion of the physics of hydrogen trap loading is given in the thesis of Landhuis [73].

6.1.2 Evaporation

Saddlepoint Evaporation

Efficient evaporation is required to produce a condensate. A description of the cooling process was given in Sec. 3.3. The first stage of evaporative cooling is magnetic saddlepoint evaporation in which the trap threshold ϵ_t is slowly lowered. Typically, the saddlepoint is lowered continuously for 260 - 300 seconds during which the magnetic field is reduced from 0.8 T to $15 - 20 \times 10^{-4}$ T. The optimum duration and functional form of $\epsilon_t(t)$ may be determined using bolometric techniques to measure the atomic density (see Sec. 3.4.1). In general, one tries to maximize the peak density n_0 of the trapped sample. Specifically, if the evaporation is too slow, dipolar decay will lead to heating of the trapped sample and a lower peak density. Conversely, if the evaporation is too fast, the sample will not maintain thermal equilibrium and some atoms will be "spilled" leading to a warmer temperature and lower peak density. In the end, one desires maximum phase space density: $\rho_D \propto nT^{-3/2}$. Maximizing peak density approximates this since atoms settled deeply into a trap are not only dense but cold.

RF Evaporation

The final cooling of the sample is accomplished using rf evaporation. Again, we try to maximize the peak density of the sample, but for temperatures below about 100 μK, bolometric measurements of n_0 become unreliable. Instead, we rely on the cold-collision frequency shift of the Doppler-free $1S$-$2S$ spectrum to determine the sample density. The cold-collision shift is discussed in Sec. 5.5.4.

The rf frequency $f(t)$ that sets the trap depth $\epsilon_t(t) = hf(t) - \theta$ is ramped according to

$$f(t) = f_{\text{start}} \left(\frac{f_{\text{end}}}{f_{\text{start}}} \right)^{\left(\frac{t}{d}\right)^{\xi}} \tag{6.1}$$

where f_{start} and f_{end} are the starting and ending frequencies, d is the duration, and ξ is the shape exponent. The starting frequency is $f_{\text{start}} = 35$ MHz, and f_{end}, ξ, and d

Parameters	Trap A	Trap B
f_{start} (MHz)	35	35
f_{end} (MHz)	5	2
ξ	1.5	1.5
d (sec.)	50	85

Table 6.1: RF evaporation parameters that maximize the mean shift of the $1S$-$2S$ spectrum in magnetic traps A and B (see Table 2.1). The rf frequency is ramped according to Eq. (6.1).

are optimized by maximizing the mean shift of the $1S$-$2S$ spectrum (see for example Fig. 5-8). The optimization is time consuming, and the results are presented in Table 6.1 for Trap A and Trap B. Note that the parameter f_{end} merely helps to define the function $f(t)$; the rf ramp may be stopped at any point along the evaporation trajectory defined by $f(t)$, allowing the experimenter to produce a trapped sample at the desired temperature and density.

6.1.3 Measuring the Trap Bias Energy

The bias energy, θ, in the Ioffe-Pritchard potential arising from the longitudinal bias field, sets the characteristic sample temperature at which the trap functional form in the radial dimension changes from predominantly linear ($T \gg \theta/k_B$) to predominantly harmonic ($T \ll \theta/k_B$). In order to know the trap depth, $\epsilon_t = h\nu_{\text{rf}} - \theta$, one must know the bias energy.

The bias energy is measured directly using rf ejection and bolometric detection. The rf frequency is swept up until atoms begin to be ejected from the trap. A typical bias energy measurement is shown in Fig. 6-1. The rf frequency is swept from 1 MHz to 3 MHz in 10 seconds. As indicated by the sharp rise in the bolometer signal, atoms begin to emerge from the trap at $\nu_\theta = 1.33(2)$ MHz, corresponding to a bias of $\theta/k_B = 64(1)$ μK. Atoms continue to be coupled out of the trap as the rf frequency increases, but the bolometer signal diminishes as the number of atoms remaining in the trap decreases. Measurement of the trap bias energy using this rf ejection

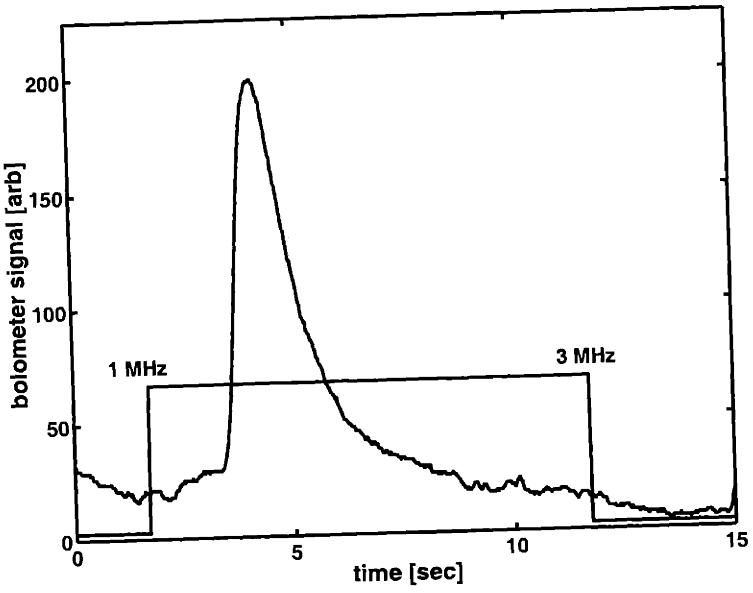

Figure 6-1: An example of a measurement of the trap bias in Trap *A*. The rf frequency is swept from 1 MHz to 3 MHz in 10 seconds. The duration of the sweep is indicated by the square pulse. The bolometer signal increases rapidly at $\nu_\theta = 1.33(2)$ MHz when atoms begin to be ejected from the trap.

technique is easy and accurate, allowing us to determine the absolute trap bias to within 20 kHz (1 μK). For applied bias currents less than 0.3 A in both Trap *A* and Trap *B*, the trap bias energy changes linearly with a slope of 18.8(3) MHz/A. In practice trap bias energies greater than 5 MHz or less than 0.5 MHz are seldom used.

6.2 Spectroscopic "Imaging" of the Sample

Spectroscopy of cold, dense samples demands excellent alignment of the long axis of the trapped sample and the propagation axis of the laser beam. A slight misalignment of the trap and beam axes leads to a drastic reduction in the quality of the spectroscopic signal. The first step to ensure good alignment was taken during construction of the cell when the dissociator lens and retromirror were fixed in place (see Sec. 4.2). These two optical elements are fixed and determine the beam path in the trapping cell. This section discusses techniques developed to correct the residual

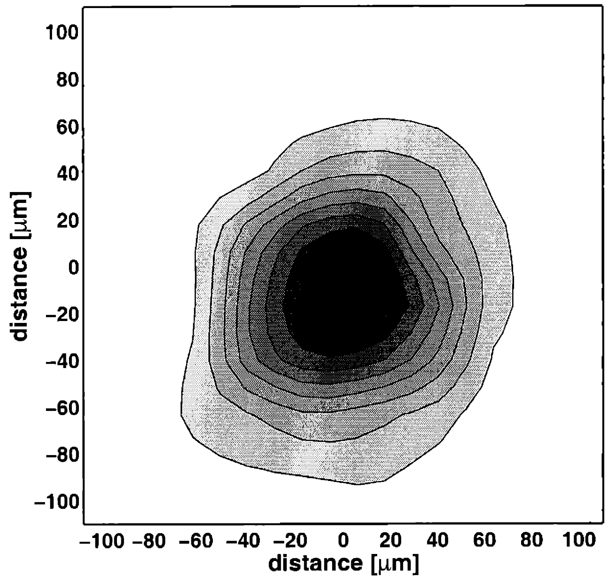

Figure 6-2: Image of sample obtained by scanning trapped atoms across the laser beam profile. The darkest regions indicate the most signal. The lightest regions are mostly background counts. The roughly circular contours indicate that the alignment between the axis of the trap and the laser beam is good. Distance is calculated from the quadrupole trim currents, i.e. 1 mA ~ 1.1 μm

misalignment between the trap and beam axes. It also introduces the technique of density selective imaging.

6.2.1 Density Selective Imaging: Laser Alignment

Some residual misalignment between the trap and beam axes exists after cooling the apparatus. Since the laser axis is not easily translated in a quantifiable and reproducible way, we translate the sample by placing trim currents in two of the bars of the quadrupole magnet. For small trim currents, x_{trim} and y_{trim}, the minimum of the magnetic trap is moved in the x and y directions, but the overall shape of the trapping potential is unchanged. For almost all non-condensed samples, the thermal radius R_{th} is larger than the beam waist.

Placing the trim currents under computer control allows us to laterally translate the trap axis while performing spectroscopy. The number of counts at a particular

$(x_{\text{trim}}, y_{\text{trim}})$ is proportional to the number of atoms excited in the column illuminated by the laser. Translating the trap in both the x and y directions and recording the number of counts at each $(x_{\text{trim}}, y_{\text{trim}})$ allows a primitive "image" of the trapped sample to be made. Figure 6-2 shows the image of a cold sample exhibiting good laser alignment. The image was obtained by tuning the laser frequency several kilohertz red of the unshifted $1S$-$2S$ resonance, preferentially exciting the atoms experiencing a larger cold-collision shift, i.e. atoms at higher densities near the center of the trap. The direct correspondence between laser frequency and sample density allows one to image only atoms at a desired density. We call this technique *density selective imaging.*

The center of the circular contours nearly coincides with the center of the trim current scan, indicating that the trap and beam axes are almost collinear. The original 10×10 image underwent a two-dimensional interpolation to reduce the graininess of the image and emphasize the circular contours. The resolution of the image is limited by the current resolution of the magnet power supplies, and the scanning rate is limited by the large induction of the superconducting quadrupole magnet.

Additional quantitative information about the beam and sample is obtained by examining cross-sections of the images. Figure 6-3 shows cross-sections taken along the x and y axes of Fig. 6-2. The solid line is a Gaussian fitted to the interpolated data with $1/e$ half widths of $x_{\text{width}} = 32 \pm 2$ μm and $y_{\text{width}} = 36 \pm 3$ μm. The functional form of the cross-section is given by the convolution of the laser intensity profile with sample density distribution. Both quantities are Gaussian in nature, as is their convolution. The $1/e$ half widths are consistent with our knowledge of the laser beam waist and the expected sample size.

In contrast Fig. 6-4 gives an example of poor alignment between the trap axis and beam axis. The laser is passing through the geometric center of the trapped sample, but a small angle exists between the two axes giving rise to the elliptical contours shown. Systematic adjustments to the laser alignment into the cryostat correct this problem. In addition an asymmetric laser intensity profile can lead to a similar result.

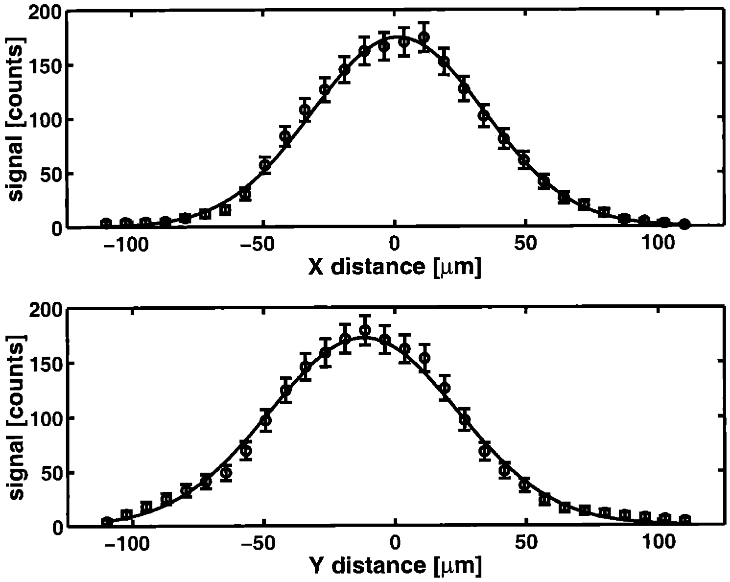

Figure 6-3: Cross-sections along the x and y axes of Fig. 6-2 are shown. The interpolated data is fitted with a Gaussian. The nearly identical fits indicate excellent sample/beam alignment. The fitted widths are consistent with our expectations of the laser beam waist and sample waist, giving us confidence in our knowledge of the excitation geometry.

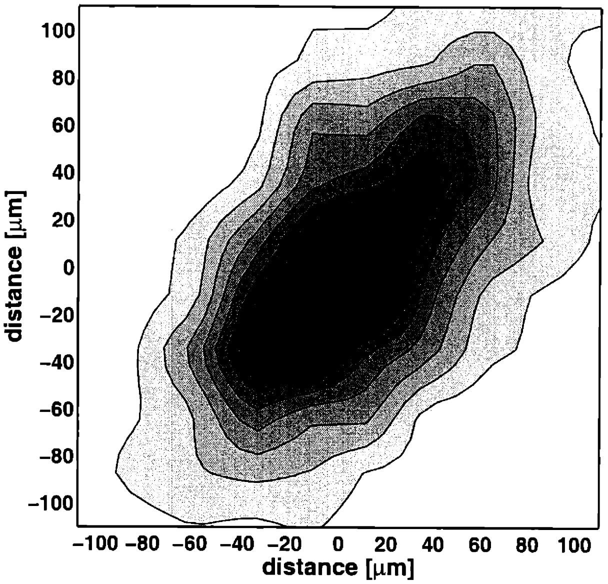

Figure 6-4: This image of the trapped sample indicates poor alignment between the laser axis and the trap axis. A small angle between the two axes results in the elliptical contours. An asymmetric laser profile can produce a similar result.

6.2.2 Density Selective Imaging: Low Density

Tuning the laser to the blue of the unshifted $1S$-$2S$ resonance allows one to selectively excite and image atoms in low-density regions. These atoms are found away from the center of the trap and appear in Fig. 6-5 having a ring-like structure. The contrast between the ring and the core is low for three reasons. First, the image is a two-dimensional projection of low-density atoms in the trap. Some low-density atoms are found near the ends of the elongated trap and absorb light near the trap axis. Second, during the time in which the image is recorded, the sample density changes. Since diploar losses are most severe near the center of the trap, the shell of low-density atoms moves toward the center of the trap further reducing the contrast. Third, there are no atoms in resonance. Rather, the low-density atoms are closer to resonance than those at higher densities.

A cross-section of the ring-like structure is shown in Fig. 6-6. The diameter of the ring is approximately 170 μm. Although the contrast between the ring and the

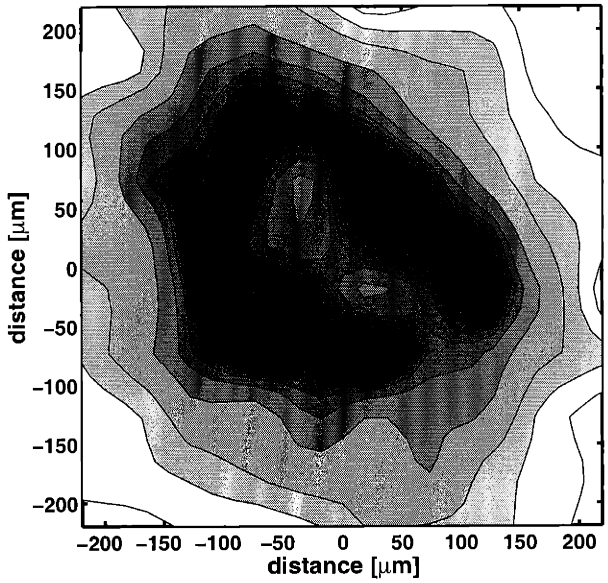

Figure 6-5: Illustration of density-selective imaging technique. The laser is tuned slightly to the blue of the $1S$-$2S$ resonance so that only atoms at low density will absorb. The resulting image shows a ring-like structure indicating that the low-density atoms surround a higher-density core as expected.

core is only 1.2, it is clear that atoms away from the trap axis on a shell of constant density have been preferentially excited.

6.3 Spectroscopic Signatures of the Condensate

The $1S$-$2S$ spectrum of the trapped gas changes dramatically when the sample is cooled into the quantum degenerate regime. New features appear in both the Doppler-sensitive and Doppler-free portions of the spectrum. Understanding these features allows us to characterize the hydrogen condensate.

6.3.1 Doppler-sensitive Condensate Spectrum

Bose-Einstein condensation takes place when the lowest energy quantum state of a system is macroscopically occupied. In a trap this occupation takes place in both *position* and *momentum* space. The position space occupation takes place in the minimum

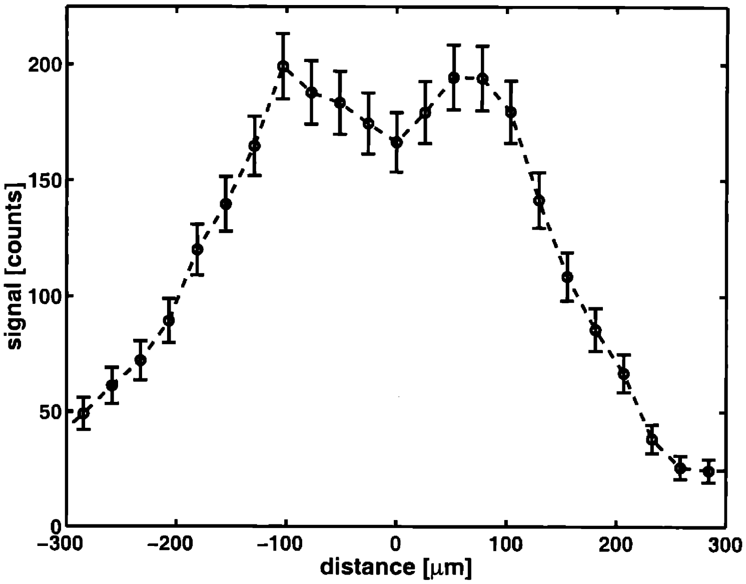

Figure 6-6: Cross-section of Fig. 6-5 showing the location of low-density regions in the trap. The atoms are excited on a shell of constant density. The low-density atoms are found away from the trap center, as expected.

of the magnetic trap. The confinement in position space dictates the momentum of the condensate through the Heisenberg uncertainty relation $\Delta x \Delta p > \hbar/2$. Since the Doppler-sensitive spectrum is a map of the momentum distribution of the atoms, one might expect a narrow, intense line to appear above the broad Doppler profile, detuned by $\Delta\nu_{\mathrm{recoil}}$ from the $1S$-$2S$ resonance. Instead the line appears red-shifted from the center of the Doppler profile and broadened by the large, inhomogeneous density of the condensate. The red-shift is due to the cold-collision shift (see Sec. 5.5.4), and the inhomogeneous density is due to the confining potential (see Eq. (2.25)).

Local Density Approximation

The general behavior of the Doppler-sensitive (DS) condensate spectrum shown in Fig. 6-7 can be understood using a local density approximation. Atoms excited from different regions of the condensate experience different frequency shifts according to the local density of perturbers. The signal size, S, at a given detuning, Δ, is

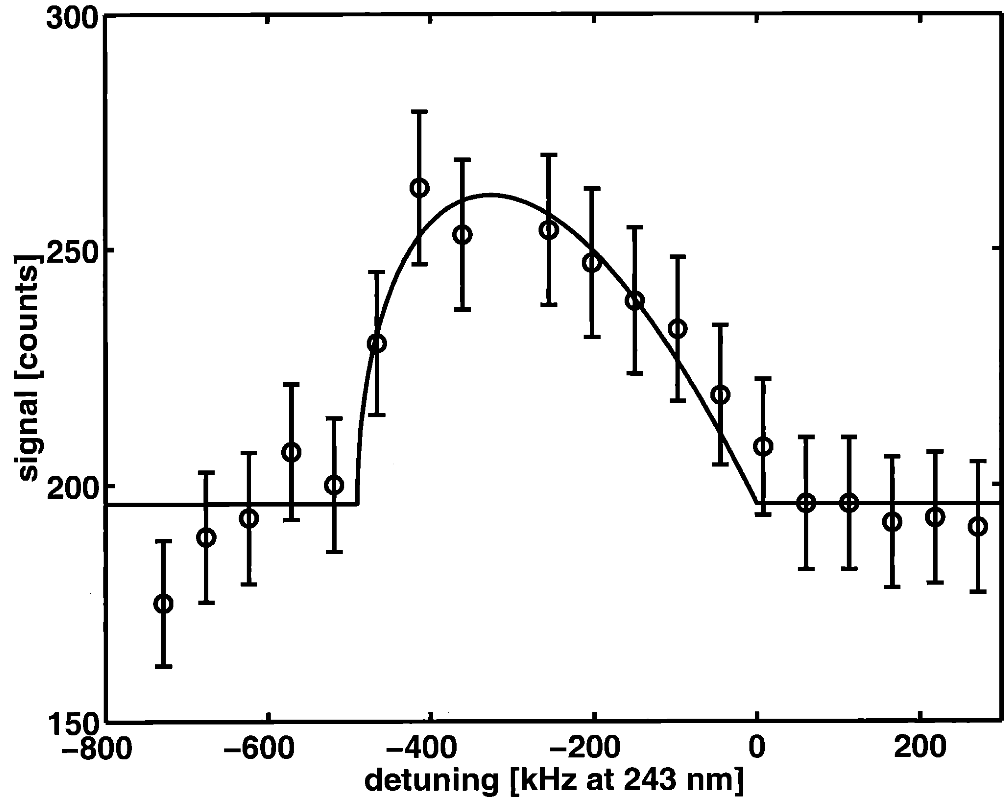

Figure 6-7: Doppler-sensitive (DS) spectrum of the degenerate gas. The zero of detuning is taken to be the center of the DS profile, shifted by $\Delta\nu_{\text{recoil}}$ from the $1S$-$2S$ resonance. The red-shifted feature is due to the condensate and is well described using the Thomas-Fermi wavefunction approximation. The solid line shows a fit to the spectrum with a peak shift of 490 ± 25 kHz. The condensate spectrum rests on top of the much broader DS profile which is treated as a constant offset in the fit.

proportional to the number of condensate atoms on a surface of constant density. In a *harmonic* potential the spectrum calculated based on this approximation involves only two parameters: the peak shift, Δ_p, and an overall scaling factor, S_0. The normalized spectrum is

$$S(\Delta) = \begin{cases} S_0 \frac{-15\Delta}{4\left(-\Delta_\mathrm{p}^{5/2}\right)} \sqrt{\Delta - \Delta_\mathrm{p}} & ; \quad \Delta_\mathrm{p} \leq \Delta \leq 0 \\ 0 & ; \quad \text{otherwise} \end{cases} \tag{6.2}$$

Note that the negative signs are required since the spectrum is red-shifted, i.e. $\Delta_\mathrm{p} < 0$. This function is nothing more than a map of the number of atoms at a given frequency (density) versus frequency (density).

The normalized spectrum rests on top of the much broader DS profile due to the nondegenerate or thermal cloud. The slight curvature of the background – the Doppler-broadened profile of the normal gas – can be neglected when fitting with Eq. (6.2). The background due to fluorescence and the DS profile are fitted with a constant found from the blue-detuned portion of the spectrum. The peak shift of the spectrum shown in Fig. 6-7 is 490 ± 25 kHz. The quality of the fit illustrates that the spectrum is well-described using the Thomas-Fermi wavefunction approximation (see Sec. 2.5.2).

Justification of the Local Density Approximation

The local density description of the excitation of atoms in the condensate is not strictly correct since any particular atom is delocalized over the entire condensate wavefunction. For this reason, Killian developed a quantum mechanical description of the condensate spectrum [66, 67].

In the quantum mechanical approach, an atom in the $1S$ electronic state prior to excitation has the condensate wavefunction as its motional quantum state. Following excitation the atom is in the $2S$ electronic state, and its motional state has been projected onto the motional eigenstates of a new effective potential. The effective potential is the sum of the magnetic trap potential and a potential created by the mean-field interaction energy for a $2S$ atom in a background gas of $1S$ atoms. For a $2S$ atom excited out of a condensate, the mean field term is $\delta E_{2S}(\mathbf{r}) = 4\pi\hbar^2 a_{1S-2S} n_{1S}(\mathbf{r})/m$. For a $1S$ condensate atom, the mean field term is $\delta E_{1S}(\mathbf{r}) = 4\pi\hbar^2 a_{1S-1S} n_{1S}(\mathbf{r})/m$. Thus the effective potential is $U_x^{eff}(\mathbf{r}) = U_{\text{ext}}(\mathbf{r}) + \delta E_x(\mathbf{r})$, where U_{ext} is the magnetic potential and x is either $1S$ or $2S$.

For $1S$ condensate atoms, the effective potential in the Thomas-Fermi approximation is flat. Since $a_{1S-2S} < 0$ and the condensate density is large, $2S$ atoms experience a stiff, attractive potential in the condensate that supports many bound $2S$ motional states. The $1S$-$2S$ spectrum consists of transitions from the condensate to $2S$ motional eigenstates of the effective $2S$ potential. To calculate the spectrum, one calculates the overlap of wavefunctions in these two effective potentials. The calculation is straightforward, in principle, and has been carried out by Killian, showing very good agreement between the quantum treatment and the local density approximation.

6.3.2 Doppler-free Condensate Spectrum

The Doppler-free (DF) portion of the spectrum is also affected by the condensate. A red-shifted and broadened feature appears whose shape and shift are different from the normal gas line. The large shift indicates the presence of high densities, and the shape implies a density distribution different from the non-condensed gas. The spectrum is shown in Fig. 6-8.

The contribution to the spectrum due to the condensate alone should be well described by Eq. (6.2). In the presence of the non-condensed gas, one expects the high-density (red) portion of the normal gas spectrum to overlap the low-density (blue) portion of the condensate spectrum. This can be seen in Fig. 6-8 where a fit using Eq. (6.2) is shown. The quality of the fit is poor, and the data cannot be described by a Thomas-Fermi density profile. The fit assumes that the red-shifted portion of the spectrum is due entirely to the condensate. The derivative of Eq. (6.2)

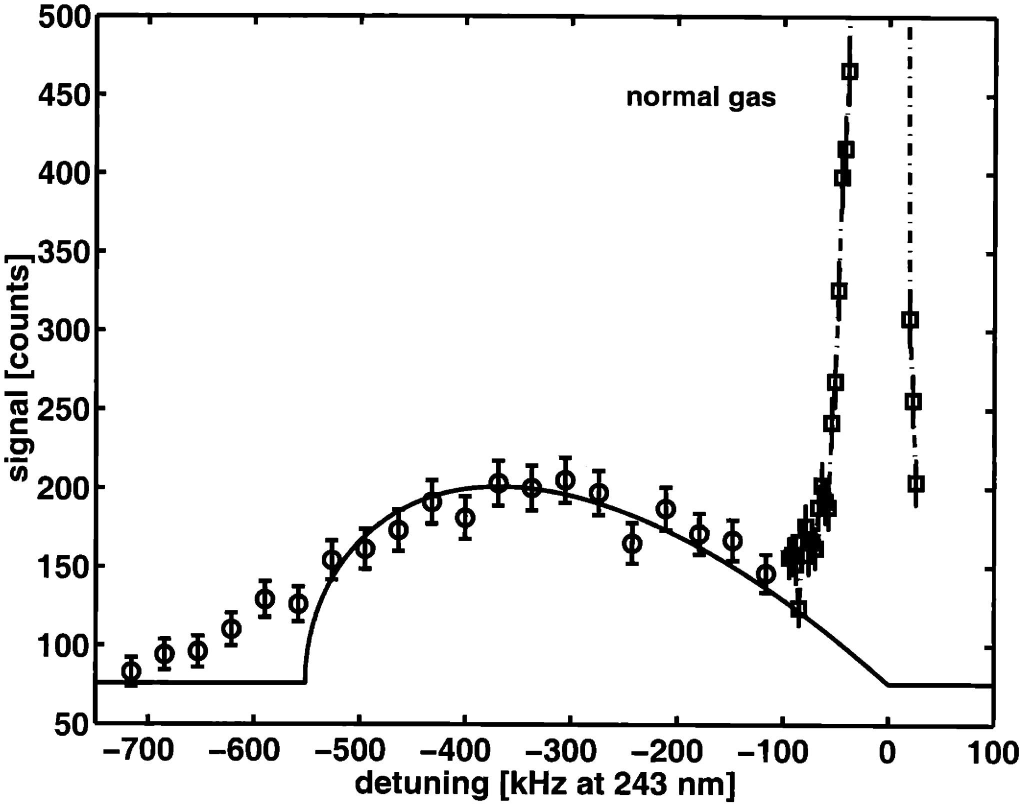

Figure 6-8: The Doppler-free spectrum of the degenerate gas. The narrow, intense feature near zero detuning is due to the normal gas and extends beyond the extent of the plot. The wide, red-shifted feature is due to the condensate. A fit to the expected Thomas-Fermi wavefunction is indicated by the solid line. Agreement is good except near the most red-shifted portion of the spectrum where additional spectral weight is present. Possible explanations for the additional signal are described in the text.

diverges near Δ_p, but the data clearly indicate that the signal at large red-shift approaches zero more slowly.

There have been several efforts to describe the spectrum shown in Fig. 6-8 involving quasicondensate droplets [18], quasiparticles [34], and an enhancement of the low-energy distribution of non-condensate particles due to strong dipolar relaxation in the condensate [58]. Each of these theories relies on a different physical mechanism to explain the spectrum, but all of them assume an idealized excitation geometry with perfect laser-sample overlap and a well-characterized laser profile. In reality, the laser beam waist is not well known, and the laser focus does not occur precisely at the same point along the trap axis as the magnetic trap minimum. Since the standing wave necessary for DF excitation is created by reflecting the incoming beam back onto itself, it is possible that the foci of the counterpropagating beams do not overlap.

Lorenz Willmann has taken the realistic excitation geometry and motion of the noncondensed atoms into account in Monte Carlo simulations of a DF $1S$-$2S$ spectrum. One such spectrum is shown in Fig. 6-9 [133], plotted on a semi-log scale to emphasize the wide, low feature extending to large red-shift. This figure should be viewed as an indication of the resulting lineshapes. It is not meant to reproduce exactly the data shown in Fig. 6-8.

The broadened spectrum in the absence of a condensate can be understood by considering the excitation of an atom moving through a region of changing density. The resonance frequency of the atom is "chirped" as it passes through the changing laser field and mean-field. The chirp gives rise to a broadening. The spectrum is the result of considering the contributions of a distribution of velocities and trajectories of atoms moving through the inhomogeneous density distribution and laser field. In the presence of a condensate the low-amplitude feature extending far to the red is due to the small fraction of thermal atoms that pass directly through the condensate. Again, their resonance frequency is chirped, broadening the already red-shifted spectrum and explaining how a signal can appear beyond the red-shifted end of the Thomas-Fermi density profile.

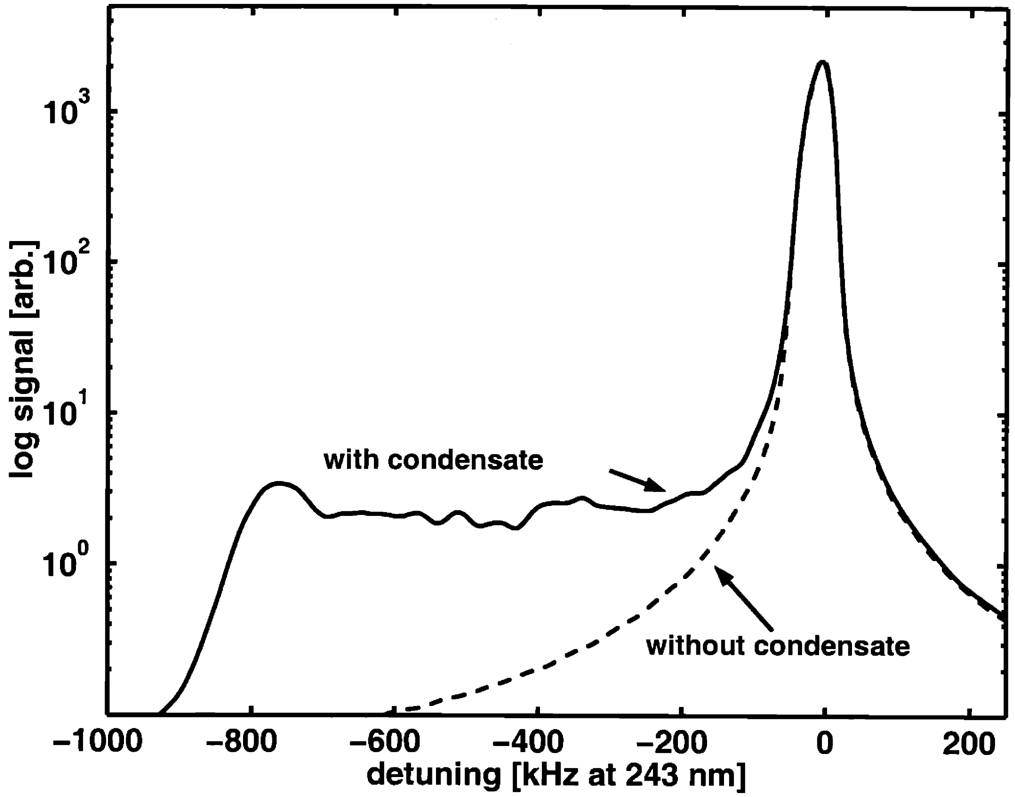

Figure 6-9: A simulated Doppler-free spectrum of the noncondensed gas. The simulation takes into account the realistic excitation geometry and the motion of atoms in the trap. The figure has been plotted on a semi-log scale to emphasize the wide, low feature due to the *normal gas* in the presence of a condensate. A similar spectrum in the absence of a condensate is indicated by the dashed line. The small wiggles on the spectrum are due to the Monte Carlo nature of the simulation.

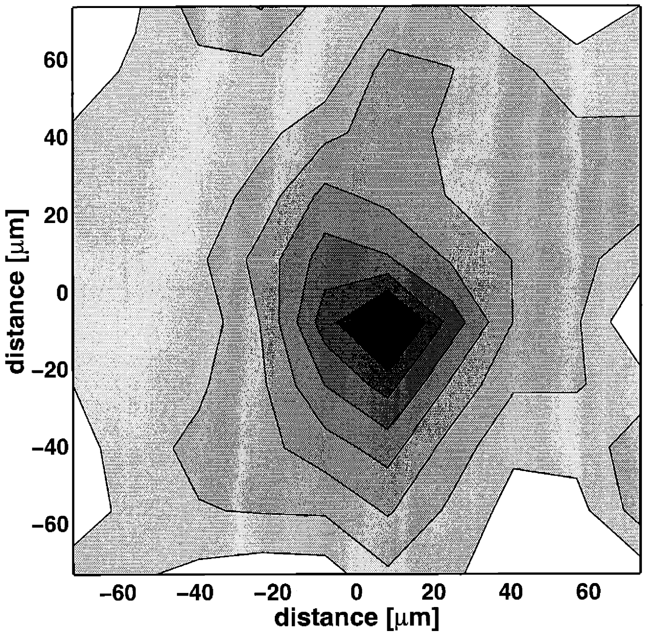

Figure 6-10: Image of a trapped hydrogen condensate. The laser is tuned 15 kHz to the red of the center of the Doppler-sensitive profile. Most of the signal counts are due to atoms in the condensate. The result is an *in situ* image of the hydrogen condensate. The apparent width of the condensate is consistent with our expectations of a 25 μm laser waist radius. Imaging the condensate also provides a sensitive check on the alignment of the trap and laser beam axes.

The calculations described here are very sensitive to the sample temperature and excitation geometry. An apparatus better designed for spectroscopy could reduce the uncertainties in excitation geometry, resulting in a sensitive way to measure the sample temperature.

6.3.3 Spatially Resolving the BEC

The smallest object that can be resolved using the density selective imaging technique is the Bose-Einstein condensate. The radial extent of the condensate is determined by setting the density to zero in Eq. (2.25): $n_c(\mathbf{r})U_0 = \mu - V_{\text{IP}}(\rho, z) = 0$. Using typical values of the chemical potential $\mu/k_B = 1 \times 10^{-6}$ μK and bias energy $\theta/k_B = 130$ μK in trap B, we find

$$\rho_{\max} = \frac{1}{\alpha}\sqrt{\mu^2 + 2\mu\theta} = 17\ \mu\text{m} \tag{6.3}$$

which is smaller than the expected laser beam waist of 25 μm. The spatial resolution of the imaging technique is given by the laser waist. Since the radial extent of the condensate is less than the spatial resolution, the apparent width of the condensate is given by the laser waist. Alternatively, the imaging process can be reversed and the smaller condensate can be used to image the laser intensity profile. This effect can be seen in Fig. 6-10 which shows a raw 10 × 10 image of the condensate.

The image of the condensate was obtained by tuning the laser 15 kHz to the red of the center of the Doppler-sensitive profile. Five scans were added together to reveal the narrow, dark feature near the center of the image. The coarse resolution is evidenced by the sharp edges of the contours shown. Since the image was taken using the DS portion of the spectrum, there is some normal gas contribution to the signal. By tuning the laser 15 kHz to the blue of the center of the DS profile and taking another image, we ensure that the condensate does not contribute to the signal. The narrow feature disappears indicating that Fig. 6-10 is an image of the condensate.

Finally, we examine the width of the feature in Fig. 6-10 by taking cross-sections in the x and y directions. The cross-sections are shown in Fig. 6-11. A Gaussian fit is still appropriate since the image is really a map of the laser intensity profile made by the condensate. The fitted $1/e$ half widths are $x = 24 \pm 5\ \mu$m and $y = 34 \pm 7\ \mu$m. Again these widths are in agreement with the expected laser waist.

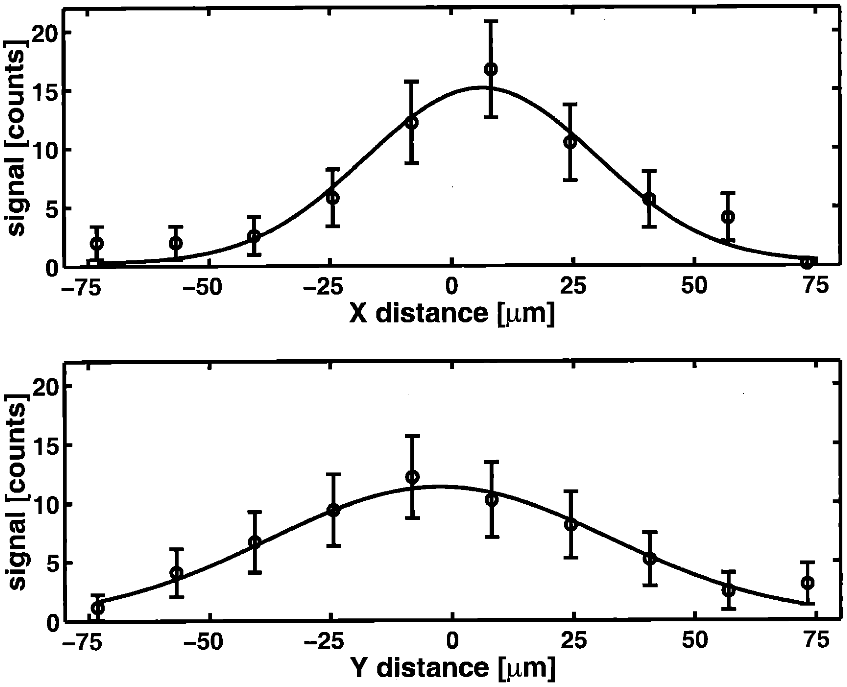

Figure 6-11: Cross-sections of the image of a hydrogen condensate are fitted with the Gaussians indicated by the solid lines. This type of fitting function is appropriate since the expected laser waist is larger than the radial extent of the condensate. In effect, the condensate has been used to make a map of the laser intensity profile, which is presumed Gaussian.

Chapter 7

Condensate Formation Experiments

The detailed observation of the formation and decay of a Bose-Einstein condensate of atomic hydrogen under various experimental conditions is the principal contribution of this thesis. This chapter presents the results of a series of condensate formation experiments conducted using the apparatus and methods described in earlier chapters. These experiments provide a survey of the effects of the important experimental parameters on the formation of the condensate.

An overview of the experimental techniques employed is given in Sec. 7.1. All of the data was obtained using $1S$-$2S$ spectroscopy. A comparison of observations made in the Doppler-free and Doppler-sensitive modes is given in Sec. 7.2. We monitor the formation of each condensate continuously using two-photon spectroscopy, and Sec. 7.3 addresses the important question of the effect of laser excitation on the formation process. Section 7.4 explores the sensitivity of the condensate to the magnetic trap shape, and Sec. 7.5 studies the coupling of the condensed and noncondensed components of the hydrogen gas.

The coupling between the condensate and thermal components in the hydrogen system differs in several ways from degenerate systems of alkali metal atoms. The differences can be traced to two characteristics of hydrogen: its small mass and small

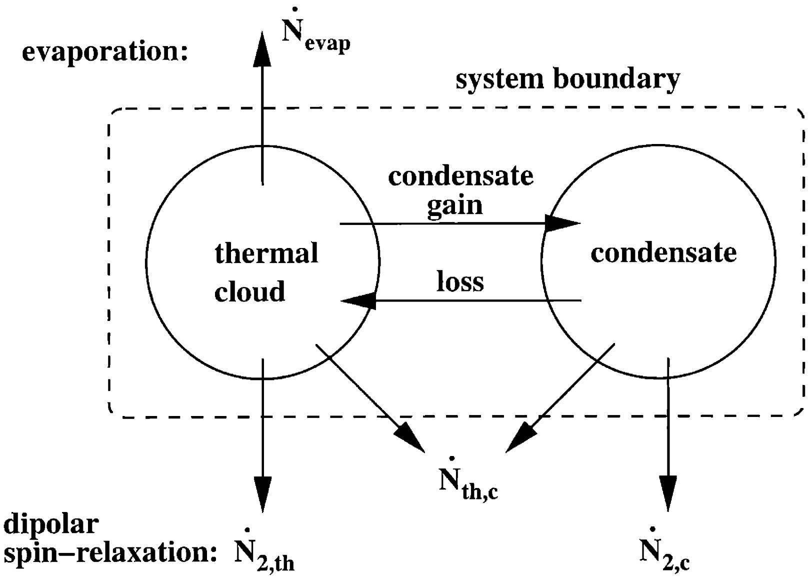

Figure 7-1: Diagram illustrating the coupling of the condensate and thermal cloud. Atoms are scattered between the condensate and thermal cloud at a rate fast compared to the loss processes. Cooling of the system is possible through evaporation from the thermal cloud. Heating is mainly due to dipolar spin-relaxation processes in the thermal cloud and condensate. The balance between heating and cooling determines the temperature and condensate fraction. This diagram is taken from Fried [32].

s-wave scattering length. Through Eq. 2.4 and Eq. 2.5, we see that at the same density a smaller mass gives rise to a higher transition temperature, $T_c \propto 1/m$. The mean field interaction between atoms leads to a spreading pressure which is proportional to scattering length. The small scattering length results in a condensate density that is relatively high in comparison to the density of the thermal cloud. Consequently dipolar spin-relaxation is much more severe in the condensate than in the thermal cloud. Losses from the low-energy portion of the system, i.e. the condensate, effectively heat the system because removal of atoms with an energy below average increases the temperature of the system. The heating is balanced by evaporative cooling, but the small scattering length of hydrogen leads to a small elastic scattering rate and limited evaporative cooling power. The combined effect of these processes is a small equilibrium condensate fraction, typically a few percent.

An intuitive grasp of the coupling between the condensate and thermal cloud is necessary to understand the experiments in this chapter. Figure 7-1 illustrates the essential processes in the degenerate hydrogen system. Elastic scattering processes exchange particles and energy between the condensate and the thermal cloud. The scattering rate between the two components is rapid compared to the loss rates in the system. Losses due to evaporation cool the system by removing particles whose energy is greater than the average energy of the system. The primary heating mechanism is dipolar spin-relaxation which tends to remove atoms whose energy is lower than average. When $\dot{N}_{2,\text{c}} \gg \dot{N}_{2,\text{th}}$, the dynamics of the system is dominated by the balance of the evaporative cooling rate and the dipolar spin-relaxation rate from the condensate.

The only rate in Fig. 7-1 that we can control experimentally is the evaporation rate. Using rf fields we can vary the rate at which atoms are removed from the thermal cloud. This suggests a class of experiments where we suddenly modify the energy distribution of the thermal cloud using rf fields and monitor the effect on the condensate. Experiments of this type are presented in Sec. 7.6 and constitute the majority of experiments that will be compared with theory in Chapter 9.

7.1 Overview of Experimental Technique

The information describing condensate formation and decay comes from measurements of the time-dependent change in the $1S$-$2S$ spectrum due to the appearance of a condensate. The purpose of this section is to explain the experimental methods used in condensate formation experiments and to provide a conceptual framework for interpretation of the data.

Hydrogen atoms are loaded, trapped, and cooled using the techniques described in Chapter 3. Using rf evaporation techniques (see Sec. 3.3.2) the sample is cooled near or below the Bose-Einstein transition. $1S$-$2S$ spectroscopy (see Chapter 5) begins prior to the formation of a condensate and monitors the formation and decay of the condensate, taking advantage of the cold-collision frequency shift (see Sec. 5.5.4). Typically the laser frequency is swept quickly back and forth over four or eight frequency points spaced throughout the portion of the $1S$-$2S$ spectrum in which the condensate signal is expected. Choosing a small number of frequency points permits good time-resolution of the condensate signal. The excellent trap-to-trap reproducibility of the experiment allows the measurement to be repeated on several successive fills in order to improve the signal to noise ratio. By interleaving sets of frequency points in alternate fills, the spectral resolution is improved, and a data set possessing both good frequency and time resolution can be obtained.

7.1.1 "Images" Describing the Condensate Formation Data

Figure 7-2 presents a typical data set describing condensate formation and decay. Panel A contains an "image" constructed from the time-resolved spectroscopic data. In this particular data set, there are 16 discrete values of detuning and 90 time points. The intensity of the condensate signal at every detuning/time point is mapped linearly to a black and white color map. Dark regions represent intense condensate signal while light regions indicate little or no condensate signal. A bilinear interpolation has been performed to enhance the image and aid in its interpretation.

The data set in Fig. 7-2(A) was taken in the Doppler-free (DF) portion of the spectrum using Trap B (see Table 2.1) with a bias potential energy of $\theta/k_{\mathrm{B}} = 123(2)$ μK. The zero of detuning is the unshifted DF $1S$-$2S$ resonance. The noncondensed sample was cooled to a temperature just above the Bose-Einstein transition, and the end of the forced rf evaporation is denoted by the vertical dashed line. After the evaporation the applied rf frequency is held constant to define the trap depth, and the sample continues to cool. Monitoring the spectrum, the condensate begins to form around $t = 5$ s as seen by the sudden appearance of a dark region at small negative detuning. The condensate then grows rapidly over the next second. Recall that the cold-collision shift is proportional to the atomic density, and the density of the condensate is in turn proportional to the number of condensed atoms. Thus, the appearance of a signal

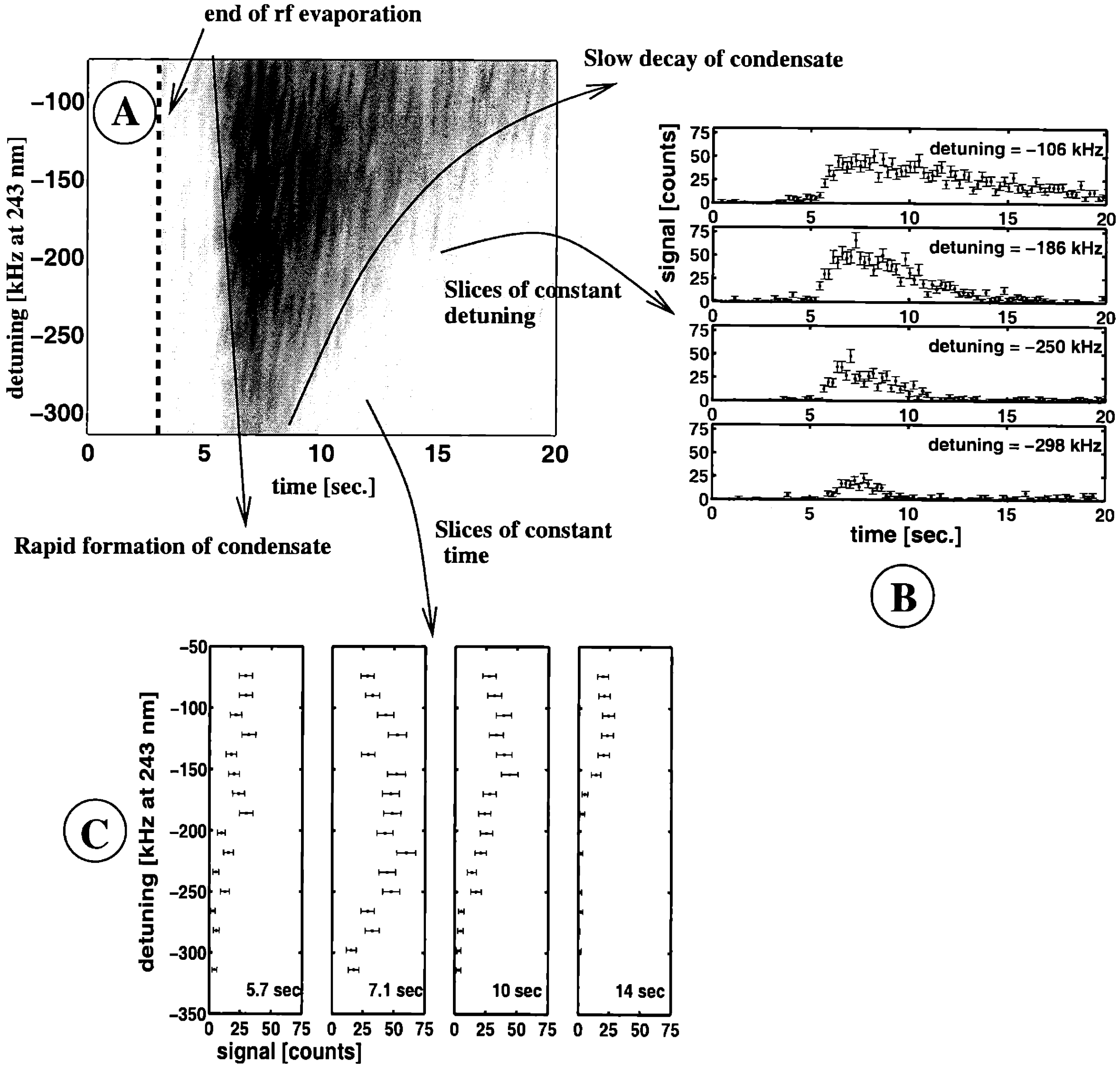

Figure 7-2: Typical condensate formation data. Panel A shows an "image" constructed from spectroscopic data. The image represents the condensate signal versus detuning as a function of time. The zero of detuning corresponds to the unshifted $1S$-$2S$ resonance. The dark regions in these images indicate the most intense condensate signal. Panel B presents slices of the spectroscopic data along lines of constant detuning. Panel C contains slices of the data along lines of constant time. A complete discussion of the panels is found in Sec. 7.1.

at larger detunings implies a larger number of atoms in the condensate. The sudden formation and growth of the condensate is delineated in Fig. 7-2(A) with an arrow.

Following its rapid growth, the condensate reaches its maximum size around $t = 7$ s when loss processes (mainly dipolar spin-relaxation) begin to take over, decreasing the condensate population. Consequently, the signal at large negative detuning disappears. The decay of the condensate is much slower than the formation because atoms lost from the condensate due to dipolar spin relaxation are continually replenished by atoms scattering into the condensate from the thermal cloud. Eventually the thermal cloud can no longer sustain the condensate, and the condensate signal fades entirely. In Fig. 7-2(A) this process takes > 15 s. The slow decay of the condensate signal is delineated with an arrow in the figure.

The utility of images like that of Fig. 7-2(A) is to provide a visual impression of condensate formation and decay. The image gives semi-quantitative information about the onset of condensation relative to the end of rf evaporation, the maximum number of atoms in the condensate, and the duration of the condensate signal. For a more detailed analysis it is necessary to examine the data along lines of constant frequency and along lines of constant time.

7.1.2 Condensate Signal at Constant Detuning

Plotting condensate formation data along lines of constant detuning allows specific densities to be monitored as a function of time. Figure 7-2(B) slices the data set of Fig. 7-2(A) along four lines of constant detuning. The condensate signal first appears around $t = 5$ s in the -106 kHz panel and progressively later in the panels with more negative detuning. This behavior corresponds to the rapid formation of the condensate. The condensate reaches its maximum *population* around $t = 7$ s; the time at which the signal reaches its maximum *amplitude* in every panel. Afterward, the condensate begins its slow decay. The signal first disappears from the most detuned panel, -298 kHz. As the condensate shrinks in size the signal disappears in progressively less detuned panels until for $t > 18$ s it remains only in the -106 kHz panel.

Presenting the data in this format permits quantitative comparison of formation onset time, the maximum amplitude of the condensate signal, and the duration of the condensate signal. This format is particularly useful for comparing formation experiments and will be used throughout this chapter.

7.1.3 Condensate Lineshape as a Function of Time

Condensate formation data can also be plotted along lines of constant time, revealing how the condensate lineshape evolves. Figure 7-2(C) slices the data set of Fig. 7-2(A) along four lines of constant time.[1] Each panel plots the detuning on the vertical axis and the amplitude of the condensate signal on the horizontal axis. The left-most panel shows the condensate just beginning to form at $t = 5.7$ s. The signal extends to a detuning of ~ -225 kHz. At $t = 7.1$ s, the condensate has reached its maximum population; the signal extends to -300 kHz and has its maximum amplitude. At later times the condensate decay is indicated by reduced signal amplitude and spectroscopic extent.

Examining the condensate lineshape as a function of time serves two purposes. First, it allows comparison of the actual lineshape with the expected lineshape, i.e. Thomas-Fermi (see Sec. 6.3). Second, if the lineshape is what we expect, a fitting procedure can be used to extract additional quantitative information from the data set. For example, fitting a Thomas-Fermi wave function to the data allows extraction of the population of the condensate as a function of time. Following the discussion of Sec. 6.3.2 (and especially Fig. 6-8), however, we see that the lineshapes in the panels of Fig. 7-2(C) are not described by a Thomas-Fermi density profile. Since the observed lineshape is not fully understood, condensate formation data taken in the Doppler-free portion of the spectrum will provide primarily qualitative and semi-quantitative information about the formation process. This topic is discussed further

---

[1] Since data points are collected sequentially in time, Figure 7-2(C) was constructed by binning a sequence of 16 detuning points in time. In this case each bin is 228 ms wide.

in the following section.

7.2 Comparison of Doppler-sensitive and Doppler-free Spectra

Identical experiments performed in the Doppler-sensitive (DS) and Doppler-free (DF) portions of the $1S$-$2S$ spectrum revealed striking differences. The differences are illustrated in the "images" presented in Fig. 7-3. In both experiments an identical rf evaporation was carried out to prepare the sample in Trap A with a bias potential energy of $\theta/k_{\mathrm{B}} = 154(2)$ μK and a temperature just above the Bose-Einstein transition. The end of the rf evaporation and the beginning of the subsequent rf hold are indicated in each panel by the vertical dashed line. Approximately one second into the rf hold the condensate grows suddenly in both the DS and the DF spectra as indicated by the sudden appearance of a dark region. The major difference occurs in the spectral extent of the condensate signal. In the DF spectrum the dark region indicating strong condensate signal is nearly uniform in intensity and extends well beyond a detuning of -400 kHz. In contrast the DS spectrum is less uniform in intensity, fading from black at -150 kHz to light grey at -350 kHz. The DS signal vanishes completely beyond -400 kHz.

The differences in the intensity and extent of the signal are even more pronounced in Fig. 7-4 where the signal at constant detuning is plotted versus time. Each row contains plots of the DS and DF spectra at a particular detuning.[2] The spectra are similar in that the condensate signal appears at the same time and decays on a similar time scale in the -140 kHz and -240 kHz panels. Comparing the amplitude of the signal at a particular time across the four detunings reveals a significant difference. The amplitude of the DS signal is largest in the -140 kHz panel. At more negative

---

[2] The zero of detuning in Doppler-free plots is the unshifted $1S$-$2S$ resonance. In the Doppler-sensitive plots the zero of detuning is the center of the Doppler profile. The detunings are given at 243 nm.

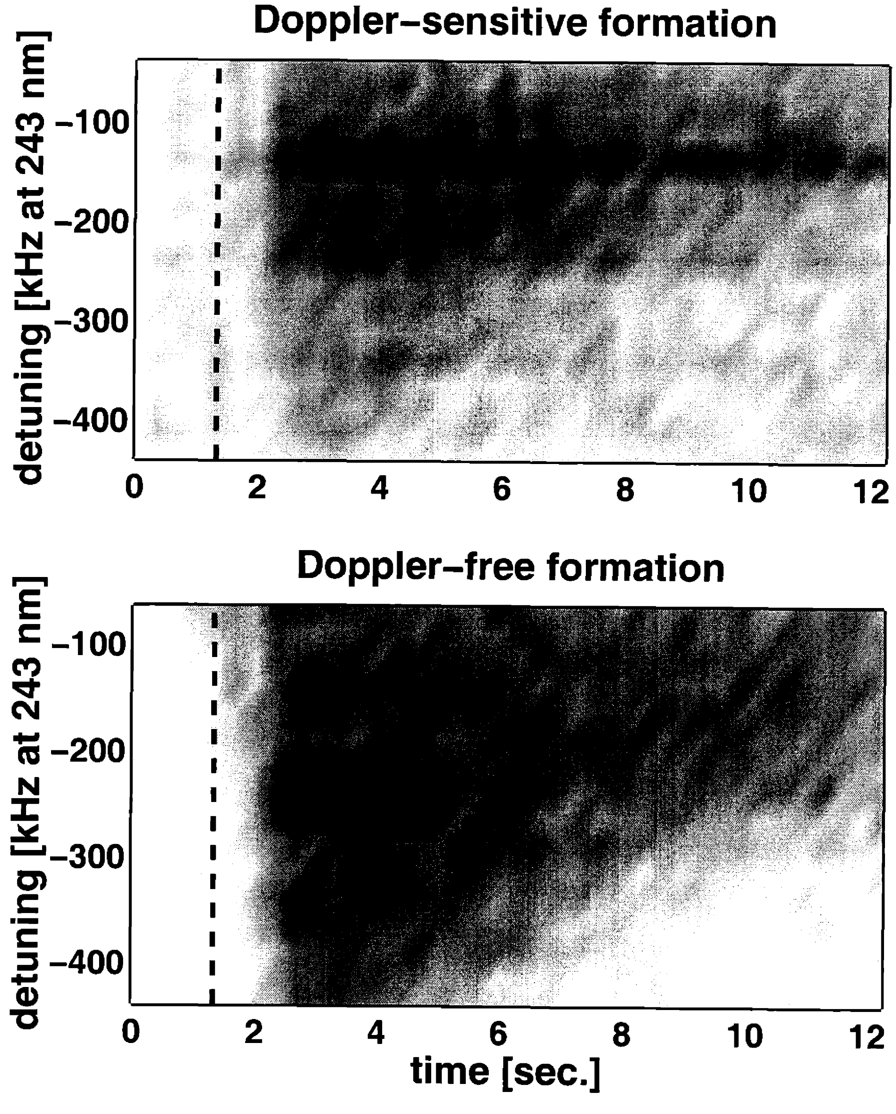

Figure 7-3: "Images" illustrating the differences between the Doppler-sensitive (DS) and Doppler-free (DF) condensate spectra. The darkest regions indicate the most intense signal. The dashed vertical line denotes the end of the rf evaporation and the beginning of the rf hold. The region of strong signal clearly extends to more negative detunings and longer times in the DF image, suggesting contributions due to the noncondensed gas as discussed in Sec. 6.3.2. These contributions make quantitative interpretation of the DF spectrum difficult.

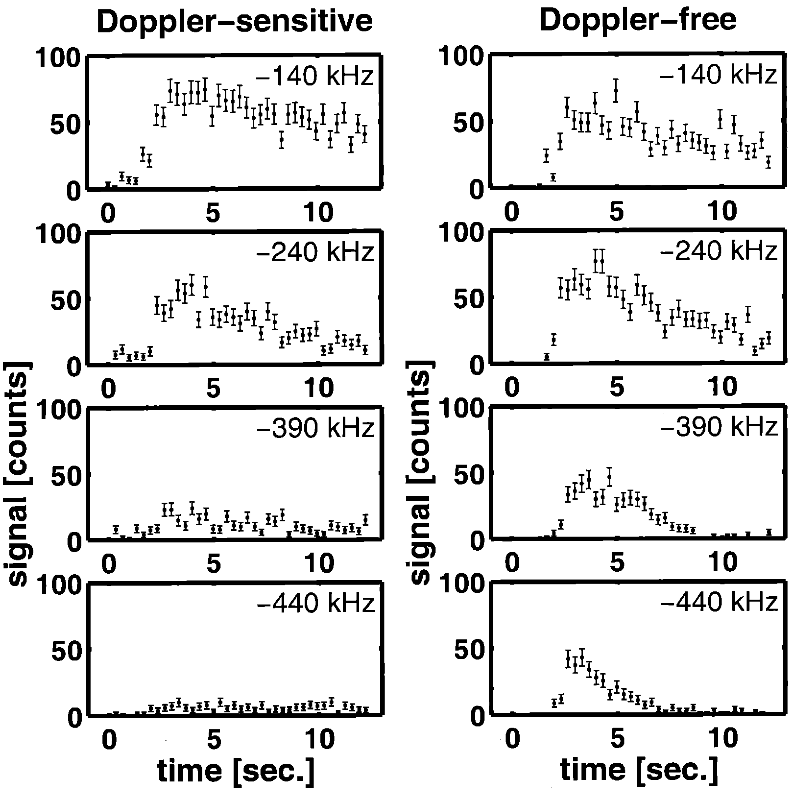

Figure 7-4: Comparison of the time evolution of the condensate signal in the DS and DF portions of the $1S$-$2S$ spectrum. The signal is compared at four different detunings for identical repetitions of a condensate formation experiment. The overall amplitude of the signal is expected to differ due to the two-photon excitation process. A strong signal is present at detunings of -390 kHz and -440 kHz in the DF spectrum. This signal must be due to noncondensed atoms since it is not present in the DS spectrum.

detunings, the signal amplitude decreases significantly, vanishing completely in the -440 kHz panel. In contrast the amplitude of the DF signal changes only slightly at different detunings. A strong signal remains in both the -390 kHz and -440 kHz panels. The uniformity of signal strength across detunings explains the homogeneity of signal intensity in Fig. 7-3.

The data presented in this section illustrate important differences between the DS and DF condensate spectra. Recall that the origin of these differences has to do with the laser excitation geometry and motion of the noncondensed atoms as described in

Sec. 6.3. The differences are illustrated in Fig. 6-7, Fig. 6-8, and Fig. 6-9. The DF condensate spectrum is not well-understood, and great care is needed in interpreting this data. In this section we have shown, however, that valuable qualitative and semi-quantitative information such as time of formation and decay time scale can be extracted reliably from DF data since these agree with values obtained from DS data. Comparative experiments can also be performed in DF mode where relative effects rather than absolute ones are observed. Experiments in the DF mode have the additional advantages of a stronger two-photon excitation and a background signal due to only fluorescence. For quantitative comparisons with theory we avoid the DF data and work exclusively with data from the DS spectrum.

7.3 Effect of Laser Excitation on Condensate Formation

One of the advantages of two-photon $1S$-$2S$ spectroscopy is the ability to interrogate the trapped atomic sample without destroying it. Nevertheless, the effect of laser excitation on the condensate formation process must be considered. The excitation process introduces one-body loss processes to the trapped sample, reducing the net rate at which kinetic processes scatter atoms into the condensate. The loss processes include photon recoil and scattering by ^{4}He boiled off of the retromirror at the bottom of the trapping cell. When a $1S$ atom is promoted to the $2S$ state through Doppler-sensitive (DS) excitation, it recoils with a velocity of $v = \sqrt{4h\nu_{\mathrm{recoil}}/m} = 3.3$ m/s, a velocity sufficient to escape the shallow trap used in formation experiments. Although an atom excited in the Doppler-free (DF) mode does not recoil during absorption, the two-photon radiative decay of the $2S$ state heats the trapped sample and can impart sufficient momentum for atoms to escape the trap. Radiative decay occurs when the excited $2S$ population is quenched by an applied electric field, and heating is due to collisions between the high-momentum quenched atoms and atoms in the trapped sample. Absorption of the uv laser by contaminants on the surface of the

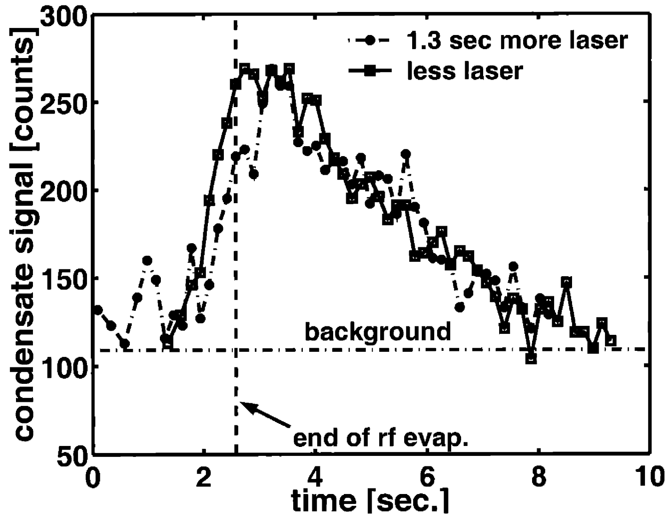

Figure 7-5: Effect of laser excitation on condensate formation experiments. The squares indicate the condensate signal as a function of time for a typical condensate formation experiment. The circles represent an identical experiment in which the laser was introduced to the sample 1.3 s earlier. The additional excitation by the laser delays the formation slightly (< 0.5 s) but has little influence on the amplitude of the signal or its decay. The connecting lines serve as guides to the eye and indicate the noise in the data.

retromirror leads to heating and causes ^{4}He to stream off of the retromirror. The stream of ^{4}He causes background gas losses to the sample. The losses are most severe in the condensate since the one-body loss rate is proportional to the density.

To investigate the effects of laser excitation, two formation experiments were performed in Trap A in which the laser was introduced into the trapping cell at different times. In Fig. 7-5 the squares indicate the total observed condensate signal versus time. The filled circles (●) represent an otherwise identical experiment in which the laser was introduced to the sample 1.3 s earlier. The earlier introduction of the laser appears to delay the formation of the condensate slightly, but the maximum condensate signal is identical. The lines connecting the data points serve as guides to the eye and give an indication of the noise in the measurements. Within the noise of the experiments, the decay of the condensate is identical in both cases.

The noise inherent in the measurements makes it difficult to determine the exact influence that the excitation process has on condensate formation. The effect is small but not negligible, and the measurements suggest that we should introduce the laser immediately prior to formation. A tradeoff, however, is the need to introduce the laser sufficiently early for the servo systems (mainly human, see Fig. 5-2) to stabilize alignment. This generally requires ~ 2 s. As we will see in Chapter 9, it is necessary to take laser losses into account when making quantitative comparisons between experiment and theory.

7.4 Effect of Trap Shape on Condensate Formation

The shape of the magnetic trap influences the formation of the condensate because it determines the volume available for condensation. For a given number of atoms, a larger volume implies a lower atomic density and a lower temperature required for condensation. Recall that the magnetic trap is characterized by ω_z and ω_ρ; the axial and radial oscillator frequencies, respectively. In the Thomas-Fermi approximation the spatial extent of the condensate is characterized by the Thomas-Fermi radius,

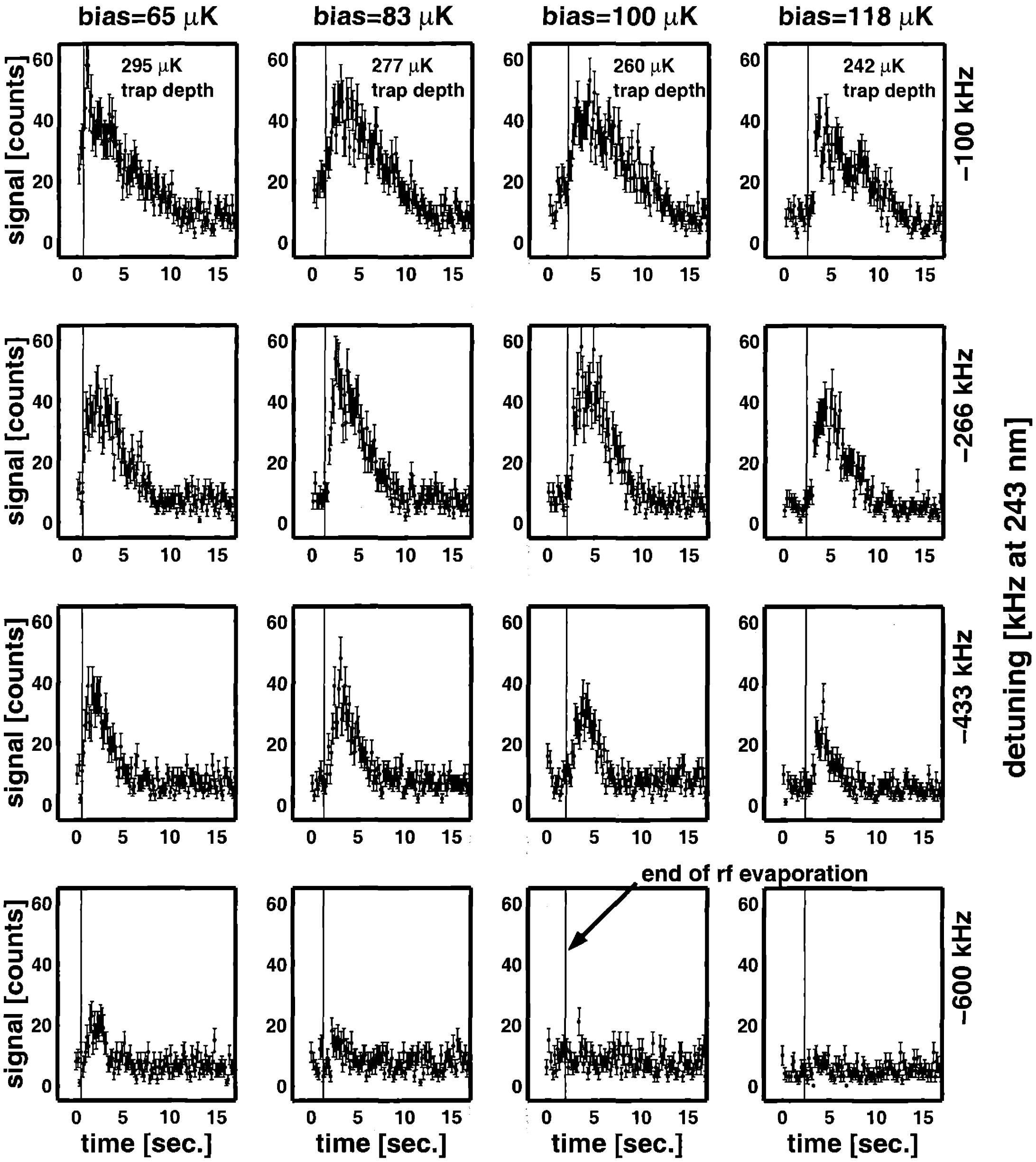

Figure 7-6: Effect of trap shape on condensate formation. The DF condensate signal at four different detunings is shown for experiments performed in Trap A using four bias field values. For unchanged radial confinement an increased bias field results in a less confining trap (see Sec. 2.7.1 and Eq. (2.38)) and a colder, less dense condensate. This can be seen by comparing the signal intensity and duration at constant detuning.

$R_{\mathrm{TF}} \sim \bar{\omega}^{-1/2}$, where $\bar{\omega} = (\omega_z \omega_\rho^2)^{1/3}$. Thus the volume of the condensate scales as $\bar{\omega}^{-3/2}$. By varying $\bar{\omega}$, that is, by changing the strength of the confining field, it is possible to change the volume available for condensation and the temperature at which the Bose-Einstein transition is crossed.

Figure 7-6 presents the results of four experiments performed in Trap A in which $\bar{\omega}$ was varied in order to influence the condensate formation process. Experimentally it is easiest to change $\bar{\omega}$ through adjustments to the bias potential energy, θ. Recall from Eq. (2.38) that the radial oscillation frequency for the condensate at $z = 0$ is given by

$$\omega_\rho = \sqrt{\frac{1}{m}\frac{\alpha^2}{\theta}} \,. \tag{7.1}$$

Each column of Fig. 7-6 contains a condensate formation experiment carried out at a particular θ. The columns are labeled with the value of θ/k_{B}. The rows correspond to a particular detuning (labeled on the right at 243 nm) from the unshifted Doppler-free $1S$-$2S$ resonance.

In each experiment rf evaporation was carried out to an ending frequency of $\epsilon_{\mathrm{rf}} =$ 7.5 MHz. The end of the rf evaporation is indicated by the vertical line in each panel. The subsequent rf hold defined a trap depth which is denoted in the upper panel of each column. In the deepest (295 μK), most tightly confined trap, condensate formation begins before the end of the rf evaporation, and a signal appears at all four detunings. Increasing θ/k_{B} reduces the radial confinement of the trap and increases the volume available for the condensate and the thermal cloud. The result is a colder, less dense condensate. The change in temperature can be seen by noting the position of the signal maximum relative to the end of the forced evaporation. The peak shifts later in time, indicating that further evaporative cooling takes place during the rf hold despite the shallower trap. The reduction in density is easily observed by following the evolution of the amplitude of the signal at a particular detuning. At -600 kHz a significant signal appears only in the 295 μK deep trap. At -433 kHz the maximum amplitude of the signal drops by almost a factor of two for a change in trap depth of

53 μK.

These experiments indicate the sensitivity of the formation process to changes in the bias field. The important point for this study is that because we can measure θ/k_{B} to within about 1 μK, and it is observed not to drift for at least a 24 hour period, changes in the bias field are unlikely to complicate quantitative comparisons between experiment and theory.

7.5 Coupling of Condensed and Noncondensed Components

In this section we examine the effect of the coupling of the noncondensed gas to the condensate as the condensate grows and eventually decays. The experiments involve varying the rf frequency applied to the trapped sample after the formation of the condensate. We begin by looking at only the condensate signal and then compare its behavior to that of the noncondensed component. These experiments not only strengthen our intuition about the condensation process, they suggest a new type of experiment for quantitative comparison of theory and experiment in which the applied rf frequency is varied suddenly to stimulate the formation of a condensate.

7.5.1 Effect of Holding RF on the Condensate

Figure 7-7 shows the results of two experiments performed in Trap A to study the effects of holding rf on the condensate. In both experiments the trapped sample was cooled to the Bose-Einstein transition using rf evaporation. The end of the rf evaporation is denoted by the vertical dashed line in each panel. In one experiment the final rf evaporation frequency is held constant to maintain a constant trap depth. The bias potential energy was measured to be $\theta/k_{\mathrm{B}} = 190(2)$ μK. The DF results of this experiment are shown in the upper half of each panel of Fig. 7-7, where the signal has been offset by 60 counts for clarity. The lower half of each panel contains

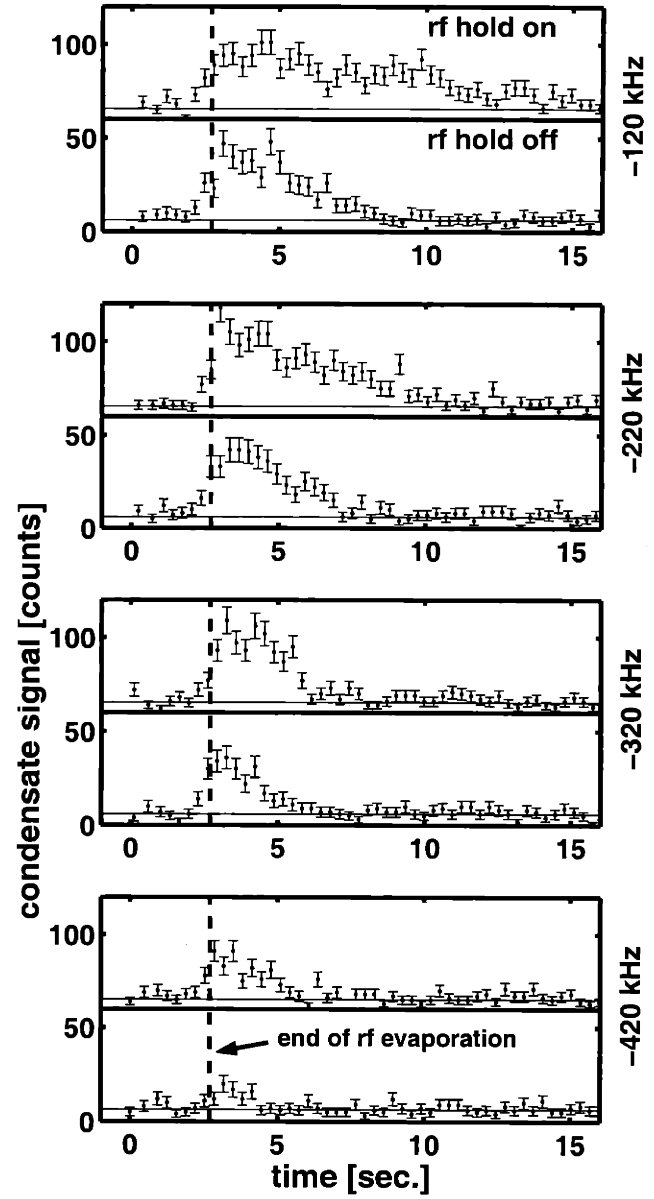

Figure 7-7: Comparison of condensate formation and decay at four different detunings with and without holding rf. The upper frame of each panel shows the DF signal with an rf field held fixed following evaporation, used to define the trap depth. The lower frame of each panel shows the DF signal in the absence of a holding field; the trap depth is defined by the magnetic field alone. The upper frame is offset by 60 counts for clarity. The rise time of the signals are nearly identical, but the amplitude and duration clearly differ. The holding rf field allows evaporative cooling to continue, leading to a larger longer-lived condensate. The solid line indicates the background signal determined from a separate counter.

the results of an otherwise identical experiment where the applied rf is switched off immediately after the rf evaporation. The condensate signal begins to increase at approximately the same time in each panel, but in the presence of holding rf the condensate continues to increase in size as indicated by the slightly larger signal amplitudes at -320 kHz and -400 kHz detuning. Although the condensate population begins to decrease shortly after the end of rf evaporation, its decay appears to be significantly slower in the presence of holding rf.

The effect of the holding rf is to sustain the condensate through continued cooling of the noncondensed component. Without holding rf the trap depth experienced by the noncondensed component increases suddenly. Thermalizing elastic collisions redistribute energy in the sample. Atoms in the low-energy portion of the energy distribution are lost from the sample due to dipolar spin-relaxation, either directly or after scattering into the condensate. The loss of low-energy atoms effectively heats the sample. Atoms with higher energy repopulate the portion of the energy distribution that was truncated by the applied rf field and lead to an increased average energy, i.e. temperature. In the absence of holding rf the net result is the warming of the noncondensed component to a point where it can no longer sustain the condensate.

Figure 7-7 demonstrates that by maintaining the rf field, the condensate grows larger and lasts longer. In some ways it also simplifies the analysis because it sets an upper limit on the energy of the system. This point is also illustrated in Fig. 7-8 where the total DF condensate signal is plotted versus time for the same experiments as in Fig. 7-7. The rise of the condensate signal is identical with and without holding rf, but the maximum amplitude and time-integrated number of counts is clearly larger with holding rf. For example, without holding rf the condensate signal has returned to near background level at $t \sim 8$ s. In contrast, with holding rf the condensate signal persists until $t > 12$ s.

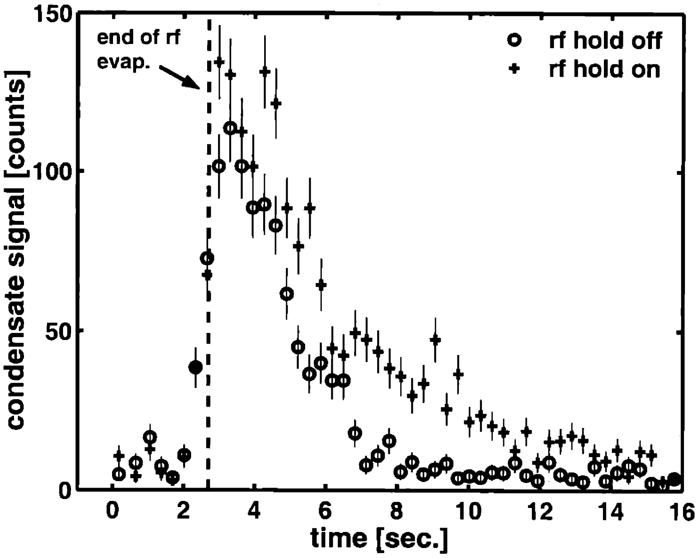

Figure 7-8: Evolution of the integrated DF condensate signal with and without holding rf. The sum of the counts recorded at each frequency point is plotted at each time point to indicate the total condensate signal versus time. With holding rf the amplitude of the signal is slightly stronger, indicating a greater condensate population, and persists for almost 7 s longer.

7.5.2 Effect of Holding RF on the Noncondensed Gas

To compare the effects of holding rf on the condensed and noncondensed components, the mean shift of the noncondensed gas is plotted as a function of time in Fig. 7-9. The experiment of Fig. 7-8 was repeated using Doppler-free (DF) spectroscopy of the noncondensed gas near the unshifted $1S$-$2S$ resonance. The resonance frequency of the two-photon transition is shifted due to the cold-collision shift as described in Sec. 5.5.4. The mean shift of the DF $1S$-$2S$ spectrum is linear with sample density with more negative shifts corresponding to higher densities. Fig. 7-9 shows that the noncondensed gas density increases rapidly during the final 2.5 s of rf evaporation. After the forced evaporation ends, the density decreases rapidly due to dipolar spin-relaxation within the thermal cloud and stimulated scattering into the condensate.

The behavior of the normal gas signal in Fig. 7-9 resembles the condensate signal of Fig. 7-8, but we cannot directly compare the time scale of decay with that of the condensate because resonance induced losses play a major role in DF spectroscopy of the noncondensed component. Nevertheless, Fig. 7-9 shows that the rf field facilitates evaporative cooling, helping to sustain the density of the noncondensed component. Without holding rf the magnitude of the shift of the normal gas is less than 2 kHz after $t \sim 8$ s. With holding rf a shift of at least -2 kHz is maintained until $t > 12$ s. Together our experiments with the rf field suggest that changes made to the normal gas have a direct impact on the behavior of the condensate. The rest of this chapter presents the results of experiments which explore condensate formation and decay following manipulation of the normal gas using rf techniques.

7.6 RF Cut Experiments

In order to make quantitative comparisons with theory, we performed two types of experiments using our ability to manipulate the trapped sample with rf magnetic fields. Our objective was to stimulate the formation of a condensate by rapidly changing the applied rf frequency. RF evaporation was used to cool the thermal cloud

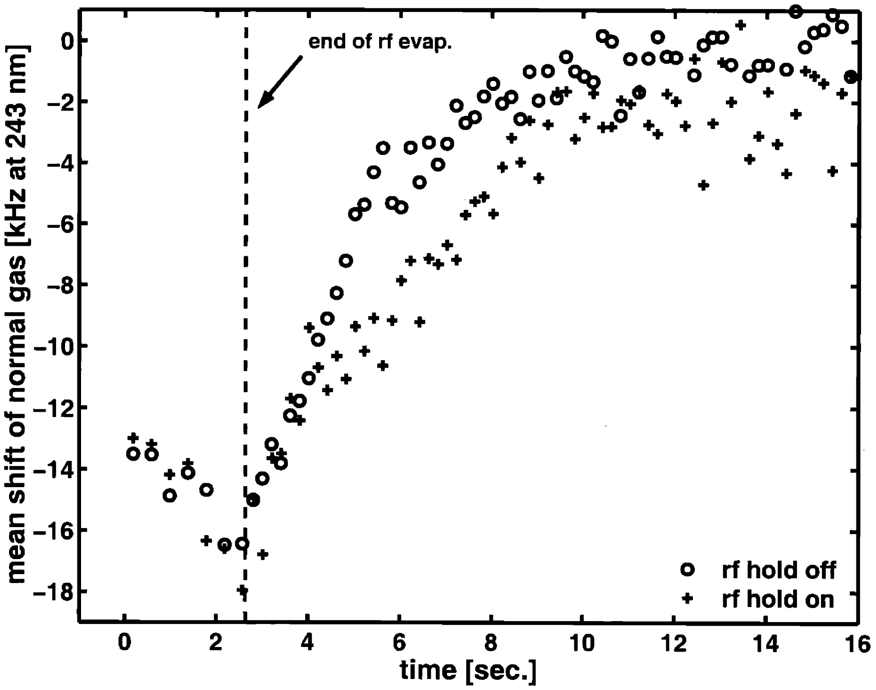

Figure 7-9: The mean shift of the DF normal gas spectrum with and without holding rf. The DF $1S$-$2S$ spectrum was recorded during the formation of a condensate, corresponding to Fig. 7-8 and Fig. 7-7. In the presence of the holding rf field (+), the mean shift returns toward zero more slowly, indicating that the rf field facilitates evaporative cooling and helps to sustain the density of the noncondensed component. We must exercise care in comparing the time scales of decay of the condensate and thermal cloud because resonance induced losses play a major role in DF spectroscopy of the thermal cloud.

to a temperature just above the transition temperature. The final frequency of the rf evaporation sweep, ϵ_{start}, controls the temperature of the sample, allowing the thermal cloud to be prepared in a well-defined initial state. A nonequilibrium situation was then created by rapidly lowering the rf frequency from ϵ_{start} to a final value, ϵ_{rf}, and holding it fixed. This rapid rf sweep, or "cut", had the effect of truncating the high-energy tail of the energy distribution, leaving the sample unstable against condensate formation. We monitored the $1S$-$2S$ spectrum from the end of rf evaporation through the rf cut and hold. In this way, we recorded the formation and decay of a single Bose-Einstein condensate. This differs from many alkali atom experiments in which the detection process destroys the condensate and the experiment must be repeated many times for nominally identical initial conditions [38, 72].

7.6.1 Varying the Ending Frequency of RF Cuts

In the first type of rf cut experiment, the sample was loaded and cooled in magnetic trap B using the methods described in Chapter 3. Forced evaporative cooling was performed for about 65 s by continuously lowering the rf frequency from 35 MHz to $\epsilon_{\text{start}} = 5.4$ MHz according to Eq. (6.1). This prepared a noncondensed thermal cloud just above the transition temperature with $N_{\text{start}} \sim 2.2 \times 10^{10}$ and $T_{\text{start}} \sim 30\ \mu$K. The minimum of the magnetic trap was determined by rf ejection to be $\theta/h = 2.75(2)$ MHz (132 μK). The oscillation frequencies for this trap were $\omega_\rho = 2\pi \times 1200$ Hz and $\omega_z = 2\pi \times 10.3$ Hz, leading to a geometric mean oscillator frequency of $\bar{\omega}/2\pi = 246$ Hz. For identical repetitions of the experiment the atom number and temperature do not vary within our experimental uncertainties. The measured minimum of the magnetic trap varies less than our experimental uncertainty of 20 kHz.

After the preparation of the thermal sample just above the transition temperature, the rf frequency is quickly lowered from $\epsilon_{\text{start}} = 5.4$ MHz to a variable ending frequency, ϵ_{rf}, in $t_{\text{rf}} = 1$ s and held constant. The trap depth resulting from the rf cut and hold is shown in Fig. 7-10. The trap depth prior to the cut was $(\epsilon_{\text{start}} - \theta/h) = 2.65(2)$ MHz (128 μK). Following the "deep" cut, indicated in the

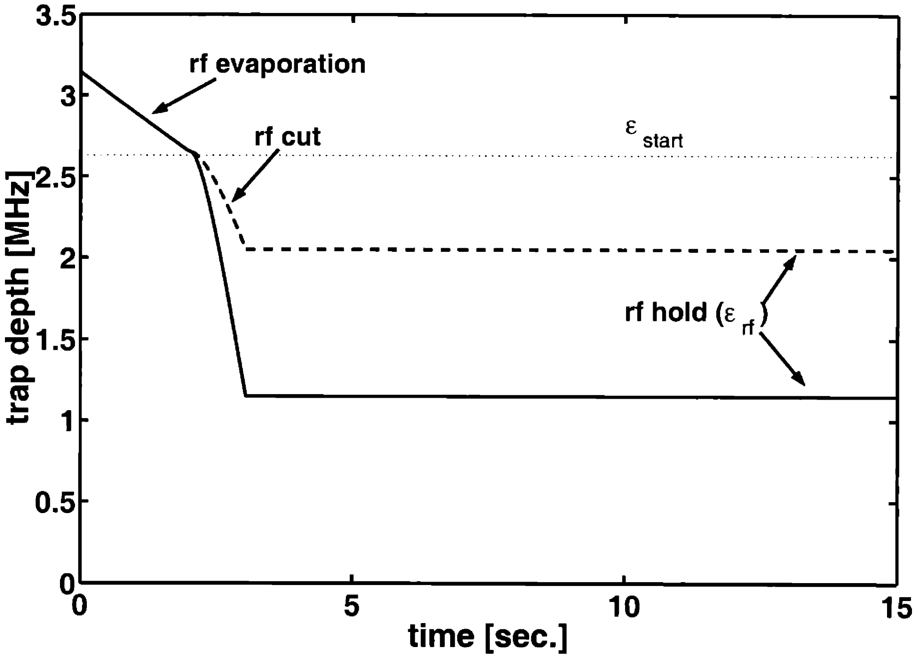

Figure 7-10: Trap depth versus time for rf cut experiments varying ϵ_{rf}. Identical rf evaporations are carried out prior to an rf cut in which the trap depth is reduced rapidly in $t_{\mathrm{rf}} = 1$ s and then held constant at one of two final values, 2.05(2) MHz ("shallow" cut) and 1.15(2) MHz ("deep" cut). The condensate forms *following* the rf cut. The formation of the condensate is monitored spectroscopically beginning near the end of the rf evaporation.

figure by the solid line, the trap depth was reduced to 1.15(2) MHz (55 μK). The "shallow" cut, indicated by the dashed line, reduced the trap depth to 2.05(2) MHz (98 μK). By truncating the energy distribution and holding the new trap depth fixed, we force the sample to equilibrate at a lower temperature.

The one second duration of the rf cut might seem long in comparison to similar cuts[3] made in alkali experiments [72, 83], but the duration of the cut can be understood in terms of the elastic scattering rate. For the ^{23}Na experiment $t_{\mathrm{rf}} = 10$ ms and the elastic scattering rate $\gamma_{\mathrm{el}} = n\sigma v \approx 500\ \mathrm{s}^{-1}$, where n is the atom density, $\sigma = 8\pi a^2$ denotes the elastic collision cross-section, and $v = 4(k_B T/\pi m)^{1/2}$ is the thermal velocity. During a 10 ms rf cut, a typical Na atom experiences 5 collisions. In comparison, for hydrogen at a density $n = 1.0 \times 10^{14}\ \mathrm{cm}^{-3}$ and temperature $T = 40\,\mu\mathrm{K}$, $\gamma_{\mathrm{el}} = 14\ \mathrm{s}^{-1}$, resulting in only 14 collisions during a 1 s rf cut. For $t_{\mathrm{rf}} < 500$ ms, we observed that the removal of thermal atoms with energy $\mu B/h > \epsilon_{\mathrm{rf}}$ was incomplete. For this reason, we chose $t_{\mathrm{rf}} = 1$ s.

Following the rf cut equilibration of the cloud by elastic collisions leads to a decreased temperature and the formation of a Bose-Einstein condensate. During the rf cut and hold, we monitored the Doppler-sensitive portion of the $1S$-$2S$ spectrum. Although the condensate signal rests on top of the broad Doppler profile, monitoring this portion of the spectrum eliminates complications due to the poorly understood Doppler-free normal gas line in the presence of a condensate (see Sec. 6.3.2). Visual impressions of the data collected during the deep and shallow cut experiments are shown in Fig. 7-11. The end of the $t_{\mathrm{rf}} = 1$ s cut is indicated in both panels by the dashed vertical line, and the zero of detuning is taken to be the center of the Doppler profile. The appearance of a dark region, indicating the presence of a condensate, occurs earlier in the deep cut experiment. The signal extends to a detuning of approximately -150 kHz and is reduced significantly by $t = 10$ s. Following the shallow cut the extent of the dark region in detuning is similar, but the dark region persists

---

[3] In the ^{23}Na experiment, the quick rf cut was *not* followed by an rf hold. Instead, the applied rf field was removed, allowing the sample to equilibrate in the magnetic trap.

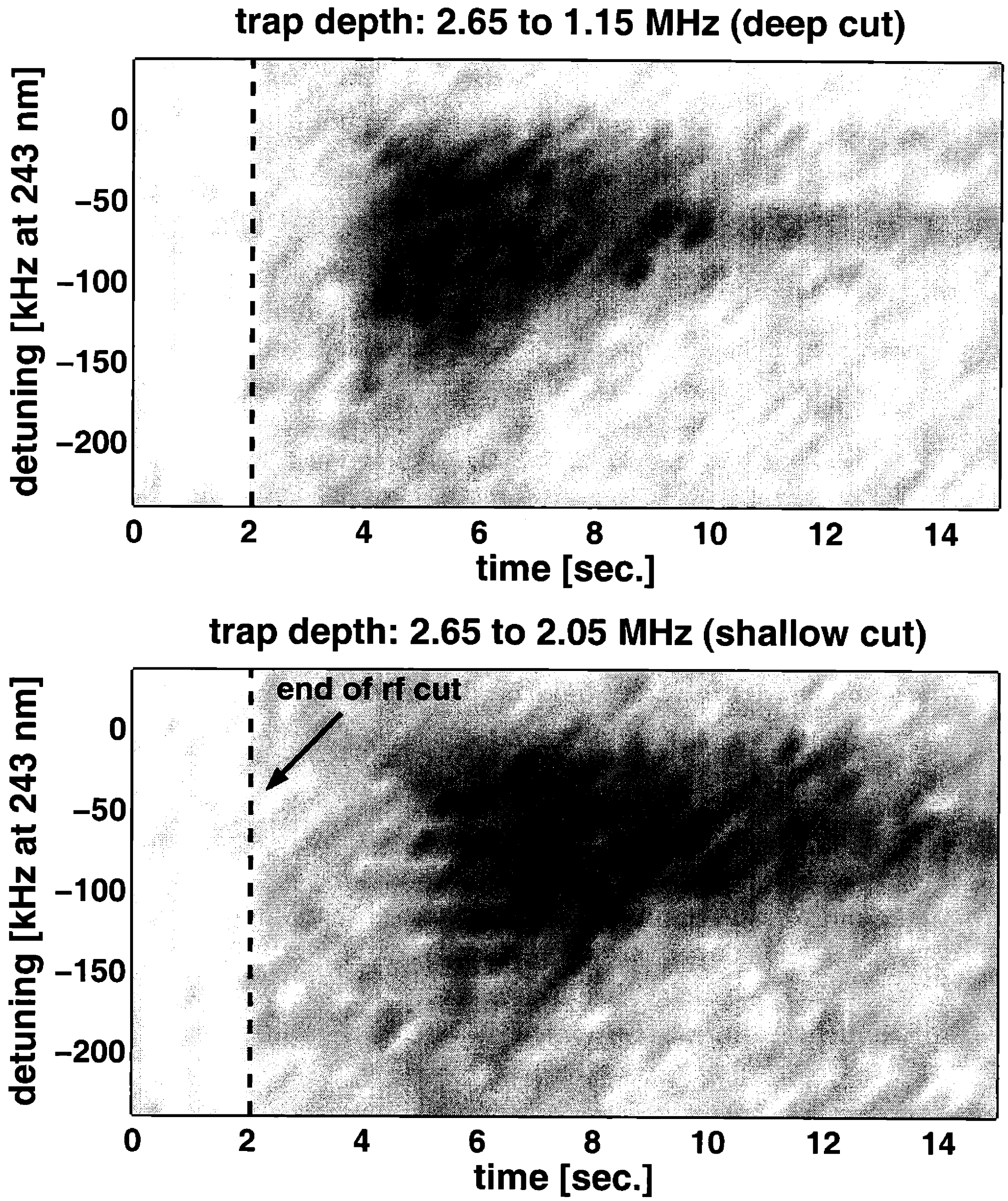

Figure 7-11: Visual impressions of rf cut experiment data obtained by varying ϵ_{rf}. The "image" represents the condensate signal versus detuning as a function of time. The zero of detuning corresponds to the center of the Doppler-sensitive profile. The dark regions in these "images" indicate the most intense condensate signal. Prior to the end of the rf cut, denoted by the dashed vertical line, the signal is weak for both cuts. For the "deep cut" (upper panel) the condensate forms at about $t = 4$ s. For the "shallow cut" the formation occurs around $t = 5$ s. The deep cut signal fades earlier because the severe rf cut removed thermal atoms necessary to sustain the condensate.

beyond $t = 12$ s, indicating a longer-lived condensate. These "images" illustrate that condensate signal appears only in the red-shifted portion of the spectrum. Also note that the Doppler profile and fluorescence background have not been subtracted. Their presence is indicated by the light grey background on which the dark condensate signal rests.

The total condensate signal with the Doppler profile and fluorescence background subtracted is shown in Fig. 7-12. The open circles ($\circ$) indicate the signal resulting from the "deep" cut with $\epsilon_{\text{rf}} = 3.9$ MHz, while the open boxes ($\Box$) show the signal due to the "shallow" cut with $\epsilon_{\text{rf}} = 4.8$ MHz. Following the rf cut, both signals rise abruptly indicating the sudden growth of a condensate. As the condensate grows in size, losses due to dipolar spin-relaxation become more severe. Eventually the growth of the condensate is overcome by this decay process, and the signal decreases in time. Only 15 s are shown in Fig. 7-12, but the condensate signal is observed to last for ~ 30 s.

The abrupt rise of the condensate signal takes place earlier for the deep cut indicating that the more severe truncation of the energy distribution brought the sample closer to degeneracy by reducing the total energy of the cloud. For the shallow cut the onset of condensate formation is delayed as the sample continues to cool in the presence of the rf hold. The slope of the rise is also steeper for the deep cut suggesting that the low-energy atoms in the trap were available for scattering into the condensate rather than for continued cooling of the sample.

The amplitude of the deep cut signal is somewhat higher than for the shallow cut. Again, this is due to the relatively large low-energy population scattering into the condensate. The amplitude of the deep cut signal cannot be sustained, however, because the number of thermal atoms remaining to feed the decaying condensate is smaller in the shallower trap. The shallow cut signal persists longer because more atoms are available to feed the decaying condensate.

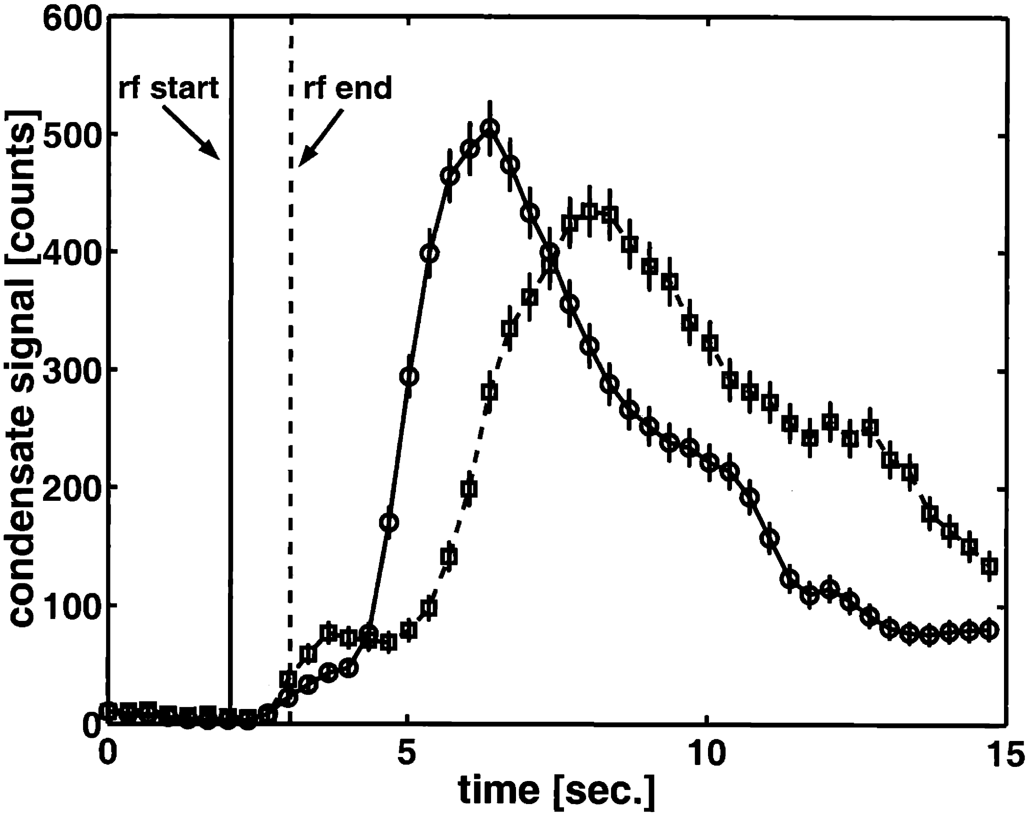

Figure 7-12: Total condensate signal versus time for the rf cut experiments in which ϵ_{rf} was varied. The DS condensate signal shown in Fig. 7-11 was summed over frequency after subtraction of the Doppler profile (see Fig. 7-13). The integrated signal was passed through a smoothing filter and is plotted here versus time. The solid line and open circles (○) correspond to the deep cut experiment, and the dashed line and boxes (□) correspond to the shallow cut. The residual undulations in the signal are due to imperfections in the subtraction of the Doppler profile.

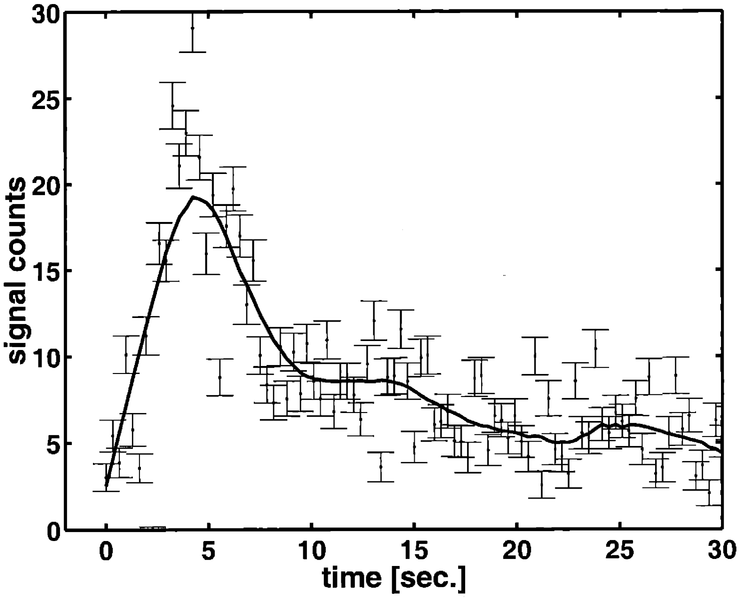

Figure 7-13: Time evolution of the Doppler-sensitive (DS) *noncondensate* signal (Doppler profile). This low amplitude signal underlies the DS condensate signal. The solid line is the result of passing the noisy profile through a smoothing filter and determines the profile which is subtracted from the total DS signal. Note that although this signal is noisy, it does not constitute a significant source of error since the DS condensate signal much larger in amplitude.

Doppler-sensitive profile underlying the condensate signal

To produce a single trace in Fig. 7-12 the Doppler-sensitive profile was monitored at 24 evenly spaced frequencies recorded in 12 identical repetitions of the experiment. Four of these frequencies were detuned blue of the center of the Doppler profile where no condensate contribution was expected. The signal recorded at these frequencies provided a measure of the Doppler profile as a function of time. Since the separation between frequency points is much less than the width of the Doppler profile, the four traces were summed together to increase signal-to-noise. The result is shown in Fig. 7-13. The signal is quite noisy and the error is larger than the statistical error shown. The remaining noise is likely due to laser intensity and alignment fluctuations. The solid line is the result of smoothing the noisy data with a moving average filter. The amplitude given by the line is subtracted from the total signal leaving only the signal due to the condensate.

Removal of the normal gas by an rf cut

Our interpretation of the rf cut experiments has relied on the assumption that the rf cut efficiently removes the noncondensed atoms that encounter the rf "knife." To test this assumption we monitored the Doppler-free normal gas signal during an rf evaporation, cut, and hold in Trap A. The integrated normal gas signal is plotted versus time in Fig. 7-14. On the same axes the trap depth as defined by the applied rf is plotted versus time. The scale of the trap depth axis was adjusted to coincide with the normal gas signal. The reduction in normal gas signal closely follows the change in trap depth.[4] During the rf evaporation the slow decrease in trap depth is accompanied by a slow decrease in normal gas signal, indicating the evaporation of atoms. The normal gas signal responds almost immediately to the sudden reduction of trap depth during the rf cut. Near the end of the rf cut, the normal gas signal appears to lag the

---

[4] There is no reason to expect that the number of normal gas atoms should be related to the trap depth by a single constant of proportionality. The comparison here is intended for qualitative purposes only.

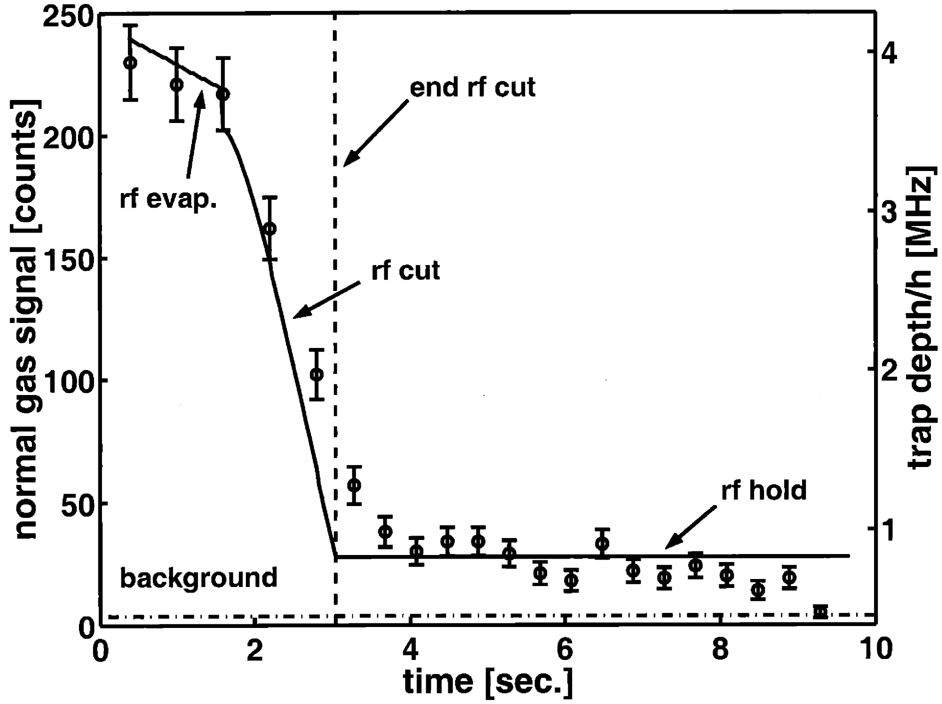

Figure 7-14: The reduction of the noncondensed gas signal resulting from an rf cut. The normal gas signal, summed over frequency for each time point, is denoted by the open circles (∘). The trap depth is determined by the frequency of the applied rf and is indicated by the solid line. The trap depth scale has been chosen to allow comparison between the changing rf frequency and the normal gas signal.

trap depth slightly, perhaps indicating that a few atoms were stranded above the rf knife. These atoms seem to disappear within the next second during the rf hold. The normal gas signal continues to decrease slowly during the rf hold due to losses such as dipolar spin-relaxation. Overall the applied rf dictates the trap depth, validating our assumption that the rf cut quickly removes the noncondensed atoms that encounter the rf knife.

A second rf cut experiment varying $\epsilon_{\rm rf}$

A second rf cut experiment was performed in which $\epsilon_{\rm start}$ was kept constant and $\epsilon_{\rm rf}$ was varied. The magnetic trapping parameters were identical: $\theta/h = 2.75(2)$ MHz, $\omega_\rho = 2\pi \times 1200$ Hz, and $\omega_z = 2\pi \times 10.3$ Hz. The trap loading for these experiments was exceptional (likely due to a fresh fill of molecular hydrogen and a thick film of superfluid ^{4}He), and the Bose-Einstein transition was crossed at a larger trap depth than in previous experiments. Following preparation of the thermal sample just above the transition temperature, the rf frequency was quickly lowered from $\epsilon_{\rm start} = 7.3$ MHz to an $\epsilon_{\rm rf}$ of 4.5 MHz or 5.0 MHz in $t_{\rm rf} = 1$ s. The initial trap depth was 4.55(2) MHz (218 μK), and the final trap depths were 1.75(2) MHz (84 μK) and 2.25(2) MHz (108 μK), respectively.

The results of the second rf cut experiment are shown in Fig. 7-15 and Fig. 7-16. Figure 7-15 shows the "images" of the cut experiment. Again the deeper cut results in earlier formation and a faster decay. In both panels the condensate signal lasts beyond $t = 10$ s, but the lower panel indicates a larger condensate signal at $t = 10$ s; in the deeper trap more noncondensed atoms remain to feed the condensate, and the condensate maintains its size for a longer period of time. The major difference between these cut experiments and the ones presented earlier is the spectral extent of the condensate signal. In the first rf cut experiment (see Fig. 7-11), the condensate spectrum did not extend beyond -200 kHz. In Fig. 7-15 there is significant spectral weight to at least -350 kHz. Recall that the cold-collision shift is proportional to number density and that the number of condensate atoms, N_c, scales with the peak

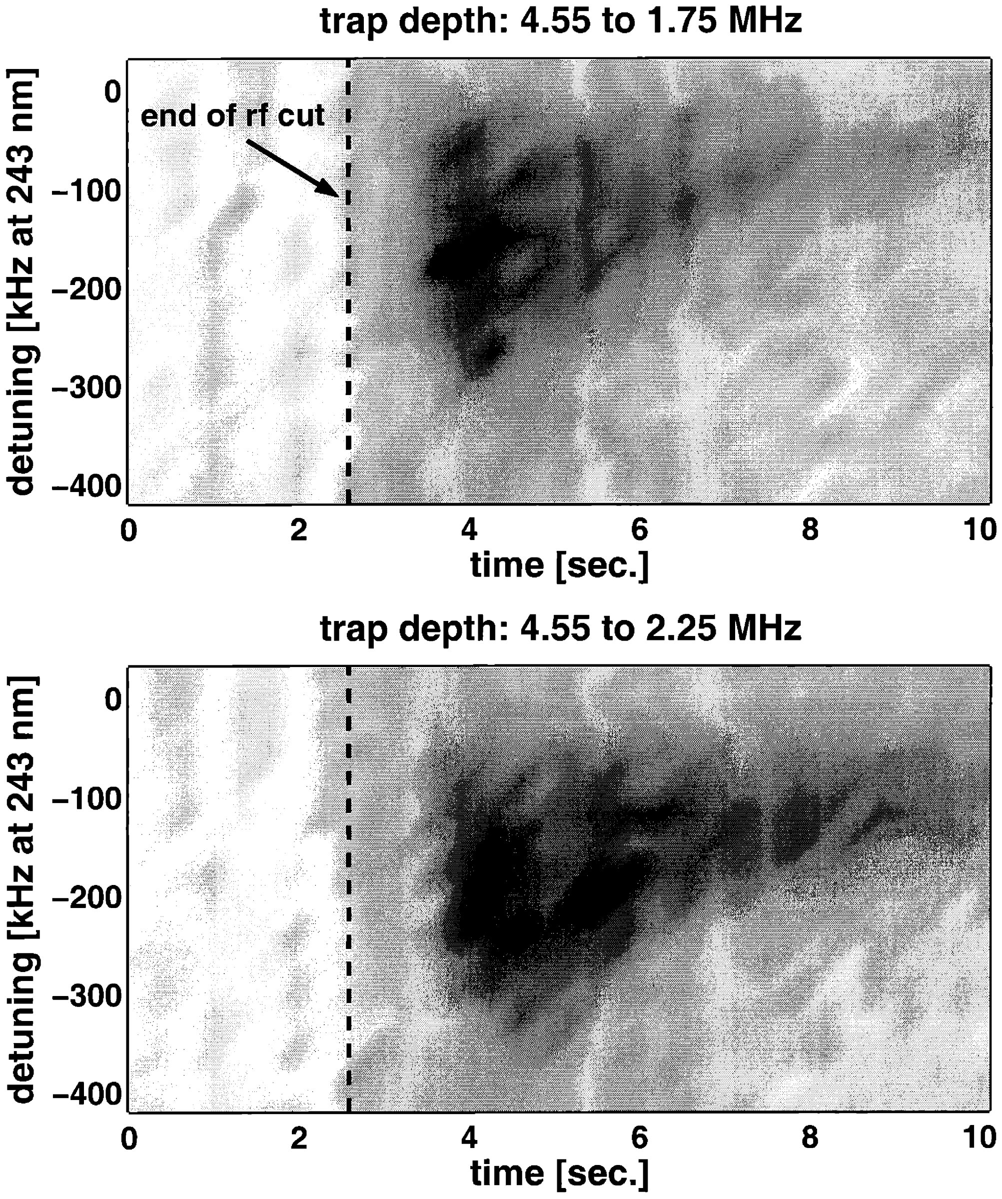

Figure 7-15: A visual impression of another rf cut experiment in which $\epsilon_{\rm rf}$ was varied. The end of the rf cut is denoted by the dashed vertical line. The dark regions indicate the strongest condensate signal, and the zero of detuning is the center of the Doppler-sensitive profile. At a final trap depth of 1.75(2) MHz (upper panel) the condensate forms about 0.5 s earlier than for 2.25(2) MHz, but this condensate is shorter lived because the number of noncondensed atoms available to replenish the condensate is diminished by the deeper cut.

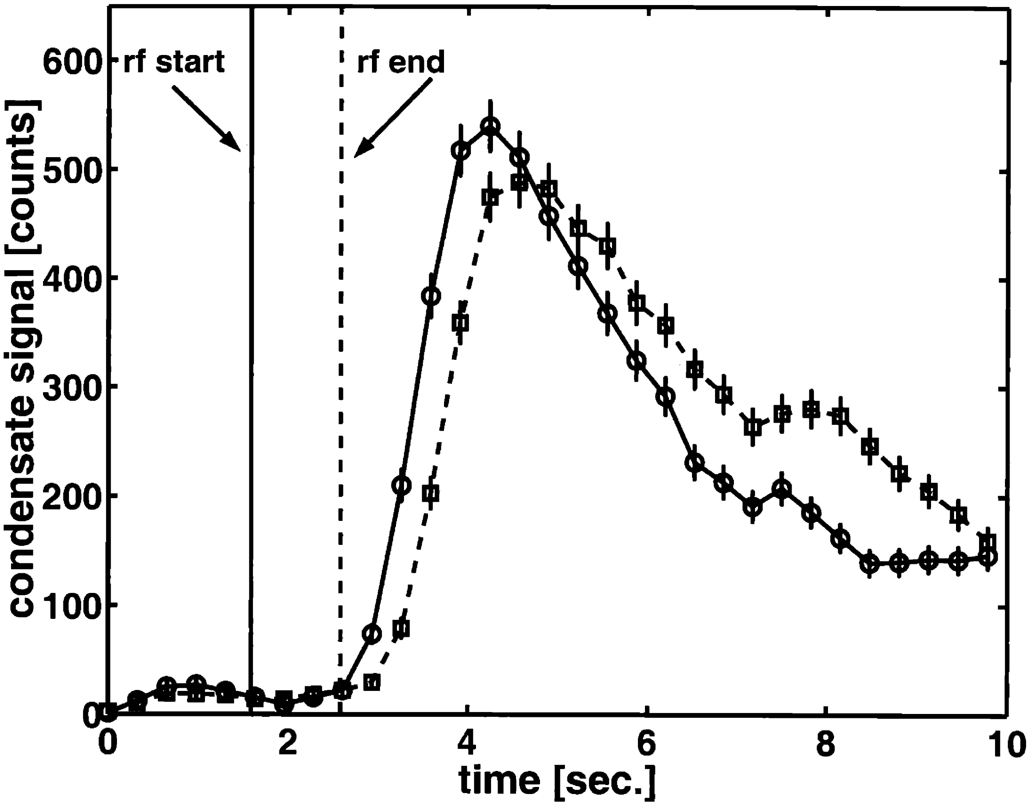

Figure 7-16: Time evolution of the condensate signal for the rf cut experiments shown in Fig. 7-15. For each time point the condensate signal was summed over frequency, and the Doppler-sensitive profile was subtracted. The resulting signal was smoothed and plotted as a function of time. The open circles (○) correspond to a change in trap depth from 4.55(2) MHz to 1.75(2) MHz in $t_{\rm rf} = 1$ s while the open boxes (□) correspond to a change from 4.55(2) MHz to 2.25(2) MHz in $t_{\rm rf} = 1$ s. The solid and dashed lines serve as guides to the eye.

density, n_{p}, as $N_{\mathrm{c}} \sim n_{\mathrm{p}}^{5/2}$. Thus, these condensates contain significantly more atoms than in the first rf cut experiment.

The total condensate signal versus time is shown in Fig. 7-16 for the second rf cut experiment. The signal due to the Doppler profile and fluorescence background has been subtracted. The open circles (○) represent the data from the deeper cut with a final trap depth of 1.75(2) MHz. The open boxes (□) represent the cut with a final trap depth of 2.25(2) MHz. In both cases, the data has been passed through a smoothing filter and lines connecting the points have been added as guides to the eye. The difference in onset time for the two cuts is less than a second with the deeper cut resulting in earlier formation. Similarly, the maximum amplitude of the signal is slightly greater following the deeper cut. In contrast to the earlier rf cut experiment shown in Fig. 7-12 the formation rates are very similar and the separation of the signal peaks is approximately equal to the difference in onset time. The difference is likely explained by comparing the relative trap depths in the two experiments. In the earlier experiment, the "deep cut" resulted in a trap depth 44% shallower than the "shallow cut." In this experiment the difference is only 22%. Thus, a significant difference in final trap depth results in a significant difference in condensate formation rate.

7.6.2 Varying the Starting Frequency of RF Cuts

To complement the experiments in which the end of the rf cut was varied, we performed rf cut experiments in which the ending rf frequency, ϵ_{rf}, was kept constant while the starting rf frequency, $\epsilon_{\mathrm{start}}$, was varied. This procedure allowed us to prepare the noncondensed sample at various points in phase space away from the Bose-Einstein transition and then truncate the thermal distribution with an rf cut, making the system unstable against condensate formation. The scheme for varying the trap depth is shown in Fig. 7-17. Three separate rf cuts were performed in Trap B with $\theta/h = 2.75(2)$ MHz, $\omega_\rho = 2\pi \times 1200$ Hz, and $\omega_z = 2\pi \times 10.3$ Hz. The ending frequency of rf evaporation took values of 8.1, 7.7, and 7.3 MHz. An rf cut of $t_{\mathrm{rf}} = 1$ s

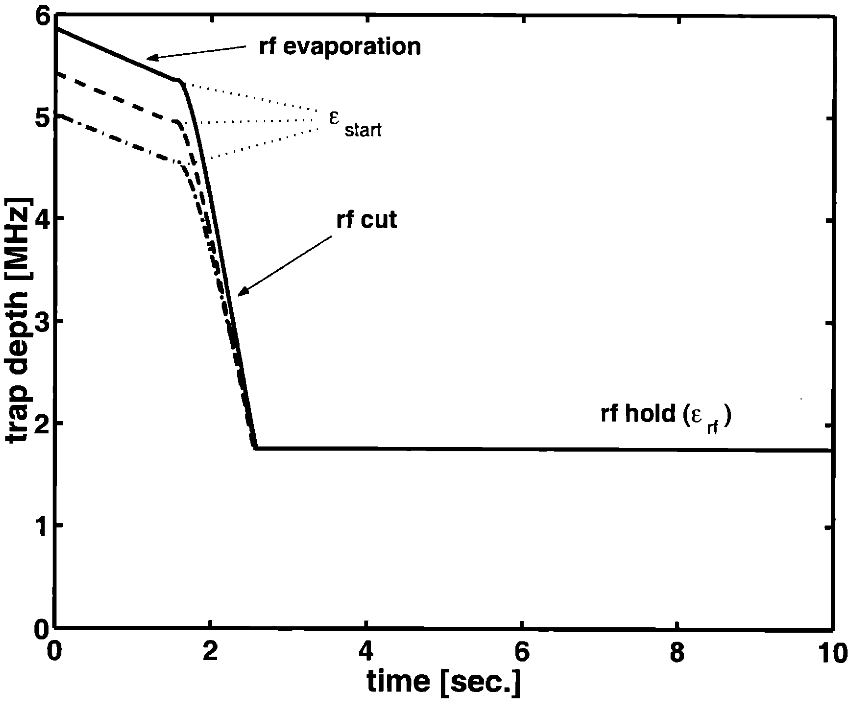

Figure 7-17: Trap depth versus time for experiments in which ϵ_{rf} is held constant and $\epsilon_{\mathrm{start}}$ is varied. By changing the frequency at which the rf cut begins, the noncondensed sample is prepared at various distances in phase space from the Bose-Einstein transition. After the rf cut the trap depth is held constant, and the condensate formation is monitored spectroscopically.

was carried out with an ending frequency of $\epsilon_{\text{rf}} = 4.5$ MHz. These cuts resulted in initial trap depths of 5.35(2) MHz (257 μK), 4.95(2) MHz (238 μK), and 4.55(2) MHz (218 μK); and a final trap depth of 1.75(2) MHz (84 μK).

The three panels of Fig. 7-18 contain images constructed from the experiments in which ϵ_{rf} was held constant and ϵ_{start} was varied. As before the dark regions indicate a strong signal due to the condensate. The end of the $t_{\text{rf}} = 1$ s rf cut is delineated by the vertical dashed line in each panel, and the zero of detuning is the center of the Doppler-sensitive profile. The initial trap depth is given above each panel, and the final trap depth is the same in each case: 1.75(2) MHz. The salient feature of these images is the relative delay between the end of the rf cut and the onset of condensate formation. The upper panel shows the sample that was prepared closest to the Bose-Einstein transition prior to the cut. Following the cut the sample cooled for less than a second before a condensate began to form. In contrast the sample shown in the lowest panel underwent significant cooling following the rf cut prior to the appearance of a condensate. The delay is understandable since this sample was prepared further from the transition in a deeper trap.

The physics underlying these experiments is similar to the rf cut experiments presented earlier in this chapter. For a condensate to form, a significant number of atoms need to be present in the lowest energy eigenstates of the trap. For the same magnetic trap and sample preparation procedure, a deeper trap will contain a warmer sample, and the warmer sample will contain fewer atoms in low energy states. Swift removal of atoms in the highest energy states, i.e. an rf cut, initiates a change in the energy distribution of the sample as it attempts to find an equilibrium temperature in the suddenly shallower trap. The larger the change in trap depth, the longer the time required for the sample to find its new equilibrium.

For a given trap the extent of the condensate signal in detuning indicates the maximum density of the condensate. The condensate signal in the upper panel of Fig. 7-18 extends slightly beyond -300 kHz. The signals in the other panels do not extend quite so far. Once the condensate appears there is little difference between

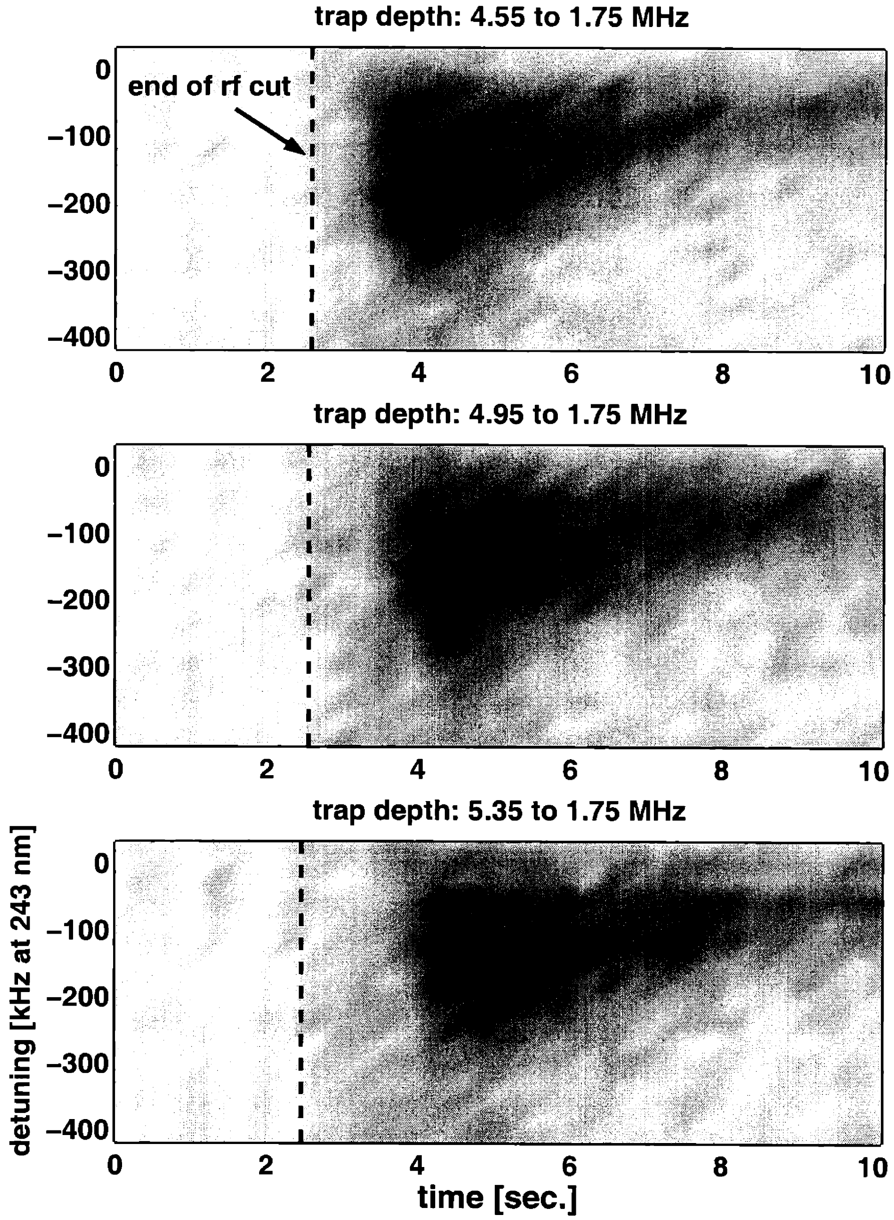

Figure 7-18: Visual impressions of condensate formation in which ϵ_{rf} is held constant and $\epsilon_{\mathrm{start}}$ is varied. In each panel the end of the $t_{\mathrm{rf}} = 1$ s cut is denoted by the vertical dashed line, and the zero of detuning is the center of the Doppler-sensitive profile. The dark regions indicate strong condensate signal. In the upper panel the noncondensed sample is prepared closest to the Bose-Einstein transition (at a trap depth of 4.55(2) MHz) and results in the earliest condensate formation. In the lowest panel the formation is delayed because additional cooling must take place to bring the sample to degeneracy. The overall signal is smaller because normal gas atoms were used for cooling rather than condensate formation.

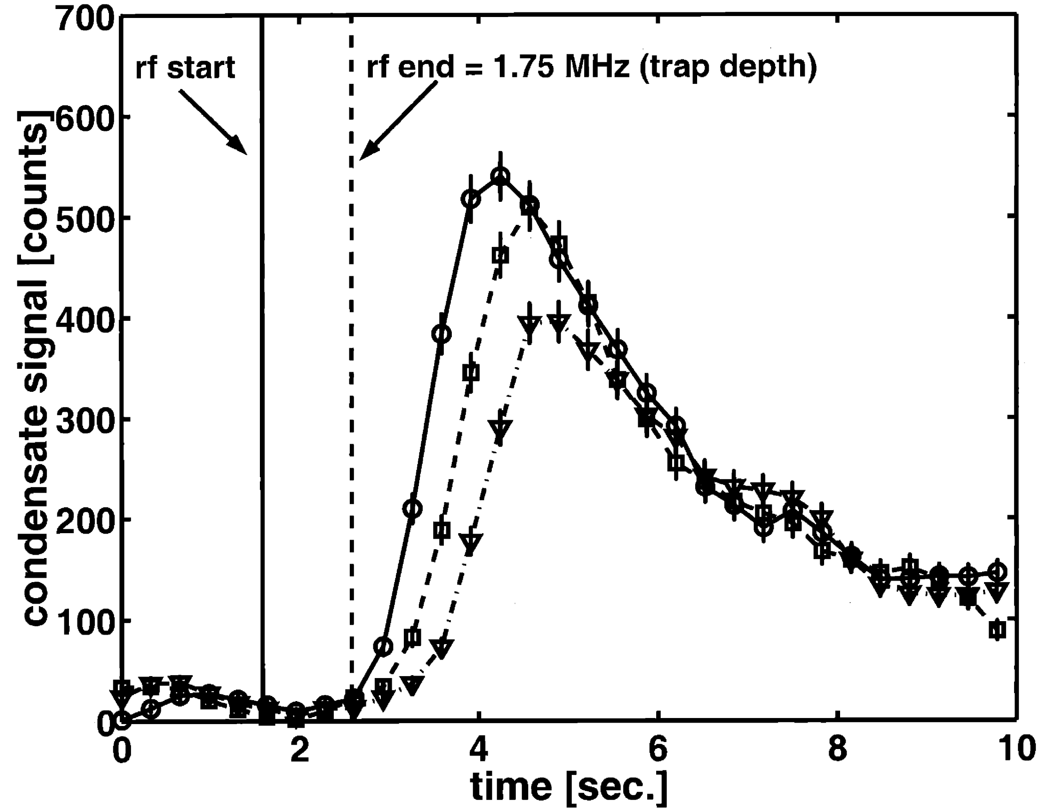

Figure 7-19: Time evolution of the condensate signal for experiments of Fig. 7-18 in which ϵ_{rf} is held constant and ϵ_{start} is varied. For each time point the condensate signal is summed over frequency and the Doppler profile subtracted. The resulting signal is passed through a smoothing filter and plotted versus time. The open circles ($\circ$) represent the sample with 4.55(2) MHz initial trap depth, the open boxes ($\square$) 4.95(2) MHz, and the open triangles ($\bigtriangledown$) 5.35(2) MHz. The sample prepared closest to degeneracy ($\circ$) results in the largest and earliest condensate. The sample prepared furthest from the Bose-Einstein transition ($\bigtriangledown$) cools significantly following the rf cut and results in a smaller, delayed condensate. An intermediate case is given by the open boxes ($\square$). Interestingly, after about 6 s the signals are indistinguishable, indicating that a dynamic equilibrium has been reached between the normal gas and condensate at this particular trap depth, 1.75(2) MHz. The lines connecting the data points serve as guides to the eye.

the three panels. After $t = 6$ s the signal appears to have similar extent and intensity in each experiment. In contrast to the experiments in which ϵ_{rf} was varied, the final trap depth in each of these experiments is identical, suggesting that after the initial transient caused by the rf cut the system finds an equilibrium size for the condensate. This idea is strengthened by the time evolution of the total condensate signal shown in Fig. 7-19.

Figure 7-19 presents the total condensate signal versus time after the counts due to the Doppler profile and background fluorescence have been removed. The data was passed through a smoothing filter, and lines connecting the data points were added as guides to the eye. This plot makes the different condensate sizes apparent in the amplitudes of the three signals. Intuitively it is sensible that the sample prepared closest to the transition results in the earliest and largest condensate. After $t = 6$ s, however, the three signals become indistinguishable. The history of how early the condensate formed or how large it became seems to be unimportant. Most likely the system finds a new equilibrium for a particular condensate size and trap depth. Once this equilibrium is found, the system can evolve in only one way.

Temperature prior to the rf cut

To characterize the trapped sample prior to the rf cut, the Doppler-sensitive (DS) profile was recorded. Recall from Sec. 5.5.2 that the rms width of the DS spectrum far from degeneracy is proportional to the square root of the sample temperature, $\Delta\nu = 0.374 \times 10^9 \sqrt{T}$ Hz K$^{-1/2}$. Figure 7-20 shows the DS spectrum immediately before the rf cut at a trap depth of 5.35(2) MHz (257 μK). In this plot the zero of detuning is the unshifted $1S$-$2S$ resonance, so that the 6.7 MHz recoil shift is apparent. The spectrum is fit with a Gaussian, yielding a Maxwell-Boltzmann temperature of 24.0 ± 1.6 μK. If this were the true temperature, the ratio of trap depth to temperature would be $\eta = 257/24 = 10.7(7)$. Referring to Fig. 3-6 and [31] we expect $\eta < 7$ for a sample following rf evaporation. The discrepancy can be traced to the statistics that the trapped sample obeys near degeneracy. Close to degeneracy the Maxwell-

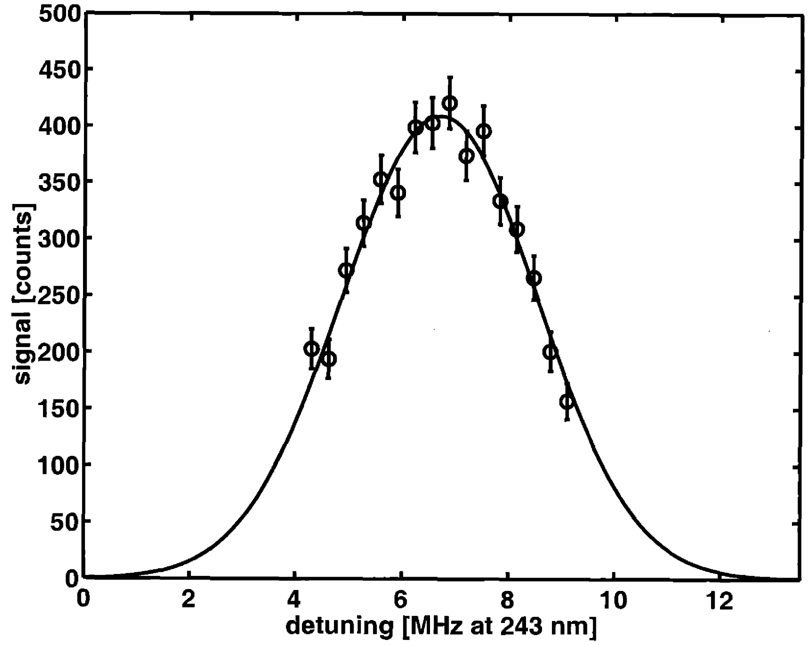

Figure 7-20: Doppler sensitive spectrum of the trapped sample at a trap depth of 5.35(2) MHz (257 μK). The solid curve is a Gaussian fit to the data, which indicates a temperature of 24.0 ± 1.6 μK when assuming a Maxwell-Boltzmann distribution.

Boltzmann fit derived from classical statistics is no longer correct. Bosons are better described by the Bose-Einstein distribution, which allows additional particles at low energies compared to its classical counterpart. The result is a narrower spectrum for a given temperature. A Maxwell-Boltzmann temperature of 24 μK corresponds to a Bose-Einstein temperature of 28 μK (see Sec. 9.1 for details of the Bose-Einstein fitting procedure). This temperature implies $\eta = 9.2$.

Multiple rf cut experiments varying ϵ_{start}

To strengthen our intuition about the formation process under variations of ϵ_{start}, additional experiments were performed with a wider range of ϵ_{start} and a constant ϵ_{rf}. The total condensate signal resulting from eleven different values of ϵ_{start} is shown in Fig. 7-21. The signals represent the sum of the number of counts recorded in the Doppler-sensitive spectrum at eight different detunings. The individual signals are offset by 200 counts for clarity, and the narrow horizontal lines provide the respective baselines. In each experiment rf evaporation was carried out until the specified trap depth was reached. A $t_{\text{rf}} = 1$ s rf cut was immediately performed, resulting in a final trap depth of 1.75(2) MHz. The beginning and end of the rf cut are indicated by the solid and dashed lines, respectively. The trap depths prior to the rf cut ranged from 5.35(2) to 2.75(2) MHz, leading to differences in the time evolution of the condensate signal.

The four signals near the top of Fig. 7-21 display behavior we have already described: the sample is evaporated to a point just above the Bose-Einstein transition, and the rf cut suddenly removes the most energetic atoms, resulting in the formation of a condensate. In each case, we speculate that the rf cut is necessary to form a condensate. In the four signals at the bottom of Fig. 7-21 the opposite situation occurs; the condensate formed prior to the rf cut. The main effect of the rf cut is to help sustain or even rejuvenate the condensate. Take for example the signal with a starting trap depth of 3.15 MHz. The condensate signal appears to have reached its maximum prior to the rf cut, but the cut sustains the amplitude of the conden-

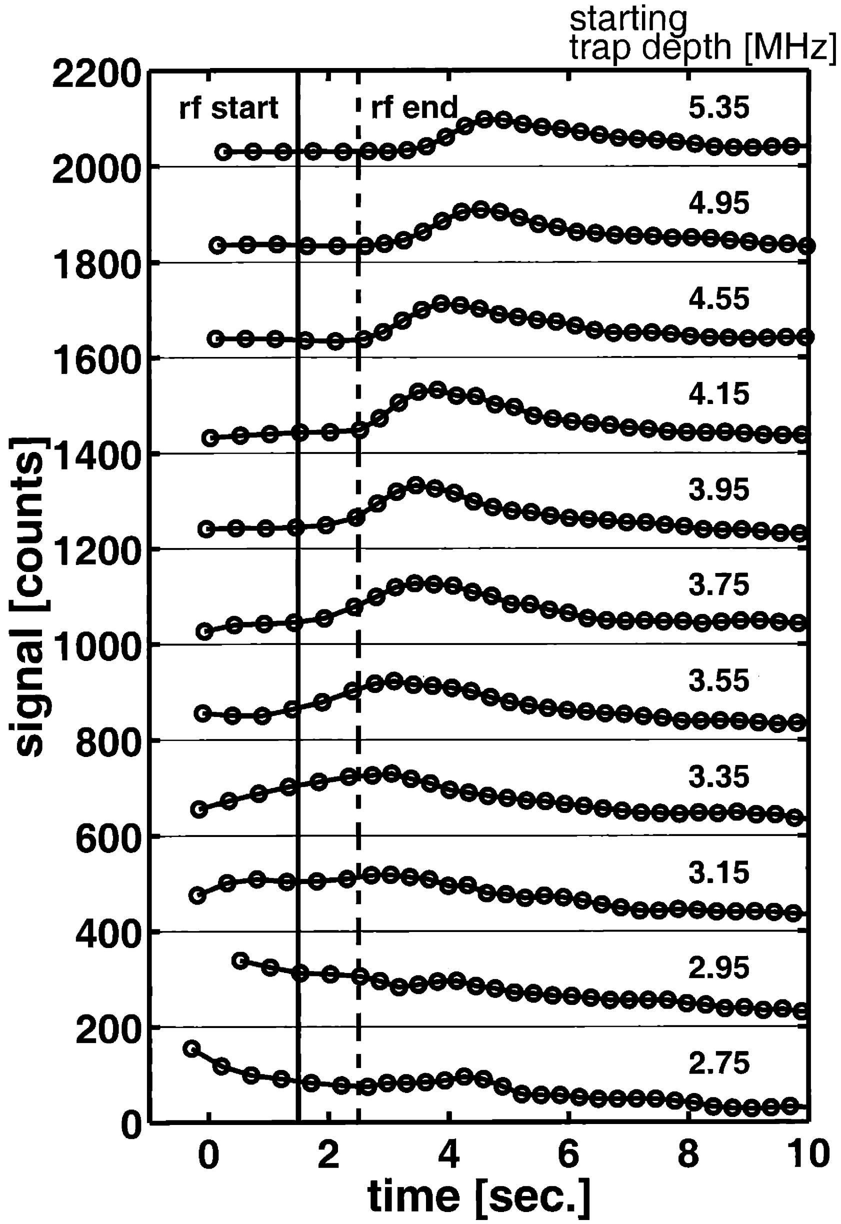

Figure 7-21: Time evolution of the condensate signal for multiple values of ϵ_{start} and constant ϵ_{rf}. The trap depth prior to a $t_{\text{rf}} = 1$ s rf cut was varied. The resulting condensate signal without the Doppler profile subtracted was smoothed using a moving average filter and is shown versus time. The traces have been offset by 200 counts for clarity. The end of the $t_{\text{rf}} = 1$ s rf cut is denoted by the vertical dashed line, and the solid lines connecting the data points serve as guides to the eye.

sate for a few seconds before the signal begins to diminish. This is in contrast to the condensates with larger starting trap depths where the maximum amplitude is immediately followed by a steady decrease in amplitude. The smallest starting trap depth, 2.75 MHz, exhibits a different behavior. The condensate is well into its decay phase when the rf cut begins. The signal amplitude stops decreasing and regains strength. In all four cases where the decrease of the condensate signal is slowed or stopped, the rf cut can be viewed as a type of evaporation that helps to sustain the population of low energy, noncondensed atoms ready to scatter into the condensate. Without this continued forced evaporation, the sample warms due to the large dipolar spin-relaxation losses taking place in the condensate and normal gas.

The remaining three signals in Fig. 7-21 represent an intermediate case in which the condensate formation process has just begun, and the rf cut accelerates formation. For example the signal with a starting trap depth of 3.75 MHz appears to be growing slowly prior to the cut. The rf evaporation alone is barely adequate to produce a condensate, but the rf cut forces the issue leading to a large condensate.

To gain further insight into the experiments of Fig. 7-21, we extracted quantities relevant to the formation process: the maximum amplitude of the condensate signal, the time at which the maximum occurs, and the time-integrated number of condensate counts observed. These quantities are presented as a function of starting trap depth in Fig. 7-22. The upper panel shows that the maximum condensate signal is observed when the sample is cooled to degeneracy without an rf cut. This makes sense because rf evaporation is a more efficient way to increase the phase space density of the sample; an rf cut is wasteful of atom number. The plot also shows that an rf cut occurring just as condensate formation begins can be helpful in obtaining a larger condensate than would otherwise occur, e.g. starting trap depths in the range 3.55 – 4.15 MHz.

The middle panel of Fig. 7-22 shows the time at which the maximum amplitude of the signal occurred. At the two smallest starting trap depths, the early time of the peak indicates that the condensate formed prior to the rf cut. The other points confirm our intuition that the further from degeneracy in phase space the sample

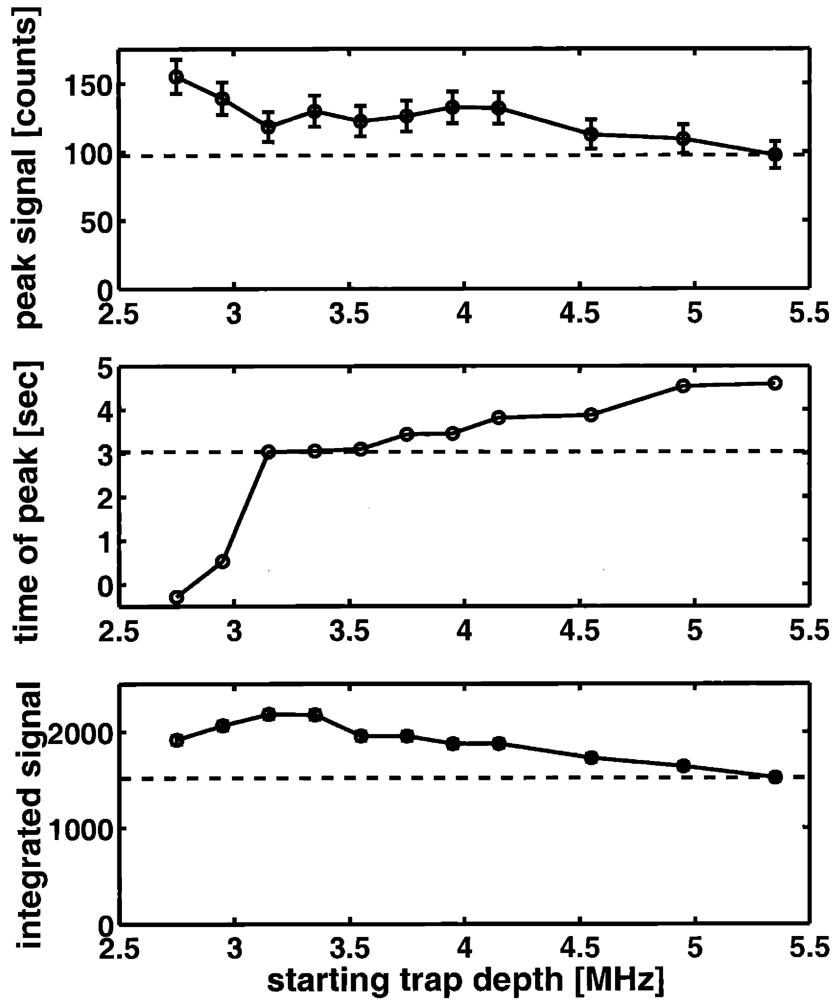

Figure 7-22: Summary of key statistics extracted from data presented in Fig. 7-21. The upper panel shows the peak condensate signal plotted versus starting trap depth. The middle panel plots the time the peak signal occurs for each starting trap depth, and the lowest panel indicates the number of condensate signal counts recorded over the 10 s interval shown in Fig. 7-21. Together this information can be used to optimize the condensate signal for size and/or duration.

starts, i.e. the larger the starting trap depth, the longer it takes to form a condensate. Finally, the lower panel presents the time-integrated condensate signal. The peak of this curve occurs at a starting trap depth of 3.15 MHz, indicating that the strategy to produce the maximum number of condensate counts over time is to evaporate the sample to degeneracy and then perform an rf cut. This strategy produces a large number of condensate counts because the rf cut causes an additional evaporation that compensates the heating (dipolar spin-relaxation) due to the presence of a condensate by evaporative cooling. Together the information contained in this plot can be used to optimize the size of the condensate or the number of condensate atoms produced over time.

7.6.3 Varying the Duration of the RF Cuts

For a given magnetic trap configuration, the rf cut experiments are characterized by three parameters: ϵ_{start} (the starting frequency of the cut), ϵ_{rf} (the ending frequency of the cut), and t_{rf} (the duration of the cut). We have presented experiments in which ϵ_{start} and ϵ_{rf} were varied. We conclude this chapter by describing experiments in which t_{rf} was varied.

Five rf cut experiments were performed in Trap A, and the resulting condensate signal was recorded at eight separate detunings in the Doppler-free portion of the spectrum. The oscillation frequencies for this trap were $\omega_\rho = 2\pi \times 1860$ Hz and $\omega_z = 2\pi \times 10.3$ Hz, leading to a geometric mean oscillator frequency of $\bar{\omega}/2\pi = 329$ Hz. The trap bottom was measured to be 3.21(2) MHz (154 μK). The sample was prepared at the threshold of degeneracy with $\epsilon_{\text{start}} = 6.75$ MHz. An rf cut was then carried out to $\epsilon_{\text{rf}} = 4.4$ MHz. The total number of counts recorded as a function of time for each of these experiments is shown in Fig. 7-23. The background fluorescence has been subtracted from the signals. The maximum signal amplitude is similar in each case and occurs at roughly the same time, indicating that the rf cut had little effect on the maximum size of the condensate. The rf cut has a profound effect on the duration of the condensate signal, however. A longer t_{rf} leads to a longer-lived condensate,

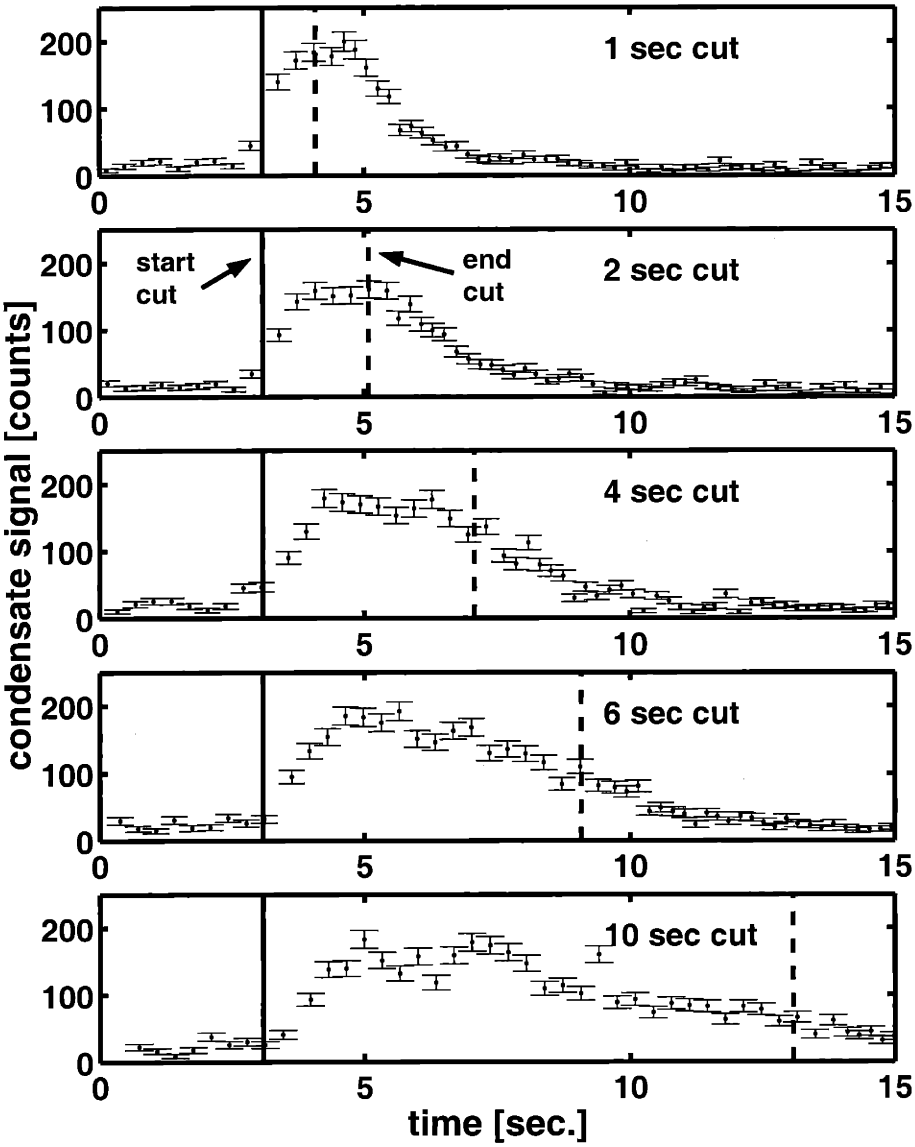

Figure 7-23: Time evolution of the condensate signal for various t_{rf}. For a given $\epsilon_{\mathrm{start}}$ and ϵ_{rf}, t_{rf} took five different values: 1 s, 2 s, 4 s, 6 s, and 10 s. The 1 s cut resulted in the fastest formation, the largest signal, but the shortest duration. In contrast, the 10 s cut resembles a continuation of rf evaporation – a smaller, delayed formation, but the longest-lived condensate. This data was taken in the Doppler-free portion of the spectrum.

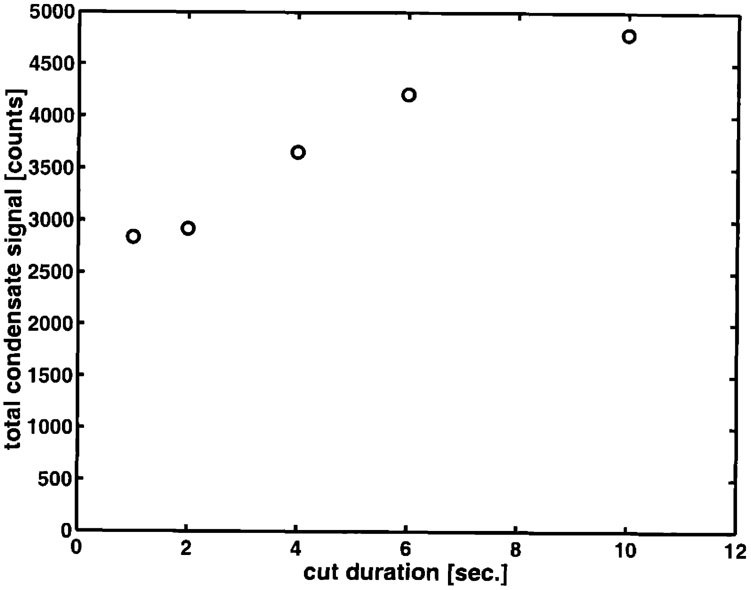

Figure 7-24: Time-integrated condensate signal versus rf cut duration. The total number of condensate counts recorded over the 15 s shown in Fig. 7-23 is plotted versus t_{rf}. As t_{rf} increases the total signal increases, reaching a plateau and indicating that the longer rf cuts resemble a continuation of the evaporation process rather than an abrupt change in trap depth.

confirming our intuition that a longer rf cut behaves less as a sudden removal of the normal gas and more as a continued forced evaporation. The time-integrated number of counts for each t_{rf} is shown in Fig. 7-24. A plateau is reached for long t_{rf} since the lifespan of the condensate is ultimately limited by the number of atoms available, not the duration of the forced evaporation.

Chapter 8

Theory of Condensate Growth in Trapped Atomic Hydrogen

A detailed theory of condensate growth and decay in trapped Bose gases is presented in this chapter in order to interpret the condensate formation experiments presented in this thesis. Early approaches to the problem of condensate growth are described in Sec. 8.1. These approaches culminated in the models of Davis, Gardiner, and Ballagh [22] and Bijlsma, Zaremba, and Stoof [7]. While quite sophisticated, these models consider only processes that contribute to the growth of the condensate. In the hydrogen system loss processes must also be considered.

In Sec. 8.2 the model previously developed by Bijlsma, Zaremba, and Stoof to describe condensate growth in a gas of atomic sodium is recapitulated. The model involves a number of complicated, linked equations. More detailed derivations, descriptions, and motivations for terms in the equations have been added. Section 8.3 describes how this theory is modified to include experimental forced evaporative cooling and the decay of the gas due to dipolar spin relaxation. The modifications presented in this section result from our collaboration with Professor Henk Stoof.[1] A detailed study of the model is made in Sec. 8.4.

---

[1] Institute for Theoretical Physics, University of Utrecht, The Netherlands

8.1 Early Theories of Condensate Growth

The problem of condensate growth in a trapped Bose gas is complicated because a theoretical analysis requires a nonequilibrium approach to the coupled dynamics of the condensed and noncondensed components of the trapped Bose gas. In particular, the theoretical description should include collisional processes that transfer atoms between the two components and loss processes that remove atoms from the trapped cloud. Several theoretical treatments have been developed and fall roughly into two categories. One class of theories describes the average value of the order parameter for BEC (the condensate wavefunction), while the other class also considers fluctuations around the mean value. Near the critical temperature for the system, inclusion of the fluctuations becomes important since the fluctuations can be large compared to the mean value.

Theories that describe both the average value of the order parameter and fluctuations have been obtained in two ways. In a series of papers, Gardiner and Zoller [36] started from a master equation for the many-body density matrix and derived an equation of motion for the one-particle density matrix by means of a perturbative treatment of the interactions. An alternative formulation was developed by Stoof [116, 117] in which field-theoretic methods were used to obtain a Fokker-Planck equation that describes the nonequilibrium dynamics of the gas. In principle, both of these approaches yield a description of the nonequilibrium dynamics that is capable of obtaining the complete probability distribution for the order parameter.

An alternative mean-field approach to the problem has been put forth by Kirkpatrick and Dorfmann [69, 68]. In their approach, one assumes that the order parameter is nonzero at all temperatures and then decouples the hierarchy of equations of motion that exist for the correlation functions of the second-quantized field operators. This again yields a perturbative expansion for the equations of motion. Numerous authors have elaborated on this approach: Proukakis *et al.* [97, 98], Walser *et al.* [130], and in the most detail for the trapped case, Zaremba, Nikuni, and Griffin [136].

The earliest quantitative calculations of condensate growth in trapped Bose gases were carried out by Gardiner *et al.* [35, 37]. In [37] an idealized case was treated by considering the growth of a condensate from a nondepletable "bath" of atoms at a fixed positive chemical potential μ and temperature T. From this treatment came a simple equation for condensate growth

$$\dot{n}_0 = 2W^+(n_0)\left\{\left(1 - e^{[\mu_C(n_0)-\mu]/k_BT}\right)n_0 + 1\right\}, \tag{8.1}$$

where n_0 is the population of the condensate, μ is the chemical potential of the thermal cloud, and $\mu_C(n_0)$ is the chemical potential of the condensate. The factor $W^+(n_0)$ is a rate describing the scattering of particles into the condensate. Its value was approximated in [37] using a classical Boltzmann distribution. The simple equation for condensate growth agreed qualitatively with condensate growth experiments in ^{23}Na [83], but there were a number of discrepancies. The observed experimental growth rates were up to 30 times larger than predicted, and the temperature dependence was opposite to that predicted. In [35] these discrepancies were addressed by removing some of the simplifying assumptions. The theoretical results improved but quantitative discrepancies remained.

The origin of the discrepancies can be partially attributed to two approximations in the calculations. The first was to largely neglect the kinetics of the noncondensate. The simulations included the time evolution of the population of low-lying states, but the higher energy states were treated by an equilibrium particle reservoir having a fixed chemical potential. This assumption is incompatible with the nonequilibrium initial state prepared by the rf cut procedure. We will see later in this chapter the explicit violation of this equilibrium assumption. The second approximation involves the effect of the mean field of the condensate on the noncondensate. This was included somewhat crudely by a linear rescaling of the low-energy density of states of the noncondensed atoms.

To improve the agreement between theory and experiment, two groups (Davis *et* *al.* [22] and Bijlsma *et al.* [7]) independently extended the earlier models of condensate growth to include the relaxational dynamics of the noncondensed component that takes place in the presence of the mean field of the condensate. Their approaches were based on similar though not identical methodologies. The results have been independently computed and are in quantitative agreement with each other [7, 22], yet neither set of calculations is able to reproduce the experimental results in every detail. In general there is good agreement between the two models and experiment [83], but situations remain where certain parameters in the models must take experimentally unacceptable values in order to fit the data.

8.2 Basic Ingredients

In this section we review the basic ingredients in the theory of condensate growth of Bijlsma *et al.* [7]. The purpose is to identify and describe the physical processes that enter into the problem of condensate growth. Although this section follows closely the work of Bijlsma [7], many descriptions and derivations have been amplified for additional clarity.

The coupled dynamics of the condensed and noncondensed portions of the trapped gas are described by a quantum Boltzmann equation for the phase-space distribution function $f(\mathbf{r}, \mathbf{p}, t)$ of the thermal cloud, and a nonlinear Schrödinger equation for the condensate wavefunction $\Psi(\mathbf{r}, t)$. This coupled set of equations is difficult to deal with, and a number of physically motivated assumptions are made to simplify the problem. The condensate is assumed to grow adiabatically, having an equilibrium thermal distribution determined by the instantaneous number of atoms in the condensate. This assumption was also made in [37] and [35]. The noncondensed component is treated by solving a semiclassical Boltzmann equation [27, 69, 68, 116, 117, 136] using the ergodic assumption [52, 56, 79, 112]. Under these assumptions, one can numerically obtain a detailed description of the growth of the condensate, including the dynamics of the noncondensed component and its mean-field interaction with the condensate.

8.2.1 Coherent and Incoherent Collisions

The equations describing the nonequilibrium dynamics of a trapped Bose gas contain the coherent dynamics of the gas due to mean-field interactions as well as the incoherent dynamics associated with atomic collisions. We start by describing the equation governing the noncondensate.

The kinetic equation

The phase-space distribution function $f(\mathbf{r},\mathbf{p},t)$ of the noncondensate is treated using a semiclassical Boltzmann equation. This treatment is justified when the largest trap level spacing $\hbar\omega$ is small compared to the thermal energy k_BT. The mean-field effects are treated in the Hartree-Fock approximation, which is justified near the critical temperature. The kinetic equation for the noncondensed atoms is [55]

$$\begin{aligned}\left\{\frac{\partial}{\partial t}+\frac{\mathbf{p}}{m}\cdot\boldsymbol{\nabla}-\boldsymbol{\nabla}U(\mathbf{r},t)\cdot\boldsymbol{\nabla}_{\mathbf{p}}\right\}f(\mathbf{r},\mathbf{p},t)&\\ =C_{12}[f,n_{\mathrm{c}}]+C_{22}[f]\ .&\end{aligned}\tag{8.2}$$

In Eq. (8.2), the second term on the left is the position space "streaming term" representing the flow (recognizing $\mathbf{p}/m=\mathbf{v}$ as the velocity) of particles out of the infinitesimal phase space volume element $\Delta V=\Delta\mathbf{p}\Delta\mathbf{r}$. The third term on the left is the momentum space streaming term due to the external field (recognizing $-\nabla U=\mathbf{F}$ as the force), where $U(\mathbf{r},t)=U_{\mathrm{ext}}(\mathbf{r},t)+2T^{2\mathrm{B}}[n_{\mathrm{c}}(\mathbf{r},t)+n'(\mathbf{r},t)]$ is the effective potential for the atoms. The effective potential consists of the sum of the external trapping potential $U_{\mathrm{ext}}(\mathbf{r},t)$ and the Hartree-Fock mean-field energy. The mean-field energy is determined by the condensate density $n_{\mathrm{c}}(\mathbf{r},t)=|\Psi(\mathbf{r},t)|^2$, the density of the thermal cloud

$$n'(\mathbf{r},t)=\int\frac{d\mathbf{p}}{(2\pi\hbar)^3}\,f(\mathbf{r},\mathbf{p},t)\ ,\tag{8.3}$$

and the two-body T-matrix $T^{2\mathrm{B}} = 4\pi a\hbar^2/m$. The s-wave approximation allows the mean-field interaction to be expressed solely in terms of the scattering length a. Finally, $C_{12}[f, n_\mathrm{c}]$ and $C_{22}[f]$ denote the Uehling-Uhlenbeck collision integrals with a cross-section $8\pi a^2$ that describes the rate of change of the distribution function due to elastic collisions.

Collision integrals

The first collision integral $C_{12}[f, n_\mathrm{c}]$ appearing on the right-hand side of Eq. (8.2) involves the collision of a condensate particle and a noncondensate particle. It is given by

$$\begin{aligned}
C_{12}[f, n_\mathrm{c}] \;\equiv\;& \frac{4\pi}{\hbar}(T^{2\mathrm{B}})^2\, n_\mathrm{c} \int \frac{d\mathbf{p}_2}{(2\pi\hbar)^3} \int \frac{d\mathbf{p}_3}{(2\pi\hbar)^3} \int \frac{d\mathbf{p}_4}{(2\pi\hbar)^3} \\
& \times (2\pi\hbar)^3\, \delta(m\mathbf{v}_\mathrm{c} + \mathbf{p}_2 - \mathbf{p}_3 - \mathbf{p}_4)\, \delta(E_\mathrm{c} + E_2 - E_3 - E_4) \\
& \times (2\pi\hbar)^3\, [\delta(\mathbf{p} - \mathbf{p}_2) - \delta(\mathbf{p} - \mathbf{p}_3) - \delta(\mathbf{p} - \mathbf{p}_4)] \\
& \times [(1 + f_2) f_3 f_4 - f_2(1 + f_3)(1 + f_4)]\,, \qquad (8.4)
\end{aligned}$$

where $f \equiv f(\mathbf{r}, \mathbf{p}, t)$ and $f_i \equiv f(\mathbf{r}, \mathbf{p}_i, t)$. The right-hand side of Eq. (8.4) is slightly different from the usual collision integral. The first delta function guarantees conservation of momentum while the second guarantees conservation of energy. The third term involving the difference of delta functions restricts the momentum integrals to collisions affecting the condensate explicitly. For example, $\delta(\mathbf{p} - \mathbf{p}_2)$ describes collisions in which a particle with initial momentum $\mathbf{p}_2$ scatters *into* the condensate, while $\delta(\mathbf{p} - \mathbf{p}_3)$ describes collisions in which a particle in the condensate with momentum $\mathbf{p}$ scatters *out of* the condensate with a final momentum $\mathbf{p}_3$.

The final term in Eq. (8.4) involving distribution functions has a subtlety. There is no distribution function f for the noncondensate since Eq. (8.4) considers only the change of the number of particles in a specific state, the condensate. The first term, $(1+f_2)f_3f_4$, is a gain term and describes particles with momenta $\mathbf{p}_3$ and $\mathbf{p}_4$ scattering into the condensate and a final state with momentum $\mathbf{p}_2$. The second term, $-f_2(1+$

$f_3)(1+f_4)$, is a loss term and represents a condensate particle and a noncondensate particle with momentum $\mathbf{p}_2$ scattering into noncondensate states with momenta $\mathbf{p}_3$ and $\mathbf{p}_4$. Since the particles are bosons there is an enhancement of scattering into the final states represented by terms $(1+f_i)$. This enhancement is known as *bosonic stimulation* and is enormously important for understanding the time scale on which a condensate forms. Intuitively, bosonic stimulation encourages scattering into final states that are already occupied, i.e. the population of the condensate grows slowly at first but once atoms begin to accumulate in the ground state of the system, scattering of particles into the condensate is greatly preferred over scattering into any other energy level.

The energy of a condensate atom in Eq. (8.4) is given by

$$E_{\mathrm{c}}(\mathbf{r},t) = \mu_{\mathrm{c}}(\mathbf{r},t) + \frac{1}{2}m\mathbf{v}_{\mathrm{c}}^2(\mathbf{r},t) \ , \tag{8.5}$$

where $\mu_{\mathrm{c}}(\mathbf{r},t)$ is the chemical potential and $m\mathbf{v}_{\mathrm{c}}(\mathbf{r},t)$ is the momentum. In contrast the energy of a noncondensate atom is

$$E(\mathbf{r},\mathbf{p},t) = \frac{\mathbf{p}^2}{2m} + U(\mathbf{r},t) \ . \tag{8.6}$$

The collision term involving noncondensate particles is given by

$$\begin{aligned} C_{22}[f] \ \equiv \ & \frac{4\pi}{\hbar}(T^{2\mathrm{B}})^2 \int \frac{d\mathbf{p}_2}{(2\pi\hbar)^3} \int \frac{d\mathbf{p}_3}{(2\pi\hbar)^3} \int \frac{d\mathbf{p}_4}{(2\pi\hbar)^3} \\ & \times (2\pi\hbar)^3\, \delta(\mathbf{p}+\mathbf{p}_2-\mathbf{p}_3-\mathbf{p}_4)\, \delta(E+E_2-E_3-E_4) \\ & \times [(1+f)(1+f_2)f_3f_4 - ff_2(1+f_3)(1+f_4)] \, , \end{aligned} \tag{8.7}$$

and can be understood in a way analogous to Eq. (8.4).

The effects of the condensate

A nonzero condensate density affects the kinetic equation Eq. (8.2) in two physically distinct ways. First, the coherent interaction with the condensate results in a shift of

$2T^{2\mathrm{B}}n_{\mathrm{c}}(\mathbf{r},t)$ in the local energies of the noncondensed atoms. Second, the presence of the condensate leads to an additional collision integral because the condensate acts as a particle reservoir for the thermal cloud with which atoms can be exchanged due to incoherent collisions. As a result the kinetic equation must be solved simultaneously with the complex nonlinear Schrödinger equation for the condensate wave function

$$i\hbar\frac{\partial\Psi(\mathbf{r},t)}{\partial t} = \left\{-\frac{\hbar^2\boldsymbol{\nabla}^2}{2m} + U(\mathbf{r},t) - T^{2\mathrm{B}}n_{\mathrm{c}}(\mathbf{r},t) - iR(\mathbf{r},t)\right\}\Psi(\mathbf{r},t)\ . \tag{8.8}$$

This equation is identical to Eq. (2.22) except for the addition of the dissipative term which is proportional to

$$R(\mathbf{r},t) = \frac{\hbar}{2n_{\mathrm{c}}(\mathbf{r},t)}\int\frac{d\mathbf{p}}{(2\pi\hbar)^3}\ C_{12}[f,n_{\mathrm{c}}]\ , \tag{8.9}$$

and describes the average rate of change of the condensate density due to elastic collisions which transfer atoms between the condensate and the thermal cloud. Note that the presence of the thermal cloud has both coherent and incoherent effects on the condensate dynamics and that the dissipative term is necessary to ensure overall particle number conservation of the entire system.

Simplifications

Although Eqs. (8.2) and (8.8) give a complete mean-field description of condensate growth, a full numerical solution of these equations is quite involved. Therefore, Bijlsma, Zaremba and Stoof introduced some physically motivated approximations. First, the mean-field effects of the thermal cloud are neglected. This is an excellent approximation under experimental conditions and implies that the effective potential for the noncondensed atoms is just $U(\mathbf{r},t) = U_{\mathrm{ext}}(\mathbf{r},t) + 2T^{2\mathrm{B}}n_{\mathrm{c}}(\mathbf{r},t)$. Using the Thomas-Fermi approximation [19] and assuming an adiabatic growth of the condensate, the nonlinear Schrödinger equation for $\Psi(\mathbf{r},t)$ is then simply solved by

$$n_c(\mathbf{r},t) = \frac{1}{T^{2B}}[\mu_c(t) - U_{\text{ext}}(\mathbf{r},t)], \tag{8.10}$$

which is identical to Eq. (2.25). For a general anisotropic harmonic potential, $U_{\text{ext}}(\mathbf{r},t) = \sum_i m\omega_i^2 r_i^2/2$, the chemical potential of the condensate is

$$\mu_c(t) = \frac{\hbar\bar{\omega}}{2}\left[15N_c(t)\frac{a}{\ell}\right]^{2/5} \tag{8.11}$$

with $\bar{\omega} = (\omega_1\omega_2\omega_3)^{1/3}$ the effective isotropic trapping frequency, and $\ell = (\hbar/m\bar{\omega})^{1/2}$ is the corresponding harmonic oscillator length. In addition, $N_c(t)$ denotes the total number of atoms in the condensate, which from Eq. (8.9) is seen to obey

$$\frac{dN_c(t)}{dt} = -\int d\mathbf{r}\int \frac{d\mathbf{p}}{(2\pi\hbar)^3}\, C_{12}[f, n_c]\ . \tag{8.12}$$

The ergodic approximation

To make the solution of the quantum Boltzmann equation more tractable, we make the ergodic approximation, which implies that the phase-space distribution function does not depend on $\mathbf{r}$ and $\mathbf{p}$ separately, but only on the combination $E(\mathbf{r},\mathbf{p},t) \equiv \mathbf{p}^2/2m + U(\mathbf{r},t)$, i.e., $f(\mathbf{r},\mathbf{p},t) = g(E(\mathbf{r},\mathbf{p},t),t)$. This approximation assumes that the equilibration of atoms within one energy level occurs on a much shorter time scale than equilibration of atoms between different energy levels. Thus, all points in phase space having the same energy are equally probable. The ergodic approximation has been widely used in the literature on kinetic theory [52, 56, 79, 112].

A simplified kinetic equation for the energy distribution function $g(\epsilon,t)$ may be derived under the ergodic assumption. To accomplish this one needs to project the distribution function from phase-space to energy

$$\rho(\epsilon,t)g(\epsilon,t) \equiv \int \frac{d\mathbf{r}\,d\mathbf{p}}{(2\pi\hbar)^3}\,\delta(\epsilon - E(\mathbf{r},\mathbf{p},t))f(\mathbf{r},\mathbf{p},t). \tag{8.13}$$

The projection yields the product of the energy distribution function $g(\epsilon, t)$ and the energy density of states

$$\begin{aligned}\rho(\epsilon, t) &= \int \frac{d\mathbf{r}\, d\mathbf{p}}{(2\pi\hbar)^3}\, \delta(\epsilon - E(\mathbf{r}, \mathbf{p}, t)) \\ &= \frac{m^{3/2}}{\sqrt{2}\pi^2\hbar^3} \int_{U\leq\epsilon} d\mathbf{r}\, \sqrt{\epsilon - U(\mathbf{r}, t)}. \end{aligned} \tag{8.14}$$

It is important to note that the density of states is defined on a variable energy range, i.e. $U_{\text{min}}(t) \leq \epsilon < \infty$ where $U_{\text{min}}(t)$ is the minimum value of $U(\mathbf{r}, t)$ at time t. The inclusion of this time-dependence was a significant step forward for Bijlsma *et al.* [7], distinguishing their work from previous work [52, 56]. (Recall that $U(\mathbf{r}, t)$ is an effective potential and depends on t in part through the time-dependent condensate density.)

Phase-space projection: kinetic equation

The density of states depends on time through the noncondensate potential $U(\mathbf{r}, t)$. For this reason we define a *weighted density of states*

$$\begin{aligned}\rho_{\text{w}}(\epsilon, t) &= \int \frac{d\mathbf{r}\, d\mathbf{p}}{(2\pi\hbar)^3}\, \delta(\epsilon - E(\mathbf{r}, \mathbf{p}, t)) \frac{\partial U(\mathbf{r}, t)}{\partial t} \\ &= \frac{m^{3/2}}{\sqrt{2}\pi^2\hbar^3} \int_{U\leq\epsilon} d\mathbf{r}\, \sqrt{\epsilon - U(\mathbf{r}, t)}\, \frac{\partial U(\mathbf{r}, t)}{\partial t} \end{aligned} \tag{8.15}$$

which depends on the time derivative of the noncondensate potential. Next, we take the derivative of $\rho_{\text{w}} g$ with respect to energy to get the relation

$$\frac{\partial}{\partial \epsilon}(\rho_{\text{w}} g) = \frac{\partial \rho_{\text{w}}}{\partial \epsilon} g + \rho_{\text{w}} \frac{\partial g}{\partial \epsilon} = -\rho_{\text{w}} g. \tag{8.16}$$

Finally, we are ready to take the phase-space projection of the kinetic equation.

The phase-space projection causes the streaming terms in Eq. (8.2) to vanish, leaving only the time derivative term. Using the definition in Eq. (8.15), the relation in Eq. (8.16), and the observation that

$$\frac{\partial\rho(\epsilon,t)}{\partial t} = -\frac{\partial\rho_{\mathrm{w}}(\epsilon,t)}{\partial\epsilon}, \tag{8.17}$$

we find the phase-space projection of the left-hand side of Eq (8.2)

$$\int\frac{d\mathbf{r}\,d\mathbf{p}}{(2\pi\hbar)^3}\,\delta(\epsilon - E(\mathbf{r},\mathbf{p},t))\frac{\partial f(\mathbf{r},\mathbf{p},t)}{\partial t} = \frac{\partial}{\partial t}(\rho g) + \frac{\partial}{\partial\epsilon}(\rho_{\mathrm{w}} g). \tag{8.18}$$

Thus our kinetic equation simplifies to

$$\frac{\partial}{\partial t}\left(\rho(\epsilon,t)g(\epsilon,t)\right) + \frac{\partial}{\partial\epsilon}\left(\rho_{\mathrm{w}}(\epsilon,t)g(\epsilon,t)\right) = I_{12}(\epsilon,t) + I_{22}(\epsilon,t) \tag{8.19}$$

where we have denoted the phase-space projections of the collision integrals by I_{12} and I_{22}:

$$\begin{aligned} I_{12}(\epsilon,t) &\equiv \int\frac{d\mathbf{r}\,d\mathbf{p}}{(2\pi\hbar)^3}\,\delta(\epsilon - E(\mathbf{r},\mathbf{p},t))\,C_{12}[f,n_{\mathrm{c}}] & (8.20)\\ I_{22}(\epsilon,t) &\equiv \int\frac{d\mathbf{r}\,d\mathbf{p}}{(2\pi\hbar)^3}\,\delta(\epsilon - E(\mathbf{r},\mathbf{p},t))\,C_{22}[f]. & (8.21)\end{aligned}$$

The evaluation of the integrals in Eq. (8.21) and Eq. (8.21) is rather complicated and is carried out in detail in [7]. We quote the results here to complete our ensemble of equations describing the kinetic evolution of the system. The collision integral for noncondensate particles I_{22} has a fairly standard form

$$\begin{aligned} I_{22}(\epsilon_1,t) = {} & \frac{m^3(T^{2\mathrm{B}})^2}{2\pi^3\hbar^7}\int d\epsilon_2\int d\epsilon_3\int d\epsilon_4\,\rho(\epsilon_{\mathrm{min}})\\ & \times\delta(\epsilon_1+\epsilon_2-\epsilon_3-\epsilon_4)\left[(1+g_1)(1+g_2)g_3g_4\right.\\ & \left.-g_1g_2(1+g_3)(1+g_4)\right] \qquad (8.22)\end{aligned}$$

where ϵ_{min} is the minimum value of the four energy variables, and the interpretation is similar to that of Eq. (8.7). The collision integral describing the interaction of condensate and noncondensate particles is slightly more complicated

$$\begin{aligned} I_{12}(\epsilon_1,t) &= \frac{m^3(T^{2\mathrm{B}})^2}{2\pi^3\hbar^7}\int d\epsilon_2\int d\epsilon_3\int d\epsilon_4\,[\delta(\epsilon_1-\epsilon_2) \\ &\quad -\delta(\epsilon_1-\epsilon_3)-\delta(\epsilon_1-\epsilon_4)]\,[(1+g_2)g_3g_4 \\ &\quad -g_2(1+g_3)(1+g_4)]\int_{U\leq\epsilon_{\mathrm{min}}} d\mathbf{r}\,n_{\mathrm{c}}(\mathbf{r},t) \\ &\quad \times S(p_2,p_3,p_4)\,\delta(E_{\mathrm{c}}(\mathbf{r},t)+\epsilon_2-\epsilon_3-\epsilon_4), \end{aligned} \tag{8.23}$$

where $S(p_2,p_3,p_4)$ is a Boolean function that takes values of 0 and 1 only (see Eq. (29) of [7]). In comparison with Eq. (8.22) we can see that there is no explicit density of states function. Instead, the remaining spatial integral acts as an effective density of states for scattering into the condensate. It can be evaluated analytically under the Thomas-Fermi approximation (see Sec. 2.5.2). We can now rewrite Eq. (8.12) as

$$\frac{dN_{\mathrm{c}}(t)}{dt} = -\int d\epsilon\, I_{12}(\epsilon,t)\ . \tag{8.24}$$

In the absence of loss processes, equations (8.19) and (8.24) together with (8.22) and (8.23) are the final equations that form the basis of the mean-field treatment of condensate growth in a trapped gas.

Variable energy range

One of the difficulties encountered in solving the kinetic equation is the time dependence of the mean-field potential $U(\mathbf{r},t)$ since it implies that the density of states in Eq. (8.14) and the energy distribution function $g(\epsilon,t)$ are defined on a variable energy range. To eliminate this problem, we introduce a shifted energy variable

$$\bar{\epsilon} \equiv \epsilon - U_{\mathrm{min}}(t), \tag{8.25}$$

which leads to a fixed energy range $0 \leq \bar{\epsilon} < \infty$. All relevant equations may be rewritten in terms of the shifted energy, simplifying the numerical solution of the kinetic equation considerably. In what follows we will continue to use ϵ as the energy variable with the understanding that we mean the shifted energy variable defined in Eq. (8.25).

Further details regarding the solution of these equations can be found in Ref. [7]. Rather than repeat that calculation [8] here, we focus instead on the modifications that are needed to apply this theory to the atomic hydrogen experiments. These modifications constitute the major theoretical contributions of this thesis.

8.3 Loss Processes

Until now only processes contributing to the growth of the condensate have been considered. Previous work [7, 22, 37], which was aimed primarily at understanding the atomic sodium experiment [83], did not require a description of the decay of the trapped gas. In the atomic hydrogen experiment, however, the decay of the gas due to inelastic two-body collisions (dipolar spin-relaxation) is severe and cannot be neglected in a quantitative comparison between theory and experiment [51]. A description of these decay processes and the modifications to the theory described above are the subjects of this section.

8.3.1 Forced Evaporative Cooling

Our first task is to incorporate the cooling procedure that is used experimentally to quench the atomic hydrogen gas below the Bose-Einstein condensation temperature. Forced evaporative cooling is accomplished using rf magnetic fields [32]. Theoretically, this means that there is an additional loss process for all atoms with an energy higher than the cut-off $\epsilon_{\mathrm{rf}}(t)$, which is determined by the frequency of the applied radio waves and is in general time dependent. Therefore, the one-body loss term

$$J_2(\epsilon, t) = -\frac{\rho(\epsilon, t) g(\epsilon, t)}{\tau_{\mathrm{rf}}(\epsilon, t)}\, \theta(\epsilon - \epsilon_{\mathrm{rf}}(t)) \;, \tag{8.26}$$

must be added to the right-hand side of Eq. (8.19), where $\tau_{\rm rf}(\epsilon, t)$ is an effective relaxation time for the evaporation that, in principle, depends on both the energy of the escaping atom and on time. This relaxation time, however, is very short compared to the time scales that are of interest for condensate growth. As a result we consider the following limit: $\tau_{\rm rf}(\epsilon, t) \to 0$.

8.3.2 Dipolar Spin-Relaxation

The next important loss process is the decay of the atomic hydrogen gas due to dipolar spin-relaxation [120, 128]. There are actually three distinct processes to consider since there can be inelastic collisions between two condensed atoms, one condensed and one noncondensed atom, and two noncondensed atoms. The first process is most straightforward to handle and leads only to a loss term on the right-hand side of Eq. (8.24) equal to

$$\begin{aligned} \left.\frac{dN_{\rm c}(t)}{dt}\right|_{11} &= -\frac{G^{\rm d}}{2}\int d\mathbf{r}\ [n_{\rm c}(\mathbf{r},t)]^2 \\ &= -\frac{G^{\rm d}}{420\pi}\frac{1}{a^2\ell}\left[15N_{\rm c}(t)\frac{a}{\ell}\right]^{7/5} \equiv J_{11}(t)\ , \end{aligned} \qquad (8.27)$$

where $G^{\rm d} \simeq 1.0 \times 10^{-15}$ cm^3/s is the well-known dipolar decay constant for doubly spin-polarized atomic hydrogen [120, 128]. The factor of one half accounts for the two-body coherence of the condensate [59, 119], and we have used Eq. (8.10) and Eq. (8.11) to carry out the integration.

To account for the effect of inelastic collisions between a condensed and a noncondensed atom, we first realize that the rate of change of the total number of condensate atoms $N_{\rm c}(t)$ and of the total number of thermal atoms $N'(t) = \int d\mathbf{r}\ n'(\mathbf{r},t)$ due to dipolar spin relaxation processes obeys

$$\begin{aligned} \left.\frac{dN_{\rm c}(t)}{dt}\right|_{12} &= \left.\frac{dN'(t)}{dt}\right|_{12} \\ &= -G^{\rm d}\int d\mathbf{r}\ n_{\rm c}(\mathbf{r},t)n'(\mathbf{r},t)\ . \end{aligned} \qquad (8.28)$$

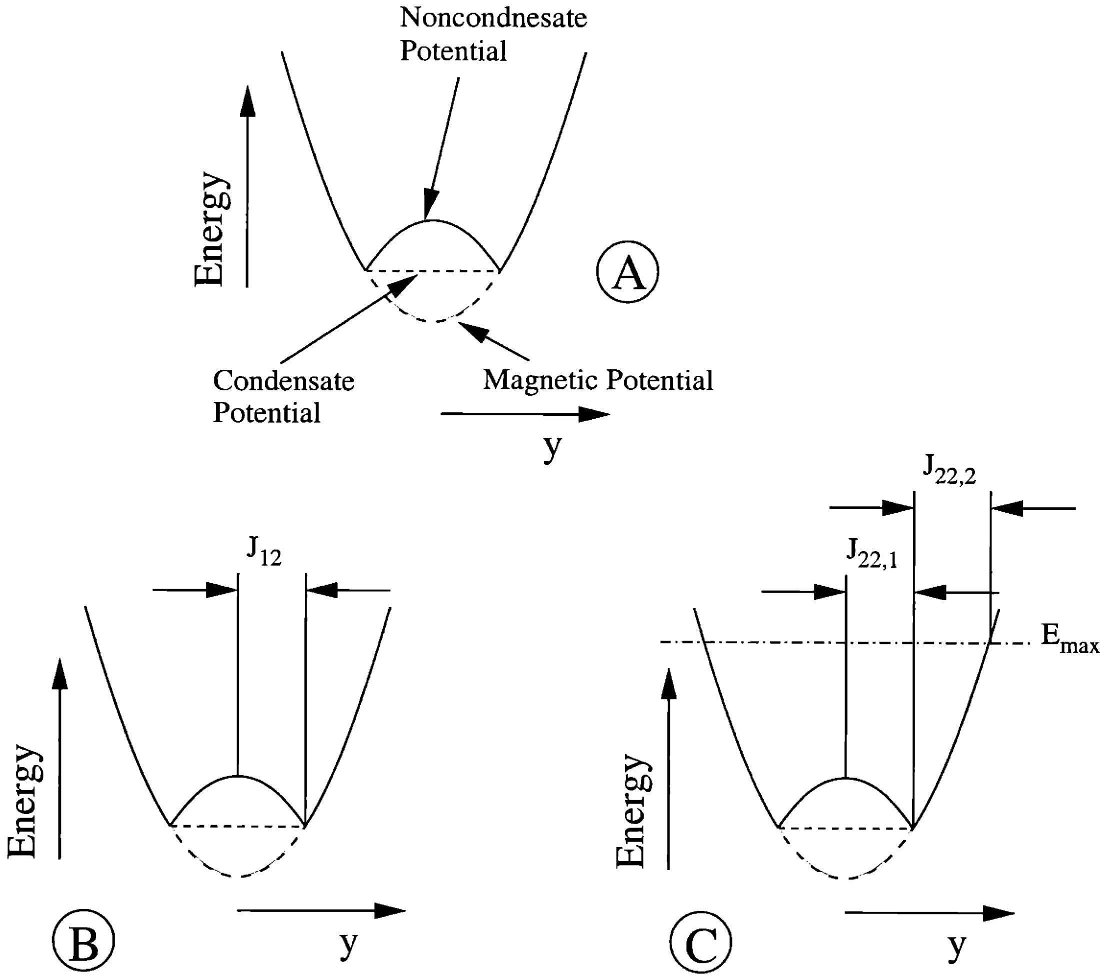

Figure 8-1: Sketch illustrating integration ranges for dipolar loss. Sketch A illustrates the effective potentials experienced by condensate and noncondensate atoms. The total effective potential (neglecting gravity) is given by the sum of the magnetic potential (parabolic) and the mean-field potential due to the condensate. Exchange effects result in a mean-field potential twice as large for the noncondensate. Sketch B indicates the range over which the two-body loss term J_{12} is calculated. This term accounts for dipolar losses between a condensate atom and a noncondensate atom. Sketch C depicts the ranges of integration for $J_{22,1}$ and $J_{22,2}$. The first term represents dipolar losses between two noncondensate atoms in the region of the condensate while the second term accounts for dipolar losses outside of the condensate.

Within our approximations we find that the latter can be written as $\int d\epsilon \, J_{12}(\epsilon, t)$ with

$$\begin{aligned} J_{12}(\epsilon, t) &= -\frac{G^{\mathrm{d}} g(\epsilon, t)}{(2\pi)^2 a \ell^2} \int_{y_1(t)}^{y_2(t)} dy \; y^2 \left(\frac{2\mu_{\mathrm{c}}(t)}{\hbar\omega} - y^2 \right) \\ &\quad \times \sqrt{\frac{2[\epsilon - 2\mu_{\mathrm{c}}(t)]}{\hbar\omega} + y^2} \, , \end{aligned} \tag{8.29}$$

$y_1(t) = (\max[0, a_-(t)])^{1/2}$, $y_2(t) = (2\mu_{\mathrm{c}}(t)/\hbar\omega)^{1/2}$, and $a_-(t) = 2(2\mu_{\mathrm{c}}(t) - \epsilon)/\hbar\omega$. The integral can also be performed analytically using

$$\begin{aligned} &\int dy \; y^2 (A - y^2) \sqrt{B + y^2} \\ &= \sqrt{B + y^2} \left\{ \frac{B(2A + B)y}{16} + \frac{(6A - B)y^3}{24} - \frac{y^5}{6} \right\} \\ &\quad - \frac{B^2(2A + B)}{16} \ln \left(y + \sqrt{B + y^2} \right) \, . \end{aligned} \tag{8.30}$$

From these results we conclude that the two-body loss term $J_{12}(\epsilon, t)$ must be added to the right-hand side of Eq. (8.19), while $\int d\epsilon \; J_{12}(\epsilon, t)$ must be added to the right-hand side of Eq. (8.24).

Inelastic collisions between two noncondensed atoms can be treated similarly by expressing the total loss rate as

$$\left. \frac{dN'(t)}{dt} \right|_{22} = -G^{\mathrm{d}} \int d\mathbf{r} \; [n'(\mathbf{r}, t)]^2 \, . \tag{8.31}$$

This can be written as the integral $\int d\epsilon \; J_{22}(\epsilon, t)$ with the integrand consisting of two terms $J_{22,1}(\epsilon, t)$ and $J_{22,2}(\epsilon, t)$. Physically, $J_{22,1}(\epsilon, t)$ corresponds to the dipolar decay occurring in the region of space containing the condensate, while $J_{22,2}(\epsilon, t)$ represents dipolar decay in the rest of the noncondensed gas. In detail, we find

$$\begin{aligned}
J_{22,1}(\epsilon,t) &= -\frac{G^{\mathrm{d}} g(\epsilon,t)}{(\pi\ell)^3}\int d\epsilon'\, g(\epsilon',t) \\
&\quad\times\int_{y_1(t)}^{y_2(t)} dy\; y^2\sqrt{\frac{2[\epsilon-2\mu_{\mathrm{c}}(t)]}{\hbar\omega}+y^2} \\
&\quad\times\sqrt{\frac{2[\epsilon'-2\mu_{\mathrm{c}}(t)]}{\hbar\omega}+y^2}\;, \qquad (8.32)
\end{aligned}$$

with $y_1(t) = (\max[0, a_-(t), a'_-(t)])^{1/2}$ and $a'_-(t) = 2(2\mu_{\mathrm{c}}(t) - \epsilon')/\hbar\omega$. Similarly we obtain

$$\begin{aligned}
J_{22,2}(\epsilon,t) &= -\frac{G^{\mathrm{d}} g(\epsilon,t)}{(\pi\ell)^3}\int d\epsilon' g(\epsilon',t) \\
&\quad\times\int_{y_2(t)}^{y_3(t)} dy\; y^2\sqrt{\frac{2\epsilon}{\hbar\omega}+y^2}\sqrt{\frac{2\epsilon'}{\hbar\omega}+y^2}\;, \qquad (8.33)
\end{aligned}$$

with $y_3(t) = (\min[0, 2\epsilon/\hbar\omega, 2\epsilon/\hbar\omega])^{1/2}$. The integrations over y can be performed analytically in terms of various elliptic functions, but because they result in rather formidable expressions we do not reproduce them here. More important for our purposes is the conclusion that the dipolar spin-relaxation in the thermal cloud can be accounted for by simply adding the loss term $J_{22}(\epsilon,t)$ to the right-hand side of Eq. (8.19).

To aid in understanding the $J_{\alpha\beta}$ integrals (Eqs. 8.29, 8.32, and 8.33), sketches illustrating the integration ranges and effective potentials are shown in Fig. 8-1. The main idea is to integrate the product of two spatially dependent densities in the presence of a potential with both magnetic and mean-field components. The integrations are straightforward but the effects of the mean-field should nevertheless be treated carefully.

8.4 Application to Atomic Hydrogen

As discussed in the previous section, the final set of coupled equations that we have to solve numerically for a realistic study of condensate growth in an atomic hydrogen gas are the kinetic equation for the distribution function of the thermal cloud

$$\begin{aligned}\frac{\partial}{\partial t}\left(\rho(\epsilon,t)g(\epsilon,t)\right)+\frac{\partial}{\partial \epsilon}\left(\rho_{\mathrm{w}}(\epsilon,t)g(\epsilon,t)\right) &= I_{12}(\epsilon,t)+I_{22}(\epsilon,t)+J_2(\epsilon,t)\\ &\quad +J_{12}(\epsilon,t)+J_{22}(\epsilon,t) \qquad (8.34)\end{aligned}$$

and the rate equation for the total number of condensate atoms

$$\frac{dN_{\mathrm{c}}(t)}{dt}=-\int d\epsilon\ I_{12}(\epsilon,t)+J_{11}(t)+\int d\epsilon\ J_{12}(\epsilon,t)\ . \qquad (8.35)$$

The aim of this section is to study the behavior of the condensate growth process under conditions typical for the atomic hydrogen experiment. To review, these experiments used H atoms in the $|F=1,m_F=1\rangle$ ground hyperfine state confined in an Ioffe-Pritchard potential. The s-wave scattering length between two ground state hydrogen atoms a is 0.0648 nm. Near the potential minimum the radial trapping frequency is $\omega_\rho=2\pi\times 1200$ Hz and the axial frequency is $\omega_z=2\pi\times 10.3$ Hz, giving an average oscillator frequency of $\omega/2\pi=246$ Hz. The axial bias is determined by an rf ejection technique to be 2.75 MHz or 132 μK.

Forced evaporative cooling is carried out by continuously lowering the frequency of an applied rf magnetic field to a final value of 5.40 MHz. A condensate has not yet formed. At this point there are N_{start} atoms in the thermal cloud at a temperature of T_{start}. Condensate growth is initiated by performing an rf "cut" and "hold." The rf frequency is lowered from 5.40 MHz to its value after the cut, ϵ_{rf}, in t_{rf} seconds and held fixed to define the trap depth. In the calculations that follow, the rf cut always begins at 5.40 MHz, and $t=0$ corresponds to the beginning of the rf cut.

The calculations were carried out using the numerical model of Eugene Zaremba[2]

---

[2] Department of Physics, Queen's University, Kingston, Ontario, Canada K7L, 3N6.

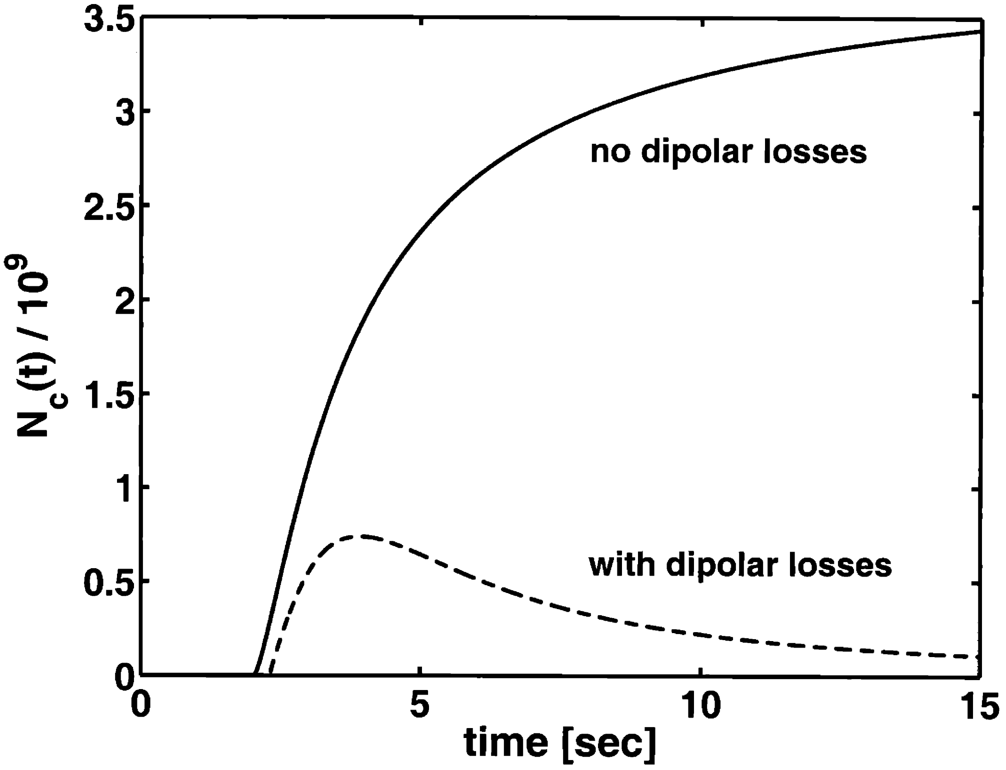

Figure 8-2: The importance of including loss processes in calculations of hydrogen condensate formation is shown. Following evaporation the rf frequency is lowered in one second from 5.4 MHz to 4.0 MHz resulting in the formation of a condensate. The solid line indicates the population of the condensate in the absence of dipolar losses. The dashed line includes dipolar losses in the calculation.

originally written for the work of Bijlsma [7]. The original code contained all of the physics described in Sec. 8.2, and we modified it to include the loss processes discussed in Sec. 8.3. A description of the numerics can be found in [7].

8.4.1 Kinetics of Condensate Growth

Importance of loss processes

The importance of loss processes in calculations of hydrogen condensate growth is illustrated in Fig. 8-2. The rf frequency is reduced from 5.40 MHz to $\epsilon_{\rm rf} = 4.00$ MHz in 1 second and held fixed, resulting in the formation of the condensate a few seconds later. The solid curve shows the expected number of condensate atoms as a function of time, $N_{\mathrm{c}}(t)$, with initial conditions, $N_{\text{start}} = 2.5 \times 10^{10}$ and $T_{\text{start}} = 50\ \mu\mathrm{K}$. It includes the time dependence of the rf cut and evaporation due to the rf hold, but it excludes the losses due to dipolar relaxation. Dipolar relaxation processes are included in the dashed curve. Clearly, the inclusion of dipolar losses is vital. The S-shaped growth curve familiar from other experiments is gone, replaced by one that turns over due to dipolar losses eating away at the condensate's core. In addition to dramatically reducing the maximum number of condensate atoms, $N_{\mathrm{c,max}}$, these loss processes are also seen to delay the growth initiation time, τ_{init}. We should emphasize that even after the initiation of condensate growth, scattering of atoms from the thermal cloud into the condensate is vital to sustaining the condensate population.

To better understand the contributions of the individual loss processes, we plot them separately in Fig. 8-3. For the same initial conditions and rf cut as before, we show the number loss versus time. Number loss due to the rf knife is shown in Fig. 8-3a. Until t_{rf} the loss rate is large because it includes both the direct effects of the cut and natural evaporation. After t_{rf} the evaporation rate relaxes to a lower value as the thermal component reaches a steady-state. Dipolar relaxation between two thermal atoms behaves similarly and is shown in Fig 8-3b. Initially the large thermal cloud allows for large loss rates, but as its size is reduced by the rf knife so is the loss rate. Interestingly, the rate appears to plateau for ~ 1.5 s before relaxing to a steady-state. Since the total thermal population is decreasing, the plateau indicates that the number density is increasing as the cooling gas settles deeper into the trap. The dipolar loss rates involving condensate atoms behave as we expect. They are important throughout the lifetime of the condensate, and the condensate-condensate loss rate dominates since dipolar relaxation is a two-body process whose rate scales as n^2.

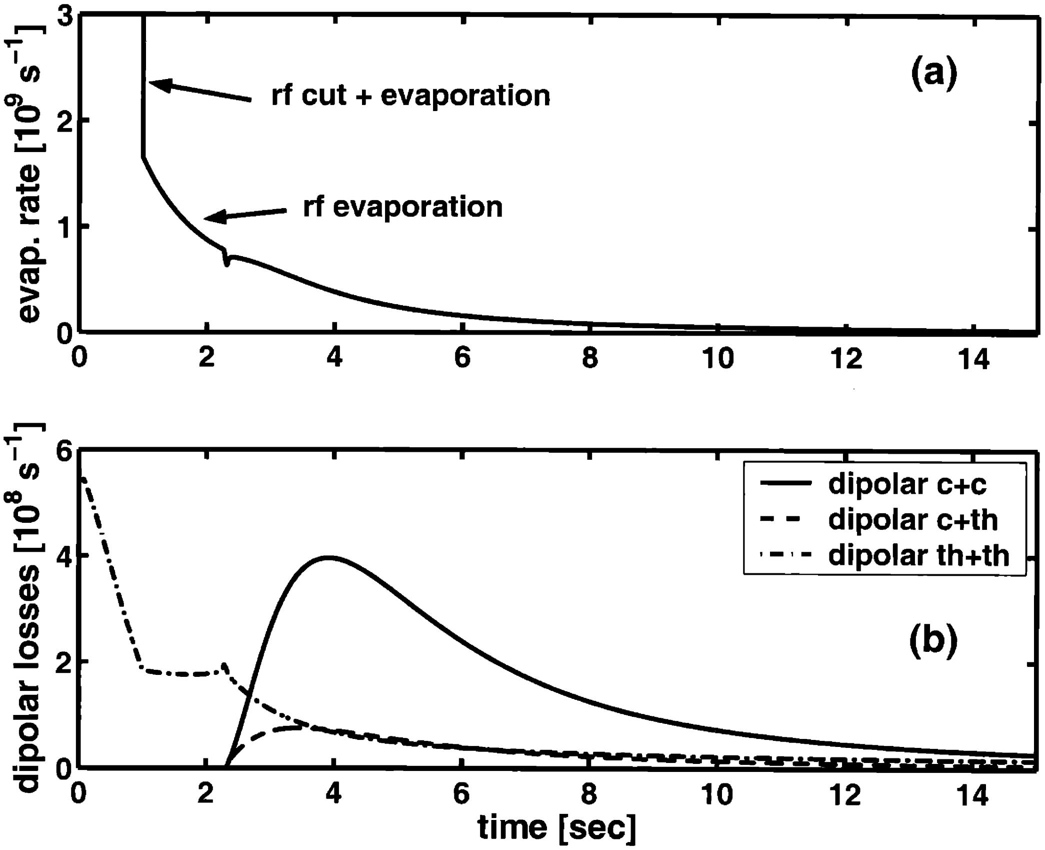

Figure 8-3: Contributions due to the various loss processes are shown. Panel (a) gives the loss rate due to removal of atoms by the rf "knife." During the first second the loss is dominated by the rf cut. Afterwards the rf knife defines the trap depth and only evaporation contributes. The evaporation rate decreases as the noncondensate cools and equilibrates to the new trap depth. Panel (b) indicates the contributions due to the various dipolar loss processes: between two condensate atoms (c+c), between one condensate and one thermal atom (c+th), and between two thermal atoms (th+th). As long as no condensate is present, dipolar relaxation in the thermal component dominates. After the condensate forms dipolar losses in the condensate dominate as expected.

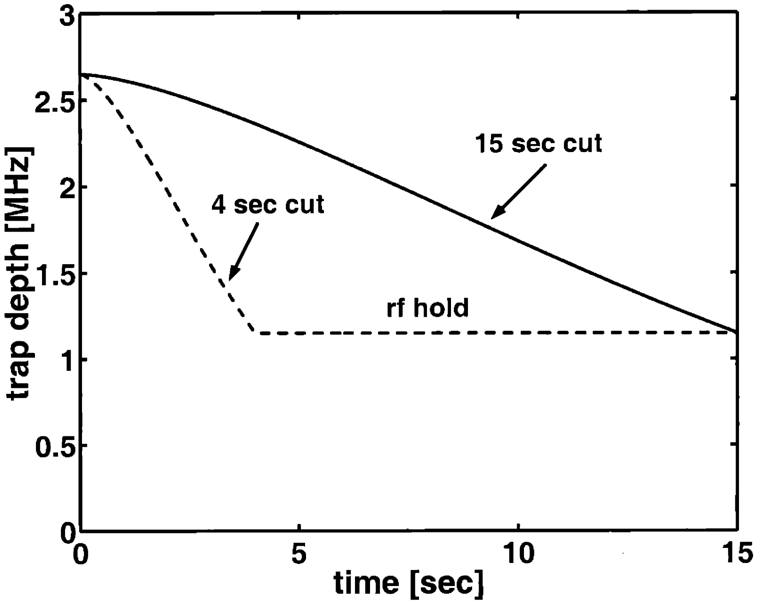

Figure 8-4: Trap depth as defined by the frequency of the rf knife. The dashed line shows an rf cut with $t_{\text{rf}} = 4$ s, while the solid line indicates a slower rf cut with $t_{\text{rf}} = 15$ s. The functional form of the rf trajectory is given by Eq. (6.1).

Condensate fraction

The competition between growth and loss processes in the hydrogen system can lead to non-equilibrium situations poorly approximated by steady-state descriptions. For example, the condensate fraction, $N_{\text{c}}(t)/N(t)$, can vary dramatically depending on t_{rf}, the duration of the rf cut. Two cuts are made to $\epsilon_{\text{rf}} = 3.90$ MHz with $t_{\text{rf}} = 4$ s and $t_{\text{rf}} = 15$ s, respectively. The trap depth resulting from these cuts is shown as function of time in Fig. 8-4. The corresponding condensate fraction versus time, $N_{\text{c}}(t)/N(t)$, is shown in Fig. 8-5a. The difference in t_{rf} changes the initiation time τ_{init} by only 0.58 s, but the condensate fraction varies by a factor of 2.8. The condensate population versus time is shown in Fig. 8-5b. The 15 s cut can be viewed as a forced evaporation to produce a condensate of $N_{\text{c,max}} = 9.1 \times 10^8$ atoms. By contrast, the 4 s cut is optimized to achieve the maximum number of condensate atoms, $N_{\text{c,max}} = 1.25 \times 10^9$, for these values of N_{start}, T_{start}, and ϵ_{rf}. In one sense, the shorter cut is wasteful

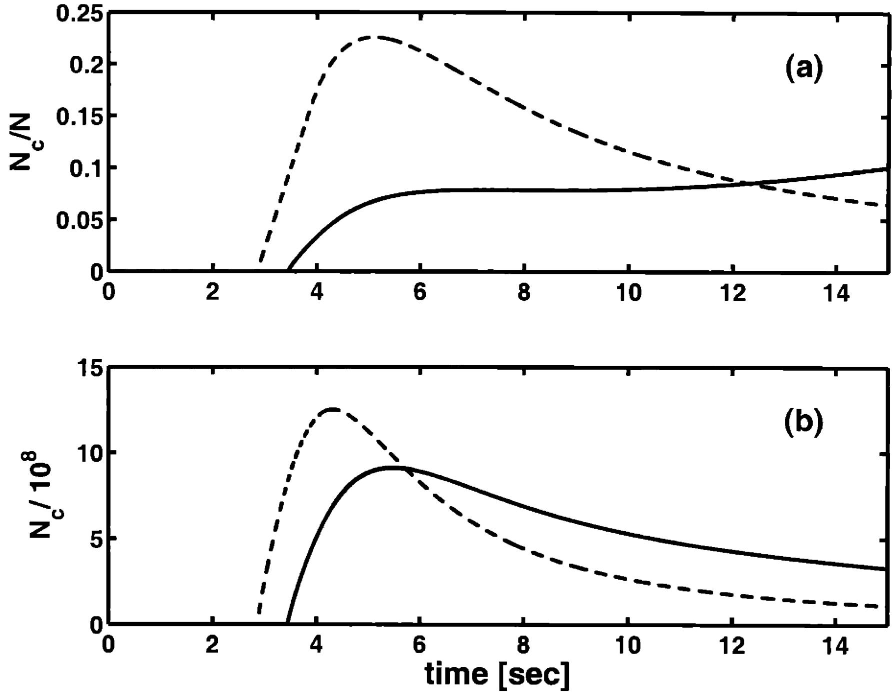

Figure 8-5: Influence of t_{rf} on the formation of the condensate. Panel (a) compares the condensate fraction $N_{\mathrm{c}}(t)/N(t)$ for the 4 s (dashed) and 15 s (solid) cuts shown in Fig. 8-4. Panel (b) gives the condensate population versus time N_{c} for the same cuts. Although the 4 s cut achieves a larger $N_{\mathrm{c,max}}$, the larger population cannot be sustained by feeding from the thermal cloud since more thermal atoms were expelled during the cut.

because it removes atoms that could be used to sustain the condensate. On the other hand, the nonequilibrium situation produced by the 4 s cut results in a larger peak condensate population and condensate fraction than could otherwise be achieved.

Initial condensate population

To completely specify the initial state in the trap prior to the rf cut, we must make a choice for the number of atoms initially in the condensate. If this number is zero, I_{12} in Eq. (8.19) is zero since only stimulated transitions into the condensate are included; there is no possibility of condensate growth. Under the experimental conditions, however, the lowest harmonic-oscillator state already has a significant thermal population

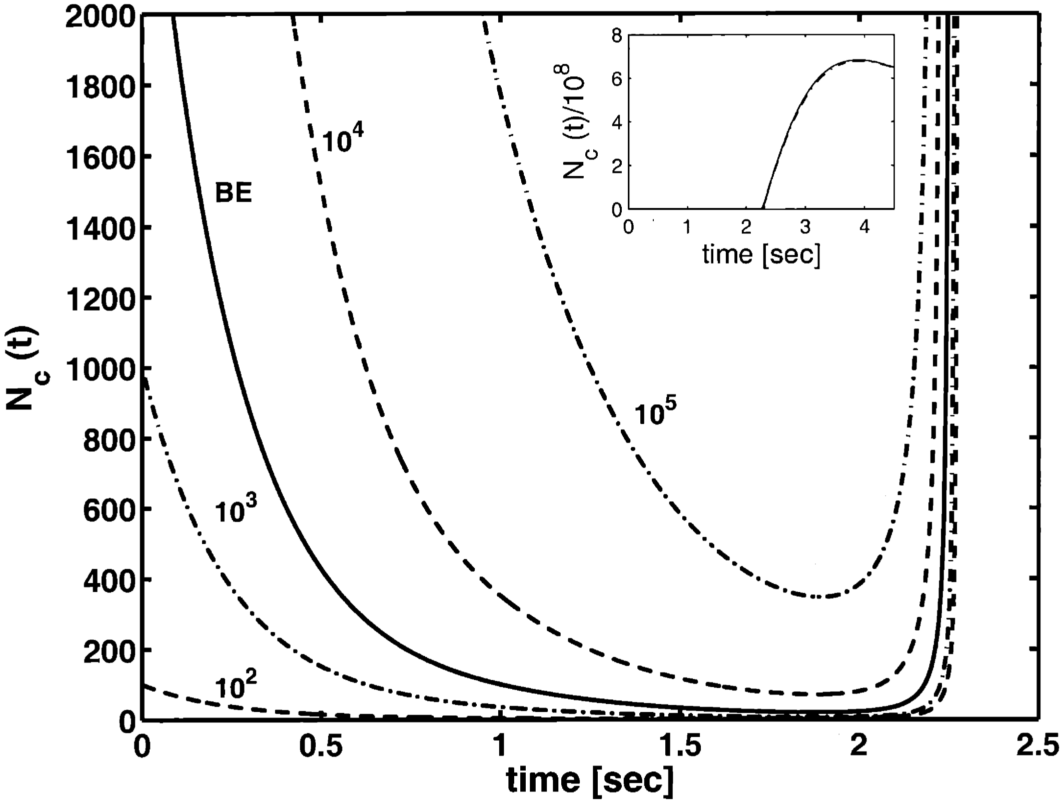

Figure 8-6: The influence of choice of initial condensate population $N_c(0)$ is shown. A variety of $N_c(0)$ are chosen and otherwise identical calculations are performed. The number of particles occupying the lowest state according to the Bose-Einstein distribution is $BE = 2814$. Dipolar loss processes cause the population of the condensate to relax, protecting against poor choices. The inset shows that the initial condensate population can be several orders of magnitude too large without affecting the gross features of the calculation.

and stimulated processes dominate. In the absence of loss processes, the calculations are somewhat sensitive to initial condensate number. We find, however, that dipolar relaxation in the condensate acts as a regulatory mechanism that protects against overestimates of initial condensate number.

The long term time evolution of the condensate turns out to be insensitive to the initial population $N_c(0)$. The dependence on $N_c(0)$ is shown in Fig. 8-6. We calculate condensate growth for $N_{\text{start}} = 2.5 \times 10^{10}$, $T_{\text{start}} = 50\ \mu\text{K}$, $\epsilon_{\text{rf}} = 3.90$ MHz, $t_{\text{rf}} = 1$ s, and various $N_c(0)$. The condensate population is seen initially to decrease

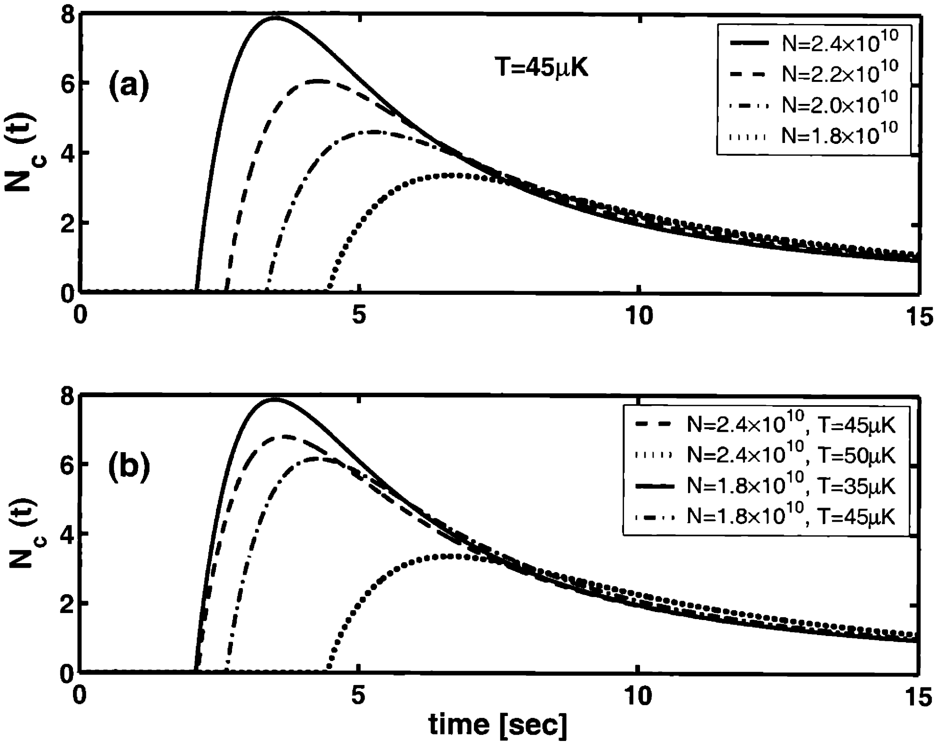

Figure 8-7: The effects of varying N_{start} and T_{start} for a particular ϵ_{rf} are shown. Panel (a) shows the effect of varying the initial population for the same initial temperature. The condensate forms more quickly for a larger N_{start} as described in the text. Panel (b) gives the result for varying T_{start} for a given N_{start}. Experimentally observable changes in N_{start} and T_{start} result in significantly different condensate formation curves.

for all values of $N_{\text{c}}(0)$ due mainly to dipolar relaxation. The scattering rate into the condensate is insufficient to sustain it at early times while the thermal cloud is relaxing. As long as the condensate number has time to relax before the initiation of growth, $N_{\text{c,max}}$ and τ_{init} vary little. For $0 < N_{\text{c}}(0) < 10^4$, the calculations are identical to within our numerical accuracy. Even for $N_{\text{c}}(0) = 10^6$, $N_{\text{c,max}}$ varies by less than 1%. Therefore, a reasonable choice for the initial condensate number is the occupation of the lowest harmonic-oscillator state at the temperature of the truncated Bose distribution, $N_{\text{c}}(0) = [\exp(3\beta\hbar\bar{\omega}/2) - 1]^{-1}$. This choice is shown by the solid line in the figure. It is important to note that the insensitivity of the calculations to $N_{\text{c}}(0)$ eliminates one fitting parameter in comparisons to experimental data.

Sensitivity to N_{start} and T_{start}

Armed with the knowledge that the calculations of condensate growth are insensitive to $N_c(0)$, we proceed to explore the sensitivity of the model to N_{start} and T_{start} for a particular ϵ_{rf}. The behavior of $N_c(t)$ for various N_{start} and T_{start} is shown in Fig. 8-7 for $\epsilon_{\mathrm{rf}} = 3.90$ MHz. The sensitivity to both parameters is easily understood. In Fig. 8-7a, the growth is calculated for $T_{\mathrm{start}} = 45\ \mu$K and various N_{start}. For smaller values of N_{start}, the sample is further in phase space from the Bose-Einstein transition. The initiation of condensate growth is delayed while the sample cools after the rf cut, and $N_{\mathrm{c,max}}$ is reduced because atoms were lost during cooling. In Fig. 8-7b, two values of N_{start} are compared with different T_{start}. For a given N_{start} a warmer sample has farther to go in phase space to reach the BEC transition. The initiation of growth is delayed in time and $N_{\mathrm{c,max}}$ is reduced. In both cases, it is important to point out that changes to N_{start} and T_{start} within the experimental uncertainties result in easily measurable differences in both $N_{\mathrm{c,max}}$ and τ_{init}.

The values of N_{start} and T_{start} are constrained by the requirement that $\mu_{th} < 0$ prior to the cut. In other words, we do not begin the calculation with a condensate population larger than the one given by the truncated Bose distribution for the lowest harmonic-oscillator state.

Experimentally it is easiest to prepare samples with identical N_{start} and T_{start} and vary ϵ_{rf}. We explore the variation of ϵ_{rf} with $N_{\mathrm{start}} = 2.5 \times 10^{10}$ and $T_{\mathrm{start}} = 50\ \mu$K in Fig. 8-8. As the cut into the initial distribution is made deeper, $N_{\mathrm{c,max}}$ at first increases due to the decreased total energy of the distribution and its correspondingly reduced final temperature. The onset time τ_{init} is also seen to decrease. At ϵ_{rf} of about 4.5 MHz ($1.85 + 2.65$ MHz), $N_{\mathrm{c,max}}$ reaches a maximum after which deeper cuts begin to remove atoms that otherwise would have contributed to the condensate, and $N_{\mathrm{c,max}}$ decreases. Interestingly, τ_{init} continues to decrease until $\epsilon_{\mathrm{rf}} \approx 3.70$ MHz.

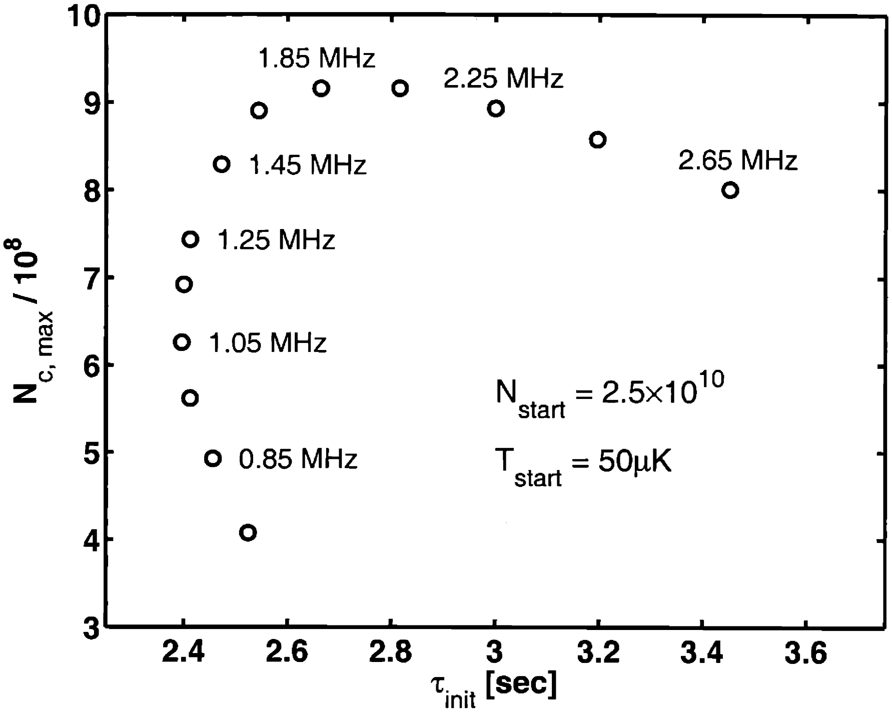

Figure 8-8: Peak condensate population and initiation time for different rf cuts. The initial energy distributions are the same for each point, $N_{\text{start}} = 2.5 \times 10^{10}$, $T_{\text{start}} = 50\ \mu\text{K}$, and trap depth 2.65 MHz. The point labels indicate the trap depth during the rf hold. As the cut deepens, the initiation time, τ_{init}, decreases and the peak condensate population, $N_{\text{c,max}}$, increases. Below a final trap depth of 1.85 MHz, the low-energy portion of the energy distribution is directly affected by the cut, and $N_{\text{c,max}}$ decreases.

8.4.2 Nonequilibrium Aspects

The formation of a Bose condensate from a cold, trapped gas is a problem of nonequilibrium kinetics. Consequently, the ideas of equilibrium theory must be applied with caution. To understand many of the results in this chapter it is useful to examine the time evolution of the energy distribution function, or more precisely, the evolution of $\rho(\epsilon, t)g(\epsilon, t)$, the product of the energy density of states and the energy distribution function. Figure 8-9 shows snapshots of the distribution function with initial conditions $N_{\text{start}} = 2.5 \times 10^{10}$ and $T_{\text{start}} = 50\ \mu\text{K}$. The rf frequency is ramped from 5.4 MHz to 4.0 MHz during the first second. The first frame shows the initial dis-

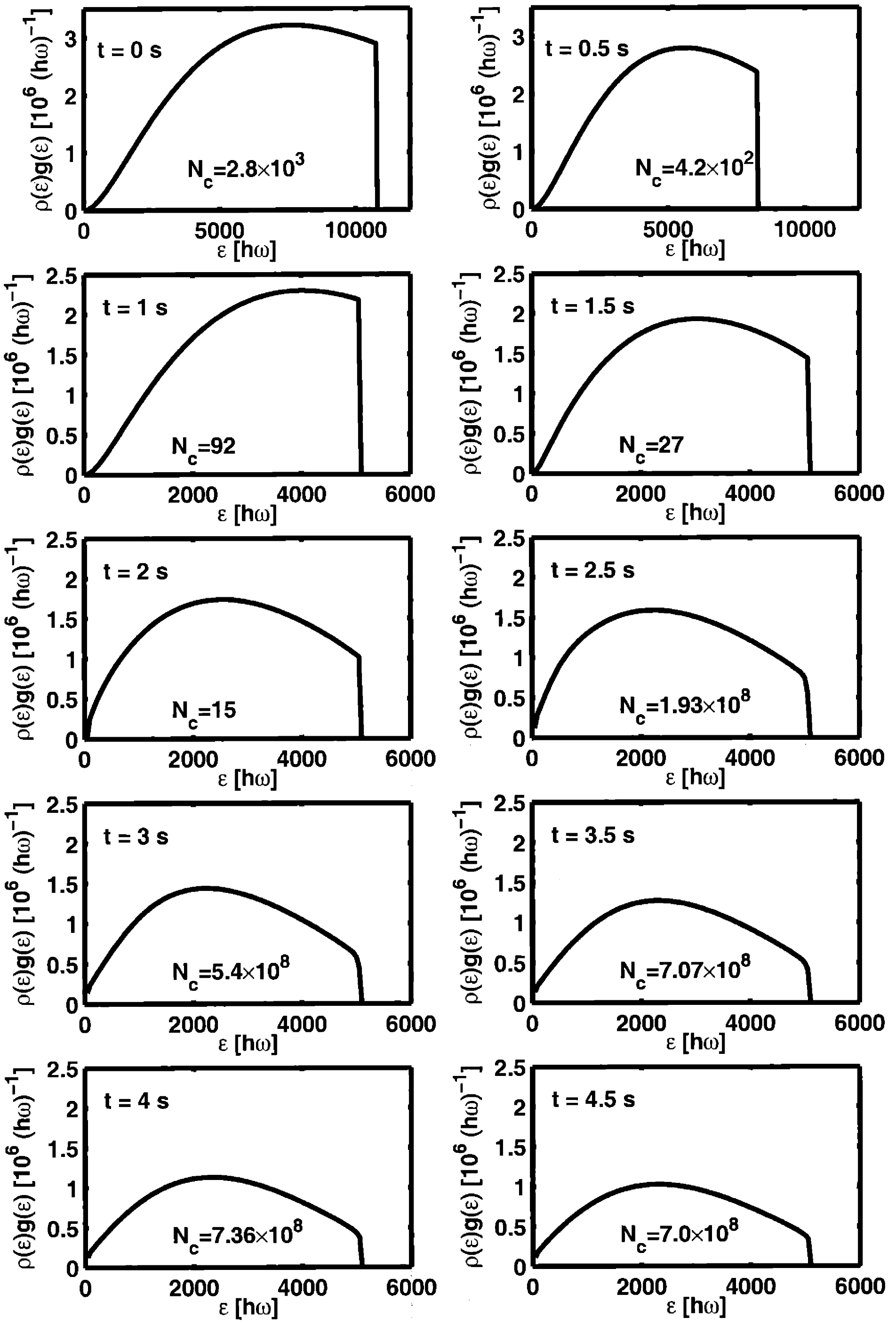

Figure 8-9: Snapshots of the energy distribution function of the normal gas are shown for initial conditions $N_{\text{start}} = 2.5 \times 10^{10}$ and $T_{\text{start}} = 50\,\mu$K. An rf cut is performed from 5.4 MHz to $\epsilon_{\text{rf}} = 4.0$ MHz in $t_{\text{rf}} = 1$ s. The snapshots reveal the evolution of the energy distribution during and following the cut, leading to the rapid onset of condensate growth at $t \sim 2.5$ s. The condensate is not shown, but its effect can be seen in the displacement of the low-energy ends of the curves for $t \geq 2.5$ s. The corresponding growth and decay curve is given by the dashed line in Fig. 8-2.

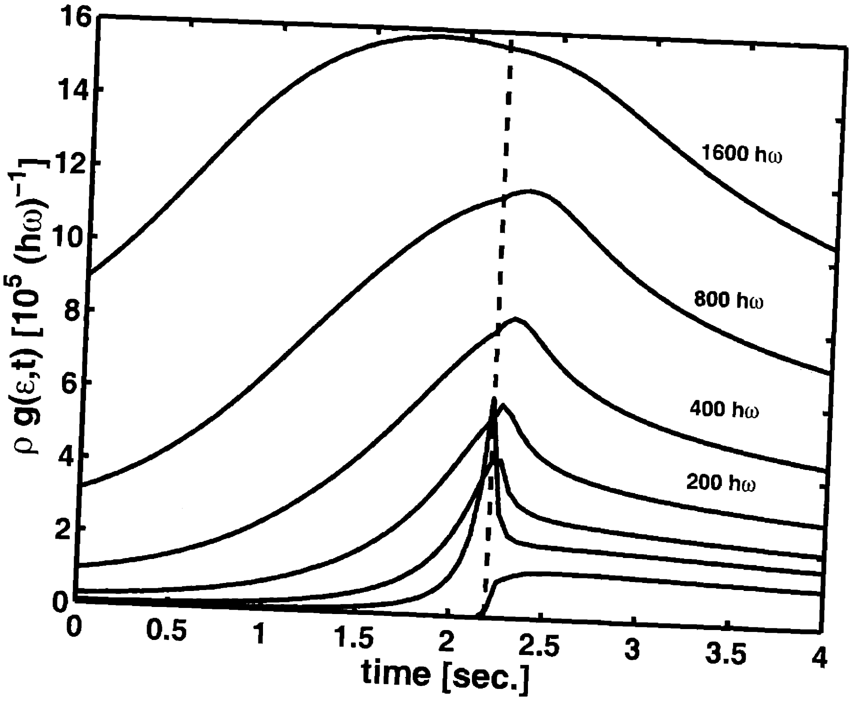

Figure 8-10: Evolution of the product of the density of states and the distribution function at energies of 25, 50, 100, 200, 400, 800, and 1600 $\hbar\bar{\omega}$. The rapid onset of condensate growth is indicated by the dashed line. The peaks all occur near the onset time, indicating that an enhanced low-energy population is present immediately preceding the appearance of a condensate.

tribution, while the second frame shows the distribution *during* the cut. Note that some cooling is taking place during the cut; it is not simply a one step truncation of the distribution. The distribution continues to evolve, and the shape is significantly different at $t = 2.0$ s. The distribution function is bulging at low energies compared to the initial distribution. The bulge is due to the flux of atoms moving away from the truncation toward lower energies. These atoms lead to the rapid growth of the condensate at $t = 2.5$ s. The condensate itself is not depicted in these snapshots, but the presence of the condensate has the effect of displacing the low-energy ends of the curves for $t \geq 2.5$ s. After the formation of the condensate, the distribution continues to relax toward equilibrium and its size diminishes due to feeding of the condensate and dipolar relaxation.

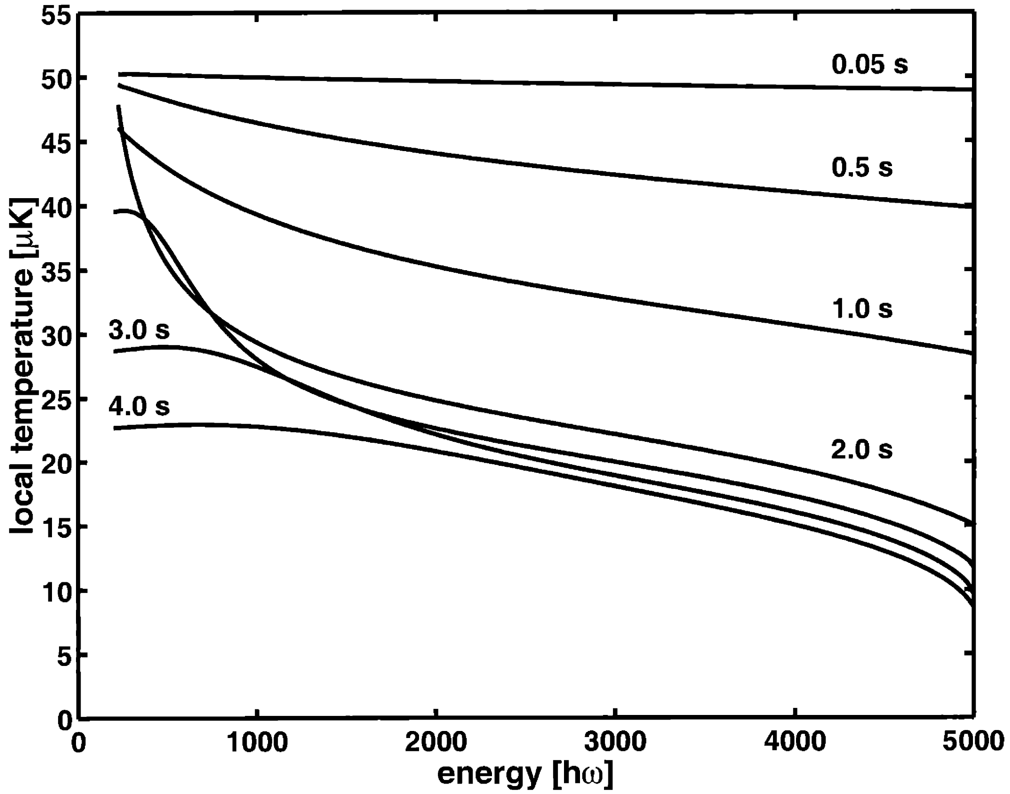

Figure 8-11: Snapshots of the local temperature at times 0.05, 0.5, 1, 2, 2.5, 3, and 4 s for initial conditions $N_{\text{start}} = 2.5 \times 10^{10}$ and $T_{\text{start}} = 50\,\mu\text{K}$. The corresponding condensate growth curve is given by the dashed line in Fig. 8-2.

The population of the low-energy levels increases significantly prior to the onset of rapid condensate growth. Figure 8-10 shows the evolution of the population of several low-energy levels. The population of the levels increases rapidly after the rf cut, reaches a maximum near the onset of rapid condensate growth (indicated by the dashed line), and then relaxes toward equilibrium $g(\epsilon) = (e^{\beta_{\text{eq}}\epsilon} - 1)$. This behavior is typical for all situations in which the growth of a condensate is observed. This figure allows one to visualize the "wave" of particles sweeping toward lower energy and triggering the formation of the condensate. Numerically the behavior of $g(\epsilon)$ prior to rapid condensate growth is consistent with the results of Bijlsma [7] and the prediction of Svistunov [125].

Another way to characterize the time evolution of the energy distribution function is to express it locally as a Bose distribution

$$g(\epsilon, t) = \frac{1}{\exp(\beta\epsilon - \beta\tilde{\mu}) - 1} \tag{8.36}$$

and fit the parameters β and $\tilde{\mu}$ to the value of the distribution function and its derivative. This procedure treats the parameters as constants, but they still depend parametrically on the energy variable ϵ and allow us to assign a local temperature and chemical potential. Figure 8-11 shows snapshots of the local temperature taken at various times during the evolution of the energy distribution. The first snapshot reflects the temperature of the initial distribution, $T_{\mathrm{start}} = 50\ \mu\mathrm{K}$. Following the rf cut, the local temperature at low energies reflects the initial Bose distribution. However, at higher energies the local temperature is significantly lower as a result of the cut. The entire distribution relaxes toward equilibrium with the low energy portion making significant progress only after the rapid condensate formation at $t \sim 2.5$ s. This figure illustrates clearly the nonequilibrium aspects of condensate formation and points out the difficulty of characterizing the entire sample with a single temperature.

Snapshots of the local chemical potential are shown in Fig. 8-12. The initial Bose distribution has a chemical potential of $\sim -2100\,\hbar\bar{\omega}$. As a result of the rf cut and subsequent formation of the condensate, the chemical potential at low energies is pinned to zero (recall that we are using a shifted energy scale) and then increases at higher energies. The rf knife defining the trap depth after the cut prevents the chemical potential at the highest energies from returning to zero. This figure again illustrates that the entire sample cannot be characterized by a single value of the chemical potential. Models that predict the scattering rate from the thermal cloud into the condensate by characterizing the thermal cloud with a single chemical potential will necessarily underestimate the true feeding rate, resulting in a smaller condensate population and condensate fraction. For this reason, a full theoretical treatment of the nonequilibrium problem is necessary for quantitative comparisons

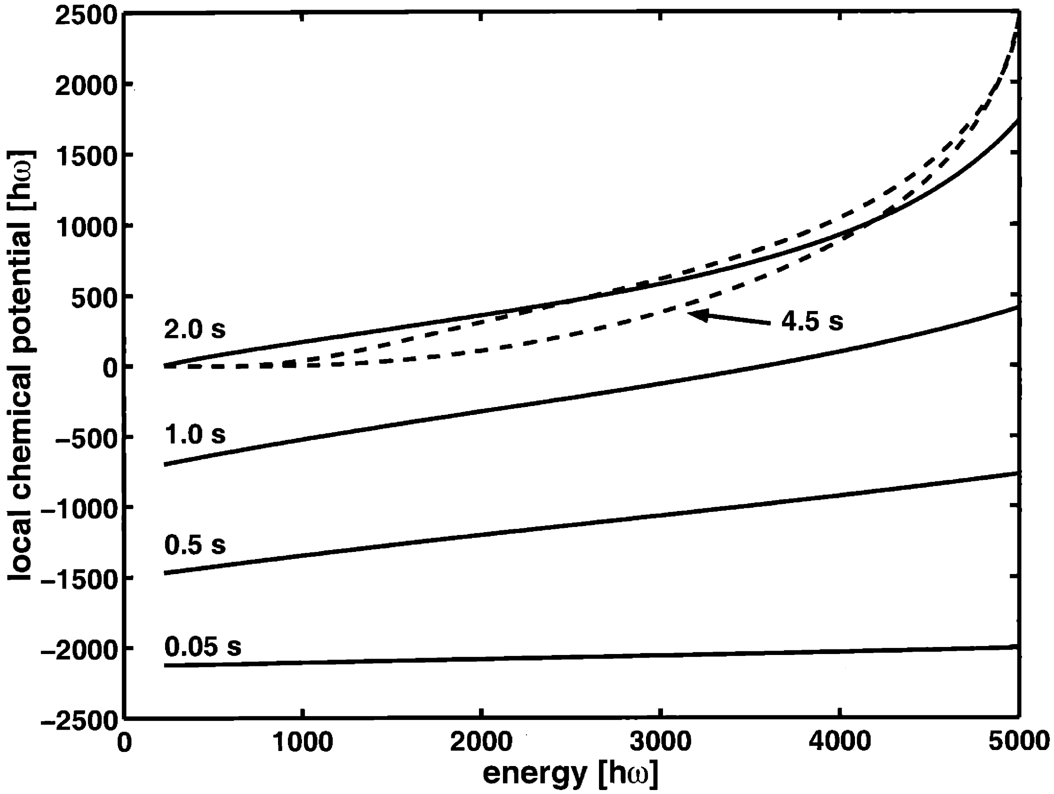

Figure 8-12: Snapshots of the local chemical potential at times 0.05, 0.5, 1, 2, 3, and 4.5 s. for initial conditions $N_{\mathrm{start}} = 2.5 \times 10^{10}$ and $T_{\mathrm{start}} = 50\,\mu\mathrm{K}$. The dashed curves occur after the formation of the condensate at $t \sim 2.5$ s and indicate the presence of a condensate because at low energies the value of the chemical potential is zero.

with experiments of condensate formation.

Chapter 9

Comparison of Experiment and Theory

The model of condensate growth in trapped atomic hydrogen presented in Chapter 8 is used to make quantitative comparisons with the rf cut experiments described in Sec. 7.6. From a theoretical point of view the rf cut experiments are ideal because the initial conditions of the sample are well-known. The magnetic trap is well-characterized by its harmonic oscillator frequencies, and the trap bottom, θ/h, is known to within 20 kHz. The rf frequency applied during the cut is precisely known because it is derived from a stable oscillator. The remaining parameters that enter the model are initial atom number, N_{start}, and temperature, T_{start}.

Although the number of atoms prior to the rf cut cannot be measured directly, the temperature of the noncondensed cloud can be determined through the width of the Doppler-sensitive spectrum. Section 9.1 discusses measurements of the sample temperature prior to the rf cut using a single-axis momentum distribution consistent with Bose-Einstein (BE) statistics. Section 9.2 discusses the necessity of including laser-induced trap losses in simulations of condensate formation and decay. The results of the temperature measurement and the time constant for laser loss are combined in Sec. 9.3 to make a quantitative comparison between simulations and rf cut experiments. The data and simulations are found to be in good agreement, and the behavior of the temperature, chemical potential, and condensate fraction are discussed.

The good agreement between condensate growth data and simulations permits us to estimate the value of a_{1S-2S}, the elastic scattering length between hydrogen atoms in the $1S$ and $2S$ states. The procedure for estimating a_{1S-2S} is described and the result is presented in Sec. 9.4.

Finally, it is expected theoretically that the collisional frequency shift of the two-photon $1S$-$2S$ resonance in a condensate of atomic hydrogen is a factor-of-two smaller than for an uncondensed gas at the same density. Confirmation of this theoretical prediction is an unresolved problem in the atomic hydrogen experiment. This chapter concludes in Sec. 9.5 with a discussion of the implications of our results on the factor-of-two problem.

9.1 Temperature Prior to the RF Cut

To properly describe the Doppler-sensitive (DS) lineshape observed in Sec. 7.6.2 one should use the Bose-Einstein occupation function (Eq. (2.1)) rather than the classical Maxwell-Boltzmann occupation function. The DS lineshape was observed near degeneracy prior to an rf cut at a trap depth of 5.35(2) MHz (257 μK). In this regime quantum degeneracy can narrow the spectrum, and fitting with the distribution function expected for a non-degenerate sample can yield artificially low temperatures. In this section the functions derived by Fried [32] to describe the degenerate gas are used to fit the DS lineshape. The essential fitting functions are presented first, followed by the resulting fits.

9.1.1 Velocity Distribution

Using the BE distribution function, Eq. (2.1), the one-dimensional momentum distribution function, $f_p(p_z)$, is obtained by integrating over the two momenta orthogonal to the $\hat{z}$ axis. The result is[1]

$$f_p(p_z; T, \mu, \epsilon_t, \varepsilon) = -\frac{2\pi m k_B T}{h^3 n(\epsilon; T, \mu, \epsilon_t)} \log\left(1 - \exp\left(\frac{\mu - \epsilon - p_z^2/2m}{k_B T}\right)\right) , \tag{9.1}$$

where T is the temperature, μ is the chemical potential, ϵ_t is the trap depth, and ε is the potential energy. The density is obtained by integrating the occupation function over all the trapped momenta, resulting in

$$n(\varepsilon; T, \mu, \epsilon_t) = \frac{g_{3/2}\left(e^{(\mu-\varepsilon)/k_B T}\right)}{\Lambda^3(T)} , \tag{9.2}$$

where $\Lambda(T)$ is the de Broglie wavelength defined in Eq. (2.5). The velocity distribution function is $f_v(v_z) = m f_p(m v_z)$.

9.1.2 Spectrum of the Velocity Distribution

Doppler-sensitive spectroscopy directly measures the one-dimensional velocity distribution $f_v(v_z)$ through the frequency shift $\Delta = \mathbf{k} \cdot \mathbf{v}$, where $\mathbf{k} = 2\pi\hat{z}/\lambda$ is the wavevector of the $\lambda = 243$ nm radiation. The Doppler-sensitive spectrum is given by considering the spectrum of atoms at each potential energy in the trap

$$S(\Delta) = S_0 \int_0^{\epsilon_t} d\varepsilon \varrho(\varepsilon) n(\varepsilon) \int_{-v_{\max}}^{v_{\max}} dv_z f_z(v_z) \delta(\Delta - k v_z) , \tag{9.3}$$

where the maximum velocity is defined through $m v_{\max}^2/2 \equiv \epsilon_t - \varepsilon$, S_0 is a normalization factor, and $\varrho(\varepsilon)$ is the potential energy density of states. For an Ioffe-Pritchard (IP) potential (Eq. (2.34))

$$\varrho(\varepsilon) = \frac{4\pi}{\alpha^2\sqrt{\beta}} \sqrt{\varepsilon}(\varepsilon + \theta) . \tag{9.4}$$

---

[1] In this formula and the ones that follow, the effect of truncating the distribution function is ignored since it is small for the trap considered here. See App. E of [32] for a prescription for including truncation effects.

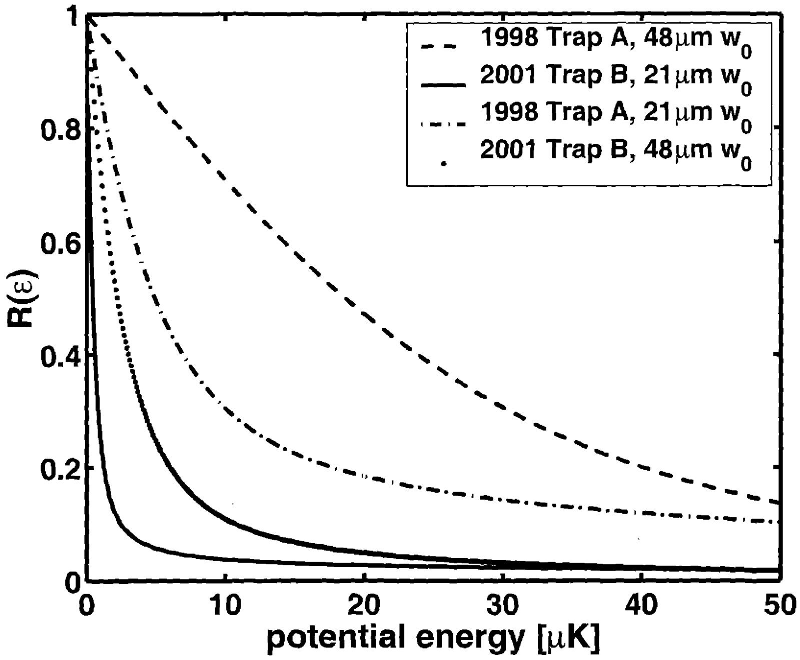

Figure 9-1: The average of the square of the laser beam intensity on an equipotential surface of energy, ε.

Carrying out the integration over velocity gives

$$S(\Delta) = \frac{S_0}{h\Lambda^2} \int_0^{\varepsilon_{\max}} d\varepsilon \varrho(\varepsilon) \log\left(1 - e^{(\mu-\varepsilon-m\Delta^2/2k^2)/k_BT}\right) , \tag{9.5}$$

but this expression neglects the spatial dependence of the exciting radiation. We assume that the laser intensity is described by Eq. (5.4) and integrate the square of the laser intensity (recall that this is a two-photon excitation) over a surface of constant potential energy ε in an IP potential. The result is a factor, $R(\varepsilon)$, that can be inserted into Eq. (9.5)

$$R(\varepsilon) = \sqrt{\frac{\beta}{\varepsilon}} \int_0^{\sqrt{\varepsilon/\beta}} dz \exp\left[-\frac{4}{\alpha^2 w_0^2} \frac{(\varepsilon+\theta)^2 - (\beta z^2+\theta)^2}{1+(z/d)^2}\right] , \tag{9.6}$$

where w_0 is the waist radius and $d = \pi w_0^2/\lambda$ is the divergence length.

The integral has been calculated for several traps and waist radii. The solid line in Fig. 9-1 indicates Trap B with $\theta/k_B = 132\ \mu\text{K}$ (see Table 2.1) and waist radius, $w_0 = 21\ \mu\text{m}$, used in the rf cut experiments in this thesis. The combination of a narrow waist and a large bias potential causes the laser to preferentially excite low-energy atoms near the bottom of the trap. As a result we are justified in neglecting truncation effects in the above formulae.

For comparison, $R(\varepsilon)$ was calculated for the trap and laser waist radius used in the 1998 condensate experiments [31, 32, 66]. The result is indicated by the dashed line in Fig. 9-1. In 1998, Trap A operated with $\theta/k_B = 34\ \mu\text{K}$, and the laser had a larger waist, $w_0 = 48\ \mu\text{m}$. This combination allowed excitation of higher energy atoms. To illustrate the individual effects of the trap shape and laser waist on $R(\varepsilon)$, two intermediate cases were calculated. The results in Fig. 9-1 are easily understood: a larger laser waist illuminates a larger volume encompassing higher energy atoms; Trap B with a high bias potential is less radially confining, allowing even low-energy atoms to reach regions of lower laser intensity.

9.1.3 Time Evolution of the Temperature

Using Doppler-sensitive (DS) $1S$-$2S$ spectroscopy the spectrum of the noncondensed gas was recorded prior to an rf cut. An rf evaporation was carried out in Trap B to a final frequency of 8.1 MHz and held constant. The trap bottom was measured to be 2.75(2) MHz. The DS spectrum was swept in frequency for ~ 30 s. The sweeps were grouped together (e.g. sweeps 1-10, 11-20, etc.) and summed. The resulting spectrum was fitted using Eq. (9.5) and Eq. (9.6). The temperatures from the fits are shown in Fig. 9-2. The time assigned to each point corresponds to the middle sweep in each group.

The fits indicate that the sample cools during the first 10 seconds after the rf evaporation. The changing temperature suggests that the sample has not quite reached equilibrium after the rf evaporation, resulting in an energy distribution that adjusts itself over the next few seconds. The constant rf field continues to remove energetic atoms, lowering the temperature and allowing the sample to settle deeper into the

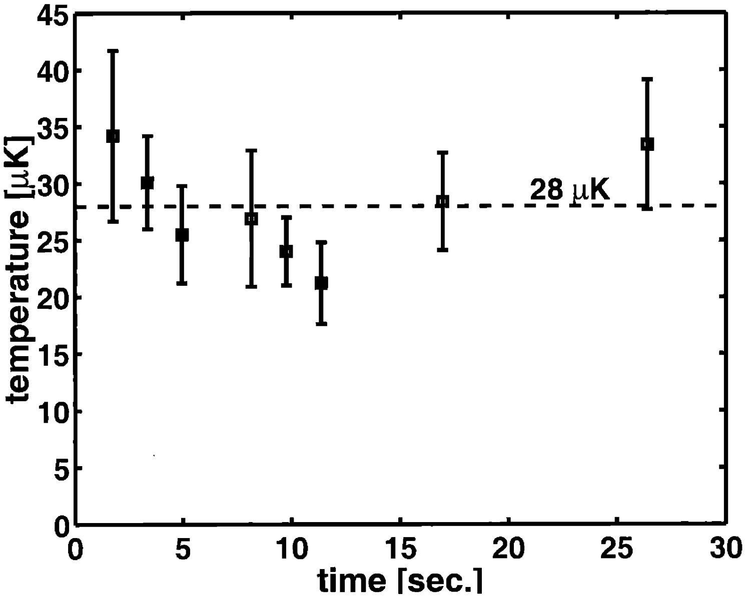

Figure 9-2: Evolution of the temperature of a nondegenerate sample. Following rf evaporation the sample was held in Trap B with $\theta/k_B = 132$ μK at a trap depth of 257 μK (5.35 MHz). The temperatures correspond to fits of a one-dimensional Bose-Einstein distribution. The chemical potential, μ, was determined self-consistently with the simulations of condensate formation described in Sec. 9.3.1.

trap. After $t = 15$ s, the fits suggest that the sample warms slightly, finding an equilibrium temperature around 30 μK.

Figure 7-20 presents the same data summed over the first 20 s and fitted with the classical (Maxwell-Boltzmann) distribution expected for a sample far from degeneracy. The classical fit yields a temperature of 24.0 ± 1.6 μK. Fitting the same data with a Bose-Einstein distribution gives 28.0 ± 2.2 μK, a 15% difference. As indicated in Fig. 9-1, the laser intensity profile and trap geometries play an important role in determining the DS spectrum. Taking these into account along with quantum statistics results in more accurate input for our simulations of condensate growth.

A problematic aspect of fitting with the Bose-Einstein distribution (BE) is the lack of knowledge of the chemical potential μ. To overcome this problem we have used our model of condensate formation, which calculates the chemical potential of the thermal cloud, to self-consistently determine μ. That is, the initial chemical potential which produces the best agreement with the condensate growth data is used to fit the BE distribution to the DS spectrum. The temperature resulting from the fit is then input to the growth simulation, and so on. The result is both reasonable and self-consistent.

9.2 Laser Losses

In Sec. 7.3 the effect of laser excitation on condensate formation was studied. Two formation experiments were performed in which the laser was introduced to the sample at different times. For the sample in which the laser was introduced earlier, the condensate formation was delayed by ~ 0.5 s, but the maximum signal and decay were identical. This ambiguous behavior left open the question of whether to include laser losses in the calculations.

Background gas losses

In simulations of condensate growth, the condensate formed earlier and decayed more slowly than the experimentally observed condensates, suggesting a loss mechanism not included in the model. Laser induced losses come in two forms: background gas losses and resonant losses. Background gas losses result from ^{4}He streaming from contaminated optical surfaces illuminated by the laser. The time constant for background gas loss, $\tau_{\rm bkgd}$, was measured to be ~ 200 s. In this measurement, the laser was tuned far off resonance and introduced into the cell for many seconds before measuring the integrated spectrum. The result was compared with a similar experiment in which the laser was absent prior to measurement of the spectrum. This time constant is sensitive to several factors: laser power, superfluid film thickness in the cell, and the quantity of contaminants on the optics. Each of these parameters changes from day to day. In particular, the condensate formation experiments were performed with the highest laser power and a saturated ^{4}He film. It is likely that the time constant is closer to $\tau_{\rm bkgd} \sim 50$ s.

Resonant losses

We can estimate the time constant for resonant losses, $\tau_{\rm res}$, by examining the rate that atoms are excited out of the condensate. During DS spectroscopy, resonant losses are dominated by excitations out of the condensate. For the largest signal shown in Fig. 7-19, the excitation rate out of the condensate is approximately 1.5×10^4 counts/laser second. For DS excitations out of the normal gas near the center of the Doppler profile, the largest excitation rate is $\sim 1 \times 10^3$ counts/laser second. During the 7.2 s following the rf cut in Fig. 7-19, 5.9×10^3 counts were recorded. In Sec. 4.2.2, the detection efficiency for cold, dense samples was estimated to be $\varepsilon_{\rm det} \sim 1.5 \times 10^{-6}$. Roughly 5.5×10^8 atoms/s are excited from the condensate. This is about 2% of the total number of atoms in the trap, suggesting a crude estimate for the time constant of resonant loss, $\tau_{\rm res} \sim 50$ s.

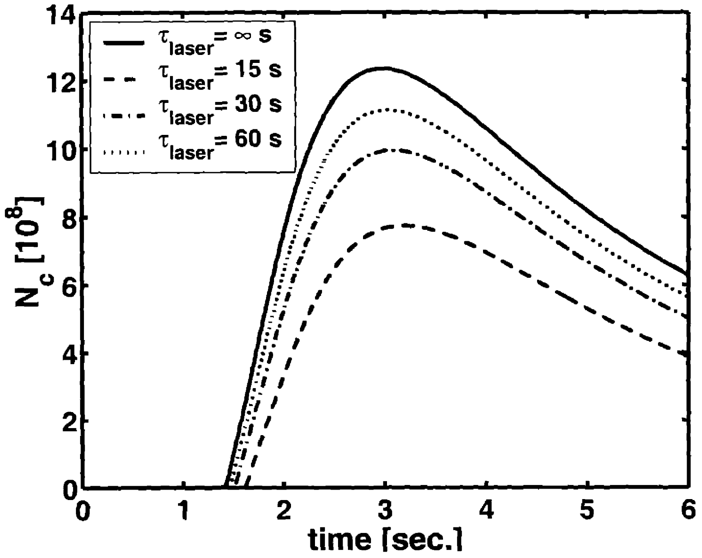

Figure 9-3: Effect of laser-induced losses on the formation of the condensate. A $t_{\text{rf}} = 1$ s rf cut from an initial trap depth of 218 μK (4.55 MHz) to a final trap depth of 84 μK (1.75 MHz) was simulated for different values of τ_{laser}. A smaller τ_{laser} indicates larger losses. Large losses due to the laser delay the formation of the condensate and enhance is decay.

9.2.1 Including Laser Losses in the Model

The effect of laser excitation on the formation of the condensate is included in the calculation in a simple way. The total number of atoms in the sample is given by $N_{\text{tot}} = N_c + N_{\text{th}}$. At each time step the total number is adjusted according to

$$\left.\frac{dN_{\text{tot}}}{dt}\right|_{\text{laser}} = -\frac{1}{\tau_{\text{laser}}} N_{\text{tot}} \tag{9.7}$$

where $1/\tau_{\text{laser}} = 1/\tau_{\text{bkgd}} + 1/\tau_{\text{res}}$.

The impact of τ_{laser} on condensate formation is shown in Fig. 9-3. Four rf cut experiments were simulated with different values of τ_{laser}. In each simulation the trap depth was lowered from 218 μK (4.55 MHz) to a final trap depth of 84 μK (1.75 MHz) in $t_{\text{rf}} = 1$ s. The behavior is predictable and indicates the necessity of including laser losses in the simulations. For small τ_{laser}, laser-induced losses delay the onset of condensate growth, slow the formation (indicated by the slope of the curves), and result in a much smaller maximum condensate population. The decay of the condensate is also accelerated. Without laser losses ($\tau_{\text{laser}} = \infty$), the population is reduced by 50% from its maximum in 3 s. If $\tau_{\text{laser}} = 15$ s, the number is reduced by 50% in 2.75 s. This may not seem significant, but recall that the dipolar spin-relaxation in the condensate scales as $N_c^{7/5}$, and without laser losses the condensate is 1.6 times bigger. Because these two condensates decay at approximately the same rate, the influence of laser losses on the lifetime of the condensate is significant. As we will see in Sec. 9.3, best agreement with experiment was found with $\tau_{\text{laser}} = 30$ s.

9.3 Comparison with the Total Condensate Signal

In this section the results of the condensate growth model and the rf cut experiments are compared. Figures 7-12, 7-16, and 7-19 presented the time evolution of the total condensate. The Doppler-sensitive profile and background fluorescence were subtracted, leaving only the spectroscopic signal due to the condensate. Since both ends of the condensate spectrum were resolved in the experiment, we assume that the number of condensate atoms is proportional to the amplitude of the signal. This assumption seems reasonable since the laser waist radius, $w_0 = 21$ μm, is larger than the radial extent of the largest condensate, ~ 10 μm. The proportionality permits scaling of the condensate signal to obtain condensate number. The scale factor is determined by a fitting procedure.

9.3.1 Varying the Starting Frequency of RF Cuts

Figure 9-4 shows the condensate growth data and the results of simulations for experiments in which the starting point of the rf cut, ϵ_{start}, was varied. The agreement is good, and the trends in the initial atom number, N_{start}, initial temperature, T_{start}, are reasonable. Recall that in these experiments the noncondensed sample was cooled to just above the Bose-Einstein transition temperature before a $t_{\text{rf}} = 1$ s rf cut lowered the trap depth to just 84 μK. The end of the rf cut is shown in each panel. The upper panel shows the time evolution of the condensate number for the sample that started furthest from the transition with an initial trap depth of 257 μK. As expected this sample had the largest initial number of atoms, $N_{\text{start}} = 2.92 \times 10^{10}$, and the highest temperature, $T_{\text{start}} = 36$ μK. In the other two panels, the rf cut begins with the sample closer to the transition. The trap depths are shallower, and the corresponding initial atom number and temperature are lower. The middle panel shows the growth of the condensate with $N_{\text{start}} = 2.81 \times 10^{10}$ and $T_{\text{start}} = 35$ μK with an initial trap depth of 238 μK. In the lower panel, $N_{\text{start}} = 2.81 \times 10^{10}$ and $T_{\text{start}} = 35$ μK for an initial trap depth of 218 μK

The following procedure was used to obtain the scaling factor necessary to compare the experiment with the simulation. An initial temperature for the simulation was chosen based on the measurements discussed in Sec. 9.1.3. It is important to note that the trap depth was not held constant following the rf evaporation as it was for the experiment presented in Fig. 9-2. The sample was given no time to equilibrate, so the earliest fitted temperature was taken as T_{start}. An estimate of the initial number, N_{start}, was made based on the density of noncondensed atoms measured using the cold-collision shift of the Doppler-free $1S$-$2S$ transition and the known trap depth and shape. The simulation was run, and the results were compared to the experimental data using a fitting procedure for the scaling factor. In most cases disagreement was obvious to the eye. New values of T_{start} and N_{start} were chosen, and the process was repeated. When it was determined that a good fit could not be obtained by adjusting T_{start} and N_{start}, τ_{laser} was changed, and the fitting process was repeated. The sensitivity to τ_{laser} is shown in Fig. 9-3. A single simulation took a few hours to run on a 850 MHz PC.

The shape of the simulated condensate formation and decay curve is sensitive to T_{start} and N_{start}. There are four features that should be examined to determine the quality of the fit by eye: the onset time of formation, the maximum amplitude, the time the maximum amplitude occurs, and the rate at which the signal decays

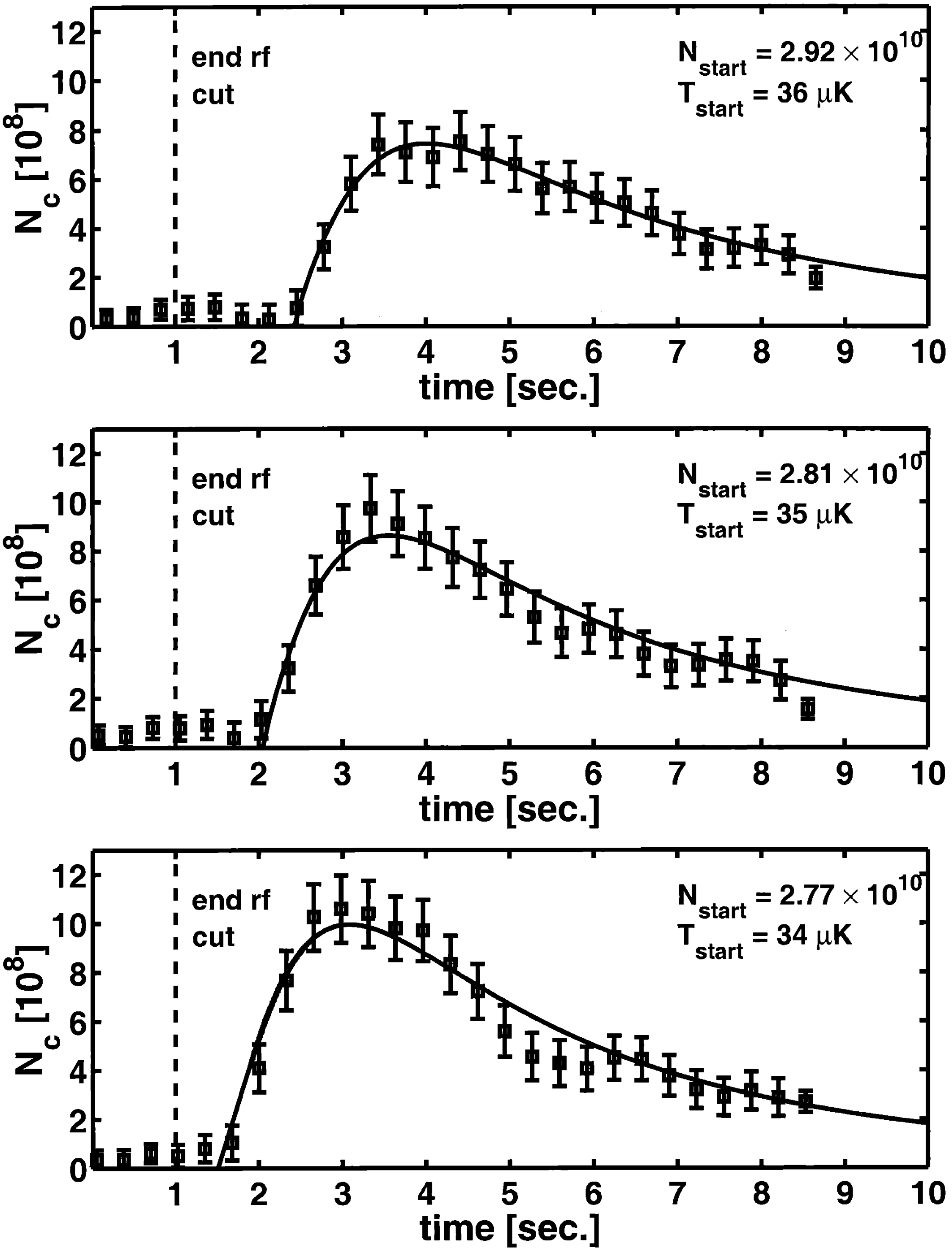

Figure 9-4: Comparison of calculations with experiments in which ϵ_{start} was varied. $\tau_{\text{laser}} = 30$ s in each calculation. The initial atom number and temperature are indicated in each panel.

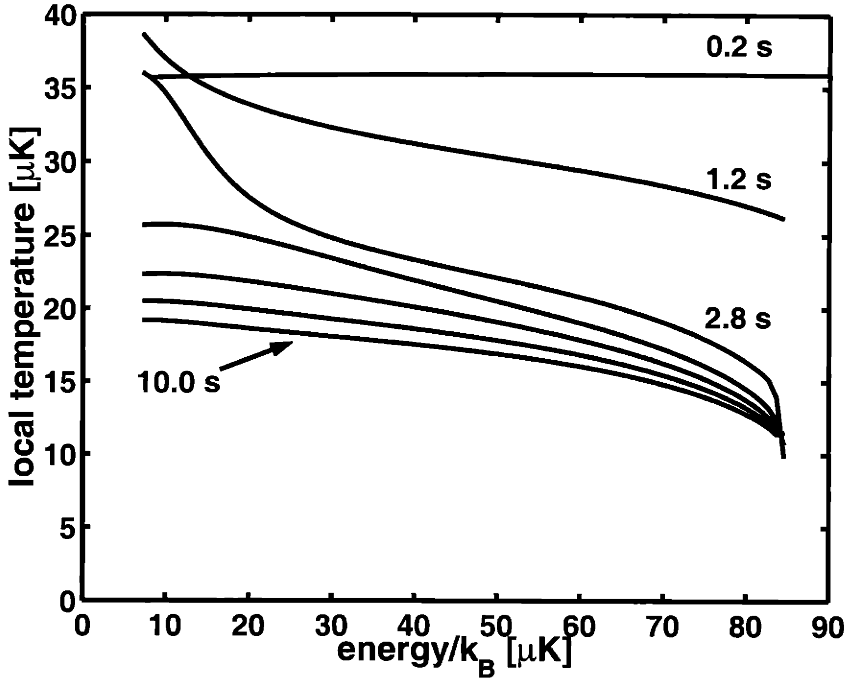

Figure 9-5: Time-evolution of temperature during an rf cut experiment.

following the maximum. For a given value of N_{start}, a 3% change in T_{start} (1 μK) results in a large change in all four features. Similarly, a 2% change in N_{start} is also noticeable. It is safe to say that the comparison is good to within 5%.

Table 9.1 summarizes the comparisons for experiments in which ϵ_{start} was varied.

Evolution of temperature

The sudden change in trap depth due to the rf cut produces a nonequilibrium situation in which the sample temperature changes rapidly. The $t_{\text{rf}} = 1$ s rf cut affects the most energetic atoms first, removing them from the trap if their energy, ϵ, exceeds the trap depth, ϵ_{t}. Following the rf cut the trap depth is held constant, and collisions within the sample redistribute the energy, causing it to equilibrate at a new, lower temperature.

During the rf cut the energy distribution deviates from equilibrium, and a uniform temperature cannot be assigned to the sample. Instead one can define a local temper-

Initial Depth [μK]	Final Depth [μK]	N_{start}	T_{start} [μK]	T_{equil} [μK]	η_{start}	η_{equil}
257	84	2.92×10^{10}	36	17	7.1	4.9
238	84	2.81×10^{10}	35	17	6.8	4.9
218	84	2.77×10^{10}	34	17	6.4	4.9

Table 9.1: Parameters describing initial and final conditions for rf cut experiments where ϵ_{start} was varied. The initial and final trap depths were defined by the applied rf field. The values of N_{start} and T_{start} were found to give best agreement between experiment and simulation. T_{equil} and η_{equil} are values from the simulation at $t = 10$ s. The best agreement was found in all cases with $\tau_{\text{laser}} = 30$ s.

ature as described in Sec. 8.4.2. Figure 9-5 shows snapshots of the local temperature versus energy at various times. The calculation corresponds to the rf cut experiment with an initial trap depth of 257 μK and a final trap depth of 84 μK and corresponds to the simulation shown in the upper panel of Fig. 9-4. At $t = 0.2$ s the rf cut has not affected atoms at energies less than 90 μK. After 1 s the trap depth has been reduced to 84 μK, and the atoms at higher energies have begun to equilibrate to the new trap depth. The rf cut produces a flux of atoms that move toward lower energies (see Sec. 9.3.1), setting the stage for the formation of a condensate. At $t = 2.8$ s the atoms at higher energy have a local temperature of ~ 20 μK, but the low-energy atoms remain at the original temperature. The formation of the condensate consumes the excess low-energy atoms, and the local temperature drops rapidly, relaxing toward its equilibrium value. The snapshot at $t = 10$ s shows the effects of truncation, but we can estimate the equilibrium temperature after the cut to be $T_{\text{equil}} \sim 17$ μK, giving $\eta = 84/17 = 4.9$.

Evolution of chemical potential

The large perturbation of the energy distribution caused by the rf cut makes it impossible to describe the trapped sample with a single chemical potential. In analogy with the assignment of a local temperature, we can describe the energy distribution with a local chemical potential. For a nondegenerate gas of bosons in equilibrium the

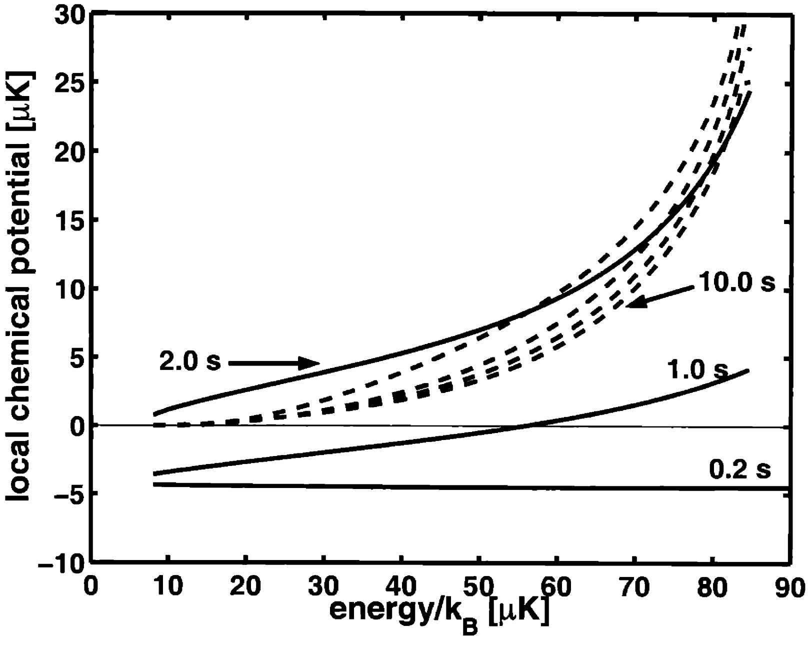

Figure 9-6: Time-evolution of the chemical potential during rf cut experiment. The chemical potential of the condensate is not shown.

chemical potential is negative, $\mu < 0$. In a system with condensed and noncondensed components in equilibrium $\mu_{\mathrm{c}} = \mu_{\mathrm{th}}$, where μ_{c} and μ_{th} represent the condensate and noncondensate chemical potentials, respectively. The rf cut experiment causes the system to evolve between these two states. Snapshots of the local chemical potential are shown in Fig. 9-6.

The rf cut causes the chemical potential of the noncondensed gas to increase rapidly, leading to a flux of particles toward lower energies and the formation of a condensate. This process is depicted in Fig. 9-6 for the rf cut experiment where the trap depth is lowered from 257 μK to 84 μK in $t_{\mathrm{rf}} = 1$ s. The calculation is identical to the one presented in the upper panel of Fig. 9-4. At $t = 0.2$ s the rf cut has not yet affected μ for particles with energies less than 90 μK. By the end of the rf cut at $t = 1$ s, the chemical potential of atoms at higher energies has increased above $\mu = 0$.[2] The negative slope in chemical potential from high to low energy indicates

---

[2] Recall that the simulation is carried out on a shifted energy scale. The chemical potential of

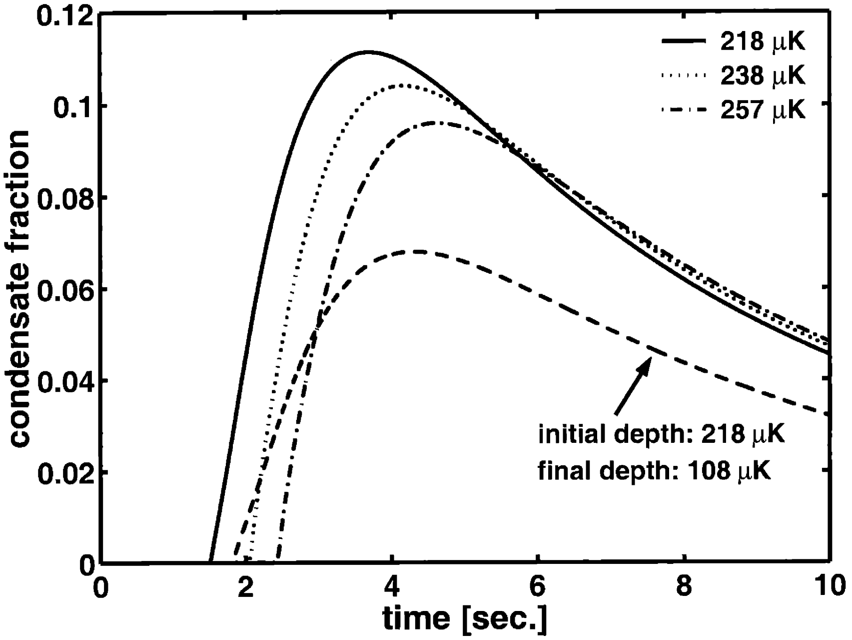

Figure 9-7: Time-evolution of the condensate fraction during rf cut experiments.

the flux of particles toward low energy. The slope becomes even steeper at $t = 2.0$ s, where $\mu > 0$ for all particles. As soon as the condensate forms, however, the excess low-energy particles is consumed by the condensate, and the local chemical potential is pinned to zero. At $t = 10$ s the slope in chemical potential remains, indicating the continued flux of particles toward lower energies.

It is important to note that without large dipolar-spin relaxation losses, Fig. 9-6 would look much different. The rf cut would still produce a condensate, but the system would approach $\mu_c = \mu_{th}$ much faster since there would be no replenishment of the condensate by the thermal cloud, i.e. no flux of particles toward lower energies.

Condensate fraction

The small elastic scattering length of hydrogen limits the equilibrium condensate fraction to a few percent. Strong dipolar spin-relaxation losses in the low-energy

---

the condensate sets the energy scale and is a function of time. See Sec. 8.2.1

portion of the system effectively heat the gas. This heating is balanced by evaporative cooling, but the small elastic scattering length limits the cooling power and in turn the condensate fraction. Even so, the rf cut procedure results in significant deviations from the equilibrium condensate fraction.

Figure 9-7 shows the condensate fraction, $f = N_c/(N_c + N_{th})$, as a function of time for four rf cut experiments. The calculations correspond to those presented in Fig. 9-4 and Fig. 9-8. The three largest fractions are attained by $t_{rf} = 1$ s rf cuts to a final trap depth of 84 μK. The largest fraction is achieved by the sample that started closest to the Bose-Einstein transition at a trap depth of 218 μK. The other samples formed later and resulted in smaller condensate fractions since fewer atoms were used during the cooling of the sample following the cut. The smallest condensate fraction, indicated by the dashed line, resulted from a $t_{rf} = 1$ s rf cut from a 218 μK deep trap to a 108 μK deep trap. The starting conditions were identical to those for the largest fraction, but the cut was less severe and more atoms were used to cool the sample following the cut, resulting in a later formation and a smaller condensate fraction.

A few seconds after formation the condensate fraction curves become indistinguishable within the errors of our calculation. This suggests that a balance has been reached between the number of atoms in the thermal cloud and the number of atoms in the condensate for a particular trap depth. Similar behavior is seen for the number of condensate atoms in Fig. 7-19.

9.3.2 Varying the Ending Frequency of RF Cuts

A second comparison between theory and experiment was made for experiments in which the ending point of the rf cut, ϵ_{rf}, was varied. The total condensate signal is plotted as a function of time in Fig. 9-8 along with simulations of the experiments. The experimental data corresponds to Fig. 7-16 in which the noncondensed cloud was cooled into a 218 μK (4.55 MHz) deep trap before a $t_{rf} = 1$ s rf cut lowered the trap depth to a variable final value. The upper panel of Fig. 9-8 shows the experiment with a final trap depth of 84 μK. The lower panel contains the result of a less severe

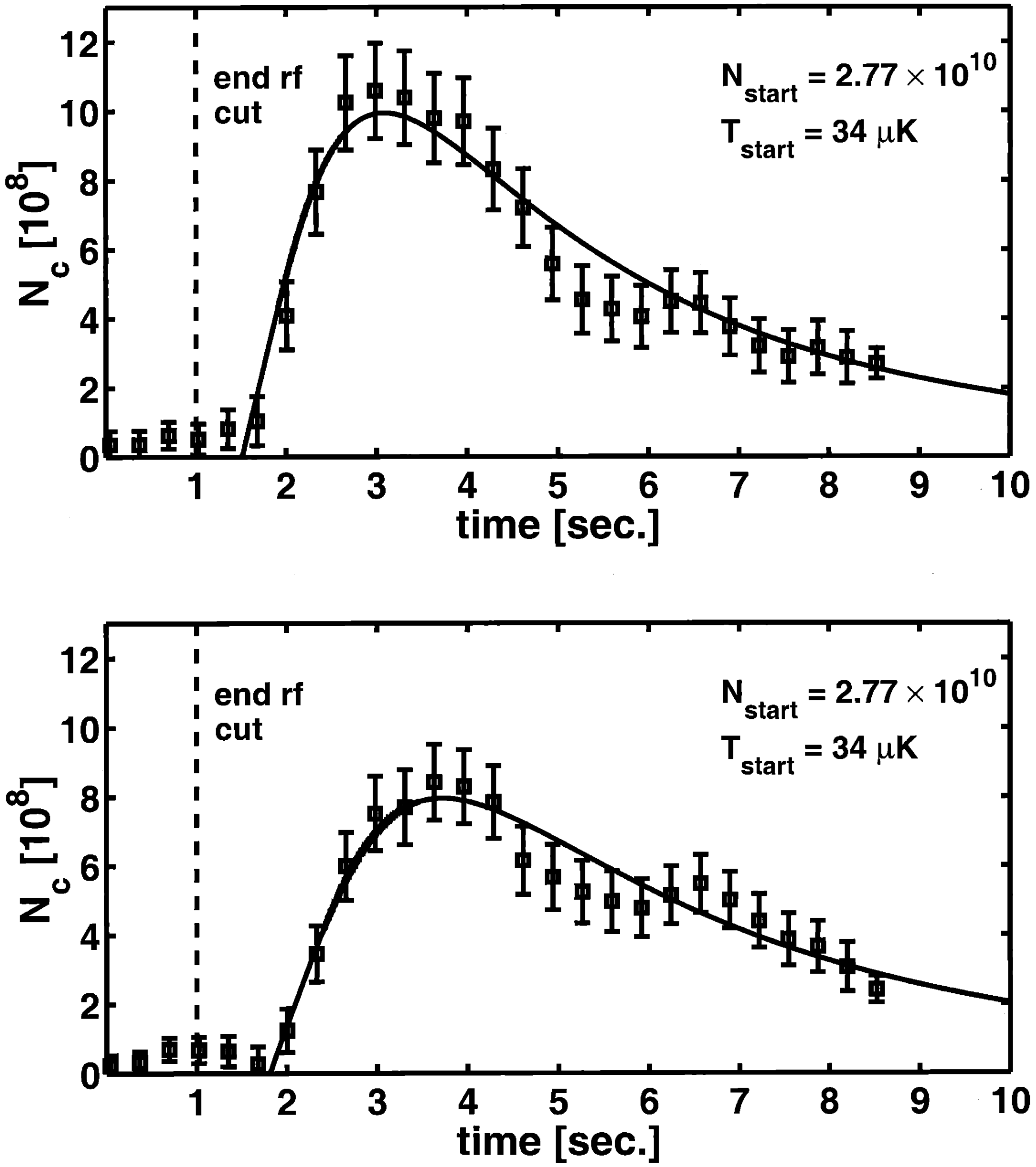

Figure 9-8: Comparison of calculations with experiments in which $\epsilon_{\rm rf}$ was varied. $\tau_{\rm laser} = 30$ s in each calculation.

rf cut to a final trap depth of 108 μK. The truncation of the energy distribution is less severe, and condensate in the lower panel takes longer to form and reaches a smaller maximum population.

The simulation again compares favorably with experiment. A fitting procedure identical to the one described in Sec. 9.3.1 was used to determine the constant required to scale the data to match the simulation. Although the physics behind the simulation is the same as for experiments in which ϵ_{start} was varied, the good agreement increases our confidence in the reliability of the model. It is important to note that identical initial conditions, N_{start} and T_{start}, produce favorable agreement between data and calculation for two different experiments. All four figures of merit (onset time, maximum amplitude, time of maximum, and decay slope) differ because the final trap depths differ. If the model were missing some key piece of physics, it would be difficult to obtain good agreement with one experiment without having poor agreement with the other.

9.4 Extracting a Value for a_{1S-2S}

The sensible values of N_{start}, T_{start}, and τ_{laser} required to obtain good agreement between calculation and the experiments in Sec. 9.3 give us confidence that we have determined the condensate population as a function of time. A second way to extract the number of condensate atoms versus time is to fit a Thomas-Fermi (TF) wavefunction to the condensate spectrum. Recall from Sec. 2.5.2 that the density profile of the condensate, $n_{\text{c}}(\mathbf{r})$, is given by Eq. (2.25). The peak condensate density, n_{p}, occurs at $\mathbf{r} = 0$ and is related to the condensate population through Eq. (2.27). During spectroscopy of the Doppler-sensitive $1S$-$2S$ transition, the cold-collision shift (see Sec. 5.5.4) maps the density distribution of the condensate, $n_{\text{c}}(\mathbf{r})$, to frequency (see Sec. 6.3.1). By extracting the peak frequency shift, Δ_{p}, we can find n_{p}, provided we know the conversion factor, χ, that relates frequency shift to density. Knowledge of n_{p} in turn allows us to find the condensate population through Eq. (2.27).

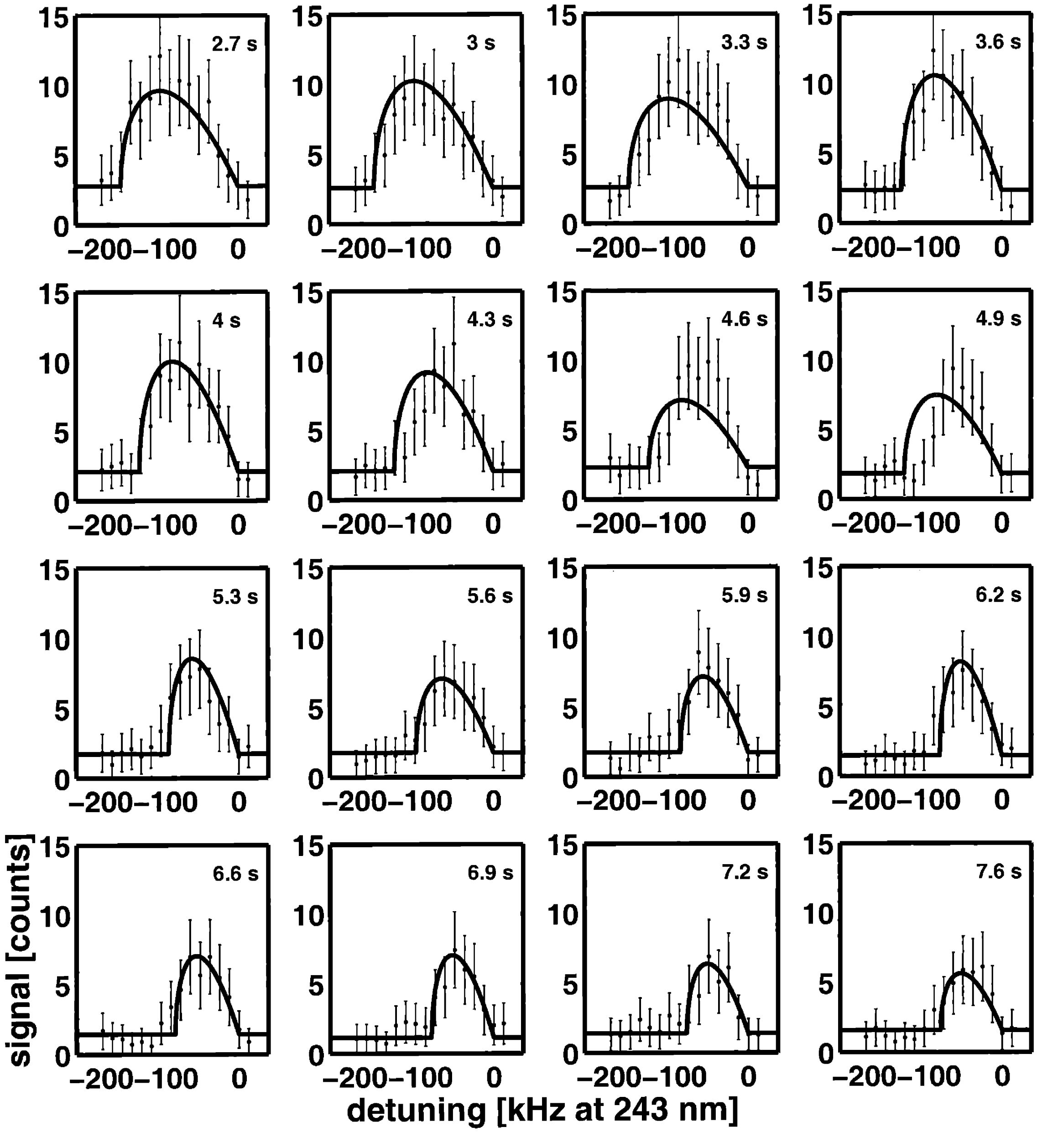

Figure 9-9: Fits of the Thomas-Fermi wavefunction to Doppler-sensitive condensate spectra. The fits to spectra taken during the decay of the condensate are better since the condensate lineshape is changing more slowly than during the growth.

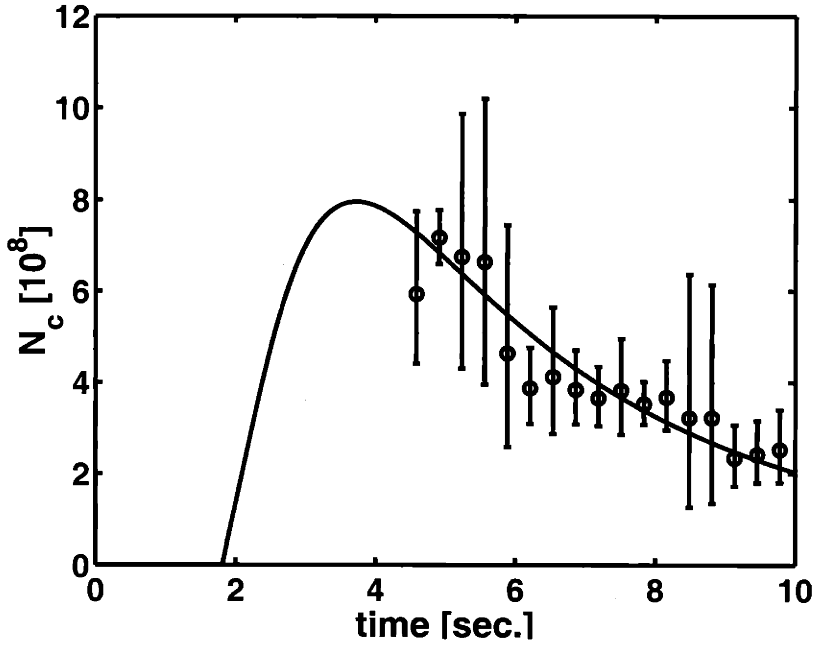

Figure 9-10: Comparison of the condensate number determined through fits of the Thomas-Fermi wavefunction and a simulation.

Figure 9-9 shows sixteen sequential Doppler-sensitive spectra taken during an rf cut experiment. Four repetitions of the experiment were added together to increase the signal-to-noise ratio. Also shown are individual fits of the Thomas-Fermi wavefunction to the spectra. Each panel is labeled with the time the spectrum was recorded, and $t = 0$ s corresponds to the beginning of the rf cut. The condensate reaches its maximum size around $t = 3$ s. Since each spectra requires 0.3 s to record, spectra taken during the decay of the condensate are better fit than spectra taken during the growth because the condensate population changes more slowly during the decay. The decay of the condensate is easily seen in the shrinking extent of the TF wavefunction: a smaller peak shift indicates a smaller peak density and a smaller condensate population.

After the Doppler-sensitive spectra were fit with the Thomas-Fermi wavefunction to determine the peak frequency shift due to the condensate, a fitting procedure was used to extract a value for a_{1S-2S}. The theory describing the cold-collision frequency shift of atoms excited out of a condensate is well-established. For a $1S$ atom excited out of a condensate in a homogeneous system, its single-photon resonance frequency is shifted by

$$\Delta\omega = \frac{4\pi\hbar n_{1S}}{m}\left(a_{1S-2S} - a_{1S-1S}\right) \tag{9.8}$$

where n_{1S} is the density of $1S$ atoms. Although the experimental system has an inhomogeneous density, it is usually argued that local density approximation (see Sec. 6.3.1) can be used to take inhomogeneity into account. The description of the observed condensate lineshape by a Thomas-Fermi wavefunction is an example of the validity of the local density approximation.

Using Eq. (9.8) and our fitted values for Δ_p, we can find n_p provided we know a_{1S-2S}. But n_p is related to N_c through Eq. (2.27), and we know $N_\mathrm{c}(t)$ from the simulations. As a result we can use a fitting procedure to determine the value of a_{1S-2S} that gives the best agreement between $N_\mathrm{c}(t)$ and $\Delta_\mathrm{p}(t)$. An example of such a fitting procedure is shown in Fig. 9-10 for the rf cut experiment in which the initial trap depth is reduced from 218 μK to 108 μK in 1 s. Fits similar to those shown in Fig. 9-9 were used to determine $\Delta_\mathrm{p}(t)$. For some data points large uncertainty in the determination of Δ_p leads to large error bars in Fig. 9-10. The result of fitting all of the data modeled with the condensate growth simulation gives best agreement with $a_{1S-2S} = -2.6 \pm 0.5$ nm.

9.5 Implications for the "Factor of Two" Problem

The cold-collision frequency shift of the $1S$-$2S$ transition in atomic hydrogen has generated several recent theoretical papers [85, 86, 90]. Each paper finds that the collisional frequency shift of the two-photon $1S$-$2S$ resonance in a condensate of atomic hydrogen is a factor-of-two smaller than for a noncondensed gas at the same density. The value of a_{1S-2S} extracted above suggests that the collisional frequency shift is the same for a condensate and noncondensed gas. This is the "factor-of-two" problem.

In 1998 we reported a value of $a_{1S-2S} = -1.4 \pm 0.3$ nm based on measurements of the collisional shift per density for excitations out of a noncondensed cloud. The shift per density was measured to be $\Delta\nu_{1S-2S} = -3.8 \pm 0.8 \times 10^{-10}\, n$ Hz cm^3, where n is the sample density. The interpretation of the data was based on the prevailing theoretical result for excitations of a homogeneous, noncondensed gas

$$\Delta\omega_{1S-2S} = \frac{8\pi\hbar n_{1S}}{m}\left(a_{1S-2S} - a_{1S-1S}\right) \ . \tag{9.9}$$

Using $a_{1S-2S} = -1.4 \pm 0.3$ nm with Eq. (9.8) leads to unreasonably high condensate populations and fractions, suggesting that there is something wrong with applying either Eq. (9.8) or Eq. (9.9) to our system. Note that comparisons with our simulations of condensate growth are sensitive to a_{1S-2S} since it is raised to the 5/2 power to obtain N_c.

The additional factor of two for the shift in the normal gas relies on correlations between the excited $2S$ state and the $1S$ background. For example, if a $2S$ atom were brought from the moon and placed into a gas of $1S$ atoms, it would be a distinguishable particle and would not be correlated with the $1S$ background. Its energy levels would be shifted by an amount $4\pi\hbar^2 a_{1S-2S} n_{1S}/m$. Thus, if the $2S$ atoms we excite are not correlated with the $1S$ background, we should not expect to see a factor of two difference in the collisional frequency shift.

It is likely that the duration of excitation plays a role in our factor of two problem. An assumption of the theories that produce Eq. (9.8) and Eq. (9.9) is that the excitation process is short compared to other time scales in the problem. In our experiments, however, a typical laser excitation pulse lasts 1 ms. The average speed for an atom at 35 μK is $v_{mp} = \sqrt{8k_BT/\pi m} = 86$ cm/s, implying that the atom can move 860 μm during the excitation! Not every atom will move this far during the laser excitation, but this estimate is enough to cast doubt on the assumption that the excitation is instantaneous. For this reason there may *not* be a factor of two difference in the collisional frequency shift for atoms excited from condensed and noncondensed clouds. Instead the frequency shift for the noncondensed gas is likely given by the result without correlations between the excited and ground states

$$\Delta\omega_{1S-2S} = \frac{4\pi\hbar n_{1S}}{m}\left(a_{1S-2S} - 2a_{1S-1S}\right) \ . \tag{9.10}$$

If this is the case, our 1998 measurement of a_{1S-2S} becomes $a^{98}_{1S-2S} = -2.8\pm0.6$ nm, in good agreement with both the value extracted in this thesis, $a^{01}_{1S-2S} = -2.6\pm0.5$ nm, and a recent theoretical calculation [87], $a^{\text{th}}_{1S-2S} = -3.0$ nm.[3]

Our explanation resolves a number of discrepancies between values of a_{1S-2S}, but it does not explain the lack of correlations during $1S - 2S$ excitation. An interesting experiment to further explore this question is to measure the mean shift of the noncondensed spectrum for various excitation pulse lengths. If the excitation pulse is short enough, it may be possible to see a change in the shift per density of the noncondensed atoms due to the reappearance of correlations between the excited $2S$ atom and the $1S$ background. Such an experiment could be viewed as a direct measurement of $g_2(\mathbf{r})$, the two-body correlation function.

---

[3] No uncertainty is given for this calculation, but it is believed accurate to within 20%.

Appendix A

Epoxy Coating of G-10 Tubes

A.1 Purpose

The first question one might ask is, "Why coat G-10 tubes with epoxy?" The answer is three-fold. First, and most importantly, if G-10 is to be used as a vacuum system component, one would like it to be leak-tight at room temperature. Even though raw G-10 is leak-tight at 4 K, one usually wishes to perform leak checks at room temperature. Second, if the tube is used as part of a superfluid jacket, one wishes phonons to reflect specularly from the tube surface in order to increase thermal conductivity. Raw G-10 has a very rough surface which would lead to diffuse reflection and a decrease in the thermal conductivity of the jacket. Finally, if the G-10 tube is to be further coated with a thin metal film, one desires a smooth, defect free surface. A properly applied epoxy coating can achieve all of these things.

A.2 Procedure

There are two important steps in creating a smooth, bubble-free epoxy coating of G-10 tubes: G-10 surface preparation and bubble-free epoxy preparation.

A.2.1 Preparing the G-10

The G-10 tubes received from Spaulding Composites [33] were dusty and rough. Because G-10 consists of a woven fiberglass fabric impregnated with epoxy, it tends to have small fibers sticking out from its surface as well as small, open voids in the epoxy. These fibers and voids are not well wetted by epoxy so they must be removed. Sandpaper of 180 grit seemed to be effective. The surface was *sanded wet* until it appeared uniform and smooth to the touch.

Sanding inside the tube was not quite as simple. A stiff rod with sandpaper attached to the outside with double-stick tape was tried. Unfortunately, the sandpaper makes only point contact with the tube, resulting in an unevenly sanded surface. A superior method employed a section of 1.5" OD red rubber hose. A 3/8" wide slit ~16" long was cut along the length of the tube to allow it to fit easily inside the 1.5" ID tube. Next, a 5" long piece of 180 grit sandpaper was attached to the outside of the hose near its end using double-stick tape. (The slit was left open.) Once inside the G-10 tube, the rubber hose expanded, making fairly uniform contact with the G-10 surface. This allowed about 14" from each end of the tube to be wet sanded evenly. To sand the center of the tube required another method.

Sanding the inside center of the tube required a modification of the rubber hose method. This time a short section (~2") was slit and covered with sandpaper. Two discs of Teflon 1/4" thick and 1-7/16" diameter were fabricated and a long nylon cord attached. The cord and discs allowed the rubber hose to be pulled through the tube. By pulling the contraption back and forth through the tube, the inside center section was sanded until the inside surface of the tube appeared uniform.

Finally, two small holes were drilled in one end of the tube to allow suspension during curing. After drilling and sanding, the inside and outside of the tube were wiped with water and then methanol. The tubes were then set aside while the epoxy was prepared.

A.2.2 Epoxy Preparation

The exact preparation will vary from epoxy to epoxy. Here Epon Resin 828 [29] and Jeffamine D-230 catalyst [57] were used. The epoxy should be mixed as follows: 100 parts Epon 828 to 32 parts Jeffamine D-230 by weight. For coating one 1.5" ID, 31" long tube, 325 g (100 parts) of 828 were mixed with 104 g (32 parts) of D-230.[1]

The two components should be mixed by folding, much like a cake. The best results were obtained while mixing at 45° C using a hot plate. Warming the mixture dramatically decreases its viscosity. As a result, any trapped air bubbles can escape. In addition the low viscosity allows the G-10 surface to be better wetted during coating. The mixture should be continuously folded until it is *completely* clear. Only a few very small air bubbles should be visible. The bubbles are removed by pumping on the epoxy mixture in a glass jar for about five minutes. The clear, bubble-free mixture is then carefully poured into a trough.

A.2.3 Coating Trough

The long tubes are covered with epoxy via roll coating. A 3" diameter, 41" long, 1/8" thick Plexiglas tube, was sawed in half along its axis. Two wooden feet were then attached to prevent it from rocking. Before each tube is coated, the Plexiglas is lined with aluminum foil turned up at the ends to form a trough.

A.2.4 Roll Coating

The G-10 tube was laid carefully into the trough of epoxy. It was then slowly rotated several times. Any air bubbles appearing on the surface were popped by hand. The tube was then gently lifted from one end. Any remaining bubbles were popped, and the tubes were placed in an oven to cure.

---

[1] For mixing I used the digital balance in the sample preparation room 13-3143. It has a 1250 g capacity.

A.2.5 Curing Oven

The curing oven consists of a 3-1/4" diameter, 36" long, 1/32" thick stainless tube wrapped with heater tape and controlled with a variac. The freshly coated tubes were suspended vertically in the oven using a small wire. The tubes cured at 40 C in the oven for 14 hours. They were then cured at 60 C for 6 hours and 90 C for one hour.

A.3 Results

Carefully following this procedure produced a shiny, bubble-free epoxy coating of the inside and outside of long (31") G-10 tubes. The most important points to remember are adequate surface preparation and warm mixing to enable de-airing of the epoxy.

Appendix B

Copper Plating of G-10 Tubes

The purpose of coating the inside of the cell tube with a thin metallic layer was discussed in Sec. 4.1.3. This appendix explains the choice of coating method and material and lists the steps involved in the coating process. It also describes the techniques used to measure the quality of the metallic coating.

B.1 Coating Methods Considered

Several coating methods were considered, but the requirement that the coating is located on the inside of a plastic-like tube eliminated most options. For example, it is common to "flash-coat" a thin metallic layer on a plastic surface. In this process, a tungsten filament coated with the metal of choice is heated until the metal boils off in a "flash." This process has the ideal geometry for coating the inside of a tube, but a G-10 tube would melt or catch fire in such close proximity to the hot filament. In the end, the process of dip coating was chosen.

In dip coating, baths of various chemicals are used to wash, prime, and plate the metal of choice. The thickness of the resulting coating is controllable by varying immersion time in the plating bath. The drawback is that there are very few metals that can be chemically plated onto a non-metallic surface. For example, we are unaware of a process that can deposit gold onto a non-metallic surface using only chemical methods. In the end, we selected copper to coat the inside of the cell for three basic reasons: copper is a good electrical conductor, copper is non-magnetic, and plating methods exist to deposit a thin layer in a confined geometry. We have no reasons to recommend against this choice in the future.

B.2 Method

The G-10 tube used in the construction of the trapping cell was coated by Epner Technologies in Brooklyn, New York. We visited the production facility to gain understanding about the coating process and to assist the coating technicians in producing a very thin film. Unfortunately, we were not allowed to witness the proprietary coating process which takes place in a series of temperature-controlled, circulating baths. However, we did learn that the coating process consists of the following steps:

1. The G-10 tube, pre-coated with Epon 828 epoxy, is roughened with 100 grit sandpaper where the coating is to be applied.
2. The tube is rinsed with plain water.
3. The tube is then placed in an "activator" solution for a few minutes. This acidic solution continues the preparation of the surface to be coated.
4. The tube is quickly rinsed with plain water.
5. The tube is placed into a "pre-coating" solution for $\sim$15 minutes. In this step a monolayer film of palladium is deposited from solution.
6. The tube is rinsed with plain water.
7. The tube is submerged in a 110 °F copper plating solution for tens of seconds. Although different lengths of time were tried, 60 seconds produced the best coating.
8. The tube is rinsed with plain water.

When the copper first plates onto the surface, it appears black in color, perhaps due to the formation of oxides. For longer plating times, it appears more reddish. For thin coatings, one should stop the plating process soon after the coating appears black. The black surface can be removed with a moistened Kim-wipe, revealing a thin copper layer.

Immediately after the plating process, the copper layer can be removed very easily. However, after 1-2 days of drying, the layer is much more robust and survives the "Scotch tape test." This test consists of firmly applying and then removing a piece of Scotch tape from the surface. If none of the coating is removed by the tape, it is considered robust.

The geometry of the tubes precludes an even coating thickness along the tube's length. The tube is immersed vertically in the plating bath, and the plating solution enters the ends of the tube. The solution near the ends of the tube is refreshed more often, resulting in a faster plating process and a gradient in the thickness of the coating. This gradient is revealed in Fig. 4-4 which shows the rf attenuation at 60 and 100 MHz at various locations along the coated tube.

B.3 Measurements

Resistance

The resistance of the applied coatings were measured using a four wire technique. The thinness of the coating makes reproducible resistance measurements difficult because the measurement probes can easily scratch through the coating. Small pads of brass shim stock (0.001“ thick) were used underneath the probes to protect the coating.

Electromagnetic field screening

Measurements of electrical screening due to the applied coating were made using two pairs of clamshell electrodes shown in Fig. B-1. These measurements were made to test the feasibility of having the Stark quenching electrodes in the helium jacket space

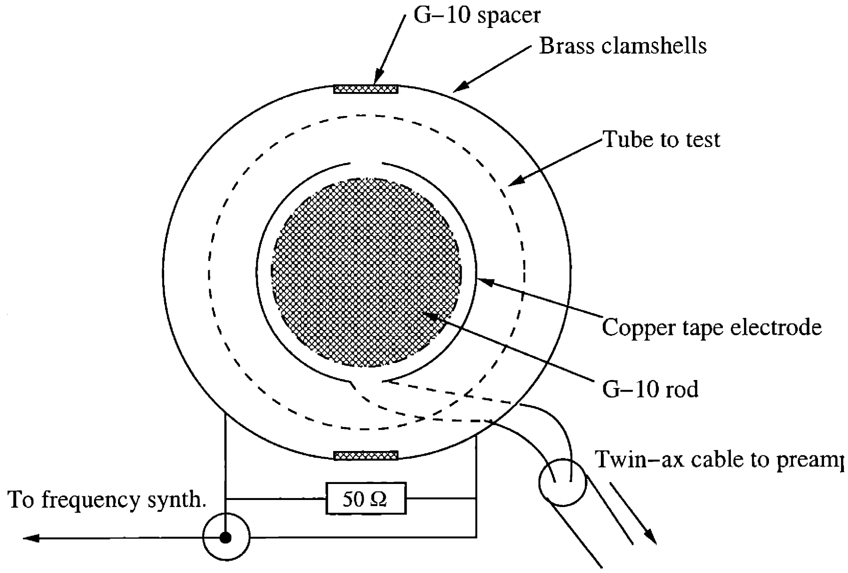

Figure B-1: Setup for measurement of electric field screening is shown. Two clamshell electrodes are used to drive and probe an applied ac electric field. RF magnetic field attenuation measurements were made using a similar arrangement in which the clamshells were replaced by two small loop antennas.

as in the previous cell design. The electrical screening by the copper-coated tube is excellent. We observed more than 82 dB suppression by the tube, corresponding to the noise floor of the network analyzer. For this reason, we used the copper coating itself to form the Stark quenching electrodes as described in Sec. 4.1.4.

The clamshells were replaced by two loop antennas and an arrangement similar to Fig. B-1 was used to measure the attenuation of rf magnetic fields by the Cu film. Attenuation measurements shown in Fig. B-2 were made by sweeping the rf frequency from 1 MHz to 100 MHz at 5 cm intervals along the length of the cell. The attenuation is less than 1 dB for the entire frequency range along most of the cell. The two locations at which the attenuation is greater than 1 dB correspond to the ends of the cell where the coating is thicker. See also Fig. 4-4.

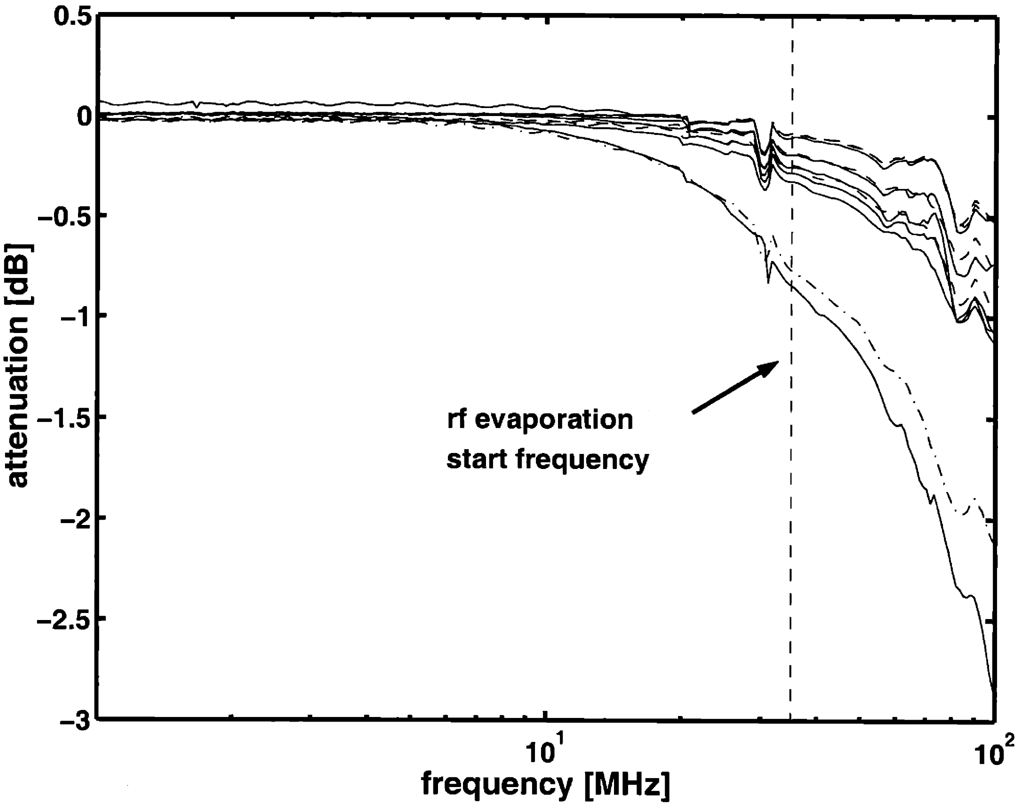

Figure B-2: The attenuation of an rf magnetic field is shown from 1 MHz to 100 MHz at 5 cm intervals along the length of the tube. Increased attenuation is found at the ends of the tube where the Cu coating is thicker.

Appendix C

Microchannel Plate Switching

To increase the detection efficiency of fluorescence photons during spectroscopy, we developed a switching scheme to rapidly change the gain of the microchannel plate detector (MCP) (see Sec. 5.3.1). In earlier experiments a Lyman-α filter was used to attenuate scatter from the 243 nm laser and prevent saturation of the detector. Unfortunately, the Lyman-α filter transmitted only 10% of the 122 nm fluorescence photons. For the experiments performed in this thesis, the Lyman-α filter was replaced by a MgF_2 window, and a switching scheme was implemented to turn on the gain of the upper MCP plate just in time to detect the Lyman-α fluorescence during each quench pulse.

The switching circuit was designed and built by Kendra Vant and Lorenz Willmann and is shown in Fig. C-1. The resistances and voltages are labelled with their room temperature values and differ by a few percent at low temperature. The switch is located outside the cryostat and controlled with a TTL signal. When the switch is closed (TTL high) the gain of the upper MCP plate is high because 675 V is applied across the plate, guiding electrons produced by the incident uv photon into the channels of the plate. When the switch is open (TTL low) the gain is low because there is only 130 V applied across the plates.

The second MCP plate is biased by 85 V with respect to the first to collect and amplify the electron shower. The 2100 V supplied to the resistive divider of the anode

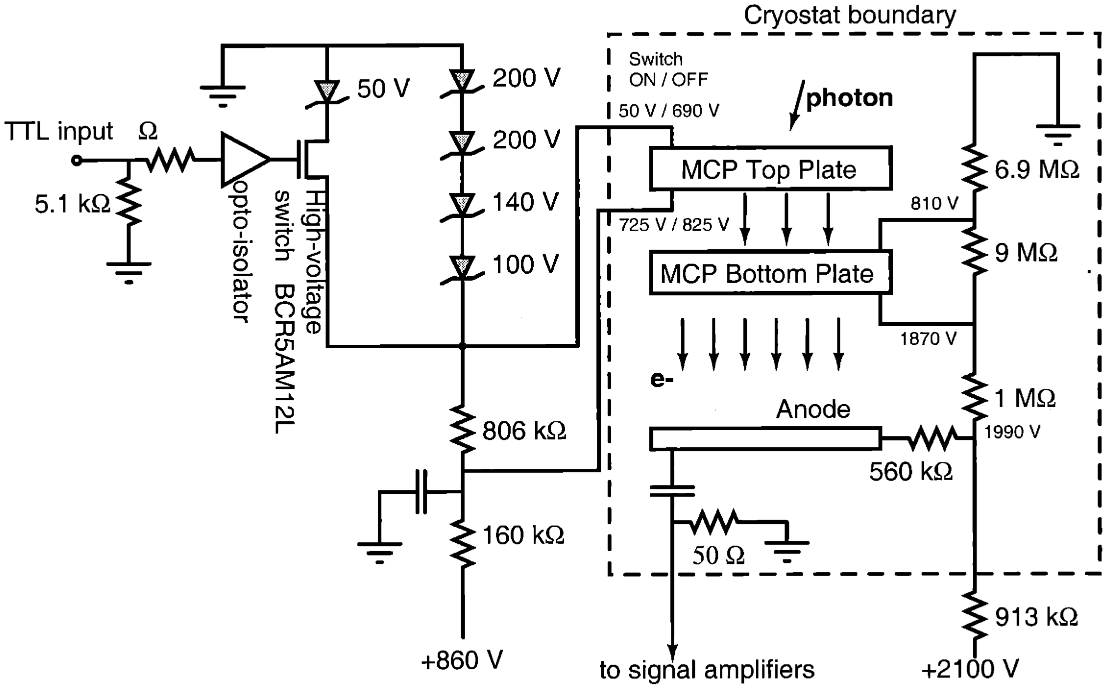

Figure C-1: Schematic of MCP switching circuit designed by Kendra Vant and Lorenz Willmann. The resistances and voltages are labelled with their room temperature values. The switch is controlled with a TTL signal enabling the voltage across the MCP Top Plate to change from 130 V to 675 V in a few microseconds. The maximum detection efficiency is reached ~ 1 ms after switching, indicating the charging time of the MCP plate.

and MCP bottom plate produces significant blackbody radiation and heats the cell bottom. To minimize heating the 2100 V supply is turned on immediately before the spectroscopy phase of the trapping cycle and turned off immediately afterwards.

The switching circuit allows the voltage across the upper MCP plate to change from 130 V to 675 V in a few microseconds, but it takes much longer for the MCP to reach maximum detection efficiency. A series of measurements were made in which we varied the time between switching on the MCP and quenching the $2S$ atoms. The number of photons incident on the detector was nominally the same. We found that the MCP requires at least 1 ms to reach maximum detection efficiency. The lead glass of the MCP plate requires a long time for electrons to charge its channels, especially at low temperature. We typically waited 1.4 ms after turning on the MCP before quenching the $2S$ atoms.

The implementation of MCP switching to increase the detection efficiency by a factor of four has been a success. The major limitation of this technique is the ~ 1 ms dead time between switching and maximum detection efficiency.

Bibliography

[1] Acheson Colloids Company, Port Huron, Michigan.

[2] M. H. Anderson, J. R. Ensher, M. R. Matthews, C. E. Wieman, and E. A. Cornell. Observation of Bose-Einstein condensation in a dilute atomic vapor. *Science*, 269:198, 1995.

[3] M. D. Barrett, J. A. Sauer, and M. S. Chapman. All-optical formation of an atomic Bose-Einstein condensate. *Phys. Rev. Lett.*, 87:010404, 2001.

[4] F. Bassani, J. J. Forncy, and A. Quattropani. Choice of gauge in two-photon transitions: $1S - 2S$ transition in atomic hydrogen. *Phys. Rev. Lett.*, 39:1070, 1977.

[5] T. Bergeman. Hartree-Fock calculations of Bose-Einstein condensation of ^{7}Li atoms in a harmonic trap for $T > 0$. *Phys. Rev. A*, 55:3658, 1997.

[6] Hans A. Bethe and Edwin E. Salpeter. *Quantum Mechanics of One- and Two-Electron Atoms.* Plenum Publishing Corporation, New York, 1977.

[7] M. J. Bijlsma, E. Zaremba, and H. T. C. Stoof. Condensate growth in trapped Bose gases. *Phys. Rev. A*, 62:063609, 2000.

[8] Note that Eq. (50) of Ref. [7] contains a misprint. The quantity a_- must be defined as $2(\mu_c - \bar{\epsilon})/\hbar\bar{\omega}$.

[9] F. Biraben, M. Bassani, and B. Cagnac. Line-shapes in Doppler-free two-photon spectroscopy. The effect of finite transit time. *J. Phys. (Paris)*, 40:445, 1979.

[10] F. Biraben, J. C. Garreau, and L. Julien. Determination of the Rydberg constant by Doppler-free two-photon spectroscopy of hydrogen Rydberg states. *Europhys. Lett.*, 2:925, 1986.

[11] N. Bogoliubov. On the theory of superfluidity. *J. Phys. USSR*, 11:23, 1947.

[12] C. C. Bradley, C. A. Sackett, and R. G. Hulet. Bose-Einstein condensation of lithium: Observation of limited condensate number. *Phys. Rev. Lett.*, 78:985, 1997.

[13] C. C. Bradley, C. A. Sackett, J. J. Tollett, and R. G. Hulet. Evidence of Bose-Einstein condensation in an atomic gas with attractive interactions. *Phys. Rev.Lett.*, 75:1687, 1995.

[14] Yvan Castin. Bose-Einstein condensates in atomic gases: simple theoretical results. In R. Kaiser, C. Westbrook, and F. David, editors, *Coherent atomic matter waves*, Lecture Notes of Les Houches Summer School 1999, page 1. EDP Sciences and Springer-Verlag, 2001.

[15] C. L. Cesar, D. G. Fried, T. C. Killian, A. D. Polcyn, J. C. Sandberg, I. A. Yu, T. J. Greytak, D. Kleppner, and J. M. Doyle. Two-photon spectroscopy of trapped atomic hydrogen. *Phys. Rev. Lett.*, 77:255, 1996.

[16] Claudio L. Cesar. *Two-Photon Spectroscopy of Trapped Atomic Hydrogen*. PhD thesis, Massachusetts Institute of Technology, November 1995.

[17] Kasturi L. Chopra. *Thin Film Phenomena*. McGraw-Hill Book Company, New York, 1969.

[18] R. Côté and V. Kharchenko. Quasicondensate droplet formation in a gas of trapped atomic hydrogen. *Phys. Rev. Lett.*, 83:2100, 1999.

[19] Franco Dalfovo, Stefano Giorgini, Lev P. Pitaevskii, and Sandro Stringari. Theory of Bose-Einstein condensation in trapped gases. *Rev. Mod. Phys.*, 71:463, 1999.

[20] K. Damle, S. N. Majumdar, and S. Sachdev. Phase ordering kinetics of the Bose gas. *Phys. Rev. A*, 54:5037, 1996.

[21] K. B. Davis, M.-O. Mewes, M. R. Andrews, N. J. van Druten, and D. S. Durfee. Bose-Einstein condensation in a gas of sodium atoms. *Phys. Rev. Lett.*, 75:3969, 1995.

[22] M. J. Davis, C. W. Gardiner, and R. J. Ballagh. Quantum kinetic theory. VII. The influence of vapor dynamics on condensate growth. *Phys. Rev. A*, 62:063608, 2000.

[23] B. DeMarco and D. S. Jin. Onset of Fermi degeneracy in a trapped atomic gas. *Science*, 285:1703, 1999.

[24] J. M. Doyle, J. C. Sandberg, N. Masuhara, I. A. Yu, D. Kleppner, and T. J. Greytak. Energy distributions of trapped atomic hydrogen. *J. of the Opt. Soc. Am. B*, 6:2244, 1989.

[25] John M. Doyle. *Energy Distribution Measurements of Magnetically Trapped Spin Polarized Atomic Hydrogen: Evaporative Cooling and Surface Sticking.* PhD thesis, Massachussetts Institute of Technology, 1991.

[26] R. W. P. Drever, J. L. Hall, F. V. Kowalski, J. Hough, G. M. Ford, A. J. Munley, and H. Ward. Laser phase and frequency stabilization using an optical resonator. *Appl. Phys. B*, 31:97, 1983.

[27] U. Eckern. Relaxation processes in a condensed Bose-gas. *J. Low Temp. Phys.*, 54:333, 1984.

[28] A. Einstein. Quantentheorie des einatomigen idealen Gases: Zweite Abhandlung. *Sitzungber. Preuss. Akad. Wiss.*, 1925:3, 1925.

[29] Miller-Stephenson Chemical Company, Inc., Danbury, CT 06810, (203) 743-4447.

[30] J. T. Folinsbee and A. C. Anderson. The Kapitza resistance to a variety of metallic surfaces below 0.3 K. *Journal of Low Temperature Physics*, 117:409, 1974.

[31] D. G. Fried, T. C. Killian, L. Willmann, S. Moss, D. Kleppner, and T. J. Greytak. Bose-Einstein condensation of atomic hydrogen. *Phys. Rev. Lett.*, 81:3811, 1998.

[32] Dale G. Fried. *Bose-Einstein Condensation of Atomic Hydrogen.* PhD thesis, Massachusetts Institute of Technology, June 1999.

[33] Spaulding Composites Co., P. O. Box 687, 1300 S. Seventh St., DeKalb, IL 60115-0867, 815-758-0096.

[34] C. W. Gardiner and A. S. Bradley. Theory of the cold collision frequency shift in $1S$-$2S$ spectroscopy of Bose-Einstein condensed and non-condensed hydrogen. Private communication, August 2001.

[35] C. W. Gardiner, M. D. Lee, R. J. Ballagh, M. J. Davis, and P. Zoller. Quantum kinetic theory of condensate growth: Comparison of experiment and theory. *Phys. Rev. Lett.*, 81:5266, 1998.

[36] C. W. Gardiner and P. Zoller. Quantum kinetic theory: A quantum kinetic master equation for condensation of a weakly interacting Bose gas without a trapping potential. *Phys. Rev. A*, 55:2902, 1997.

[37] C. W. Gardiner, P. Zoller, R. J. Ballagh, and M. J. Davis. Kinetics of Bose-Einstein condensation in a trap. *Phys. Rev. Lett.*, 79:1793, 1997.

[38] J. M. Gerton, D. Strekalov, I. Prodan, and R. G. Hulet. Direct observation of growth and collapse of a Bose-Einstein condensate with attractive interactions. *Nature*, 408:692, 2000.

[39] K. Gibble and S. Chu. Laser-cooled Cs frequency standard and a measurement of the frequency shift due to ultracold collisions. *Phys. Rev. Lett.*, 70:1771, 1993.

[40] T. J. Greytak and D. Kleppner. In G. Grynberg and R. Stora, editors, *New Trends in Atomic Physics*. North-Holland, Amsterdam, 1984.

[41] E. P. Gross. Structure of a quantized vortex in boson systems. *Nuovo Cimento*, 20:454, 1961.

[42] E. P. Gross. Hydrodynamics of a superfluid condensate. *J. Math. Phys.*, 4:195, 1963.

[43] A. H. Guth. Inflationary universe: A possible solution to the horizon and flatness problems. *Phys. Rev. D*, 23:347, 1981.

[44] T. W. Hänsch and B. Couillaud. Laser frequency stabilization by polarization spectroscopy of a reflecting reference cavity. *Opt. Commun.*, 35:411, 1980.

[45] T. W. Hansch, S. A. Lee, R. Wallenstein, and C. Wieman. Doppler-free two-photon spectroscopy of hydrogen $1S$-$2S^*$. *Phys. Rev. Lett.*, 34:307, 1975.

[46] M. E. Hayden, M. D. Hürlingmann, and W. N. Hardy. Measurement of atomic-hydrogen spin-exchange parameters at 0.5 K using a cryogenic hydrogen maser. *Phys. Rev. A*, 53:1589, 1996.

[47] C. E. Hecht. The possible superfluid behavior of hydrogen atom gases and liquids. *Physica*, 25:1159, 1959.

[48] P. C. Hendry, N. S. Lawson, R. A. M. Lee, P. V. E. McClintock, and C. H. D. Williams. Generation of defects in superfluid He-4 as an analog of the formation of cosmic strings. *Nature (London)*, 368:315, 1994.

[49] H. F. Hess, G. P. Kochanski, J. M. Doyle, N. Masuhara, D. Kleppner, and T. J. Greytak. Magnetic trapping of spin-polarized hydrogen. *Phys. Rev. Lett.*, 59:672, 1987.

[50] Harald F. Hess. Evaporative cooling of magnetically trapped and compressed spin-polarized hydrogen. *Phys. Rev. B*, 34:3476, 1986.

[51] T. W. Hijmans, Yu. Kagan, G. V. Shlyapnikov, and J. T. M. Walraven. Bose condensation and relaxation explosion in magnetically trapped atomic hydrogen. *Phys. Rev.B*, 48:12886, 1993.

[52] M. Holland, J. Williams, and J. Cooper. Bose-Einstein condensation: Kinetic evolution obtained from simulated trajectories. *Phys. Rev. A*, 55:3670, 1997.

[53] R. Holzwarth, Th. Udem, T. W. Hänsch, J. C. Knight, W. J. Wadsworth, and P. St.J. Russell. Optical frequency synthesizer for precision spectroscopy. *Phys. Rev. Lett.*, 85:2264, 2000.

[54] M. Houbiers and H. T. C. Stoof. Stability of Bose condensed atomic ^{7}Li. *Phys. Rev. A*, 54:5055, 1996.

[55] Kerson Huang. *Statistical Mechanics.* John Wiley & Sons, New York, second edition, 1987.

[56] D. Jaksch, C. W. Gardiner, and P. Zoller. Quantum kinetic theory. II. Simulation of the quantum Boltzmann master equation. *Phys. Rev. A*, 56:575, 1997.

[57] Texaco Chemical Company, Houston, TX 77056.

[58] Yu. Kagan and A. E. Muryshev. The spectral properties of non-condensate particles in Bose-condensed atomic hydrogen. *Phys. Lett. A*, 278:159, 2000.

[59] Yu. Kagan, B. V. Svistunov, and G. V. Shlyapnikov. Effect of Bose condensation on inelastic processes in gases. *JETP Lett.*, 42:209, 1985.

[60] Yu. M. Kagan, B. V. Svistunov, and G. V. Shlyapnikov. Kinetics of Bose condensation in an interacting Bose gas. *Sov. Phys. JETP*, 75:387, 1992.

[61] R. Kallenbach, C. Zimmerman, D. H. McIntrye, and T. W. Hänsch. A blue dye laser with sub-kilohertz stability. *Opt. Commun.*, 70:56, 1989.

[62] W. Ketterle, K. B. Davis, M. Joffe, M. A. Martin, and D. E. Pritchard. Invited oral presentation at the Annual Meeting of the Optical Society of America, Toronto, Canada, October 3-8 1993.

[63] W. Ketterle and N. J. van Druten. Evaporative cooling of trapped atoms. In *Advances in Atomic, Molecular, and Optical Physics*, volume 37, page 181. Academic Press, New York, 1996.

[64] T. W. B. Kibble. Topology of cosmic domains and strings. *J. Phys. A*, 9:1387, 1976.

[65] T. C. Killian, D. G. Fried, L. Willmann, D. Landhuis, S. Moss, T. J. Greytak, and D. Kleppner. Cold collision frequency shift of the $1S$-$2S$ transition in hydrogen. *Phys. Rev. Lett.*, 81:3807, 1998.

[66] Thomas C. Killian. *1S-2S Spectroscopy of Trapped Hydrogen: The Cold Collision Frequency Shift and Studies of BEC.* PhD thesis, Massachusetts Institute of Technology, February 1999.

[67] Thomas C. Killian. $1S$-$2S$ spectrum of a hydrogen Bose-Einstein condensate. *Phys. Rev. A*, 61:033611, 2000.

[68] T. R. Kirkpatrick and J. R. Dorfman. Transport coefficients in a dilute but condensed Bose-gas. *J. Low Temp. Phys.*, 58:399, 1985.

[69] T. R. Kirkpatrick and J. R. Dorfman. Transport in a dilute but condensed nonideal Bose-gas – kinetic equations. *J. Low Temp. Phys.*, 58:301, 1985.

[70] S. Klarsfeld. Radiative decay of metastable hydrogenic atoms. *Phys. Lett.*, 30A:382, 1969.

[71] D. Kleppner. Trapped atomic hydrogen. In G. F. Bassani, M. Ignuscio, and T. W. Hänsch, editors, *The Hydrogen Atom*, page 103. Springer-Verlag, Berlin, 1989.

[72] M. Köhl, T. W. Hänsch, and T. Esslinger. Growth of Bose-Einstein condensates from thermal vapor. *cond-mat/0106642*, 2001.

[73] David Landhuis. *Decay of Metastable Hydrogen.* PhD thesis, Harvard University, 2001.

[74] S. A. Lee, R. Wallenstein, and T. W. Hänsch. Hydrogen $1S$-$2S$ isotope shift and $1S$ Lamb shift measured by laser spectroscopy. *Phys. Rev. Lett.*, 35:1262, 1975.

[75] E. Levich and V. Yakhot. Time evolution of a Bose system passing through the critical point. *Phys. Rev. B*, 15:243, 1977.

[76] E. Levich and V. Yakhot. Time development of coherent and superfluid properties in the course of a Lambda-transition. *J. Phys. A*, 11:2237, 1978.

[77] A. D. Linde. A new inflationary universe scenario - a possible solution of the horizon, flatness, homogeneity, isotropy and primordial monopole problems. *Phys. Lett. B*, 108:389, 1982.

[78] F. London. On the Bose-Einstein condensation. *Phys. Rev.*, 54:947, 1938.

[79] O. J. Luiten, M. W. Reynolds, and J. T. M. Walraven. Kinetic theory of evaporative cooling of a trapped gas. *Physical Review A*, 53:381, 1996.

[80] O. J. Luiten, H. G. C. Werij, I. D. Setija, M. W. Reynolds, T. W. Hijmans, and J. T. M. Walraven. Lyman-α spectroscopy of magnetically trapped atomic hydrogen. *Phys. Rev. Lett.*, 70:544, 1993.

[81] California Fine Wire Company, Grover Beach, CA 93433.

[82] N. Masuhara, J. M. Doyle, J. C. Sandberg, D. Kleppner, and T. J. Greytak. Evaporative cooling of spin-polarized hydrogen. *Phys. Rev. Lett.*, 61:935, 1988.

[83] H.-J. Miesner, D. M. Stamper-Kurn, M. R. Andrews, D. S. Durfee, S. Inouye, and W. Ketterle. Bosonic stimulation in the formation of a Bose-Einstein condensate. *Science*, 279:1005, 1998.

[84] C. Monroe, E. Cornell, C. Sackett, C. Myatt, and C. Wieman. Measurement of Cs-Cs elastic scattering at $T = 30\ \mu$K. *Phys. Rev. Lett.*, 70:414, 1993.

[85] M. O. Oktel, T. C. Killian, D. Kleppner, and L. S. Levitov. Cold collision frequency shift of an optical spectrum of a trapped gas, 1999.

[86] M. O. Oktel and L. S. Levitov. Optical excitations in a nonideal Bose gas. *Phys. Rev. Lett.*, 83:6, 1999.

[87] T. Orlikowski, G. Staszewska, and L. Wolniewicz. *Molecular Physics*, 96:1445, 1999.

[88] R. K. Pathria. *Statistical Mechanics.* Butterworth Heinemann, Oxford, first edition, 1972.

[89] W. Pauli. The connection between spin and statistics. *Physical Review*, 58:16, 1940.

[90] C. J. Pethick and H. T. C. Stoof. Collisional frequency shifts of absorption lines in an atomic hydrogen gas. *Phys. Rev. A*, 64:013618, 2001.

[91] P. W. H. Pinske, A. Mosk, M. Weidemüller, M. W. Reynolds, T. W. Hijmans, and J. T. M. Walraven. Resonance enhanced two-photon spectroscopy of magnetically trapped atomic hydrogen. *Phys. Rev. Lett.*, 79:2423, 1997.

[92] P. W. H. Pinske, A. Moske, M. Weidemuller, M. W. Reynolds, T. W. Hijmans, and J. T. M. Walraven. One-dimensional evaporative cooling of magnetically trapped atomic hydrogen. *Phys. Rev. A*, 57:4747, 1998.

[93] L. P. Pitaevskii. Vortex lines in an imperfect Bose gas. *Sov. Phys. JETP*, 13:451, 1961.

[94] Frank Pobell. *Matter and Methods at Low Temperatures.* Springer, Berlin, second edition, 1996.

[95] D. E. Pritchard. Cooling neutral atoms in a magnetic trap for precision spectroscopy. *Physical Review Letters*, 51:1336, 1983.

[96] D. E. Pritchard, K. Helmerson, and A. G. Martin. In S. Haroche, J. C. Gay, and G. Grynberg, editors, *Atomic Physics*, volume 11, page 179. World Scientific, Singapore, 1989.

[97] N. P. Proukakis and K. Burnett. Generalized mean fields for trapped atomic Bose-Einstein condensates. *J. Res. Natl. Stand. Technol.*, 101:457, 1996.

[98] N. P. Proukakis, K. Burnett, and H. T. C. Stoof. Microscopic treatment of binary interactions in the nonequilibrium dynamics of partially Bose-condensed trapped gases. *Phys. Rev. A*, 57:1230, 1998.

[99] J. Reichert, M. Niering, R. Holzwarth, M. Weitz, Th. Udem, and T. W. Hänsch. Phase coherent vacuum-ultraviolet to radio frequency comparison with a mode-locked laser. *Phys. Rev. Lett.*, 84:3232, 2000.

[100] A. Robert, O. Sirjean, A. Browaeys, J. Poupard, S. Nowak, D. Boiron, C. I. Westbrook, and A. Aspect. A Bose-Einstein condensate of metastable atoms. *Science*, 292:461, 2001.

[101] J. L. Roberts, N. R. Claussen, S. L. Cornish, E. A. Donley, E. A. Cornell, and C. E. Wieman. Controlled collapse of a Bose-Einstein condensate. *Phys. Rev. Lett.*, 86:4211, 2001.

[102] P. A. Ruprecht, M. J. Holland, K. Burnett, and M. Edwards. Time-dependent solution of the nonlinear Schrödinger equation for Bose-condensed trapped neutral atoms. *Phys. Rev. A*, 51:4704, 1995.

[103] S. Sachdev. *Quantum Phase Transitions.* Cambridge University Press, Cambridge, 1999.

[104] C. A. Sackett, J. M. Gerton, M. Weiling, and R. G. Hulet. Measurements of collective collapse in a Bose-Einstein condensate with attractive interactions. *Phys. Rev. Lett.*, 82:876, 1999.

[105] C. A. Sackett, H. T. C. Stoof, and R. G. Hulet. Growth and collapse of a Bose-Einstein condensate with attractive interactions. *Phys. Rev. Lett.*, 80:2031, 1998.

[106] J. J. Sakurai. *Modern Quantum Mechanics.* Addison-Wesley, Reading, Massachusetts, revised edition, 1994.

[107] Jon C. Sandberg. *Research Toward Laser Spectroscopy of Trapped Atomic Hydrogen.* PhD thesis, Massachusetts Institute of Technology, May 1993.

[108] F. Pereira Dos Santos, J. Léonard, J. Wang, C. J. Barrelet, F. Perales, E. Rasel, C. S. Unnikrishnan, M. Leduc, and C. Cohen-Tannoudji. Bose-Einstein condensation of metastable helium. *Phys. Rev. Lett.*, 86:3459, 2001.

[109] D. V. Semikoz and I. I. Tkachev. Kinetics of Bose condensation. *Phys. Rev. Lett.*, 74:3093, 1995.

[110] I. D. Setija, H. G. C. Werij, O. J. Luiten, M. W. Reynolds, T. W. Hijmans, and J. T. M. Walraven. Optical cooling of atomic hydrogen in a magnetic trap. *Phys. Rev. Lett.*, 70:2257, 1993.

[111] I. F. Silvera and J. T. M. Walraven. Spin-polarised atomic hydrogen. In D. F. Brewer, editor, *Progress in Low Temperature Physics*, volume X. North-Holland, Amsterdam, 1986.

[112] D. W. Snoke and J. P. Wolfe. Population dynamics of a Bose gas near saturation. *Phys. Rev. B*, 39:4030, 1988.

[113] H. T. C. Stoof. Formation of the condensate in a dilute Bose gas. *Phys. Rev. Lett*, 66:3148, 1991.

[114] H. T. C. Stoof. Nucleation of Bose-Einstein condensation. *Phys. Rev. A*, 45:8398, 1992.

[115] H. T. C. Stoof. Atomic Bose gas with a negative scattering length. *Phys. Rev. A*, 49:3824, 1994.

[116] H. T. C. Stoof. Initial stages of Bose-Einstein condensation. *Phys. Rev. Lett.*, 78:768, 1997.

[117] H. T. C. Stoof. Coherent versus incoherent dynamics during Bose-Einstein condensation in atomic gases. *J. Low Temp. Phys.*, 114:11, 1999.

[118] H. T. C. Stoof and M. Bijlsma. Dynamics of fluctuating Bose-Einstein condensates. *J. Low Temp. Phys.*, 124(3,4), 2001.

[119] H. T. C. Stoof, A. M. L. Janssen, J. M. V. A. Koelman, and B. J. Verhaar. Decay of spin-polarized atomic hydrogen in the presence of a Bose condensate. *Phys. Rev. A*, 39:3157, 1989.

[120] H. T. C. Stoof, J. M. V. A. Koelman, and B. J. Verhaar. Spin-exchange and dipole relaxation rates in atomic hydrogen: Rigorous and simplified calculations. *Phys. Rev. B*, 38:4688, 1988.

[121] W. C. Stwalley and L. H. Nosanow. Possible "new" quantum systems. *Phys. Rev. Lett*, 36:910, 1976.

[122] Emerson & Cumming Inc., Canton, Massachusetts.

[123] E. L. Surkov, J. T. M. Walraven, and G. V. Shlyapnikov. Collisionless motion of neutral particles in magnetostatic traps. *Phys. Rev. A*, 49:4778, 1994.

[124] E. L. Surkov, J. T. M. Walraven, and G. V. Shlyapnikov. Collisionless motion and evaporative cooling of atoms in magnetic traps. *Phys. Rev. A*, 53:3403, 1996.

[125] B. V. Svistunov. Highly nonequilibrium Bose condensation in a weakly interacting gas. *J. Mosc. Phys. Soc.*, 1:373, 1991.

[126] A. G. Truscott, K. E. Strecker, W. I. McAlexander, G. B. Partridge, and R. G. Hulet. Observation of Fermi pressure in a gas of trapped atoms. *Science*, 291:2570, 2001.

[127] J. H. Tung, X. M. Ye, G. J. Salamo, and F. T. Chan. Two-photon decay of hydrogenic atoms. *Phys. Rev. A*, 30:1175, 1984.

[128] R. van Roijen, J. J. Berkhout, S. Jaakkola, and J. T. M. Walraven. Experiments with atomic hydrogen in a magnetic trapping field. *Phys. Rev. Lett*, 61:931, 1988.

[129] J. T. M. Walraven. In G. L. Oppo, S. M. Barnett, E. Riis, and M. Wilkinson, editors, *Quantum Dynamics of Simple Systems.* Institute of Physics Publishing, Bristol, 1994.

[130] R. Walser, J. Williams, J. Cooper, and M. Holland. Quantum kinetic theory for a condensed bosonic gas. *Phys. Rev. A*, 59:3878, 1999.

[131] R. L. Walsworth, I. F. Silvera, E. M. Mattison, and R. F. C. Vessot. Measurement of a hyperfine-induced spin-exchange frequency shift in hydgrogen. *Phys. Rev. A*, 46:2495, 1992.

[132] M. Weitz, F. Schmidt-Kaler, and T. W. Hänsch. Precise optical Lamb shift measurements in atomic hydrogen. *Phys. Rev. Lett.*, 68:1120, 1992.

[133] L. Willmann. Private communication, September 2001.

[134] W. Wing. On neutral particle trapping in quasistatic electromagnetic fields. *Prog. Quant. Elect.*, 8:181, 1984.

[135] I.A. Yu. *Ultracold Surface Collisions: Sticking Probability of Atomic Hydrogen on Superfulid* ^4He. PhD thesis, Massachussetts Institute of Technology, 1993.

[136] E. Zaremba, T. Nikuni, and A. Griffin. Dynamics of trapped Bose gases at finite temperatures. *J. Low Temp. Phys.*, 116:277, 1999.

[137] W. H. Zurek. Cosmological experiments in superfluid-helium. *Nature (London)*, 317:505, 1985.